GSI

6th Workshop on Heavy-Charged Particles in Biology and Medicine

Baveno
September 29, 30 and October 1, 1997

Book of Abstracts

G. Kraft, K. Langbein

29 - 17

6th Workshop on Heavy-Charged Particles in Biology and Medicine

Baveno
Sept. 29, 30 and October 1, 1997

Book of Abstracts

Editors: G. Kraft & K. Langbein

PREFACE

The idea to organize this meeting in the lovely landscape of northern Italy was born two years ago when we thought that the heavy-ion therapy at GSI would have already started then with patient treatment and that for the TERA project the first building would be under construction.

However, we have been too optimistic and we have not yet reached these goals. Heavy-ion therapy at GSI is close to start. All necessary tests have been performed and the test protocols are submitted to the government. The installation of a novel control and safety system, that fulfills the laws for the application of beams in therapy, took much more effort than anticipated. Also the dosimetry of a scanned carbon beam turned finally out to be more difficult than predicted by the specialists. In addition, inverse treatment planning including the dependence of RBE on the particle spectrum and the tissues' radiosensitivity is a complex and tedious task, again taking more time than suggested before.

In order to cover at least some of these aspects in greater detail we decided to change the topics of our workshop so that treatment planning and dosimetry are found to be more extended than before. But the basic radiobiology like DNA damage, cell inactivation and mutation are still essential parts of the program.

An independent session of modelling, however, disappeared simply by asking the modellers to calculate with their approach the specific case of the inactivation by a particle beam penetrating a water like tissue and to compare it with measurements. Since only a few responses came they are now integrated in the treatment planning session.

Finally, I hope that the session of clinical results, new techniques and future projects will provide strong motivations for the work still to be done in the future.

Gerhard Kraft

6th Workshop on Heavy-Charged Particles in Biology and Medicine
Baveno, Sept. 29, 30 and October 1

Introduction

L. Skarsgard
(Cancer Research Center,
Canada)

Radiobiology with Heavy Charged Particles: A
Historical Review

A

DNA Damage and Repair
K. Prise, B. Rydberg (Chair)

Oral Presentations

1. Kevin Prise
   (Mount Vernon Hospital,
   Northwood, UK)

   A Study of DNA Fragmentation Patterns in Cells
   Irradiated with Charged Particles: Evidence for non-
   random Distributions

2. Björn Rydberg
   (LBNL Berkeley, USA)

3. Gisela Taucher-Scholz
   (GSI, Darmstadt, Germany)
4. Mauro Belli
   (INFN, Rome, Italy)
5. Kai Rothkamm
   (Univers, Gießen, Germany)
6. Bernd Dusemund
   (Univers. d. Saarlandes,
   Germany)
7. Zengquan Wei
   (Chin. Aca. of Sc. Lanzhou,
   China)

Track-Structure Effects on Biological Targets: DNA
Double-Strand Break Induction and Rejoining
DNA Damage Induction and Processing after
Irradiation with Different Light Ions
Heavy-Ion-Induced DNA Double-Strand-Breaks in
Yeast and Man: Differences and Similarities
Structural and Quantitative Aspects of Radical
Formation after Heavy-Ion Bombardment

Carbon-Ion-induced DNA Double-Strand Breaks in
Melanophore B_{16}

Posters

8. Erik Höglund
   (Uppsala Univers., Sweden)
9. Daniela Keller
   (GSI, Darmstadt, Germany)
10 Wolfgang Schonert
   (GSI, Darmstadt, Germany)
11 Barbara Weiland
   (Uni. des Saarlandes,
   Homburg, Germany)
12 Anne-Kathrin Hoffmann
   (Uni. des Saarlandes,
   Homburg, Germany)

Initial DNA Fragmentaion Induced by Radiation of
Different Linear Energy Transfer
Double-Strand Break Induction along a Particle Track:
Visualization of Different Fragment Sizes
Investigation of Radiation Induced DNA Breaks Using
Scanning Tunneling Microscopy
Free Radicals from DNA after Irradiation with Heavy
Ions or X-Rays: a Highfield EPR Study at 8.7T and 245
Ghz
Heavy-Ion-Induced Damage to DNA Constituents:
Product Formation

B

1. Walter Schimmerling
   (NASA, Washiington, USA)
2. Thomas Streibel
   (Univers. Siegen, Germany)
3. Manfred Schäfer
   (DLR Cologne, Germany)

Space Research (Chair Walter Schimmerling)

Oral Presentations

Radiation in Space

Cross Sections and Kinematics of Proton nduced
Fragmentation of Carbon
Inactivation Probalility as a Function of the Distance
from the Particle's Path Measured with Spores of
Bacillus Subtilis and Using an Image Analyzing System

C

1. Sylvia Ritter
   (GSI, Darmstadt, Germany)
2. Marco Durante
   (Univers. Federico „Neapel II",
   Italy)
3. Karin Füssel
   (GSI, Darmstadt, Germany)
4. Jürgen Kiefer
   (Strahlenzentrum,Univers.
   Gießen, Germany)
5. Fumio Yatagai
   (Inst. Phys. Chem.Res.,
   Saitama, Japan)
6. Hermann Rink
   (Univers. Bonn, Germany)
7. Shigemitsu Tano
   (Jap. Atom. Energ. Res. Inst,
   Takasaki, Japan)

Mutation and Chromosome Aberration
S. Ritter (Chair)

Oral Presentations

Particle-Induced Chromosome Aberration and
Mutations:an Overview
Heavy-Ion-Induced Chromosomal Aberrations
Analyzed by Fluorescence in Situ Hybridization

Comparison of RBE for Inactivation and Chromosomal
Damage of High-Energy Carbon Ions
Mutations Induced by Heavy-Ions: Cross Sections,
RBE and Molecular Patterns

Analysis of Mutations in the Human HPRT Gene
Induced by Heavy-Ion Irradiation

HPRT Mutations in V79 Cells: Type of Lesions
Dependent on LET
Structural Changes of DNA in Heavy-Ion-Induced
Mutants on Arabidopsis

Posters

8. Robert Katz
   (Univers. of Nebraska, USA)
9. Paul Schmidt
   (Strahlenzentrum,Univers.
   Gießen, Germany)

Track Theory Estimates of Single Particle Traversals of
Cell Nuclei
Molecular Spectra of Heavy-Ion-Induced Mutations

D

1. Koichi Ando
   (Nat. Inst. Rad. Science, Chiba,
   Japan)
2. Jürgen Debus
   (Univers. Heidelberg,
   Germany)
3 Claudia Fournier
   (GSI, Darmstadt, Germany)

Cell and Tissue Radiobiology
K. Ando (Chair)

Oral Presentations

Mouse Skin Damages Caused by Fractionated
Irradiation with Carbon Ions

Conformal Radiotherapy with Volume-Scanned Carbon
Ions - Relative Biological Effectiveness in the Rat
Spinal Cord
Human Fibroblasts as a Model for Healthy Tissue in
Radiotherapy

| 4. | Hiroshi Watanabe (Jap. Atom. Res. Energ. Inst. , Takasaki, Japan) | Influence of Penetration Controlled Irradiation with Charged Particles on Tobacco Pollen |

4. Hiroshi Watanabe
   (Jap. Atom. Res. Energ. Inst. , Takasaki, Japan)
   Influence of Penetration Controlled Irradiation with Charged Particles on Tobacco Pollen

5. L. Distel
   (Univers. Erlangen-Nürnberg, Germany)
   First Biological Experiments at the Vertical Proton Beam

6. Milos Lokajicek
   (Academy of Science, Prague, Czech Republic)
   Inactivation Mechanism of Different Radiation Kinds, Shapes of Survival Curves and Deviations from LQ Model

7. D. Choudhary
   (Jawaharlal Nehru Univers., New Dehli, India)
   Effect of 45 MeV 7Li and 68 MeV ^{16}O Charged Particles on Biological Membranes

Posters

8. Martin Moosburger
   (Ludwig-Max.-Univers. München, germany)
   Status of the Vertical Beam Facility at the Munich Tandem Accelerator

9. Mayank Srivastava
   (Jawaharlal Nehru Univers., New Dehli, India)
   Effects of 45 MeV and 68 MeV Charged Particles on Microsomal Membrance Fluidity

10 A. Touati
   (Univers. Paris 7 and 6, France)
   Experimental Determination of the Contribution of Carbon K-Ionizations to the RBE for Cell Inactivation by Ultrasoft X-Rays

11 Gianfranco Grossi
   (Inst Sup. San. and INFN, Roma, Italy)
   Survival of Human Cells Exposed to Acute and Fractionated Doses of Low-Energy Protons

12 Daniel Zukowski
   (Uni Mainz, Germany)
   Cellular Response of V79 Spheroids Exposed to High Energy Carbon Ions

13 Mirjam Fritsch
   (Uni Erlangen, Germany)
   First Experiments at a Vertical Proton Beam

E

Treatment Planning I: The Role of Clinical RBEs
A. Kellerer (Chair)

Oral Presentations

1. A.Kellerer (Introduction)
   (LMU, Munich, Germany)
   Accounting for Radiation Quality in Heavy Ion Therapy

2. Michael Scholz
   (GSI, Darmstadt, Germany)
   Estimation of Clinical RBE for Carbon Therapy

3. Alessandro Campa
   (Inst Sup. San. and INFN, Roma, Italy)
   RBE evaluation of Therapeutic Proton Beams in Computer Simulations

4. Andrea Ottolenghi
   (Uni. Milano, INFN, Italy)
   Analysis of a Slowing down 150 MeV Proton Beam in Water: Physical Characteristics and Effectiveness in Inducing DNA Clustered Damage

5. Robert Katz
   (Univers. of Nebraska, USA)
   Treatment Planning Problems with Range Modulated Heavy Ion Beams

Posters

6. Nina Tilly
   (Uni. Stockholm, Sweden)
   The Contribution by Inelastic Nuclear Interactions to the RBE of Protons

F

Treatment Planning II: Dose Optimization and Inverse Planning
M. Benassi (Chair)

Oral Presentations

1. Oliver Jäkel
   (DKFZ, Heidelberg, Germany)

   Treatment Planning for Heavy Ion Irradiation I

2. Michael Krämer
   (GSI, Darmstadt, Germany)

   Treatment Planning for Heavy Ion Irradiation II

3. Yoshihisa Takada
   (Uni. Tsukuba, Japan)

   SOBP Formation by Two-Dimensional Array of Cone Filter

4- Uli Weber
   (GSI, Darmstadt, Germany)

   Bragg-Peak Widening Using a Ripple Filter

5. Enzo Menapace
   (ENEA, Bologna, Italy)

   The Role of Nuclear Constants for Applications Related to the Proton Radiotherapy

6. Dieter Schardt
   (GSI, Darmstadt, Germany)

   Nuclear Fragmentation of 270 MeV/u ^{12}C Ions in Water

7. Ivan Petrovic
   (Vinca, INS, Belgrade, Yugoslavia)

   SRNA: A Monte Carlo Code for Proton Transport Simulation

Poster

8. Angela Mitaroff
   (GSI, Darmstadt, Germany)

   Investigation of Treatment Planning Using Biological and Thermoluminescence Detectors

G

Dosimetry Kanai/Goitein (Chair)

Oral Presentations

1. Tatsuaki Kanai
   (Chiba, Japan)

   Three-Year Experiences of Heavy-Ion Dosimetry at HIMAC

2. Adolf Coray
   (PSI, Villingen, Switzerland)

   Monitoring the Dose Delivery for the Spot Scanning at PSI

3. S. Onori
   (Ist. di San., Rome, Italy)

   Recent Developments in the Measurement of Dose Distributions in the Framework of the Top Project

4. Maurizio Rosetti
   (ENEA, Rome, Italy)

   Proton Energy Determinations in Water and in Tissue-Like Material

5. Günter Hartmann
   (DKFZ Heidelberg, Germany)

   Carbon Ion Dosimetry at GSI Using Ionization Chambers

6. Marco Donetti
   (INFN, Torino, Italy)

   First Results on Magic Cube 3-D Dosimeter

7. Oliver Geiss
   (GSI, Darmstadt, Germany)

   TLD Dosimetry of Heavy-Ion Beams

8 R.F. Laitano
   (ENEA, Rome, Italy)

   Effects of Thermal Conduction and Convection on Temperature Profile in a Water Calorimeter for Proton Beams

9. Antonio Guerra
   (ENEA, Rome, Italy)

   Water Calorimetry with Thermistor Bridge Operated in DC and AC Mode: Comparative Results

Posters

10 Belinda Bathelt
   (GSI Darmstadt, Germany)

   Film Dosimetry with Heavy-Charged Particles

11 G.C. Bonazzola
   (INFN, Torino, Italy)

   A VLSI Circuit for the Charge Measurement of a Strip Ionization Chamber

12	Caterina Brusasco (GSI Darmstadt, Germany)	A Detection System for the Verification of 3-D Dose Distributions in light-ion Radiotherapy
13	E. Casnati (Uni. Ferrara and INFN, Italy)	Effects of the Inhomogeneity between Wall and Gas in Ionometric Proton Dosimetry
14	E. Gargioni	Effects of Thermal Conduction and Convection on Temperature Profiles in a Water Calorimeter for Proton Beams
15	Peter Heeg (Uni. Klin. Heidelberg, Germany)	Development and Application of an Initial Quality Assurance Program for Dosimetry at GSI
16	Marija Radojcic (VINCA Belgrade, Yugoslavia)	Absorbed Dose Distribution Measurements in Radiotherapy
17	Ulla Ramm (Uni. Klin. Frankfurt, Germany)	Heavy-Ion Dosimetry with Magnetic Resonance Imaging of Polymer Gels

H

Clinical Results of Particle Therapy and New Techniques
G. Munkel (Chair)

Oral Presentations

1.	Gudrun Munkel (PSI Villingen, Switzerland)	New Techniques and Clinical Results of Particle Therapy - Introduction
2.	Ira Spiro (Harvard Uni. Boston, USA)	Clinical Experience with Protons at the Harvard Cyclotron Laboratory and Future Plans at the North-East Proton Therapy
3.	J.Slater (Loma Linda, USA)	Loma Linda Results
4.	Hirohiko Tsujii (Nat. Inst. of Rad. Snc. Chiba, Japan)	Clinical Trials of Carbon-Ion Therapy at NIRS
5.	Jörg Pawelke (FZ Rossendorf, Dresden, Germany)	Positron Emission Tomography for Quality Assurance of Heavy Ion Therapy
6.	Terence Boehringer (PSI Villingen, Switzerland)	Quality Assurance Procedures for the Proton-Therapy Project
7.	Christian Schilling (PSI Villingen, Switzerland)	Real Time Tumor Tracking
8.	Bernd Voss (GSI Darmstadt, Germany)	Requirements, Design and Performance of a Monitoring System for Heavy-Ion Radiotherapy

Poster

| 9. | Rainer Hinz
(FZ Rossendorf, Dresden, Germany) | Pre-Clinical Studies on PET Monitoring of Heavy Ion Therapy at GSI Darmstadt |
| 10 | Martin Moosburger
(LMU Munich, Germany) | A Detectorsystem for Proton Radioagraphy at PSI |

I

Status Reports and Future Developments

Oral Presentations

| 1. | U. Amaldi (Chair)
(CERN, Geneva, Switzerland) | Overview of the World Landscape of Hadrontherapy and the Projects of the TERA Foundation |
| 2. | G. Kraft | Heavy-Ion Therapy at GSI - A Status Report |

(GSI Darmstadt, Germany)

3. T. Auberger   Status AUSTRON
    (Uni. Vienna, Austria)

4. P.J. Bryant   Progress of the Proton-Ion Medical Machine Study
    (CERN Geneva, Switzerland)   (PIMMS)

5. M. Pavlovic   Gantries for light-ion cancer therapy
    (GSI Darmstadt, Germany)

6. S. Frullani   A Linear Accelerator for Oncological Protontherapy:
    (Ist. Sup. San. Rome, Italy)   TOP-LINAC

RADIOBIOLOGY WITH HEAVY CHARGED PARTICLES: A HISTORICAL REVIEW

Lloyd D. Skarsgard, Department of Medical Biophysics, B.C. Cancer Research Centre and TRIUMF, Vancouver, Canada

Berkeley, where it all began

The development at Berkeley of the first cyclotron by Ernest O. Lawrence and M.S. Livingston in 1932 marked the beginning of this field of investigation, since it provided the first means of accelerating heavy charged particles to high energy. In 1939 a larger 60" cyclotron, the Crocker Medical Cyclotron was completed, to be followed in 1948 by the 184" synchrocyclotron which continued in clinical use until the late 1980's. Initially the main biological and clinical use of these cyclotron beams (protons, deuterons, $\propto$-particles) was to produce fast neutrons. However, by the early 1940's a young graduate student of Louis Alvarez, Cornelius Tobias, began accelerating carbon ions in the 60" cyclotron. After a hiatus brought on by WWII, he and his colleagues at Berkeley returned to studies of accelerated charged particles, examining both the physical characteristics and biological effects of beams of high energy deuterons and $\propto$-particles. By the early 1960's a very comprehensive program of radiobiological studies on heavy charged particle beams had developed at Berkeley, led by Tobias. Initially, the beams were provided by the Heavy Ion Linear Accelerator, HILAC, which was capable of accelerating many different heavy ions to energies up to 10 MeV/amu (a similar accelerator was developed about this time at Yale University). In 1974 the BEVALAC (a marriage of the HILAC and the BEVATRON, a synchrotron) went into operation at Berkeley, providing energies up to 2 GeV/amu. This program continued until the 1990's and involved many staff and trainees at Berkeley as well as visiting scientists from other institutions around the world. In recent years, since Tobias' retirement, Eleanor Blakely has led this program.

The first clinical treatments with heavy ion beams at Berkeley began in 1954, using protons and deuterons and later plateau helium ions. The first treatments were not for malignant disease but rather the ion beams were used for radiosurgery: pituitary ablation and later, arteriovenous malformations (AVM). This was due in part to the severe late effects observed by Stone and his colleagues in cancer patients treated with neutrons from the Crocker Medical Cyclotron during the late 30's and early 40's. However radiation treatment of cancer with helium ion beams from the 184" synchrocyclotron began in the late '60's. In 1975, radiotherapy using the much heavier ions from the BEVALAC got underway, under the direction of Dr. Joseph Castro. These clinical programs continued until 1992 when, unfortunately, funding for the operation of the accelerators at Berkeley was discontinued.

Radiobiological studies of high LET radiations were also conducted at other centers during the early '60's, notably by Dr. Eddie Barendsen, using alpha particles and deuterons from the Hammersmith Cyclotron in London. Barendsen and his colleagues produced some of the first comprehensive plots of RBE and OER vs LET for mammalian cells, using these beams at Hammersmith. At about the same time, the biological effects of heavy ion beams in mammalian cells were examined by Deering and Skarsgard on the Yale HILAC.

Other proton and heavier ion facilities

By the early 1950's a 230 cm proton synchrocyclotron had been developed at Uppsala University in Sweden. Borje Larsson, a graduate student, was charged with developing a pituitary irradiation facility at Uppsala, patterned on the Berkeley system. Larsson also carried out biological studies using these proton beams. By the late 1950's and early '60's proton beams were in use at Uppsala for both small field cranial radiosurgery and large field, fractionated radiotherapy of tumours, the latter under the direction of Dr. Sten Graffman. This program continued until 1976, when it was interrupted for reconstruction of the accelerator. Treatments recommenced in 1989.

The third institution to use proton beams clinically was Harvard/MGH, instigated by neurosurgeons Dr. William Sweet and Dr. Ray Kjellberg. Their interest, again, was radiosurgery with

protons and they solicited the assistance of Andreas Koehler of the Harvard Cyclotron group, to develop the precise beam direction techniques needed for Bragg peak pituitary ablation, and later for treatment of AVM's. This radiosurgery work began in 1961. About 10 years later, tumour treatment with proton beams was initiated, first for small ocular tumours and later, with the arrival of Dr. Herman Suit, for larger tumours which required fractionated treatment. At present, the Harvard/MGH group has treated nearly 3 times as many patients as any other heavy charged particle facility. Many biological studies have also been carried out on the Harvard Cyclotron beam in an effort to determine the correct dose-scaling RBE for protons, in relation to high energy photons (an RBE of 1.1 is commonly used for protons).

The late 1960's also saw the launching of proton beams for clinical use (both radiosurgery and radiotherapy) at several of the proton beam facilities in the USSR: Dubna, Moscow and St. Petersburg. Again, radiobiological studies were carried out to define the RBE of the proton beams.

In Japan, proton therapy was started at NIRS, Chiba in 1979 with a 70 MeV beam, and at the University of Tsukuba in 1983, with a large field 250 MeV beam. Then, in 1994 the magnificent HIMAC facility at NIRS started treating patients with heavy ion beams from their dedicated medical synchrotron which provides ion beams of energy 100-800 MeV/amu. Dr. Tsujii directs the clinical program at HIMAC and radiobiological studies have been carried out by Dr. Ando and his colleagues.

The first heavy particle facility to be built expressly for medical use was the Loma Linda proton beam facility, developed under Dr. James Slater's direction, which began patient treatment in 1990. It uses 3 gantries for both small and large field treatments, and has a very active clinical program. The Paul Scherer Institute (PSI) in Switzerland launched a successful proton therapy program in 1984, using the 72 MeV proton beam from the injector to their cyclotron-driven pion facility (described below). They recently inaugurated a new 200 MeV proton beam facility which will be used for larger field treatments.

The growing interest in proton therapy during the last 10 years or so has been quite remarkable, with clinical programs being launched in the U.K. (Clatterbridge), France (Orsay, Nice), Belgium (Louvain), South Africa (NAC), Canada (TRIUMF) and the United States (UCSF/Davis, IUCF-Indiana). Several more are under development or being planned, including Berlin (Germany), Groningen (Netherlands), INFN, ISS and TERA (Italy), and several others. And a new dedicated medical proton beam facility, the Northeast Proton Therapy Center (NPTC), will be completed at MGH in 1998, replacing the Harvard Cyclotron program. A very similar dedicated proton therapy facility is being developed at Kashiwa, Japan, also scheduled for completion in 1998.

Another important program is the heavy ion facility which has been under development at GSI (Darmstadt) since the mid 70's. It is scheduled to begin patient treatment in December '97, but for many years the group directed by Dr. Gerhard Kraft has obtained important new information on a wide range of biological effects of heavy ions. Similarly, the group at ISS, Rome, directed by Dr. M. Belli has carried out interesting studies on the biological effects of low energy (< 7 MeV) protons from the INFN-Legnaro van de Graaff accelerator.

Pion Facilities

During the 1970's three facilities were developed to produce secondary beams of negative pi-mesons (pions) for radiotherapy. These were in Los Alamos, USA (LAMPF), Villigen, Switzerland (SIN, now PSI) and Vancouver, Canada (TRIUMF). In each case, the secondary pion beam was produced by bombarding a target with a very intense proton beam of ~ 500 MeV, from large accelerators constructed primarily for particle physics research. Since relatively little was known about the biological effects of the combination of nuclear fragments released upon pion capture (star formation), extensive radiobiological studies were carried out at all 3 facilities prior to patient treatment. Patient treatment began in the late 70's and continued until the early 90's.

The presentation will attempt to briefly review some of radiobiological data on the effects of heavy charged particles and to discuss the influence of those studies on the clinical application which followed. (e-d. /MG)

6th Workshop on Heavy-Charged Particles in Biology and Medicine
Baveno, Sept. 29, 30 and October 1

Introduction

L. Skarsgard
(Cancer Research Center, Canada)

Radiobiology with Heavy Charged Particles: A Historical Review

A

DNA Damage and Repair
K. Prise, B. Rydberg (Chair)

Oral Presentations

Kevin Prise
(Mount Vernon Hospital, Northwood, UK)

A Study of DNA Fragmentation Patterns in Cells Irradiated with Charged Particles: Evidence for non-random Distributions

Björn Rydberg
(LBNL Berkeley, USA)

Gisela Taucher-Scholz
(GSI, Darmstadt, Germany)

Track-Structure Effects on Biological Targets: DNA Double-Strand Break Induction and Rejoining

Mauro Belli
(INFN, Rome, Italy)

DNA Damage Induction and Processing after Irradiation with Different Light Ions

Kai Rothkamm
(Univers, Gießen, Germany)

Heavy-Ion-Induced DNA Double-Strand-Breaks in Yeast and Man: Differences and Similarities

Bernd Dusemund
(Univers. d. Saarlandes, Germany)

Structural and Quantitative Aspects of Radical Formation after Heavy-Ion Bombardment

Zengquan Wei
(Chin. Aca. of Sc. Lanzhou, China)

Carbon-Ion-induced DNA Double-Strand Breaks in Melanophore B_{16}

Posters

8. Erik Höglund
(Uppsala Univers., Sweden)

Initial DNA Fragmentaion Induced by Radiation of Different Linear Energy Transfer

9. Daniela Keller
(GSI, Darmstadt, Germany)

Double-Strand Break Induction along a Particle Track: Visualization of Different Fragment Sizes

10 Wolfgang Schonert
(GSI, Darmstadt, Germany)

Investigation of Radiation Induced DNA Breaks Using Scanning Tunneling Microscopy

11 Barbara Weiland
(Uni. des Saarlandes, Homburg, Germany)

Free Radicals from DNA after Irradiation with Heavy Ions or X-Rays: a Highfield EPR Study at 8.7T and 245 Ghz

12 Anne-Kathrin Hoffmann
(Uni. des Saarlandes, Homburg, Germany)

Heavy-Ion-Induced Damage to DNA Constituents: Product Formation

A STUDY OF DNA FRAGMENTATION PATTERNS IN CELLS IRRADIATED WITH CHARGED PARTICLES: EVIDENCE FOR NON-RANDOM DISTRIBUTIONS

K.M. Prise, H.C. Newman, M. Folkard and B.D. Michael

Gray Laboratory Cancer Research Trust, PO Box 100, Mount Vernon Hospital, Northwood, Middlesex, HA6 2JR, UK.

Understanding the mechanistic relationship between yields of DNA double-strand breaks (dsb) and biological effectiveness for different qualities of ionising radiation is a key goal of radiobiological research. Relating the differences in track structure of charged particles to the yields and distributions of DNA damage in cellular systems is fundamental to developing biophysical models of radiation effectiveness. Many studies have related the yields of dsb to biological effectiveness for radiations of differing LET. In most studies, the yields of dsb have been found to vary very little with radiation quality with values of RBE remaining around 1.0, in contrast to RBE values for cell killing which increase to a peak of around 4 at ~100keV/μm in mammalian cell systems (e.g Prise, 1994). These studies have been done with techniques principally designed to measure small changes in the average yields of dsb in the bulk of DNA. As radiation tracks interact with cellular DNA the patterns of energy deposition have consequences both for the distribution of damage and its complexity. Many modelling studies have predicted that, as LET increases there is an increased clustering of damage on the DNA leading to multiply damages sites of around 1-20 bp in size (see for example; Goodhead and Nikjoo, 1989; Ward, 1995). It has also been predicted that damages may be correlated over larger distances related to the repeating unit structures of cellular chromatin (Holley and Chatterjee, 1996). Given this background it is clear that techniques which measure clustering of damage and distributions of breaks within cells need to be developed.

Pulsed field gel-electrophoresis for the measurement of DNA dsb has become the technique of choice for studies on radiation damage to cells. It has advantages over previous techniques in that it gives molecular weight information and detects changes after doses as low as 1 Gy. Recently, we have used two separation protocols which have allowed us to separate fragments ranging from <10 kbp to >5.7 Mbp (Newman *et al.*, 1997). We have compared the fragmentation patterns of DNA from Chinese hamster V79 cells irradiated with 240 kV X-rays or α-particles with an LET of 110 keV/μm. The total migration of DNA into the gel, typically referred to as the FAR (Fraction Activity Retained) method, shows that migration is higher from X-irradiated cells than from those irradiated with α-particles, giving RBE values of less than 1.0. This agrees with other studies in the literature using this form of analysis on pulsed field gels (e.g Stenerlöw *et al.*, 1996) and using other techniques such as neutral sedimentation gradients (e.g. Jenner *et al.*, 1992). By analysing the distribution of DNA on the gels versus molecular weight, however it is possible to gain information as regards the distributions and absolute yields of dsb. Plots of the intensity of DNA versus molecular weight show that at molecular weights below 0.4 Mbp the amount of DNA from α-particles irradiated cells increases relative to that of X-irradiated cells. By correcting for the range of fragments sizes in each section of the gel and dividing by the mean molecular weight it is possible to determine the number of fragments versus fragment size. From this approach it is clear that the numbers of fragments produced by X-rays and α-particles are significantly different. Using a random breakage model, the X-ray data gives a breakage frequency of 8.02 dsb/Gbp/Gy. The α-particle data are poorly fitted by a random breakage model. In particular there is an increased frequency of breaks in the 8 - 300 kbp region leading to 3.4 dsb/Gbp/Gy in addition to the 7.8 dsb/Gbp/Gy predicted by a random breakage model. These finding suggest that methods of analysis such as the FAR

method underestimate the yields of dsb in cells irradiated with charged particles and that in these cells dsb are non-randomly distributed. Similar conclusions have been reached by other workers studying fragment distributions in human fibroblasts (Rydberg, 1996; Löbrich *et al.*, 1996). The non-random distribution of breaks after high LET irradiation has been attributed to the interaction of radiation tracks with the repeating unit structures of cellular chromatin, such as the 30nm chromatin fibres and higher order loop domains leading to the production of regionally multiply damaged sites (Rydberg, 1996). However further experimental evidence is required to confirm this view. Overall, including these additional fragments RBE's for dsb induction by high LET particles are higher (~1.3 in our study). However they are still significantly lower than those found for cellular endpoints such as cell killing and suggest that the localised complexity of breaks and reparability of damage may also be important factors.

Acknowledgement

References

Goodhead, D. T., and Nikjoo, H. (1989). Track structure analysis of ultrasoft X-rays compared to high and low LET radiations. *International Journal of Radiation Biology* **55**, 513-529.

Holley, W. R., and Chatterjee, A. (1996). Clusters of DNA damage induced by ionizing radiation: Formation of short DNA fragments I. Theoretical Modelling. *Radiation Research* **145**, 188-199.

Jenner, T. J., deLara, C. M., O'Neill, P., and Stevens, D. L. (1993). Induction and rejoining of DNA double-strand breaks in V79-4 mammalian cells following γ and α-irradiation. *International Journal of Radiation Biology.* **64**, 265-273.

Löbrich, M., Cooper, P. K., and Rydberg, B. (1996). Non-random distribution of DNA double-strand breaks induced by particle irradiation. *International Journal of Radiation Biology* **70**, 493-503.

Newman, H. C., Prise, K. M., Folkard, M., and Michael, B. D. (1997). DNA double-strand break distributions in X-ray and α-particle irradiated V79 cells: evidence for non-random breakage. *International Journal of Radiation Biology* **71**, 347-363.

Prise, K. M. (1994). Use of radiation quality as a probe for DNA lesion complexity. *International Journal of Radiation Biology.* **65**, 43-48.

Rydberg, B. (1996). Clusters of DNA damage indcued by ionizing radiation: Formation of short DNA fragments II. Experimental detection. *Radiation Research* **145**, 200-209.

Stenerlöw, B., Blomquist, E., Grusell, E., Hartman, T., and Carlsson, J. (1996). Rejoining of DNA double-strand breaks induced by accelerated nitrogen ions. *International Journal of Radiation Biology* **70**, 413-420.

Ward, J. F., Milligan, J. R., G.D.D.Jones, and R.C.Fahey. (1995). Multiply damaged sites. In *Radiation damage in DNA: Structure/function relationships at early times*, A. F. Fuciarelli and J. D. Zimbrik, eds. (Columbus, Ohio: Battelle Press), pp. 45-53.

Repair of Clustered DNA Damage Caused by High LET Radiation in Human Fibroblasts.

B. Rydberg, M. Löbrich and P. K. Cooper.
Lawrence Berkeley National Laboratory, Life Sciences Division, Building 934, One Cyclotron Road, Berkeley, CA 94720, USA.

In contrast to most other DNA damaging agents, clustering of lesions on DNA is a basic characteristic of ionizing radiation. The most obvious manifestation of this characteristic is the presence of DNA double-strand breaks, which can be considered as clusters of two single-strand breaks. Considering the relative frequency of different classes of lesions, with base-damage being the most prevalent, it is quite clear that base-damage must also be clustered, and double-strand breaks and single-strand breaks may frequently have associated base lesions. Clusters at the local scale of a few (<20) base-pairs have been called Locally Multiply Damaged Sites (LMDS) (Ward, 1985). Although direct experimental evidence is lacking, high LET radiation presumably produces more complicated LMDSs than low LET radiation, as modeled theoretically (Chatterjee and Holley, 1991). Due to the organization of chromatin into nucleosomes, 30 nm chromatin fibers and fiber loops, clustering occurs as well at a higher level as shown experimentally by analyzing DNA fragment size distributions of irradiated cells (Löbrich et al., 1996; Rydberg, 1996). Clusters over the approximate range of 80 - 2000 bp are influenced by the local organization of the 30 nm chromatin fiber (Rydberg, 1997) and have been called Regionally Multiply Damaged Sites (RMDS). Clusters over larger regions of DNA up to about 200 kbp have been detected after relatively high doses of high LET radiation (Löbrich et al., 1996). Presumably, non-random distribution of breaks will be present in even larger segments of DNA at sufficiently low doses of high LET radiation when the number of particle tracks per chromosome is small.

The high relative biological effectiveness of high LET radiation compared to sparsely ionizing radiation is likely to be due to the increased clustering. However, what is not clear is the mechanism by which clustering affects the biological outcome, or the relative contribution of clustering at different levels. Theories have been developed that emphasize clustering at different scales. For example, the dual theory of radiation action (Kellerer and Rossi, 1972) emphasizes lesion interactions over μm distances, which would correspond to large clusters in the kbp-Mbp range. The LMDS concept, on the other hand has drawn attention to the smallest scale of a few nucleotides (Goodhead et al., 1993). In view of recent experimental data demonstrating that LET-

dependent clustering also occurs at intermediate levels, this question can be considered more generally.

We will present data for induction and removal of thymine glycols after low and various high LET radiations, induction and rejoining of DNA double-strand breaks induced by He particles (2-8 MeV LET ~60-150 keV/μm) and other ions as measured by the FAR assay, and measurements of the correct rejoining of DNA double-strand breaks by the use of the hybridization assay (Löbrich et al., 1995) for various radiations with LETs up to 150 keV/μm (Table I).

Ion	Energy (MeV/n)	LET (keV/μm)
He	0.5-2	60-150
He	32	7
N	30	97
Fe	950	150

Table I. Particles used.

We find that our data is best accounted for by considering the effects of clustering. Thymine glycols were found to be induced with a yield that is largely independent of LET (up to our maximum of 150 keV/μm). Removal of these lesions, on the other hand, is slower as LET increases. We hypothesize that this is due to clustering of lesions at the LMDS level of a few nucleotides, which could cause interference with enzymatic repair processes. Such an effect has previously been documented *in vitro* using model systems (Chaudhry and Weinfeld, 1995). For DNA double-strand breaks induced by the low-energy He particles and other ions, we find a striking increase of breaks that remain unrepaired 20-24 hrs post-irradiation with increasing LET. However, since each cluster of several breaks will be detected only as one break with the FAR assay, a considerable amount of rejoining could go undetected within the clusters. The data for correct rejoining after a dose of 80 Gy, using the hybridization assay, suggest that misrejoining is independent of LET. We still do not know whether this will change at lower doses, as misrejoining might be dose dependent with a saturation at higher doses, or whether the misrejoining is cell cycle dependent (the present experiments used cells in G0). However, the method will not detect misrejoing that occurs within clusters, which could be a significant factor

TRACK-STRUCTURE EFFECTS ON BIOLOGICAL TARGETS: DNA DOUBLE-STRAND BREAK INDUCTION AND REJOINING

G. TAUCHER-SCHOLZ, D. KELLER, G. BECKER and G.KRAFT
Gesellschaft für Schwerionenforschung
Planckstraße 1, 64291 Darmstadt, Germany

Radiobiological studies on the molecular action of heavy ions have become increasingly important in view of the application of particle beams in radiotherapy. One of the advantages of the latter is the characteristic dose-depositon profile for particle irradiation showing a drastic increase at the end of the ion path. This is also reflected at the molecular level, when the induction and rejoining of the critical lesions, namely DNA double-strand breaks (DSB), are monitored along the particle trajectory [1].

In order to understand the mechanisms of heavy ion interaction with biological targets however, we must keep in mind the non-homogeneous character of dose distribution of accelerated particles. Heavy ions are able to deliver high amounts of energy within small volumes at a nanometer scale, and the resulting spatial distribution of dose deposition events plays a fundamental role in quality and quantity of lesions produced.

The influence of track structure can be inferred from theoretical modeling to some extent, but has also been verified in various experimental studies for different biological endpoints including cell inactivation and mutations ([2] and ref. therein).

For DSB induction in mammalian cells, the few systematic data available over a wide range of radiation qualities [3, 4] point out a general increase of effectivity per particle with increasing LET, and a drastic decrease for the very heavy ions. In the present contribution, a compiled dataset of cross sections for DSB production obtained in Chinese hamster ovary (CHO) cells is presented to exemplify the effect of the pattern of energy deposition on this endpoint (Figure 1).

Cross sections (σ_{DSB}) reveal the effectivity of a particle to produce a DSB and are expressed in μm^2 normalized to a DNA size of 10^6 dalton. They were calculated from fluence effect curves for DSB induction obtained by means of conventional electrophoresis and densitometry after fitting of an equation derived by Blöcher as previously described [5]. As fluence response curves were fitted up to a fraction of 50% of DNA retained, a non-random distribution of breaks occurring for the very low energy particles ([6] and ref. therein) would not influence the parameters obtained from the Poissonian elution fits due to the large number of cells and DSB. In the lower fluence range however, a deviation from the Blöcher fit is observed for low energy heavy ions, showing a greater proportion of fragments small enough to be eluted than predicted by the Poissonian breakage based elution fit. In this case, DSB induction cross sections obtained from the fit are reflecting the yield of randomly distributed clusters of DNA breaks per particle.

In Fig. 1 the dataset obtained for carbon and oxygen ions corresponds to approximately the same charge and can be taken to compare σ_{DSB} values for one ion species of energies between 4 and 400 MeV/u covering an LET of 14 to 400 keV/μm. Clearly, an increase of cross sections proportional to dose per particle, i.e. LET, is observed up to 100 keV/μm,
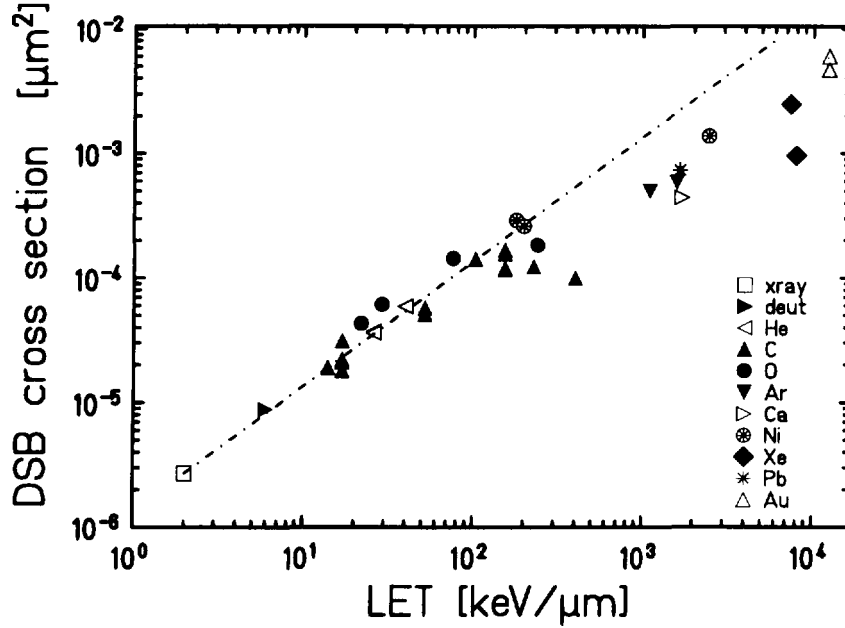
Figure 1: Cross-sections (normalized to 10^6 da) for the induction of DSBs in CHO cells versus LET. The line represents the RBE=1 relationship. Ion species used for irradiation are indicated in the legend

followed by a levelling off, where a further increase of ionization density does not enhance the probability of DSB production anymore. In this system the Relative Biological Efficiency (RBE) for DSB induction does not significantly exceed one. The plateau at higher LET has also been described for DSB induction in yeast [7], although at a significantly higher level of DSB per particle (normalized to the same DNA size).

For higher Z particles an increase above the plateau is observed, leading to individual curves for each ion species, as known for other endpoints. This reflects the higher ionization density within the radial extension of the track for these particles. It is also interesting to look at the σ_{DSB} of the 1000 Mev/u Pb ions and the 9.9 MeV/u Au ions of comparable Z in Fig. 1. Even at these very high LETs an increase in ionization density can give rise to greater σ_{DSB}, due to the large reduction in the extension of the 2^{ary} electron range going from the very high energy Pb ions to the lower energy particles. Thus, the drastic decrease of σ_{DSB} as a consequence of the "thin-down" of the maximum 2^{ary} electron range is only apparent at a lower energy range (see Xe ions of 10 and 15 MeV/u, Fig. 1).

A further biological endpoint addressed in our cellular DSB studies is the rejoining of DSB in mammalian cells. The fraction of DSB remaining unrejoined after a certain period of repair incubation of irradiated cells under culture conditions was used as an indicator of quality of DSB produced. A compilation of data of fraction of damage remaining after 3 h rejoining was plotted versus LET (not shown). For X-rays and high energy carbon ions (LET around 20 keV/μm) no more than 10% of DSB remain unrejoined after 3 h incubation. As LET increases, when carbon and oxygen ions are considered a continuous increase in the fraction of damage remaining is observed up to 150 keV/μm. At higher LET, the

fraction of unrejoined damage does not further increase and a plateau (corresponding to about 50% of unrejoined DSB after 3 h) is apparent.

By comparing these results with the σ_{DSB}-LET dependence in Fig. 1, it becomes clear that a change in quality of DSB with increasing LET producing lesions more difficult to be repaired, must result in an enhancement of cell lethality for these ions. around 100 keV/μm. This has indeed found to be the case, giving rise around 100 keV/μm to the well known peak of RBE for cell inactivation of high-LET radiation.

References

[1] Heilmann, J., Taucher-Scholz, G., Haberer, T., Scholz, M., and Kraft, G. *Int. J. Radiat. Oncol. Biol. Phys.* **34**, 599–608 (1996).

[2] Blakely, E. *Radiat. Environ. Biophys.* **31**, 181–196 (1992).

[3] Weber, K. and Flentje, M. *Int. J. Radiat. Biol.* **64**, 169–178 (1993).

[4] Heilmann, J., Rink, H., Taucher-Scholz, G., and Kraft, G. *Radiat. Res.* **135**, 46–55 (1993).

[5] Heilmann, J., Taucher-Scholz, G., and Kraft, G. *Int. J. Radiat. Biol.* **68**, 153–162 (1995).

[6] Newman, H., Prise, K., Folkard, M., and Michael, B. *Int. J. Radiat. Biol.* **71**, 347–363 (1997).

[7] Ikpeme, S., Löbrich, M., Akpa, T., Schneider, E., and Kiefer, J. *Radiat. Environ. Biophys.* **34**, 95–99 (1995).

'E'

DNA damage induction and processing after irradiation with different light ions

M. Belli[1], F. Cera[2], R. Cherubini[2], M. Dalla Vecchia[2], S. Favaretto[2], L. Levati[1], G. Moschini[2], O. Sapora[1], G. Simone[3], M. A. Tabocchini[1] and P. Tiveron[2]

[1] Istituto Superiore di Sanità and INFN-Sezione Sanità, Rome, Italy

[2] Laboratori Nazionali di Legnaro-INFN, Legnaro, Italy

[3] Istituto FRAE-CNR, Bologna and INFN-Sezione Sanità, Rome, Italy

While there is strong experimental evidence for the dependence of cellular effects such as cell inactivation, mutation induction, oncogenic transformation on radiation quality, it is still an open question how it affects the quality of lesions at DNA level. It is widely accepted that DNA double strand breaks (dsb) are the major lesions responsible for cellular effects. However, the relative insensitivity on particle LET of the initial yield of DNA dsb, as measured by the techniques currently used, in mammalian cells irradiated with light ions arises the problem of identifying the presence of complex, less repairable lesions (Goodhead, 1995). This task can be accomplished either by development of direct methods able to detect clustered lesions (see Prise 1994 for a review) or by indirect approaches aimed at studying processing of DNA lesions.

To this purpose, we have studied the induction of DNA dsb and the time course of their rejoining in V79 cells irradiated with light ions. These data can be compared with those for cell inactivation and mutation induction, already obtained on the same cell line, using the same irradiation facility at the Laboratori Nazionali di Legnaro, that showed a distinct LET dependence of the RBE for cell inactivation and HPRT mutations (Belli et al., 1993, Cherubini et al., 1995, Cera et al., in press). DNA dsb induced by low energy protons and helium ions were measured with the Constant Field Gel Electrophoresis (CFGE). Four different beams, namely protons of 11 and 31 keV/μm and He-4 ions of 51.5 and 104 keV/μm, have been chosen. Gamma-rays have been used as reference. The results on the initial yield of DNA damage were similar to those previously obtained with the low-speed sedimentation technique (Belli et al., 1994), showing no significant dependence of dsb yield on radiation type and LET (Fig. 1).
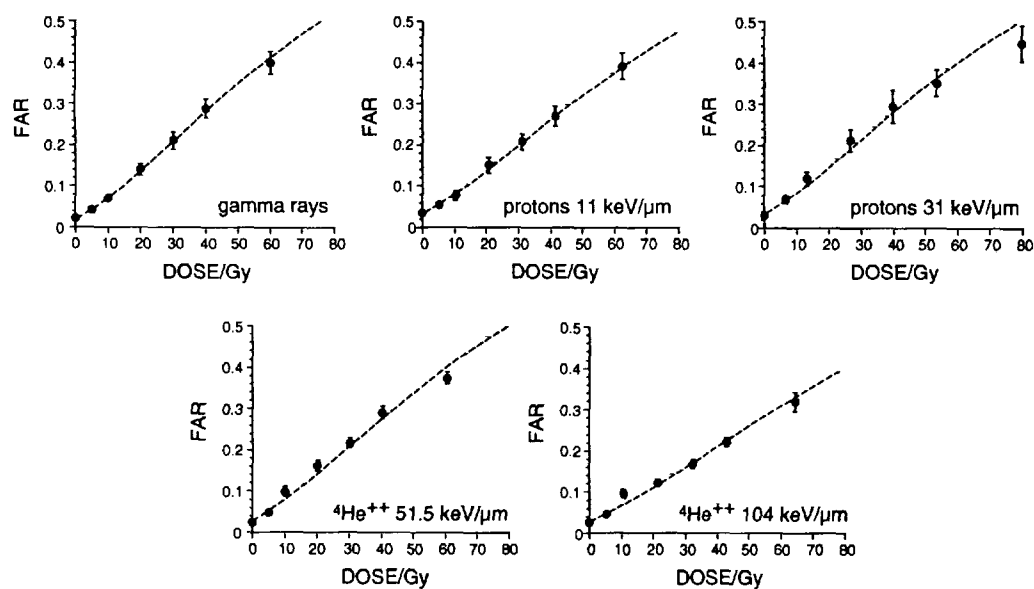
Fig. 1.   Initial yield of DNA dsb as a function of the dose as measured by GFGE (FAR method)
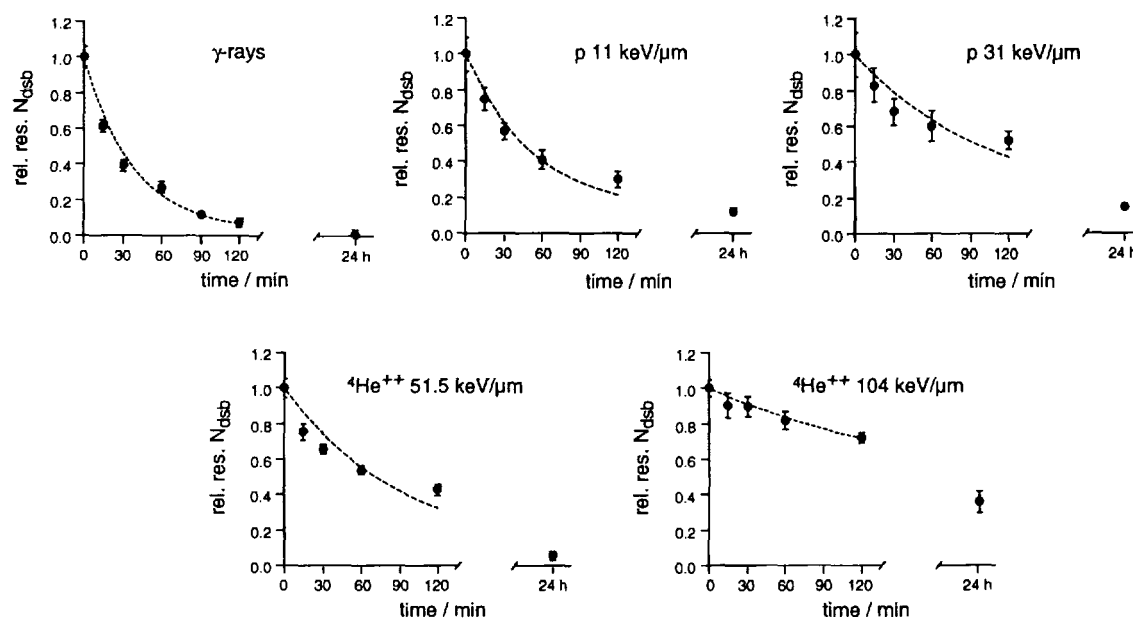

Fig. 2.   Rejoining kinetics of DNA dsb as a function of incubation time at 37°C.

The time course of remaining dsb was studied after a dose of about 40 Gy for a period of time from 15 to 120 min. One more point at 24 h after irradiation was also considered (Fig. 2).

These results showed that the rejoining kinetics, in contrast with the initial yield, depend on both radiation type and LET: for similar amounts of initial damage, gamma-ray induced dsb are rejoined faster than dsb induced by light ions and, for each ion, the rejoining is slower on increasing LET.

The low level of residual damage after long time incubation (24 h) doesn't allow to detect possible differences among different radiations (except for 104 keV/μm He-4 ions). Instead, the residual damage left unrejoined at relatively short time (2 h) shows a dependence on radiation quality that is qualitatively consistent with the dependence found for cell inactivation and mutation induction.

From these studies it appears that rejoining kinetics can give an indirect evidence of different lesion complexity.

However, a better understanding of the relationship between radiation induced DNA damage and the functional changes observed at cellular level requires elucidating: (i) the role of rejoining fidelity (Löbrich et al., 1994 a and b) as a further step in damage processing and (ii) the dependence of the fragmentation pattern on radiation quality (Löbrich et al., 1996; Newman et al., 1997) that reflects damage association due to the interplay between the track structure and the chromatin organization.

Acknowledgments

Authors are indebted to Mr. I. Motti for his help during irradiation at LNL.

Part of this work was carried out within a scientific agreement between the ISS and the FRAE-CNR.

References

Belli, F. Cera, R. Cherubini, A. M. I. Haque, F. Ianzini, G. Moschini, O. Sapora, G. Simone, M. A. Tabocchini and P. Tiveron, Inactivation and mutation induction in V79 cells by low energy protons: re-evaluation of the results at the LNL facility. *Int. J. Radiat. Biol.* **63**, 331-337, 1993

Belli, F. Cera, R. Cherubini, F. Ianzini, G. Moschini, O. Sapora, G. Simone, M. A. Tabocchini and P. Tiveron, DNA double-strand breaks induced by low energy protons in V79 cells. *Inter. J. Radiat. Biol.* **65**, 529-536, 1994

F.Cera, R.Cherubini, M.Dalla Vecchia, S.Favaretto, G.Moschini, P.Tiveron, Belli, F. Ianzini, L. Levati, O. Sapora, M. A. Tabocchini and G. Simone, Cell inactivation, mutation and DNA damage induced by light ions: dependence on radiation quality. *Radiat. Prot. Dos.* (in press)

R.Cherubini, F.Cera, M.Dalla Vecchia, S.Favaretto, A.M.I.Haque, G.Moschini and P.Tiveron, Biological effectiveness of light ions for cell inactivation and mutation induction on V79 cells. *Fifth Workshop on Heavy Charged Particles in Biology and Medicine, GSI-Report-95-10,* ISSN 0171-4546, 1995

Goodhead, Molecular and cellular models of biological effects of heavy ion radiation. *Radiat. Environ. Biophys.*, **34**, 67-72, 1995

Löbrich, P. K. Cooper and B. Rydberg, DNA double strand breaks induced by high-energy Neon and Iron ions in human fibroblasts. II. Probing individual NotI fragments by hybridization. *Radiat. Res.* **139**, 142-151, 1994 (a)

Löbrich, S. Ikpeme and J. Kiefer, DNA double-strand breaks in mammalian cells by pulsed-field gel electrophoresis: an approach using restriction enzymes and gene probing. *Int. J. Radiat. Biol.* **65**, 623-630, 1994 (b)

Löbrich, P. K. Cooper and B. Rydberg, Non-random distribution of DNA double-strand breaks induced by particle irradiation. *Int. J. Radiat. Biol.* **70**, 493-503, 1996

Newman, K.M. Prise, M. Folkard and B.D. Michael, DNA double-strand break distribution in X-ray and α-particle irradiated V79 cells: evidence for non-random breakage. *Int. J. Radiat. Biol.* **71**, 347-363, 1997

Prise, Use of radiation quality as a probe for DNA lesion complexity. *Int. J. Radiat. Biol.* **65**, 43-48, 1994

HEAVY ION-INDUCED DNA DOUBLE-STRAND BREAKS IN YEAST AND MAN: DIFFERENCES AND SIMILARITIES

M. Löbrich, K. Rothkamm, and J. Kiefer

Strahlenzentrum der Justus-Liebig-Universität Gießen
Leihgesterner Weg 217
35392 Gießen, Germany

DE98F5466

INTRODUCTION

Experimental evidence suggests that DNA double-strand breaks (dsbs) are the most significant biological lesions with regard to radiation-induced cell killing, chromosomal aberrations and mutation induction in many biological systems (Frankenberg *et al.* 1981). Although complex biological endpoints appear to be strongly influenced by radiation quality with maximum RBEs considerably above unity at LETs around 100 keV/μm (Thacker 1992), the induction of dsbs in mammalian cells was recently found to depend only slightly on LET (Heilmann *et al.* 1993, Weber and Flentje 1993, Rydberg *et al.* 1994, Löbrich *et al.* 1994). In contrast to this situation, yeast measurements show a close parallelism between dsb induction and cell inactivation for ions with different LET, resulting in RBEs for dsb induction of more than one in the LET range of 100 to 300 keV/μm (Löbrich *et al.* 1993, Ikpeme *et al.* 1995).

In an attempt to explain the inconsistencies in the RBE-LET relationship for dsb induction in mammalian cells in comparison with other biological endpoints, theoretical (Holley and Chatterjee 1996) and experimental (Rydberg 1996, Löbrich *et al.* 1996, Newman *et al.* 1997) approaches demonstrate clustering of breaks after particle irradiation. The observed excess DNA fragments in the size range of 100 bp to 300 kbp are probably due to the organization of DNA in the 30 nm chromatin fiber and higher order structures. The measurements indicate that densely ionizing radiations are more effective in producing small DNA fragments but less effective in the generation of large fragments when compared to X-rays. As typical assays for the determination of dsb induction rates measure breaks on a Mbp-scale, clustering of dsbs is not registered. Therefore an underestimation of breaks is inherent in these techniques.

The repair of dsbs in mammalian cells as well as in yeast shows a fast and a slow component and seems to be retarded after high LET irradiation with a larger proportion of breaks being unrejoined after several hours of repair incubation (Ritter *et al.* 1977, Blöcher 1988, Rydberg *et al.* 1994, Frankenberg-Schwager *et al.* 1994). This has been taken as an indication that dsbs produced by high LET radiation are more severe and complex, possibly explaining the high biological effectiveness of densely ionizing radiations.

TECHNIQUES

Most of the recently developed approaches for dsb measurement are based on pulsed-field gel electrophoresis (PFGE). As the chromosomes of the yeast *Saccharomyces cerevisiae* are sufficiently small to be completely resolved by PFGE, dsb induction and repair rates can easily be determined by measuring the loss and reconstitution of a chromosomal band in an ethidium bromide-stained gel (see Löbrich *et al.* 1993 and Ikpeme *et al.* 1995 for details). In order to avoid contamination of the band of interest with fragments from other chromosomes one can either examine the

uppermost band or hybridize with a single copy probe to obtain only chromosome-specific signals (Rothkamm 1997).

In mammalian cells the chromosomes are too large to enter the gel. The most common method to measure radiation-induced dsbs in this system is an electrophoretic elution technique called FAR (fraction of DNA radioactivity released from the plug into the gel). Correlation of the FAR value with the number of breaks induced requires calibration, usually utilizing ^{125}I decay. As this assay is based essentially on the analysis of average molecular weight of the radiation-induced fragments, all dsb rejoining events in the entire genome are registered independent of their quality.

An alternative technique for dsb measurement in mammalian cells involves generation of genomic DNA fragments on a Mbp scale by digestion with rarely cutting restriction endonucleases (e.g. *Not*I) and probing of individual *Not*I fragments by hybridization, thus resembling the yeast case. This approach allows the direct quantification of dsbs within defined genomic regions and, when applied to repair studies, measures exclusively correct rejoining of DNA ends. A detailed description of the FAR and the hybridization assay can be found elsewhere (Rydberg *et al.* 1994, Löbrich *et al.* 1994)

RESULTS AND DISCUSSION

For dsb quantification after particle irradiation, the yeast system involves intensity measurement of the uppermost band in the ethidium bromide-stained gel. The mammalian cell system, in contrast, employs the measurement of the band representing the restriction fragment of interest. In either case the signal intensity decreases exponentially with radiation dose thus indicating a linear dsb induction with dose.
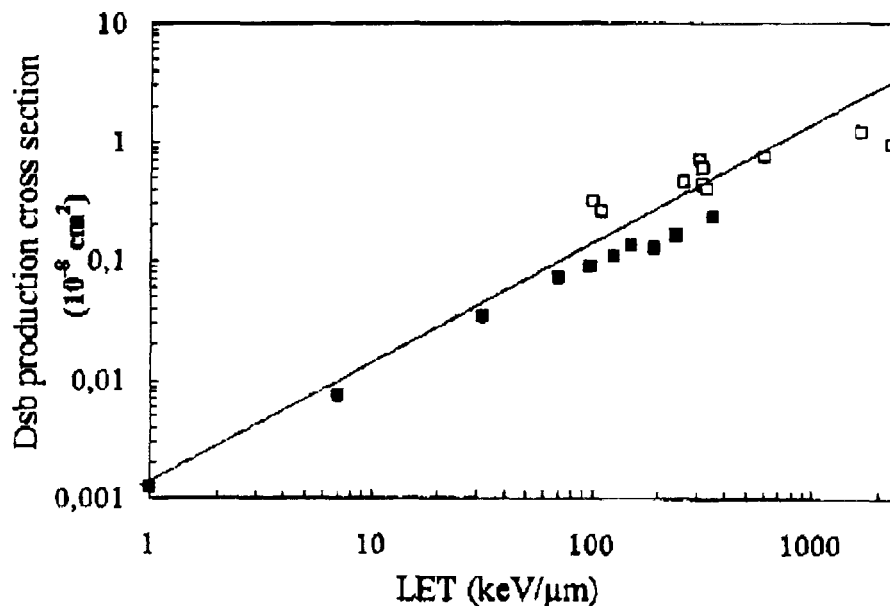

Fig. 1: Double-strand break production cross-sections for human fibroblasts (closed symbols, measured with the hybridization assay, taken from Löbrich 1997) and the diploid yeast strain 211+B (open symbols, PFGE, taken from Ikpeme *et al.* 1995) plotted vs. particle LET. The cross-sections were normalized to 10^9 g/mol. The line indicates a relative biological effectiveness of unity compared to the break induction in human fibroblasts after 225 kVp X-irradiation (LET of 0.2 keV/μm).

Figure 1 shows increasing dsb induction cross-sections (normalized to 10^9 g/mol) for the yeast and the mammalian cell system as a function of particle LET. The dsb induction rate for sparsely ionizing radiation was found to be comparable for yeast and mammalian cells which results in a single straight line indicating RBE values of unity. The data obtained with mammlian cells clearly show RBE values below unity in the LET range of a few hundred keV/μm while the corresponding cross-sections for yeast cells indicate RBE values of more than one between 100 and 300 keV/μm. However, it has been reported (Rydberg 1996, Löbrich *et al.* 1996, Newman *et al.* 1997) that in mammalian cells due to the non-random induction of breaks after particle irradiation a considerable underestimation of the dsb induction rate occurs if conventional assays are employed. All these techniques measure Mbp-spaced breaks but do not resolve clusters of breaks. If the clustering is resolved by analyzing the entire fragment distribution, RBE values for the induction of dsbs of more than one are also found for mammalian cells. Since the degree of clustering depends on the spatial organization of the genomic DNA, different effects could be expected for yeast vs. mammalian cells. Whether such a hypothetical difference in the distribution of radiation-induced fragments might account for the observed difference in RBE vs. LET dependence awaits clarification.

Repair of dsbs in mammalian cells was measured with the FAR and the hybridization assay. Table 1 summarizes the results for 5 different radiation types. Generally, the non-rejoining frequency increases with the LET of the particles while the misrejoining frequency remains approximately constant with LET.

Considering the dsb rejoining results in combination with the observed increase in RBE for cell killing, it is tempting to speculate that incorrect rejoining events serve to allow survival with consequences for other biological endpoints. The increased biological efficiency for cell killing for high-LET radiation might rather be a consequence of a higher proportion of non-rejoined breaks.

Table 1: Repair of dsbs in mammalian cells (taken from Löbrich *et al* 1995 and Löbrich 1997)

Radiation	LET (keV/μm)	% dsbs not correctly rejoined after 15-25 h	% dsbs not rejoined at all after 15-25 h	% dsbs misrejoined after 15-25 h
X-ray	(0.2)	30	2	28
He	71	40	7	33
N	97	40	10	30
He	125	47	18	25
Fe	150	38	10	28

Dsb repair in yeast differs from that in mammalian cells as homologous recombination constitutes the predominant pathway for dsb rejoining in this cell system. Consequently, the proportion of breaks being incorrectly rejoined would be expected to be far below values of 25 to 30% as found in the mammalian cell system. However, the kinetics for all rejoining events show - similar to the situation in mammalian cells - a fast and a slow component with a higher fraction of non-rejoinable breaks with increasing LET (Frankenberg-Schwager et al. 1994).

REFERENCES

Blöcher, D., DNA double-strand break repair determines the RBE of α-particles, *Int. J. Radiat. Biol.* **54**, 761-771 (1988).

Frankenberg, D., M. Frankenberg-Schwager, D. Blöcher, and R. Harbich, Evidence for DNA double-strand breaks as the critical lesions in yeast cells irradiated with sparsely or densely ionizing radiation under oxic or anoxic conditions, *Radiat. Res.* **88**, 524-532 (1981).

Frankenberg-Schwager, M., R. Harbich, S. Beckonert and D. Frankenberg, Half-life values for DNA double-strand break rejoining in yeast can vary by more than an order of magnitude depending on the irradiation conditions, *Int. J. Radiat. Biol.* **66**, 543-547 (1994).

Heilmann, J., H. Rink, G. Taucher-Scholz, and G. Kraft, DNA strand break induction and rejoining and cellular recovery in mammlian cells after heavy-ion irradiation, *Radiat. Res.* **135**, 46-55 (1993).

Holley, W. and A. Chatterjee, Clusters of DNA damage induced by ionizing radiation Formation of short fragments. 1 Theoretical modeling, *Radiat. Res.* **145**, 188-199 (1996).

Ikpeme, S., M. Löbrich, T. Akpa, E. Schneider, and J Kiefer, Heavy ion-induced DNA double-strand breaks with yeast as a model system, *Radiat. Environ. Biophys.* **34**, 95-99 (1995).

Löbrich, M., S. Ikpeme, P. Haub, K.J. Weber, and J. Kiefer, DNA double-strand break induction in yeast by X-rays and α-particles measured by pulsed-field gel electrophoresis, *Int. J. Radiat. Biol.* **64**, 539-546 (1993).

Löbrich, M., B. Rydberg, and P.K. Cooper, DNA double-strand breaks induced by high-energy neon and iron ions in human fibroblasts. II. Probing individual NotI fragments by hybridization, *Radiat. Res.* **139**, 142-151 (1994).

Löbrich, M., B. Rydberg, and P.K. Cooper, Repair of X-ray-induced DNA double-strand breaks in specific Not I restriction fragments in human fibroblasts: Joining of correct and incorrect ends, *Proc. Natl. Acad. Sci. USA*. **92**, 12050-12054 (1995)

Löbrich, M., P.K. Cooper, and B. Rydberg, Non-random distribution of DNA double-strand breaks induced by particle irradiation, *Int. J. Radiat. Biol.* **70**, 493-503 (1996).

Löbrich, M., Induction and repair of DNA double-strand breaks in human fibroblasts after particle irradiation, *Adv. Space Res.*, in press, (1997).

Newman, H.C., K.M. Prise, M. Folkard, and B.D. Michael, DNA double-strand break distributions in X-ray and α-particle irradiated V79 cells: evidence for non-random breakage, *Int. J. Radiat. Biol.* **71**, 347-363 (1996).

Ritter, M.A., J.E. Cleaver, and C.A. Tobias, High-LET radiations induce a large proportion of non-rejoining DNA breaks, *Nature* **266**, 653-655 (1977).

Rothkamm, K., Ein Hybridisierungsverfahren zum Nachweis von DNA-Doppelstrangbrüchen in Saccharomyces cerevisiae, *Diplomarbeit, Universität Giessen* (1997).

Rydberg, B., M. Löbrich, and P.K. Cooper, DNA double-strand breaks induced by high-energy neon and iron ions in human fibroblasts. I. Pulsed-field gel electrophoresis method., *Radiat. Res.* **139**, 133-141 (1994).

Rydberg, B., Clusters of DNA damage induced by ionizing radiation: Formation of short DNA fragments. II. Experimental Detection, *Radiat. Res.* **145**, 200-209 (1996).

Thacker, J., Radiation-induced mutations in mammalian cells at low dose rates, *Advances in Radiation Biology*, Vol. 16. Edited by: O.F. Nygaard, W.K. Sinclair, and J.T. Lett (San Diego, CA, Academic), pp. 77-124 (1992).

Weber, K.J. and M. Flentje, Lethality of heavy ion-induced DNA double-strand breaks in mammalian cells, *Int. J. Radiat. Biol.* **64**, 169-178 (1993).

Structural and quantitative aspects of radical formation after heavy ion bombardment

B. Dusemund, A.K. Hoffmann, B. Weiland, J. Hüttermann

Fachrichtung Biophysik, Klinikum Bau 76, D-66421 Homburg, Germany

Irradiation of cells with both sparsely ionising radiation like X-rays or with heavy ions causes modifications in the DNA nucleotide constituents which may lead to strand breaks, mutations and cell death or may cause cancer. Initial stages of these damage pathways can be monitored by investigating the free radicals and the molecular products formed in suitable model systems. Therefore, several aspects of the build-up mechanism of radicals and their subsequent reactions have been of long standing interest in the field of molecular radiation biophysics.

In this report we present a summary of our recent attempts aiming at clarifying some basic structural and quantitative aspects of free radical formation in DNA constituents and in DNA as well as of product analysis from nucleotide model compounds. One of our goals is to compare between effects of X-irradiation and heavy ion bombardment under identical conditions in order to shed light on the unknown mechanisms of high LET particles at a molecular level. The exploration of quantitative aspects of free radical formation mechanisms in solid samples after exposure gives an insight into the pathways of the so-called direct radiation damage, which involves deposition of energy in the target molecule itself. This part is assumed to dominate the high-LET radiation actions on cells. Specifically, the dose response of the samples and its dependence from LET allows to calculate G-values and thus radiation efficiencies and you can compare. We present new theoretical models for describing the experimental dose response curves of nucleic acid constituents and discuss the underlying mechanistic consequences.

Free radicals induced by heavy ion bombardment are mainly products of the ionisation pathway due to the reaction with electrons generated by interactions of the primary radiation with the target. The pathway from free radical species to products is a topic which is at present hardly understood; its elucidation is another, major aim of our studies. We shall present the first results obtained from solid nucleotide constituents for which release of unaltered base was found to be a major quantitative effect.

Finally, the first results from heavy ion bombarded, dry DNA are shown for which the samples were irradiated at about 100 K and annealed. Again, the results are discussed in relation to X-irradiated DNA.

Modelling dose-response curves (B. Dusemund)

Placing first the attention on build-up mechanisms of free radicals we measure their concentrations in solid samples in dependence of dose for radiations of different qualities. In this way the direct radiation action is modelled.

The concentration of the radicals with the applied dose is typically nearly linear at small doses and levels off to a saturation plateau at higher doses. The curves are usually fitted with the formula

$$C = C_\infty (1 - \exp(-D/D_{37})) \qquad [1]$$

in which C is the radical concentration and D the radiation dose. D_{37} is the dose at which the level of C is reduced to 63% of the saturation level C_∞.
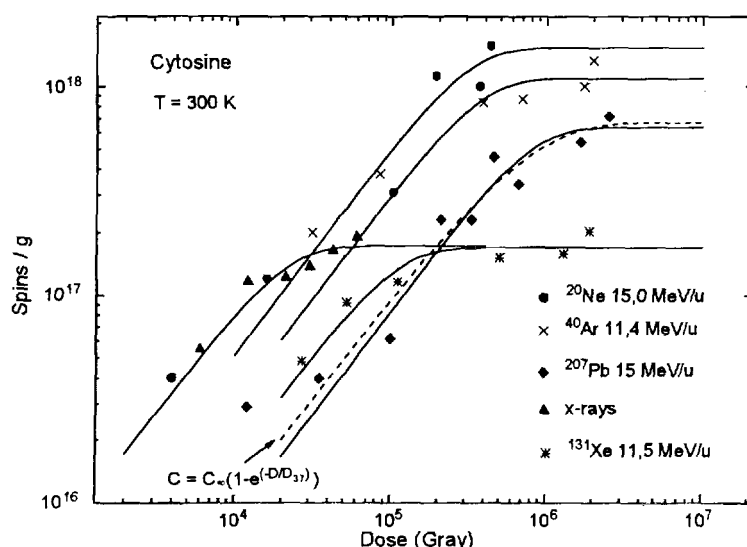
Fig.1. dose response curves from cytosine, for different kind of particles

The (initial) radiation-chemical yield (G-value), defined as number of free radicals formed per $1.6*10^{-17}$ J (100 eV) energy absorbed, can be derived from the development of equ. [1] at low doses to give $G = C_\infty/D_{37}$. It is possible to fit data points like those given in Fig.1 quite well with this formula. The model underlying equ. [1] is a differential equation, with constant term in the build-up of radicals and a first order destruction with dose. If we reformulate more generally $dC/dD = k_1N_0 - k_2*C$ with $k_2 = 1/D_{37}$ again but now being termed 'destruction' constant. In this case one finds $C_\infty = k_1N_0/k_2$ in equ. [1] which means that the G-value or, in this picture, the production rate k_1N_0 is C_∞/D_{37}, N_0 the number of molecules per volume.

This model is presently accepted in the literature for analysing free radical dose-response data. It gives, however, no physical insight into the mechanisms of the dose-dependence of radical stabilisation. Both the G-value and the saturation concentrations are found to be highly depending on the kind of irradiation. As a consequence in this model, it is impossible to handle the formula with constant building and destruction factors. Furthermore it is not obvious why particles with a high LET have lower G-values and saturation values than particles with a lower LET. The first attempt we made was to model the differential equation in the hope to become a better result at least with the aim to get for all kind of irradiation an underlying intrinsic building constant.

We examined the following equations:

a) $dC/dD = k_1N_0 - k_3*C^2$ b) $dC/dD = k_1N_0 - k_2*C - k_3*C^2$

The solid lines in Fig.1 are modelled with formula a). However, the same goodness of the fit could be achieved with equation b). Thus, it is possible to fit the data with all three formulae very well and there is no numerical criterion to decide, which is the right one. Moreover, the basic problem remains in all cases that there is underlying a build-up constant, which is the same for every particle.

Consider now what happens in a single track, in the case of heavy ion bombardment. Using an old theory of /Butts and Katz, 1967/, which first described effects inside a particle track, by calculations of δ-electron distribution around the track and introducing in this theory a radical - radical destroying mechanism, it was possible to calculate G-values for heavy ions with intrinsic building and destruction constants /Dusemund et al., 1997/. The results for the data taken from Fig. 1 are given in Figure 2. The idea behind it is that the produced δ-electrons are

mainly irradiated perpendicular to the track. They form radicals when hitting the target molecules.

Fig. 2 measured and calculated G-values for cytosine

The number of radicals formed by this electrons is depending on the dose, that means it is depending on the distance from the track core. The dose decreases with $1/r^2$ from the core of the track. Furthermore, the dose is depending on the kind of irradiation. The dose around the particle track as well as the number of radicals initially build is increasing with increasing LET, which means with heavier and slower particles. However, the measured data show the opposite behaviour. Therefore, we introduced a radical-radical destroying mechanism, which is depending on the distance of the radicals. At places with a high concentration of radicals, the recombination is so strong that it rests at the end a lower number of radicals as at places with a low concentration. With this idea it was possible to calculate G-values with an intrinsic building constant for all kind of heavy particle irradiation.

Release of unaltered bases from DNA constituents (A.-K. Hoffmann)

As models for nucleic acids, pyrimidine nucleotides irradiated as solid, polycrystalline samples were used in order to study explicitly the chemical consequences of direct radiation action. As first product, the release of unaltered ba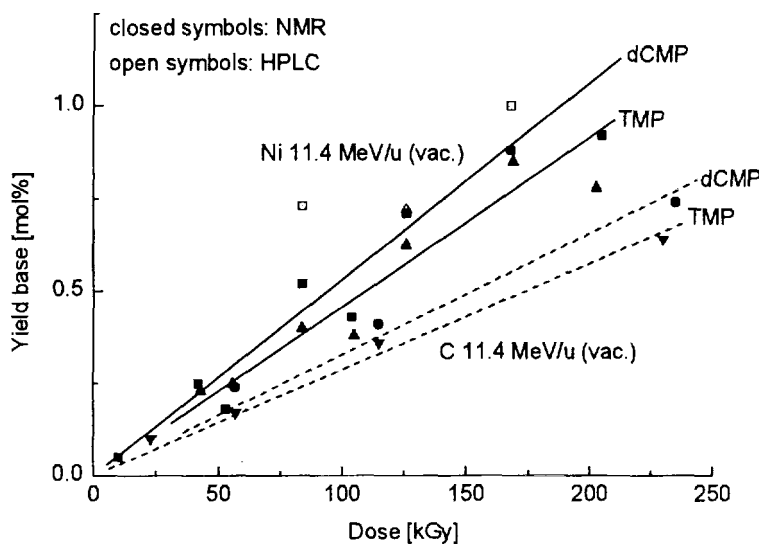ses after dissolving the irradiated samples in aqueous solution could be demonstrated to occur and was investigated quantitatively using HPLC and ^{1}H-NMR. Samples of thymidine 5'-mono-phosphate (TMP) and 2'-deoxycytidine 5'-mono-phosphate (dCMP) were irradiated in the beam vacuum at 300 K with Ni (11.4 MeV/u) and C (11.4 MeV/u). The main diamagnetic products after dissolving the samples in deuterium oxide were the free thymine or cytosine base, respectively. Fig. 3

Fig. 3: Dose dependent base release from TMP and dCMP

shows the dose dependent base release of the pyrimidine nucleotides after heavy ion bombardment.

The increase in the yield of free bases was linear with dose up to 200 kGy. The bombardment with carbon ions (LET 134 keV/μm) effected a lower base release than the bombardment with nickel ions (LET 2252 keV/μm). The radiation chemical yields (G values) were estimated to be in the order of 10^{-7} mol J^{-1}.

In DNA and DNA constituents the G values for free radicals decrease with increasing LET; this might be attributed to an increase of the ion radical recombination. Thus, if the radical recombination after heavy ion bombardment results in the formation of diamagnetic products, e. g. the unaltered base, this would increase the yield of products with increasing LET.

The G values for the base release after heavy ion bombardment with nickel were nearly the same as for X-irradiation in the absence of oxygen (controls).

The action of ionising radiation with the target results in the formation of radical anions and cations which can protonate or deprotonate, respectively. A quantitative study of the direct effect of X-irradiation in an air atmosphere on TMP and dCMP in the presence of an electron scavenger (riboflavin) at a dose of 180 kGy was carried out.

The electron scavenger would be in competition with the pyrimidine nucleotide molecules for delocalised electrons, thus reducing the number of radical anions for a given dose of radiation. In the presence of riboflavin the yield of the free base was not reduced, so the free base is probably a diamagnetic product of the radical cation.

Free radical formation in dry DNA upon irradiation with X-rays or heavy ions at low temperature (B. Weiland)

X-irradiation of dry DNA at 77 K and stepwise annealing to room temperature leads to a series of EPR spectra from which altogether eight different patterns can be isolated with the knowledge of scavenger experiments and EPR at high frequencies (245 GHz) /Weiland et al., 1997/.

Five of them can be assigned to the one electron oxidized guanine base, the one electron reduced thymine and cytosine bases, the thymine allyl radical and the H addition radical at C6 of the thymine base. Three patterns, a triplet (about 2.9 mT of total splitting), a quartet (5.3 mT) and a sharp singlet (0.8 mT) remain unassigned so far. Heavy ion bombardment (e. g. Zn 5 MeV/u, LET = 3860 keV/mm) at about 100 K with a dose of 16 kGy does not alter the kind and composition of radicals compared to X-irradiation at 77 K with a dose of 80 kGy. Higher doses (up to 500 kGy) lead to a slightly stronger contribution of the quartet species. Fig. 4 shows
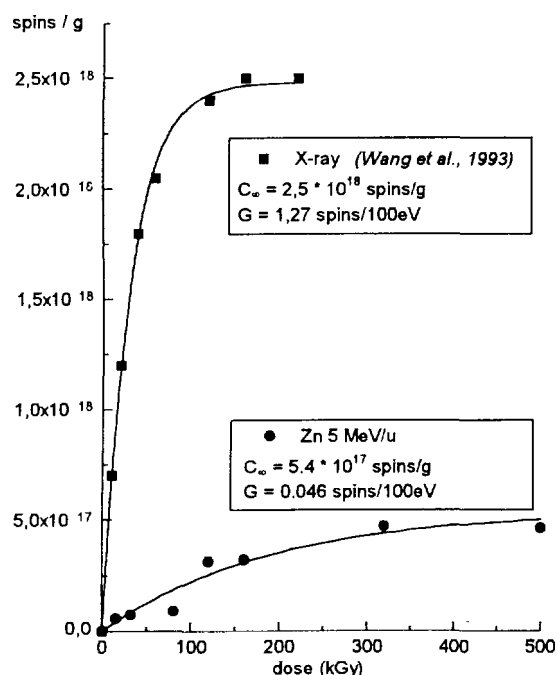

Fig. 4 Quantitative analysis of EPR spectra after X-irradiation at 77 K /Wang et al., 1993/ and bombardment with Zn ions (5 MeV/u, LET = 3860 keV/μm) at about 100 K and short annealing to about 180 K

exponentially fitted curves of data from quantitative EPR measurements of dry DNA after X-irradiation at 77 K /Wang et al., 1993/ and bombardment with Zn ions (5 MeV/u, LET=3860 keV/mm) at about 100 K, respectively. In the latter case sample transfer from the vacuum beam line leads to a short annealing to about 180 K and thereby to a loss of about 20% of the total number of radicals. Nevertheless, the fitting numbers indicate a significant lower G-value and saturation value for the bombardment with Zn ions (for the numbers see Fig. 4). Summarising these results, we find no significant differences in the qualitative composition of EPR spectra after X- or heavy ion irradiation, whereas the quantitative analysis shows a much higher formation rate and saturation number of radicals after X-irradiation.

References

Dusemund, B., Schaefer, A. Hüttermann, J. Adv. Space Res., 1997, accepted for publication
Butts, J.J., Katz, R., 1967, Radiat. Res. 30, 855-871
Weiland, B., Hüttermann, J. and Van Tol. J., 1997, Acta Chem. Scand. 51, 585-92.
Wang, W., Becker, D. and Sevilla, M. D., 1993, Radiat. Res. 135, 146-54.

Acknowledgement

Carbon ion induced DNA double-strand breaks in melanophore B_{16}

Wei Zengquan, Zhou Guangming, Wang Jufang, Gao Qingxiang*, He Jing, Li Qiang, Li Wenjian, Xie Hongmei, Cai Xichen, Huang Tao, Dang Bingrong and Han Guangwu

(Institute of Modern Physics, Chinese Academy of Sciences   Lanzhou 730000, P.R.China)
*(Lanzhou University   Lanzhou 730000, P.R.China)

Abstract DNA double-strand breaks (DSBs) in melanophore B_{16} induced by plateau and extended Bragg peak of 75 MeV/u $^{12}C^{6+}$ ions were studied by using a technique of inverse pulsed-field gel electrophoresis (PIGE). DNA fragment lengths were distributed in two ranges: the larger in 1.4 Mbp-3.2 Mbp and the smaller in less than 1.2 Mbp. It indicates that distribution of DNA fragments induced by heavy ion irradiation is not stochastic and there probably are sensitive sites to heavy ions in DNA molecules of B_{16}. Percentage of DNA released from plug (PR) increased and trended towards a quasi-plateau ~ 85% as dose increased. Content of the larger fragments decreased and flattened with increasing dose while content of the smaller ones increased and trended towards saturation.

Keywords: heavy ion, melanophore B_{16}, DNA double-strand break, inverse pulsed-field gel electrophoresis,

Introduction

DSBs of DNA are generally considered as the most important initial lesion in interaction between ionizing radiation and biological targets. Non-repaired DSBs can result in loss of genetic information and lead to reproductive death of cells. Mis-repaired DSBs will cause chromosomal rearrangement such as translocation, inversion and so on and then produce genetic variation or death of cells. Therefore, radiobiologists all put special emphasis on the study of DSBs so that they can further understand mechanisms of radiobiological effects.

The usual methods studying DSBs have mainly sedimentation, viscoelastometry and non-denaturing filter elution. However, these techniques can only separate DNA molecules of less than 10^7 daltons and, moreover, they all are restricted by some factors. In 1984, Schwartz reported a pulsed-field gel electrophrosis (PFGE) technique which can have separated molecular weight extend to 5 × 10^9 daltons. Thus, it makes a great convenience for studying DSBs.

The present work studied DSBs of DNA in melanophore B_{16} induced by plateau and extended Bragg peak of 75 MeV/u $^{12}C^{6+}$ ions by using FIGE technique.

1. Materials and Methods

1.1 Cell culture and plug preparation

The melanophore B$_{16}$ was purchased from Institute of Tumor Research, Chinese Academy of Medicine Sciences. The cancer cells were grown in RMPI-1640 medium (*Gibco* product) supplemented with 20% calf serum at 37°C and 5% CO_2. Then they were transferred to petri-dishes in 5×10^4 cells/ml. After incubation for 48 h, the cells were trypsinized and collected by centifugation (1500 rpm) for 5 min and followed by washing three times with D-Hank's solution and diluting up to 1×10^7 cells/ml to form cell suspension. The cell suspension was added into 1% agarose with low-melting-point (*Sigma* product) in an equal volume. The mixture was immediately pipetted in a plug mould and allowed to solidify. The solidified plugs were 4 mm in thickness. They were taken out from the mould and put into lysis solution (1 mg/ml proteinase K (*Sigma* product), 1% SDS, 0.5 mol/l EDTA, 10 mmol/l Tris-HCl, pH 8.0) at 50°C for 48 h. Finally, the plugs were washed three times with TE (1 mmol/l EDTA, 10 mmol/l Tris-HCl, pH 8.0) and kept in EDTA (0.5 mol/l, pH 8.0) at 4°C.

1.2 Irradiation

The plugs were irradiated with plateau and extended Bragg peak of 75 MeV/u $^{12}C^{6+}$ ions at HIRFL (Heavy Ion Research Facility in Lanzhou). After extending Bragg peak, the widths of plareau and peak were 8 mm and 5 mm, respectively. Average LET of the plateau in the range of 0-4 mm was 43.2 keV/μ m in water. Average LET of the extended Bragg peak in the width of 5mm was 65.2 keV/μ m in water. In order to obtain confident results, every three plugs as a group were irradiated at the same dose and acquired an average value. After irradiation, the plugs were kept in EDTA (0.5 mol/l, pH 8.0) at 4°C.

1.3 Electrophoresis

Before electrophoresis, 0.8% agarose (*Huamei Company* product) gel with 0.5 μ g/ml ethidium bromide was cast in $1 \times$ TBE (89 mmol/l Tris-HCl, 89 mmol/l boric acid, 2.5 mmol/l EDTA, pH 8.0) buffer. The plugs were inserted into wells of the gel in the electrophoresis chamber. The yeast chromosome, *Saccharomyces serevisiae* (*Sigma* product) whose maximum molecular weight was 2.2 Mbp, was used as standard DNA molecule. Electrophoresis was carried out in $0.5 \times$ TBE buffer for 72 h at 36 V and 12°C by using DF-4 type alternating pulse electrophoresis apparatus. Ratio of running time along positive and negative directions was 5:1. After electrophoresis, the gel was taken photo and fluorescence-scanned by using CS-910 type Dual-wavelength TLC scannor (*Shimadzu*). Excitation and emission wavelength was 254 nm and 600 nm, respectively.

2. Results and discussions

2.1 Distribution of the DNA fragments

Fig.1 (A) and (B) show the fluorescence-scans of DNA fragments in gel running lanes and the content distribution of DNA fragment sizes in the gel lanes for plateau irradiation. The extended Bragg peak irradiation is similar in that to the plateau irradiation. It is seen from Fig.1 that DNA fragment lengths of samples irradiated by the plateau were distributed in two ranges: the larger in 1.4 Mbp-3.2 Mbp and the

smaller in less than 1.2 Mbp. It indicates that the size distribution of DNA fragments is not stochastic. It seems that there are sensitive sites to heavy ions in DNA molecules of B_{16}. Meanwhile, there were DNA fragments entering gel in control sample. For this reason, the results were corrected for the control background.

Table 1 shows that the contents of DNA fragments of the two size ranges after correction for the control background. It can be seen from the table that as the dose increased, the content of larger size fragments decreased and one of the smaller size fragments increased. It shows that low dose induced mainly larger size fragments due to fewer events of energy deposition on a DNA molecule and high dose could make DNA molecules break into smaller fragments due to more events of energy deposiyion on a DNA molecule. In the dose range from 60 to 100 Gy, the content of smaller fregments trended towards saturation and one of larger fragments flattened. At 110 Gy for extended peak irradiation, the former decreased drastically while the latter increased evidently. These phenomena may be mainly attributed into fragment crosslinking and/or clustering.

Table 1   Distribution of DNA fragments induced by plateau and extended Bragg peak of C ions

dose	plateau irradiation		extended Bragg peak irradiation	
	corrected content of DNA fragments (%)		corrected content of DNA fragments (%)	
(Gy)	in 1.4-3.2 Mbp	in less than 1.2 Mbp	in 1.4-3.2 Mbp	in less than 1.2 Mbp
0	0	0	0	0
10	35.43	5.75	37.91	7.11
20	33.33	15.33	—	—
30	28.11	36.70	35.06	17.93
40	23.99	39.41	26.32	44.44
50	20.27	45.85	30.41	46.38
60	8.00	61.76	—	—
80	—	—	12.53	66.11
90	10.91	69.45	9.60	72.11
100	8.20	69.25	10.31	71.77
110	—	—	27.94	49.68

2.2 Induction of DSB

As shown in Fig.2 (not corrected for the control background), PR increased with increasing dose and trended towards a quasi-plateau ~ 85%. Cedervall et al found also that as the dose increased, PR trended towards a quasi-plateau ~ 81%[1]. It was reported that although 1000 Gy irradiation, there was 2% DNA remained in the well[2]. However, at 1000 Gy all the DNA fragment lengths should be less than 5 Mbp which were able to run out of well. The abnormality may be resulted from duplicate forks, cosslinking and so on[3].

Because distribution of DNA fragments induced by heavy ion irradiation is not stochastic, the four methods[1] reported by Cedervall et al can not applied to evaluating the breakage level of DNA DSBs. Meanwhile, there is not linear correlation between PR and dose, yield of DSB can not be easily obtained. In order to obtain the breakage level and the yield of DSB quantitatively, a methodology is needed to be developed.

References

[1] Cedervall, B., et al., Radiat. Res., **143**,1995:8-16

[2] Schneider, M., et al., Radiat. Env. Biophys., **33**(2),1994:111-124

[3] Wlodek, D., et al., Int.J.Radiat.Biol., **60**,1991:779-790
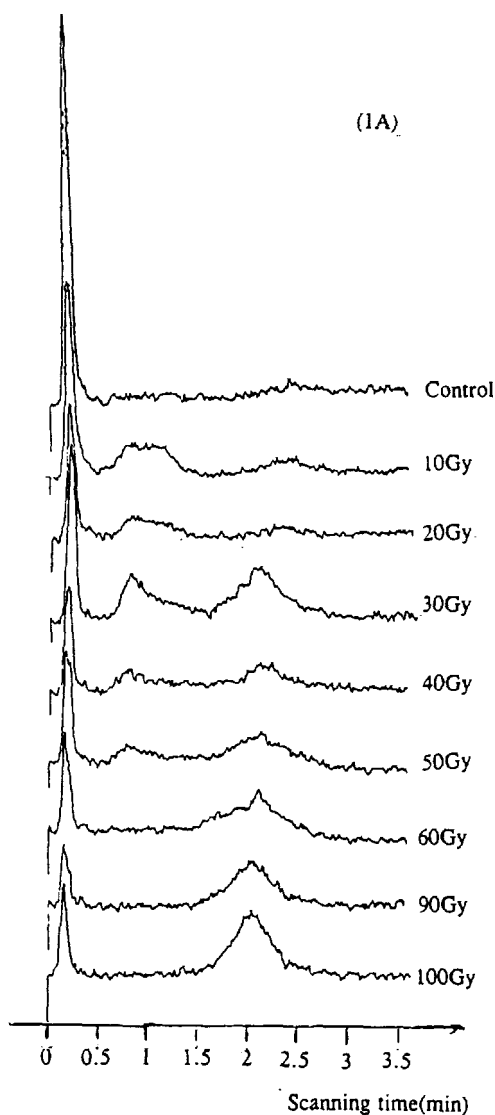
Fig.1 Distribution of DNA fragments in the gel lanes(1A) and content distribution of DNA fragment sizes(1B) for the plateau irradiation
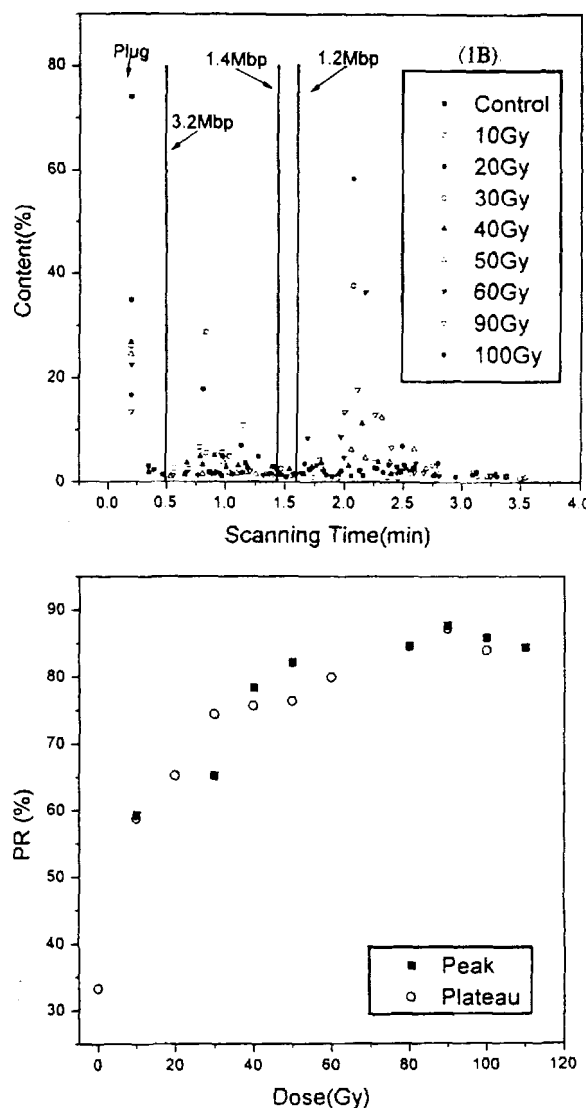
Fig.2 The percentage of DNA released from the plug(PR) induced by 75MeV/u $^{12}C^{6+}$

Initial DNA fragmentation induced by radiation of different linear energy transfer.

Erik Höglund[a], Bo Stenerlöw[a], Jörgen Carlsson[a] and Erik Blomquist[b]

[a] Division of Biomedical Radiation Sciences, Uppsala University
Box 535, S-751 21 Uppsala, SWEDEN

[b] Department of Oncology, Uppsala University, Akademiska sjukhuset
S-751 85 Uppsala, SWEDEN

Introduction

As the ionisation density increases, the relative biological effectiveness (RBE) for reproductive cell death and many other biological endpoints, increases. For radiation with high linear energy transfer (LET), as α-particles or low energy ions, the high ionisation density often is reported not to lead to an increase in the initial number of DNA double-strand breaks (DSB), *e.g.* Heilmann *et.al.* [1]. Theoretical calculations predict more complex DSB when the LET increases [2,3,4] and it is possible that the complexity determines the biological effectiveness. However, recent experimental data [5,6,7] shows that DSB are non-randomly induced by high LET radiation. The induced breaks, leading to small, and intermediate sized DNA-fragments, were detected by more detailed analysis of the DNA fragment size distributions. Compared to results from conventional analysis of DSB, this clustering leads to a 1.7-2.8 -fold increase in RBE for DSB induction [6]. It could be that RBE for the induction of DSB following irradiation with LET is underestimated when scored by the conventional assay.

In the present study, size distributions of DNA molecules were analysed after irradiation of low passage normal human fibroblasts with gamma photons (^{60}Co), and high LET nitrogen ions (125 keV/μm). Two different pulsed-field gel electrophoresis (PFGE) protocols, optimised for separation of fragments in the 1-10 Mbp range (conventional PFGE assay) and the 10 kbp-1.64 Mbp range respectively, were used. It is evident from our data, and other detailed analyses of DNA fragment size distributions following radiation, that high LET radiation is more effective compared to low LET radiation, in producing fragments shorter than a few hundred kilobase-pairs. These fragments are in the same size region as the solenoid loop structure that is attached to the nuclear matrix in interphase cells. Such fragments might appear due to interactions between the particle tracks and these higher order structures of the chromatin.

Materials and Methods

Normal human skin fibroblasts, GM5758 (Human Genetic Mutant Cell Repository, Camden, NJ), were grown under standard conditions in MEM-Eagle (Earle's salt base) supplemented with 10% foetal calf serum, 2 mM L-glutamine, 100 mg/ml streptomycin and 100 IU/ml penicillin, and 2x concentration of vitamins, essential and non-essential amino acids. Cells of passage 7 to 10 were plated in 25 cm^2 flasks or 30 mm culture dishes 10-12 days before irradiation. At the time for irradiation the cultures were confluent and non-dividing. Cells were grown in 740 Bq/ml [methyl-^{14}C]thymidine (Amersham), or 3700 Bq/ml [^{3}H]thymidine (Amersham, UK) for 4-5 days, and the label was chased with fresh medium 2-3 days before irradiation. Agarose plugs with 2.5-3 x 10^6 cells/ml were prepared prior to irradiation as earlier described [8]. The plugs were irradiated with photons, (^{60}Co), 0.7-1.0 Gy/min in a multi-well plate containing 0°C serum-free medium, and with accelerated N ions at 125 keV/μm, at the Bio-Medical Unit at the The Svedberg Laboratory in Uppsala [8]. All irradiation were carried out on ice, and the cells were placed on ice 45-60 minutes prior to irradiation. After lysis and washing, the agarose plugs were loaded onto an agarose gel and the DNA was separated by two PFGE protocols, optimised in two different size intervals, (1-10 Mbp at 1.4 V/cm, pulses ramped from 3 h to 1 h during 74 h, and 10 kbp-1.64 Mbp at 7 V/cm for 17 h, 10 s, 40 s and 70 s pulses during 7 h, 5 h and 5 h respectively). The gels were stained with ethidium bromide in distilled water for visualisation of DNA distributions and the size markers *Schizosaccharomyces pombe* (FMC), *Saccharomyces cerevisiae* and *Lambda* DNA-PFGE markers (Pharmacia Biotech). Each lane in the FAR gel was cut at the location of the 5.75 Mbp marker (the largest chromosome of *S. pombe*). The lanes in the intermediate gel were cut into segments containing DNA fragments with specified sizes in the range 48-1640 kbp (se Figure 1), according to the DNA size markers. The incorporated activity in each gel slice were counted in a liquid scintillation counter, giving the fraction activity released (FAR), or the fragment size distribution of the DNA in the lanes. The total number of DSB per unit length of DNA was calculated from the DNA fragment distributions. The fraction of incorporated activity in each size zone of the lanes were divided by the average DNA size in that zone, and summed up for all the size zones in the lanes, giving the total number of breaks per unit length of DNA. For fragment sizes >1.6 Mbp, a model assuming random distribution of breaks were used [9].

Results and Discussion

For conventional DSB assays, as PFGE optimised for detection of large fragments in the range of 5-12 Mbp, the RBE for DSB induction is generally below unity [1], and a clear decrease in the relative yield is seen as the LET increases. To investigate the distribution of DSB at intermediate sizes, we analysed DNA fragments in six size intervals between 0 and 1640 kbp. In Figure 1 the fraction of DNA within different size zones is plotted *vs* radiation doses of ^{60}Co photons and 125 keV/μm N ions. In panel a it is shown that photons, at least

for doses above 40 Gy, are more efficient in producing fragments larger than approximately 1 Mbp, while for all fragments smaller than about 600-700 kbp, the high LET radiation is more efficient (panels c, d, e and f). Similar results after irradiation with Fe and N ions [6], and α-particles [7] have been reported earlier. Despite small differences between our results and the earlier reported data, the general behaviour is the same; high LET radiation is more effective in producing shorter DNA fragments. This demonstrates that the DSB induction pattern for high LET radiation can not be fitted into random breakage models, and the number of ion-induced DSB could not be calculated by assuming random distribution of breaks. There is a higher probability for the formation of small and intermediate sized fragments after high LET radiation, maybe due to breaks correlated with the periodicity of DNA folding in higher order chromatin [10].
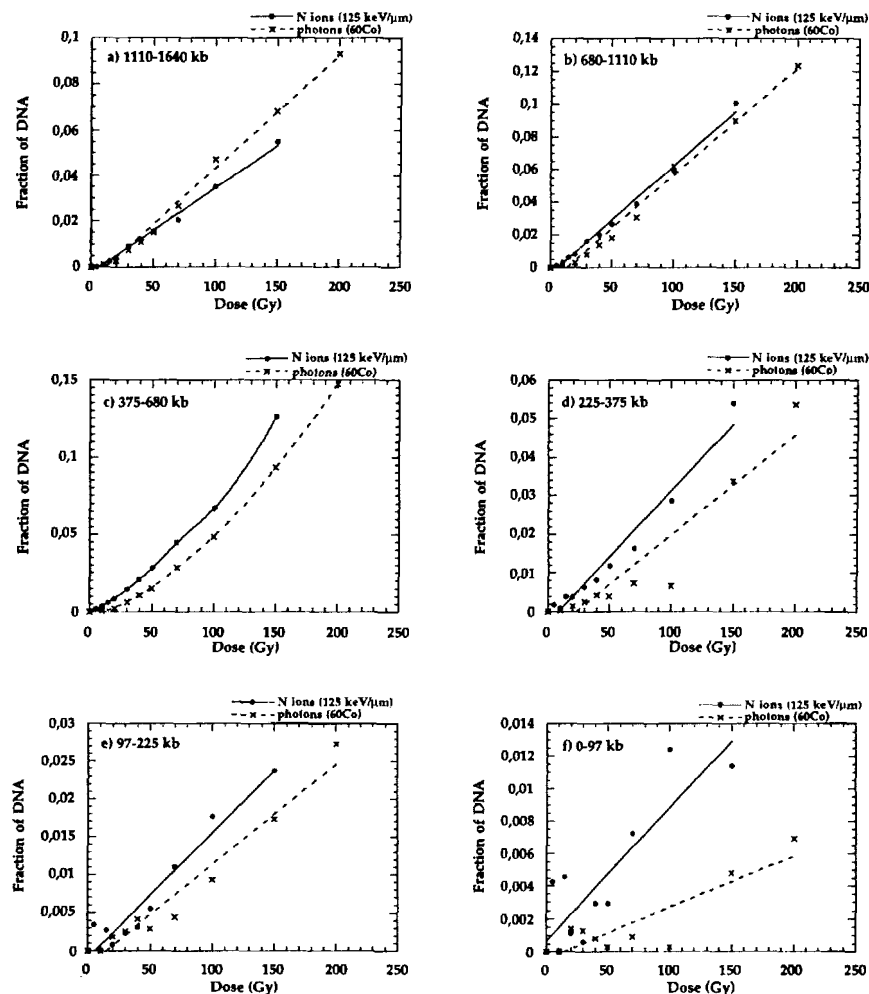

Figure 1. The fractions of DNA in the different size zones of the gel are plotted as a function of radiation dose for the two different radiation qualities. Data points are mean values from two, or three experiments for the photons and the nitrogen ions respectively.

By dividing the fraction of DNA in each size zone by the average DNA size in the zone, a good approximation of the true number of DSB can be obtained. The total induction yields of DSB for the two radiation qualities, when calculated in this manner, were $4.7\pm0.1 \times 10^{-9}$ and $7.6\pm0.4 \times 10^{-9}$ DSB/bp/Gy for photons and N ions respectively, giving an RBE for DSB induction of about 1.6. This was significantly higher than the RBE of 0.9 as earlier obtained for these ions by the conventional PFGE assay [7]. However, the fragment distribution after irradiation with low LET photons did not deviate from the random breakage model. The clustering of breaks may also affect the DSB repair, either by increasing the misrepair or by generating a larger fraction of unrejoined fragments. Experiments along this line are in progress.

Acknowledgement

References

1. Heilmann, Taucher.Scholz, G. and Kraft, G., Induction of DNA double-strand breaks in CHO-K1 cells by carbon ions. *Int. J. Radiat. Biol.*, **68**, 153-162 (1995).
2. Goodhead, D. T., The initial physical damage produced by ionizing radiations. *Int. J. Radiat. Biol.*, **56**, 623-634 (1989).
3. Barendsen, G. W., Mechanisms of cell reproductive death and shapes of radiation dose-survival curves of mammalian cells. *Int. J. Radiat. Biol.*, **57**, 885-896 (1990).
4. Holley, W. R. and Chatterjee, A., Clusters of DNA damage induced by ionizing radiation: Formation of short DNA fragments. I. Theoretical modeling. *Radiat. Res.*, **145**, 188-199 (1996).
5. Rydberg, B., Clusters of DNA damage induced by ionizing radiation: Formation of short DNA fragments. II. Experimental detection. *Radiat. Res.*, **145**, 200-209 (1996).
6. Löbrich, M., Cooper, P. K. and Rydberg, B., Non-random distribution of DNA double-strand breaks induced by particle irradiation. *Int. J. Radiat. Biol.*, **70**, 493-503 (1996).
7. Newman, H. C., Prise, K. M., Folkard, M. and Michael B. D., DNA double-strand break distributions in X-ray and α-particle irradiated V79 cells: evidence for non-random breakage. *Int. J. Radiat. Biol.*, **71**, 347-363 (1997).
8. Stenerlöw, B., Blomquist, E., Grusell, E., Hartman, T. and Carlsson, J., Rejoining of DNA double-strand breaks induced by accelerated nitrogen ions. *Int. J Radiat. Biol.*, **70**, 413-420 (1996).
9. Blöcher, D., In CHEF electrophoresis a linear induction of dsb corresponds to a nonlinear fraction of extracted DNA with dose. *Int. J. Radiat. Biol.*, **57**, 7-12 (1990).
10. Filipski, J., Leblanc, J., Youdale, T., Sikorska, M. and Walker, P. R., Periodicity of DNA folding in higher order chromatin structures. *The EMBO Journal*, **9**, 1319-1327 (1990).

Double-strand break induction along a particle track: visualization of different fragment sizes

D. Keller, G. Taucher-Scholz and G. Kraft
GSI, Postfach 110552, 64291 Darmstadt

DNA double-strand breaks (dsb) are considered to be the most relevant type of damage after irradiation with ionizing radiation.

DNA is associated with histones and other chromosomal proteins giving rise to packed chromatin. For this reason the cellular environment is strongly protective as has already been shown in various studies. The aim of this study is to understand the influence of chromatin packaging on DNA fragmentation along a particle track over a wide LET range.

Dose-depth-profiles for dsb induction have already been measured for particles penetrating through cells embedded in agarose slabs [1]. Using a modification of this technique the separation of different fragment sizes produced by dsb breakage was additionally achieved. The application of this assay comparing fragmentation induced in cells and in decondensed chromatin under conditions of equal radiosensitivity should help to elucidate the influence of packaging.

For the experiment human AG-Fibroblasts were embedded in agarose plugs of 12 cm length [1]. Conditions for cell permeabilization and preparation of histone-depleted chromatin in the large plugs were established based on a protocol reported by Elia and Bradley [2]. Extracted chromatin in the plugs was then incubated in a solution containing the radical scavenger DMSO in order to achieve similar dsb yields in protected chromatin and in cells.

The appropriate concentration was determined in a separate experiment. The results are shown in fig. 1.
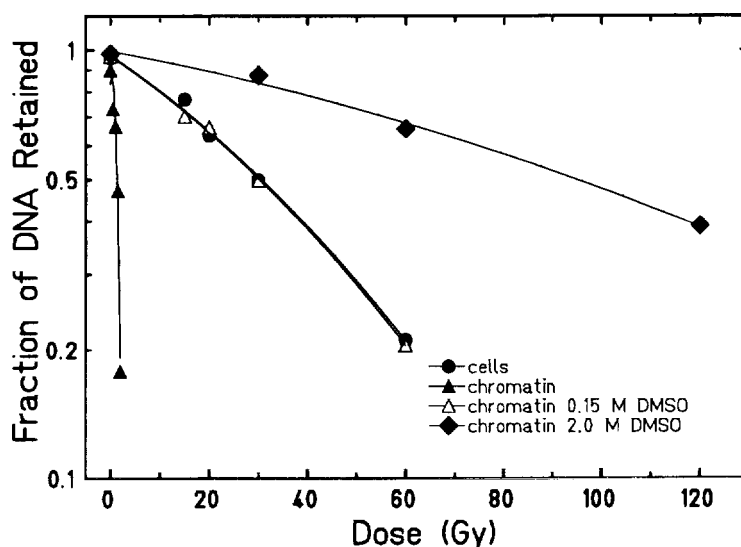

Figure 1: Human AG-fibroblast cells were embedded in agarose and histone depleted chromatin was prepared and incubated in 0.15 M and 2.0 M DMSO. After irradiation with X-rays cells were lysed and DNA was separated by electrophoresis. After ethidium bromide staining the fluorescence pattern were evaluated densitometrically. DNA dsb-induction is plotted as the fraction of DNA retained versus dose. Dsb yields obtained for the chromatin substrate correspond to those in cells.

After embedding of cells a preparation of histone depleted chromatin was carried out in the large plugs, followed by an incubation in DMSO - solution at the concentration that was found to imitate the protective cellular environment.

In the next step the histone-depleted chromatin plug incubated in 0.15 M DMSO was exposed to 195 MeV/u carbon ions. Irradiation was performed at the horizontally positioned agarose slab in a polystyrene tank filled with ice-cold PBS. To minimize diffusion of DMSO out of the plug it was covered with foil leaving the beam entrance free. The irradiation was chosen to place a 140 Gy isodose extended Bragg - peak at a depth of 8 cm over an extension of 1 cm.

After irradiation the permeabilised cells in the gel-slab were completely lysed and subjected to electrophoresis. Two previously described procedures, gradient- and pulsed-field-gelelectrophoresis were newly combined to get a pattern of fragments along the particle trajectory. A first step of abrupt increasing of voltage leads to stopping of fragments of sizes down to about 3 Mbp. In further steps fragment sizes between 3 and 1.0 Mbp are stopped. Finally fragments between 1000 and 50 kbp are separated in a pulsed field.

After ethidium bromide staining the fluorescence pattern of the DNA was evaluated densitometrically. The increase of DNA-fragmentation with penetration depth up to the extended Bragg-peak can be observed.
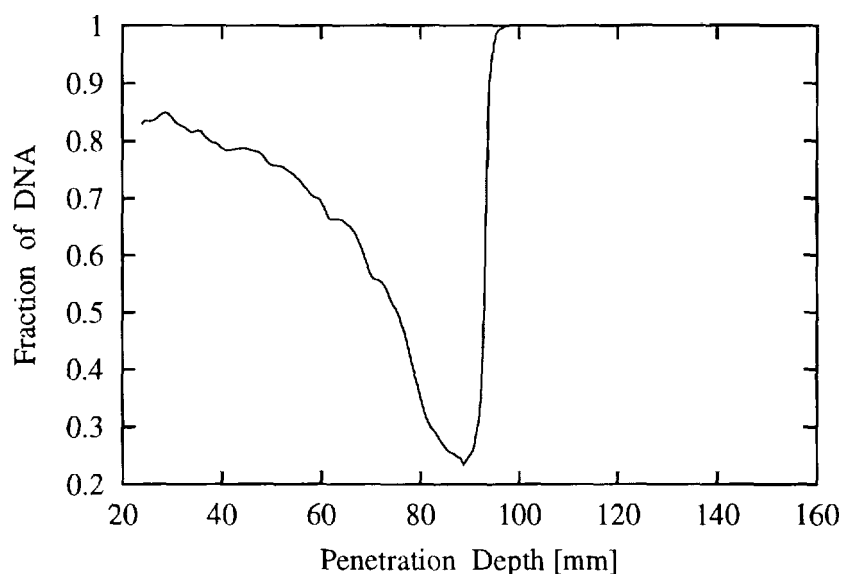

Figure 2: After irradiation with C 195 MeV/u a large plug containing histone-depleted chromatin incubated in 0.15 M DMSO solution was subjected to complete lysis and DNA was electrophoretically separated as described above. The amount of fragments between 1000 and 50 kbp after ethidium bromide staining and densitometrical evaluation was expressed as fraction of total DNA content and plotted as a function of penetration depth.

As an example in fig. 2 the yield of small fragments between 1000 and 50 kbp is plotted as fraction of total DNA versus penetration depth. The extension of the Bragg-peak is clearly visualized due to the production of small fragments and the abrupt decrease of fragments greater than 3 Mbp. Further on a shifting of fragmentation size along the penetration depth in visualized. This is a consequence of both an increase of LET and a concomitant increase of dose.

The comparison with DNA fragmentation in cells embedded and irradiated in large plugs and analyzed as described above will be investigated in further experiments.

References

[1] J. Heilmann et *al. Int. J. Oncology Biol. Phys.*,Vol. 34, 3, 599 - 608 (1996)
[2] M. C. Elia and M. O. Bradley   *Cancer Research*, 52, 1580 - 1586, (1992)

Investigation of radiation induced DNA breaks using Scanning Tunneling Microscopy

W. Schonert and G. Kraft
GSI, Planckstr. 1, D-64291 Darmstadt

The most important types of radiation induced DNA lesions are single (SSBs) and double strand breaks (DSBs). For detection and quantification of these lesions different experimental methods are in use today. One commonly used method, among others, is the analysis of plasmid DNA:
Plasmid DNA, natively in a compact supercoiled configuration, allows the determination of SSB– and DSB induction by monitoring the relaxation or linearization of the molecules. The different DNA configurations can be evaluted by agarose gel electrophoresis and densitometry [1].

However, with this method it is not possible to differentiate specific types of lesions in individual molecules. The effect is detected only by integration over many identical molecules ($> 10^7$), but qualitative differences in damage induction (as proposed between low- and high-LET radiation) can not be resolved.
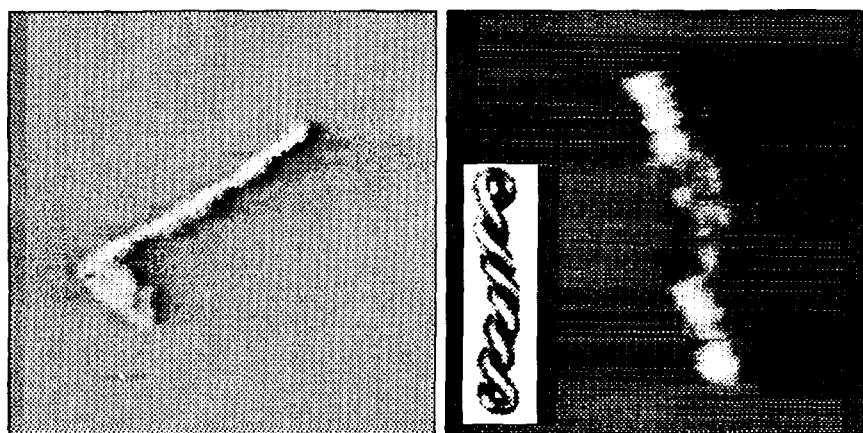

Figure 1: STM images of intact supercoiled plasmid molecules (left: 339 nm × 409 nm, right: 275 nm × 333 nm).

In this contribution we present Scanning Tunnelling Microscope (STM) [2] as a novel method to study individual molecules. With STM the surface of a sample is scanned with a very sharp tip. With a voltage applied a tunneling current can be measured that depends exponentially on the topography of the surface. The high vertical

and lateral resolution of STM offers the new possibility to image individual DNA molecules and to get a realistic visual impression of radiation defects on the molecular level. Because the imaging process is principial non-contactive, influences on the biological samples are kept to a minimum. Although the conduction mechanism for imaging biological molecules with STM is not totally understood, DNA has been imaged by several groups (see for example [3, 4, 5]).

We employed a home-made pocket-sized STM with a maximum scanning range of about 3 μm. For our investigation a 4000 bp supercoiled plasmid was used. The molecules were dissolved in aqueous buffer solution. A drop of this DNA-containing solution was applied directly onto the surface of a graphite-layer and evaporated on air. Scanning was always performed under atmospheric conditions.
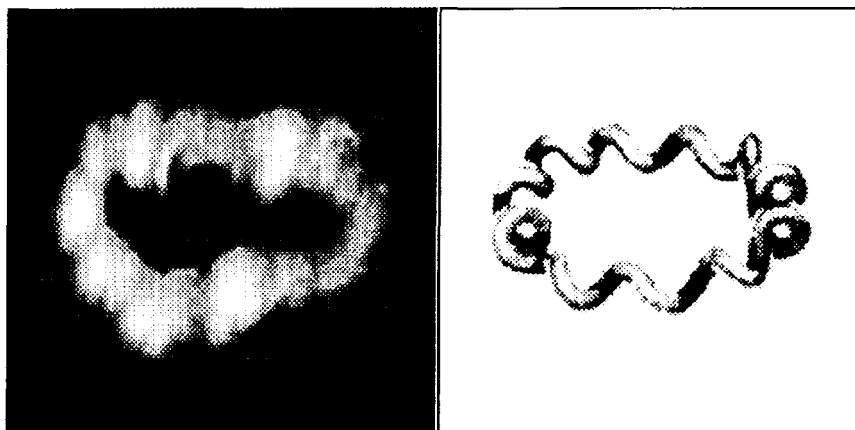

Figure 2: Relaxed circle, prepared by X-ray induced single-strand nicking of supercoiled molecules (250 nm × 200 nm).

In Fig. 1 plasmid molecules are shown in their native configuration. The supercoiled fine structure can be observed by zooming in to smaller scan sizes and may result in the linear appearance of the features. The observed dimensions (length about 300 nm and width about 20 nm) are in the range one can expect from topological considerations.

To induce conformational changes, the solution was irradiated with 400 Gy X-rays before dropping it onto the substrate and evaporating. After irradiation a completely different morphology of the plasmids was observed: Both relaxed circles (Fig. 2) and linearized molecules (Fig. 3) could be found on the substrate. Although the presence of mostly relaxed open circles has been prooven by gel electrophoresis, the occurence of relaxed circles was very few in our STM images.

The lengths of linearized plasmid molecules (Fig. 3) measured from our STM images were in good agreement with the expected molecular length (slightly larger than 1 μm). The enlarged width of the molecules, which where about 5 to 10 times larger than the 2 nm width of B-DNA, can be explained by the hydration shell.

Figure 3: STM image (1173 nm $\times$ 1140 nm) of linearized plasmid DNA after irradiation.

In summary, we demonstrated the possibility to image plasmid DNA in its three configurations with STM. For a routine employment of STM there are some methodical improvements necessary to enhance immobilisation of the molecules on the substrate and to increase the reproducability of the images. However, STM represents an interesting additional tool for imaging DNA under ambient conditions and qualitative analysis of DNA damage .

References

[1] G. Taucher-Scholz *et. al. Adv. Space Res.* **12**(2-3), (2)73–(2)80 (1992)

[2] G. Binnig and H. Rohrer, Surface Science **126**, 236–244 (1983)

[3] S.M. Lindsay *et. al.*, *J. Vac. Sci. Technol.* **A(11)4**, 808–815 (1993)

[4] D.P. Allison *et. al.*, *J. Vac. Sci. Technol.* **A(11)4**, 816–819 (1993)

[5] R. Guckenberger *et. al.*, *Science* **266**, 1538–1540 (1994)

FREE RADICALS FROM DNA AFTER IRRADIATION WITH HEAVY IONS OR X-RAYS: A HIGHFIELD EPR STUDY AT 8.7 T AND 245 GHZ

Barbara Weiland[*], Jürgen Hüttermann[*] and Johan van Tol[&]
[*]Fachrichtung Biophysik, Universität des Saarlandes, Klinikum Bau 76, D-66421 Homburg/Saar
[&]Grenoble High Magnetic Field Laboratory MPI-F/CNRS, BP 166, F-38042 Grenoble Cedex 9

Free radical formation in an early stage of radiation damage to DNA can be modelled by irradiating isolated DNA and DNA components at low temperature and investigating the free radicals by Electron Paramagnetic Resoncance (EPR) spectroscopy. In order to enhance the identification of the strongly overlapping component spectra in DNA by g-factor separation, we applied EPR at 245 GHz (8.7 T). Our aim was first to characterize the free radicals in dry DNA after irradition with X-rays or heavy ions by comparison with spectra of radicals from X-irradiated nucleotides. Furthermore, we studied the influence of intercalating (proflavine) or non-intercalating agents (riboflavine, azomycine, potassium hexacyanoferrate) in low concentrations on the radical formation in DNA. We also searched for the influence of water of hydration after X-irradiation.

The highfield spectra confirmed the initial presence of at least three primary radicals, the oxidized guanine as well as the reduced cytosine and thymine species after X-irradiation. No significant difference of spectral composition was found upon heavy ion bombardment with different nuclei. However, quantitative analysis of X-band spectra after irradiation with Zn ions (5 MeV/u, LET = 3860 keV/μm) at about 100 K resulted in a much lower G-value as well as a lower final number of radicals in the saturation part of the dose response curve than after X-irradiation. Intercalating and non-intercalating agents which act as electron scavengers were effective in preventing the formation of the reduced DNA radicals after X-irradiation as well as after heavy ion bombardment of dry DNA. At higher humidity the reduction of the cytosine seemed to be favoured above thymine according to its higher electron affinity. The relative yield of the oxidized guanine base was found to be reduced with increasing water content. Whereas the efficiency of the intercalating proflavine was comparable to the non-intercalating riboflavine in dry DNA after X-irradition, it was strongly reduced in the presence of a hydration layer.

DE98F5393

DE010818174

HEAVY ION INDUCED DAMAGE TO DNA CONSTITUENTS: PRODUCT FORMATION

Anne-Kathrin Hoffmann and Jürgen Hüttermann, Fachrichtung Biophysik, Universität des Saarlandes, Klinikum Bau 76, D-66421 Homburg, Germany

Important effects of ionizing radiation on living organisms are attributed to chemical modifications induced within DNA. At an early stage irradiation leads to the formation of free radicals which are precursors of alterations like modified bases and strandbreaks. Direct radiation action involves deposition of energy in the target molecule itself. Free radicals induced by heavy ion bombardment in the direct radiation action mode are mainly products of the ionization pathway due to the reaction with electrons generated by interactions of the primary radiation with the target. The action of ionizing radiation with the target results in the formation of radical anions and cations which can protonate or deprotonate, respectively. The pathway from free radical species to products is a topic which is at present hardly understood; its elucidation is the major aim of our studies.

DNA and its constituents irradiated as solid samples were used in order to study explicitly the direct radiation effect. As first product, the release of unaltered bases after dissolving the irradiated samples in aqueous solution could be demonstrated to occur and was investigated quantitatively using HPLC and ^{1}H-NMR. Samples of pyrimidine nucleotides were irradiated in the beam vacuum with Ni (11.4 MeV/u) and C (11.4 MeV/u) at 300 K. The main diamagnetic products after dissolving the samples in deuterium oxide were the free thymine or cytosine base, respectively. The increase in the yield of free bases was linear with dose up to 200 kGy. The radiation chemical yields (G values) were estimated to be in the order of 10^{-7} mol J^{-1}. The G values for the base release after heavy ion bombardment with nickel were nearly the same as for X-irradiation in the absence of oxygen (controls). Two other diamagnetic products of irradiated thymidine 5′-monophosphate (TMP) were the diastereoisomers of the 5,6-dihydroadduct, which were recently identified by NMR at 800 MHz. A quantitative study of the direct effect of X-irradiation on TMP in the presence of an electron scavenger (riboflavin) at a dose of 180 kGy was carried out. Riboflavin would be in competition with the pyrimidine nucleotide molecules for delocalised electrons, thus reducing the number of radical anions for a given dose of radiation. This is reflected by a reduction in the observed yields of the 5,6-dihydroadducts of about 70%. On the contrary the free base is probably a diamagnetic product of the radical cation, because the yield is not reduced in the presence of the electron scavenger.

B

Space Research (Chair Walter Schimmerling)

Oral Presentations

1. Walter Schimmerling
   (NASA, Washiington, USA)
2. Thomas Streibel
   (Univers. Siegen, Germany)
3. Manfred Schäfer
   (DLR Cologne, Germany)

Radiation in Space

Cross Sections and Kinematics of Proton nduced
Fragmentation of Carbon
Inactivation Probalility as a Function of the Distance
from the Particle's Path Measured with Spores of
Bacillus Subtilis and Using an Image Analyzing System

RADIATION IN SPACE

W. Schimmerling, J. W. Wilson, F. Cucinotta, and M-H Y. Kim
National Aeronautics and Space Administration
Washington, DC 20546-0001
United States of America.

Human crews engaged in the exploration of space will be exposed to weightlessness and to space radiation. The effects of radiation exposure thus need to be considered in the context of weightlessness. Removal of the force of gravity results in structural and functional changes, especially in weight-bearing muscle, bone, and connective tissue. Changes also occur during space flight in endocrine, hematological, immunological, metabolic, nutritional and gastrointestinal, renal, sleep, biological rhythms, and temperature regulation; changes in pharmacokinetics and pharmacodynamics may further confound crew health care. Changes in immune function may be related to living in a "closed environment" -- the space habitat, the effect of stress during launch or landing, inhibition of white cell maturation due to microgravity or other factors.

Outside the protection afforded by the Earth magnetic field and atmosphere, the main penetrating components of ionizing space radiation are protons (and some heavier particles) emitted in the course of solar energetic particle (SEP) events, and protons and the energetic nuclei of other elements (HZE – high atomic number Z and energy E – particles) that constitute galactic cosmic rays (GCR).

The SEP protons have energies up to several hundred MeV and intensities that can increase by four or five orders of magnitude within a few hours during a solar disturbance. In an unshielded environment, SEP particle fluxes have the potential to cause acute radiation effects, but several techniques, such as seeking refuge in a well shielded "storm shelter", can be used to keep the dose from SEP particles within acceptable limits. The important open questions related to SEP events deal with the solar physics of their origin. While some biological questions remain about the radiation risk induced by protons, the physical aspects of their interaction with matter are relatively well-known. Thus, from the point of view of radiation protection, given adequate monitoring and warning, the risk can be predicted fairly accurately and managed using operational procedures.

This is not the case for GCR particles, which present new and significant problems for radiation protection, that have not yet been resolved. These heavy particles, with energies of several hundred MeV per nucleon, will suffer nuclear interactions in spacecraft materials that result in fragmentation of the projectile as well as of the targert. The HZE particles are highly penetrating, with ranges comparable to body dimensions and their linear energy transfers (LET) are in the range of 10 to several thousand keV/μm.

The relative biological effectiveness (RBE) of high-energy heavy ions has been measured for various end-points. It increases non-linearly as a function of LET from ~ 30 to ~ 100 keV/μm, with a peak around 100 keV/μm and possibly a slow decline toward higher LET values. The quality factor, Q, used in radiation protection, is correlated conceptually with RBE. Average quality factors, Q, for the GCR component, evaluated using measured distributions of LET and internationally recognized assumptions regarding the dependence of Q on LET [1,2] are between 2.3 and 3.4 [3].

Current radiation limits (Table I) apply only to low Earth orbit activities, such as the Interna-

tional Space Station. Short-term radiation limits for astronauts are intended to ensure that exposure to space radiation does not result in acute effects. Annual and career limits are

TABLE I. Low Earth orbit radiation limits [1]

	Blood-forming organs (5 cm depth) Sv	Eye (0.3 cm depth) Sv	Skin (0.01 cm depth) Sv
30-day	0.25	1.0	1.5
Annual	0.5	2.0	3.0
Career	2.0 + 0.075 x (age - 30) for males 2.0 + 0.075 x (age - 38) for females		

intended to limit the risk to be less than an "acceptable risk" [4]. The acceptable risk is currently defined by the NCRP [1] as a 3 per cent excess probability of fatal cancer above the working US population background rate. To provide some context for these limits, some known radiation effects are listed in Table II. They have been generated on the basis of material collected by the NCRP and discussed in their report.

Table II. Selected end-points for radiation exposure.

Dose (Gy)	Dose Equivalent (Sv)	Endpoint
	0.10	Recommended annual limits for planned or special emergency exposure (NCRP)
0.15		Threshold for blood count changes in a population, low LET, single, high dose-rate exposure (actually, .15 - .25 Gy)
0.50		Threshold for nausea and vomiting within 10 hours (range: 0.5-1.0 Gy) for occasional healthy, unmedicated adult. Threshold for blood count changes in an individual, low LET, single, high dose-rate exposure
	0.50	Threshold dose equivalent estimate for detectable lens of the eye opacities; range is 0.5-2.0 Sv
1.00		Effective threshold for vomiting; low LET, single, high dose-rate exposure
1.50		Effective threshold for mortality; low LET, single, high dose-rate exposure
	2.50	Threshold dose equivalent estimate for permanent sterility in females; single brief exposure of ovaries; range is 2.5-6.0 Sv
3.20		LD50 for mortality with minimal supportive care; low LET, single, high dose-rate exposure; actual values; 3.2 - 3.6 Gy
	3.50	Threshold dose equivalent estimate for permanent sterility in males; single brief exposure of testes
4.60		LD50 for mortality with supportive medical treatment; low LET, single, high dose-rate exposure; actual values; 4.6-5.4 Gy
	5.00	Threshold dose equivalent estimate for visual impairment (cataracts)
6.00		Median effective dose for erythema

There are large uncertainties associated with estimation of the risk from long-term exposure to HZE [5]; they are sufficiently large to prevent a meaningful definition of this risk at the present time. The conventional prediction of risk due to HZE particles for a given mission proceeds by evaluating the interplanetary space radiation environment during the mission. For a given spacecraft mass distribution and assumptions about the geometry of crew member bodies, radiation transport calculations [6] are used to calculate the radiation field inside the spacecraft and at crew organs. The cancer risk associated with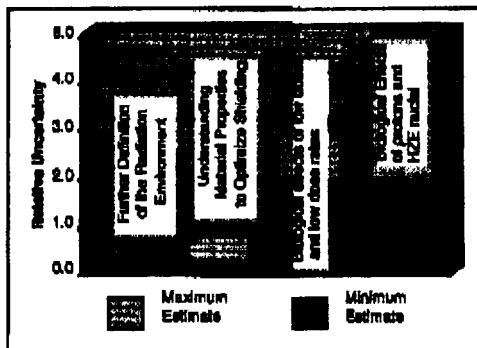 the physical dose is estimated based on extrapolation of the risk obtained from atomic bomb survivor studies, corrected for dose rate effects and for the different biological effectiveness of HZE particles. A Task Group of the US National Academy of Sciences recently estimated [5] the resulting uncertainties to be within a factor of 4-15, distributed as shown in Figure 1, among the various components of risk in this model of risk estimation.

Figure 1. Uncertainty attributed to various components of risk estimation [5].

A substantive research program is currently sponsored by NASA, with collaboration of other national and international agencies, using ground-based simulation of space radiation to develop the radiobiological knowledge required to predict risk from HZE particles accurately enough to define radiation limits for the human exploration of space. Typically, the questions that need to be addressed include:

- What are the cancer risks of exposure to the protons and high-energy nuclei of galactic cosmic rays?
- How do the thickness and composition of shielding affect the rate of cell death and chromosome aberrations induced by this radiation?
- Estimates of human genetic risk are based on studies of radiation-induced genetic alterations in rodents. Can studies be conducted that will increase confidence in these estimations?
- Is there a risk to the central nervous system from exposure to heavy ions at the level that would occur during long missions in deep space?

- How do the selection and design of the space vehicle affect the radiation environment in which the crew has to survive?

There exists an emerging consensus that the uncertainties can only be reduced by advances in the understanding of the basic science underlying risk estimates. The intention is to make a different approach to risk estimation possible, as shown schematically in Fig. 2. Some relevant aspects of this program will be described.
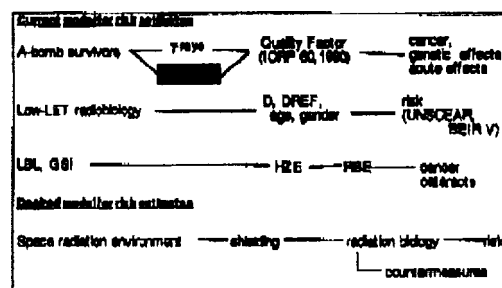

Figure 2. Strategies for risk estimation.

- 3 -

4. REFERENCES

[1]   NATIONAL COUNCIL ON RADIATION PROTECTION AND MEASUREMENTS. Guidance on Radiation Received in Space Activities. NCRP Report 98. Bethesda, MD (1989)

[2]   ICRP. 1990 Recommendations of the International Commission on Radiological Protection. ICRP Publication 60. Annals of the ICRP, 21: No. 1-3, Pergamon Press, Oxford (1990)

[3]   BADHWAR, G.D.,et al. Intercomparison of Radiation Measurements on STS-63 Radiation Meas. 26(6): (1997) 901-916

[4]   NATIONAL COUNCIL ON RADIATION PROTECTION AND MEASUREMENTS. Acceptability of Risk From Radiation - Application to Human Space Flight. Symposium Proceedings No. 3. Bethesda, MD (1997)

[5]   TASK GROUP ON THE BIOLOGICAL EFFECTS OF SPACE RADIATION. Radiation Hazards to Crews of Interplanetary Missions: Biological Issues and Research Strategies. Washington, DC. Space Studies Board Commission on Physical Sciences, Mathematics and Applications, National Research Council. National Academy Press (1996)

[6]   WILSON, J.W., TOWNSEND, L. W., SCHIMMERLING, W., KHANDELWAL, G.S., KHAN, F., NEALYJ .E., CUCINOTTA, F.A., SIMONSEN, L.C., SHINN, J.L. AND NORBURY, J.W., Transport Methods and Interactions for Space Radiations. NASA Reference Publication 1257, National Aeronautics and Space Administration, Washington, DC, (1991) 616 p.

CROSS SECTIONS AND KINEMATICS OF PROTON INDUCED FRAGMENTATION OF CARBON

T.STREIBEL, H.RÖCHER, G.HÜNTRUP AND W.HEINRICH

Department of Physics, University of Siegen, D-57068 Siegen, Germany

INTRODUCTION

For satellites flying in near earth orbits (altitudes of less then 500km) there is a significant contribution to the absorbed dose for astronauts and electronic devices caused by radiation effects in which a large amount of energy is transferred by a single particle. These effects can be caused by either the direct ionization of a cosmic ray heavy ion or alternatively by the ionization of short range target fragments which were produced inside the material by the interaction of cosmic ray particles especially of those of the radiation belts. The trapped particles in the inner radiation belt mainly are protons with energies extending up to several 100 MeV. Such protons are encountered by satellites crossing the edge of the inner radiation belt in the South Atlantic Anomaly (SAA). To allow predictions of possible radiation hazards the characteristics of the interactions of these protons with C-, O- and Si-nuclei, representing the target nuclei of biological material and electronic devices, is of importance and must be understood in detail. We have studied the proton induced fragmentation of C at an energy of about 70 MeV in inverse kinematics.

EXPERIMENT

We have used a method to study target fragmentation processes in inverse kinematics, where the nuclei collide with hydrogen in a target material. CR-39 plastic nuclear track detectors were mounted up- and downstream a C- and CH_2-target.
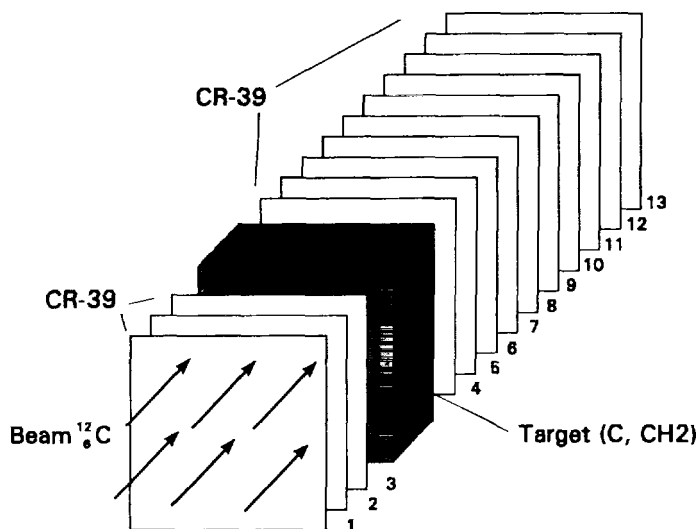

Figure 1: Schematic set-up of the experiment.

The trajectories and charges of incoming beam particles and outgoing fragments were measured in these set-ups. Details of our experimental technique and the method to determine cross sections were described by Brechtmann and Heinrich (1988). From the cross sections and angular distributions measured for these two targets the cross sections and distributions for the interaction with H-target can be determined. This is possible using the statistical subtraction method which considers the relative abundance of the elements C and H in the targets C and CH_2.

At energies below 100AMeV our experimental technique can only be used if the targets are not too thick. The energy loss of the beam particles and fragments is proportional to the square of their charge. As a consequence, fragments of the same charge which have been produced at different positions inside the target have different energies when they leave the target. That means that fragments of different charges may have the same energy loss. The size of the measured etch cones is defined by their energy loss (REL_{200}). For a charge calibration of the CR-39 detectors it is necessary that the distributions of track size still show distinct peaks. This restriction limits the thickness of the targets. To achieve results with high statistical significance we have used 8 stack with CH_2- and 4 stacks with C-targets, because the number of fragments produced inside the thin targets is small. In our experiment irradiated at the SIS at GSI Darmstadt, we used C ions at 80 AMeV. This leads to a mid target energy of 66 and 68 AMeV for C- and CH_2-target respectively. The schematic set-up of our experiment is shown in fig. 1. We have used 3 foils (0.6mm) of CR-39 up- and 10 foils downstream a target (3mm). The stack area is $10\times10cm^2$. Each set-up was irradiated with about 50000 particles. From the number of incoming beam particles and outgoing fragments with different charges we have determined the production cross sections for the fragments with charges Z>2 produced in interactions of C with the different target nuclei. The results for the partial charge changing cross sections are shown in fig. 2.
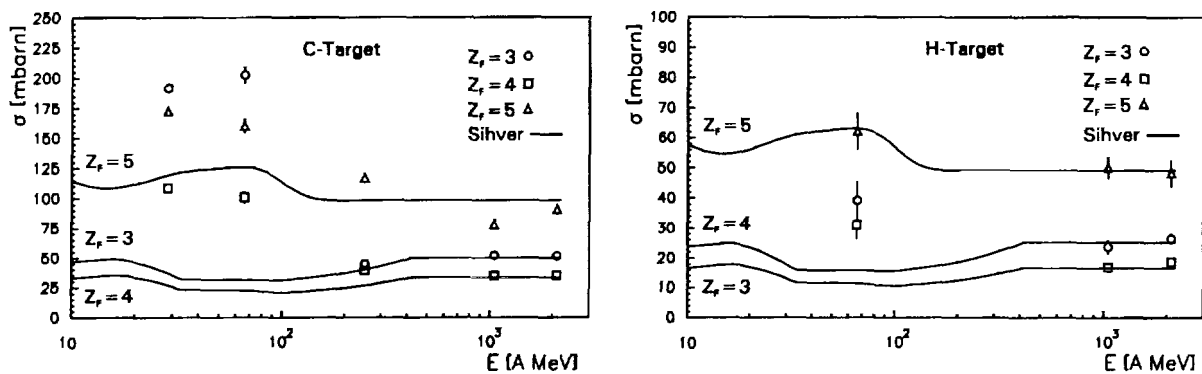

Figure 2: Measured partial cross sections at about 66 AMeV compared to model predictions of (Sihver et al.,1993) and to other data. For C-target: 28.7AMeV (Czudek et al.,1991), 250AMeV (Kidd et al.,1988). For C- and H-target: 1.05 and 2.1 AGeV (Olson et al.,1983).

The measured cross sections for C- and H-target are compared to data measured at different energies (see caption). In addition the predicted cross sections using the semiempirical formula of Sihver et al. (1991) are shown. For H-target at low energies it can be seen that the cross sections for the production of fragments of charge number Z=3 and Z=4 significantly differ from the predicted values. The cross section for the production of fragments of charge number Z=4 is smaller than 'hat for the production of fragments with charge number Z=3. This is caused by the instability of ^8Be which decays quasi simultaneously into two α-particles. In fig. 3 the distribution of emission angles of the fragments with charge numbers Z=3, 4, and 5 measured against the mean beam axis for the C-targets is shown. We have compared these distributions to model predictions using the so called Goldhaber model (Goldhaber,1974). At high energies, the fragments of a nucleus are emitted almost isotropically in the rest system of the fragmenting nucleus. The momentum components for the coordinate parallel to the beam direction and the two coordinates perpendicular to it are Gaussians with a standard deviation which is given by the model of Goldhaber (1974). In the rest system of the fragmenting nucleus these distributions for the two axes perpendicular to the beam direction are centered at zero, whereas the distribution of the momentum component parallel to the beam direction is slightly shifted to negative values. This can be attributed to a small amount of momentum which is transferred to the fragmenting projectile (Olson et al.,1983). The Goldhaber model is a statistical model which describes the transverse momenta of fragments produced in high energy interactions where the interaction can be described as a sudden process. This model underestimates the measured angular distributions (at 66AMeV) at high emission angles. At low energies Winsburg et al. (1980) have studied the kinematics of proton induced target fragmentation. For the description of their observations they used the two-vector-model. The study of experiments at different energies showed that the longitudinal momentum component increases with the falling energy of the proton and has a maximum at E=70MeV. At this energy, the momentum transfer to the fragmenting nucleus is about 70% of the value for a compound nucleus with a completely stopped proton. For C at 28.7AMeV and N at 60AMeV Czudek et al. (1991) and Glasow et al. (1990) have also observed an increased momentum transfer to the fragmenting nucleus in projectile fragmentation experiments.
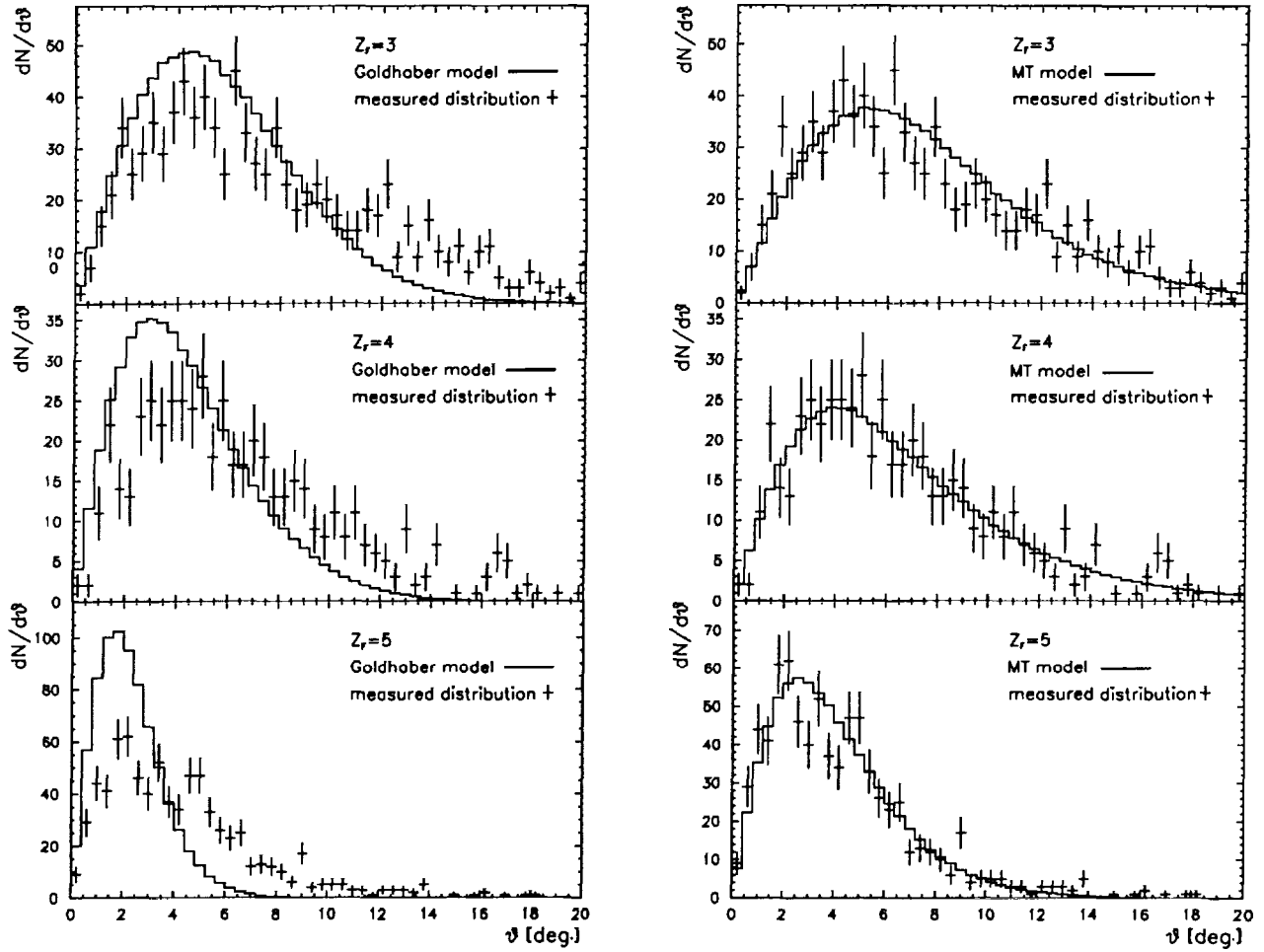
Figure 3: **left side**: Measured distribution of fragment emission angles (C-target) in comparision to the predictions of the Goldhaber model. **right side:** The same measured angular distribution in comparison to the momentum transfer (MT)-model described in the text.

We have used a phenomenological model for the explanation of our measured fragment emission angle distributions. Our model uses the two vector-model-description of the interaction of the fragmenting nuclei and is based on some general assumptions. The three Cartesian vector-components of the projectile fragment in its rest frame are described by the Goldhaber model. Additionally there is a momentum transfer p_- against the beam direction with a maximum $p_c(A_F)$ given by the momentum which is transferred by the building of a compound nucleus. The momentum transfer (MT) is distributed as described by a probability-distribution $f(p_-)$ of the type:

$$f(p_-) = A\exp(\frac{-p_-}{p_1}) + (1 - A)\exp(\frac{p_- - p_c}{p_2})$$

$$p_i = \kappa_i p_c(A_F), i = 1,2$$

Where A_F is the mass number of the fragment and the κ_i are parameters varied adjusting the model to our measured angular distributions. A is given by the normalization of $f(p_-)$. The result of our MT-model which was used in a Monte Carlo program sampling fragment emission angle distributions is shown in fig. 3. The measured distributions are well described by this model. In the next step we have transformed our model predictions to the proton induced target fragmentation. The results are shown in fig.4. The momentum distributions for fragments of charge Z=3,4, and 5 were calculated with the MT-

model. In comparison the predictions of the Goldhaber model without any momentum transfer in beam direction are shown. The momentum distributions calculated under the assumption of the formation of a compound nucleus give upper limits for the uncertainty of our MT-model predictions.
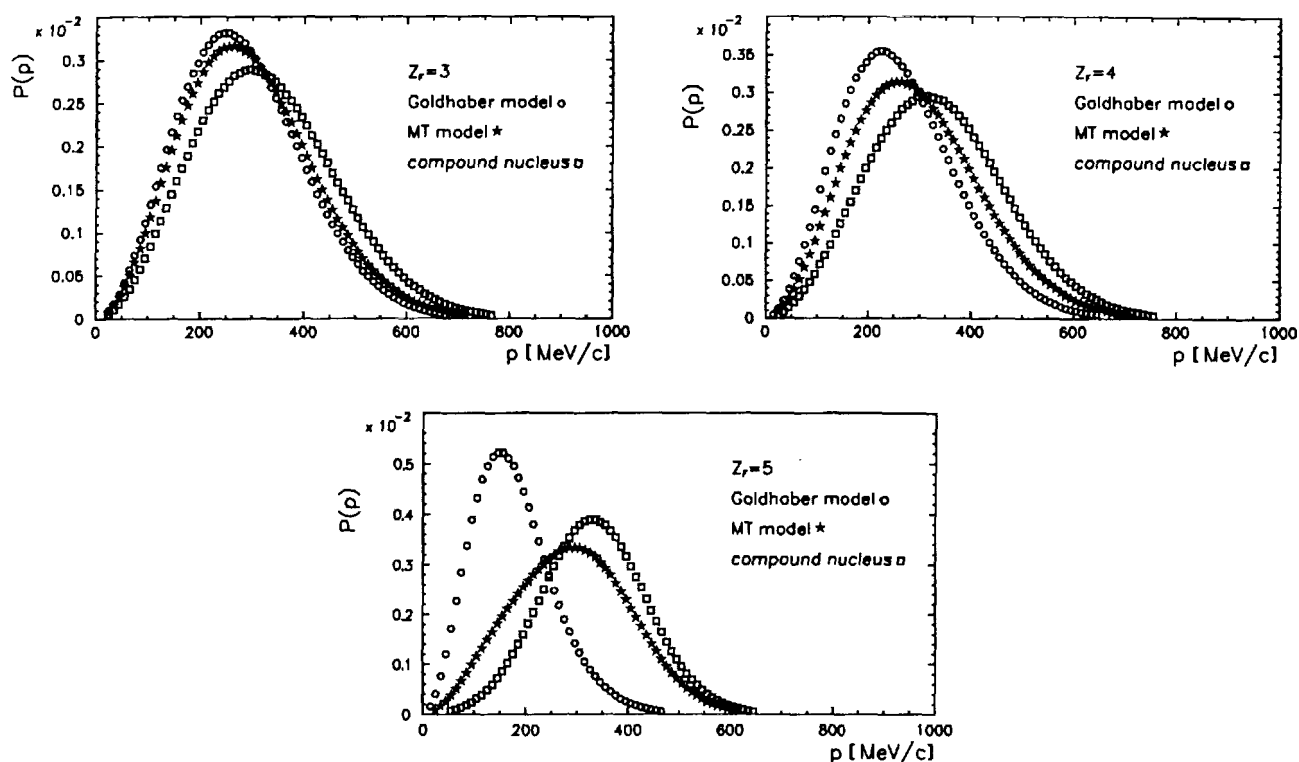

Figure 4: Momentum distributions for target fragments of C produced in interactions with 66 MeV protons.

A B   CONCLUSIONS

Charge changing fragmentation cross sections for C at a proton energy of about 70 MeV were measured. The discrepancies oetween measurement and model predictions indicate the necessity of further investigations. We have also measured distributions of fragment emission angles which can be described using a model with a momentum transfer to the fragmenting nucleus. The developed model leads to predictions for momentum distributions of proton induced target fragments of C at small energies.

REFERENCES

C. Brechtmann and W. Heinrich (1988) *Nucl. Instr. and Meth.* **B29**, 675.

J. Czudek et al. (1991) *Phys. Rev.* **C 43(3)**, 1248.

R. Glasow et al. (1990) *J. Phys. G:Nucl. Part. Phys.* **16**, 1089.

A.S. Goldhaber (1974) *Phys. Lett.* **B53**, 306.

J.M. Kidd, P.J. Lindstrom, H.J. Crawford, and G. Woods (1988) *Phys. Rev.* **C 37(6)**, 2613.

D.L. Olson, B.L. Berman, D.E. Greiner, H.H. Heckmann, P.J. Lindstrom, and H.J. Crwaford (1983) *Phys. Rev.* **C 28(4)**, 1602.

L. Sihver, C.H. Tsao, R. Silberberg, T. Kanai, and A.F. Barghouty (1993) *Phys. Rev.* **C 47(3)**, 1225.

L. Winsberg, E.P. Steinberg, D. Henderson, and A. Chrapkowski (1980) *Phys. Rev* **C 22(5)**, 2108.

INACTIVATION PROBABILITY AS A FUNCTION OF THE DISTANCE FROM THE PARTICLE'S PATH MEASURED WITH SPORES OF BACILLUS SUBTILIS AND USING AN IMAGE ANALYZING SYSTEM

Schäfer[+] M., Jauster[*] R., Halling[*] H. and Schmitz[+] C.
[+] DLR Köln, [*] KFA Jülich, Germany

A microscopical method is described which allows to measure the radial inactivation probability of single heavy ion tracks with individual biological objects. The system is given schematically in Fig. 1.
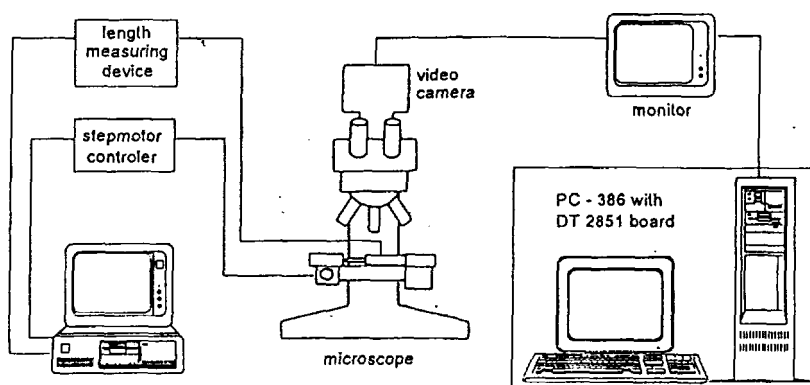

Fig. 1 Scheme of the evaluation technique with microscope,
scanning device and CCD camera and image analyzing system

Wild type spores of Bacillus subtilis (Marburg strain) in a dormant and dry state were used. Freshly prepared spores were distributed on polycarbonate foils which serves as a track detector. Spores have a small sensitive target with a geometrical cross section of 0.22 μm^2 and are highly radioresistant compared to the vegetative cells of the same strain. From exponential X-ray survival curves we measure a radiosensitivity of 0.0018 Gy^{-1}. The spores on the foils were irradiated with Uranium ions at the UNILAC facility (GSI, Darmstadt). The initial energy (11.4 MeV/u) of the ions was reduced when penetrating an Ti exit window (5 μm) and a following air layer (18 mm). The final energy of 8.86 MeV/u at the spore layer was calculated using energy range tables (Northcliffe and Schilling 1970, Hubert et al. 1980).

Reference marks were introduced mechanically in the detector by a glass capillary before starting the evaluation. Heavy ion tracks were made visible by track etching after the biological survival test. Microscopical images were taken with a

CCD camera (VC 1900, Sanyo). They were digitized with a DT2851 board (Data Translation) with a resolution of 512 * 512 pixels and 256 grey levels and stored in a computer. During the analysis 5 images were stored in the extended memory.

Image analysis was performed with the program SP *(spore project)* developed for this special type of radiobiological problem. It allows to detect the boundary of the objects automatically using a threshold value determined from the histogram of grey values. The boundary was stored as a chain code (Freeman 1974) in a data file. which is used the determine the centre of mass and the size of each object for further classification. It allows manual corrections with respect to the biological parameters for the spore outgrowth (dead, living), to measure the centre coordinates again, to exclude artefacts or spores changing their location.

The centre coordinates of the marks seen in both types of images (spore, track) allow to superimpose the spore and the track images mathematically by least square methods. Track coordinates are transferred into the spore image coordinate system. Thus, impact parameters can then be calculated with a high accuracy of better than 0.15 μm. The controls were measured with the same method.
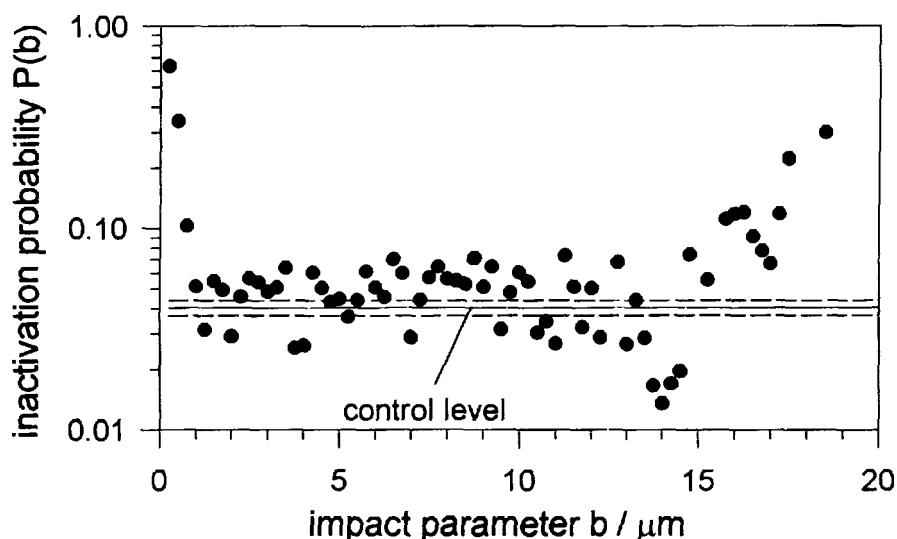
Fig. 2 Radial inactivation probability measured as the fraction of dead spores in a defined impact parameter interval of 0.25 μm. The control level is given with the standard deviation.

The inactivation probability around single Uranium ions with an energy of 8.86 MeV/u is given in Fig. 2. The values were determined by pooling the spores in certain impact parameter intervals of 0.25 μm. The radial inactivation probability

showing -(1) low killing for direct particle hits, (2) increasing effect levels for increasing distance from the particle track and (3) a non-monotonous behaviour as a function of the distance- do not agree with common theoretical expectations. Important is the finding that the effect drops down to control level when particles hit the boundary of the spore between 0.75μm and 1.0μm. With respect to the other experiments described for such type of measurement (Facius et al. 1983, Schäfer et al. 1994) the ion fluence was reduced drastically to $5*10^5/cm^2$. At this low value the influence of further ions in the vicinity ot the spore is also reduced.

REFERENCES:

Northcliffe L.C. and Schilling R.F., 1970, Nuclear Data Tables, A7, 223

Hubert, F., Fleury, A., Bimbot, R. and Gardes, D., 1980, Range and stopping power tables for 2.5 - 100 MeV/nucleon heavy ions in solids, *Annales de Physique*, **5**, (Suppl.), 1 -214

Freeman, H., 1974, Computer Processing of Line Drawing Images, *Computer Surveys*, **6**, 57-97

Facius, R., Schäfer, M., Baltschukat, K. and Bücker, H., 1983, Inactivation probability of heavy ion-irradiated Bacillus subtilis spores as a function of the radial distance to the particle's trajectory. *Advances in Space Research*, **3** (No. 8) 85 - 94

Schäfer, M., Facius, R. and Reitz, G., 1994, Inactivation of induvidual Bacillus subtilis spores in dependence on their distance to single accelerated heavy ions, Advances in Space Research **14**, (No. 10), 1039 - 1046

C

Mutation and Chromosome Aberration
S. Ritter (Chair)

Oral Presentations

1. Sylvia Ritter
(GSI, Darmstadt, Germany)
Particle-Induced Chromosome Aberration and
Mutations:an Overview
2. Marco Durante
(Univers. Federico „Neapel II",
Italy)
Heavy-Ion-Induced Chromosomal Aberrations
Analyzed by Fluorescence *in* Situ Hybridization
3. Karin Füssel
(GSI, Darmstadt, Germany)
Comparison of RBE for Inactivation and Chromosomal
Damage of High-Energy Carbon Ions
4. Jürgen Kiefer
(Strahlenzentrum,Univers.
Gießen, Germany)
Mutations Induced by Heavy-Ions: Cross Sections,
RBE and Molecular Patterns
5. Fumio Yatagai
(Inst. Phys. Chem.Res.,
Saitama, Japan)
Analysis of Mutations in the Human HPRT Gene
Induced by Heavy-Ion Irradiation
6. Hermann Rink
(Univers. Bonn, Germany)
HPRT Mutations in V79 Cells: Type of Lesions
Dependent on LET
7. Shigemitsu Tano
(Jap. Atom. Energ. Res. Inst,
Takasaki, Japan)
Structural Changes of DNA in Heavy-Ion-Induced
Mutants on *Arabidopsis*

Posters

8. Robert Katz
(Univers. of Nebraska, USA)
Track Theory Estimates of Single Particle Traversals of
Cell Nuclei
9. Paul Schmidt
(Strahlenzentrum,Univers.
Gießen, Germany)
Molecular Spectra of Heavy-Ion-Induced Mutations

DE98F5456

Particle-induced chromosome aberrations and mutations: an overview

S. Ritter

GSI, Planckstr. 1, D-64291 Darmstadt, Germany

Energy depositions by sparsely and densely ionizing radiation in the cellular DNA are responsible for deleterious radiobiological effects like the induction of chromosome aberrations, gene mutations and cell transformation. However, due to differences in the spatial pattern of energy deposition the action of charged particles is qualitatively different from that of sparsely ionizing radiation. By the use of refined molecularbiological methods a deeper insight into the molecular events underlaying particle induced genetic changes has been obtained. Therefore this overview will focus on progress in chromosome and mutation studies achieved by the application of new techniques. Furthermore, recent relevant data on longterm genetic effects of densely ionizing radiation will be summarized.

Chromosome aberrations

For the evaluation of radiation-induced chromosomal changes the use of the fluorescence in situ hybridization (FISH) technique provides a powerful alternative to conventinonal cytogenetic methods like R- and G-banding (Gray et al., 1994). FISH allows a fast and accurate detection of chromosomal damage and is now applied to study the correct and incorrect repair of radiation induced lesions in metaphase chromosomes (Salassidis et al, 1994) as well as in interphase (PCC) chromosomes (Durante et al., 1996). In this context the examination of stable aberrations like translocations is particularly important (Lucas et al., 1992). Stable aberrations are a visible manifestation of misrepair and cells carrying such aberrations are at risk for neoplastic transformation.

In accordance with chromosome data measured with conventional staining techniques (Ritter et al., 1996 and references therein) first experimental results obtained by the FISH-technique confirm that specific alterations in the spectrum of aberration-types occur with increasing LET (Durante et al., 1997). These alterations could be used as biomarkers of radiation quality.

Mutation induction

Refined techniques like the molecular analysis of particle-induced mutations by restriction fragment length polymorphism or polymerase chain reaction (PCR) techniques provide a deeper insight into the relationship between initial DNA damage and the ultimate structure of mutations. While the majority of spontaneous mutants exhibits point mutations, radiation-induced mutants show deletions of varying size. The relative percentage of large-scale deletions is found to depend on dose and LET (Zhu et al., 1996). Mapping of the intragenic deletion breakpoints exhibits a non-random distribution of breakspoints indicating that neighboring sequences may also be involved in the formation of radiation-induced mutagenesis (Park et al., 1995).

Longterm genetic effects

Recent studies investigating the longterm effects of ionizing radiation in the progeny of cells surviving the acute radiation exposure reveal a destabilization of the genome many generations postirradiation (reviewed by Morgan et al., 1996). This genomic instability manifests in a diverse set of biological endpoints including the de novo occurrance of chromosome aberrations (Khadim et al. 1992, Martins et al. 1993) and the late appearance of gene mutations (Chang and Little, 1992). The molecular and genetic processes underlaying genomic instability are still unclear and little information exists, so far, on the magnitude of this effect and its dependence on radiation quality. However, there is increasing evidence that the loss of the stability of the genome is one of the most important features of tumor cells.

References

Chang, W.P. and J.B. Little, J.B., 1992, Persistently elevated frequency of spontaneous mutations in progeny of CHO cells surviving X-irradiation: association with delayed reproductive death phenotype. Mutation Research, 270, 191-199.

Durante, M. et al., 1996, Rejoining and misrejoining of radiation induced chromatin breaks. I. Experimets with human lymphocytes. Radiat. Res. 145, 274-280.

Durante et al., 1997, this issue.

Gray, J.W. et al, 1994, Flourescence in situ hybridization in cancer and radiobiology, Radiat. Res. 137, 275-289.

Khadim, M.A. et al., 1992, Transmission of chromosomal instability after plutonium alpha-particle irradiation. Nature, 355, 738-740.

Lucas, J.N., 1992, Rapid translocation frequency analysis in humans decades after exposure to ionizing radiation. Int. J. Radiat. Biol., 62, 53-63.

Martins, M.B. et al., 1993, Specific chromosome instability induced by heavy ions: a step towards transformation of human fibroblasts? Mutation Res. 285, 229-237.

Morgan, W.F., et al., 1996, Genomic instability induced by ionizing radiation, Radiat. Res. 146, 247-258.

Park, M.S., Molecular analysis of Gamma-ray induced mutations at the hprt locus in primary human skin fibroblasts by multiplex polymerase chain reaction, Radiat. Res. 141, 11-18.

Ritter, S., 1996, Comparison of chromosomal damage induced by X-rays and Ar ions with an LET of 1850 keV/μm in G_1-phase V79 cells, Int. J. Radiat. Biol. 69, 155-166.

Salassidis K., 1994, Dicentric and translocation analysis for retrospective dose estimation in humans exposed to ionizing radiation during the Chernobyl nuclear power plant accident, Mutation Res. 311, 39-48.

Zhu L.X., 1996, Cellular and molecular analysis of mutagenesis induced by charged particles of defined linear energy transfer, 1996, Radiat. Res. 145, 251-259.

HEAVY ION-INDUCED CHROMOSOMAL ABERRATIONS ANALYZED BY FLUORESCENCE *IN SITU* HYBRIDIZATION

M.Durante[12], L.Cella[1], Y.Furusawa[3], K.George[4], G.Gialanella[12], O.Greco[1], G.Grossi[12], M.Pugliese[12] and T.C.Yang[4]

1 Department of Physics, University "Federico II", Naples, Italy
2 INFN, Naples, Italy
3 NIRS, Chiba, Japan
4 NASA Lyndon B.Johnson Space Center, Houston, Tx, USA

a. Introduction

Cytogenetic effects of heavy ions are poorly known. Extensive work on hamster cells at GSI in Darmstadt [1-3] showed that heavy ions are very efficient in producing mitotic delay and/or interphase death in cycling cells. These effects interfere with chromosome analysis at metaphase. Clastogenicity of heavy ions has also been assayed in interphase by using the premature chromosome condensation (PCC) technique [4-6], but chromosome exchanges cannot be observed in solid stained PCC samples.

We have investigated the effectiveness of heavy ions in the induction of chromosomal aberrations in mammalian cells by the recent technique of fluorescence *in situ* hybridization (FISH) with whole-chromosome probes. FISH-painting was used both in metaphase and interphase (prematurely condensed) chromosomes. The purpose of our experiments was to address the following problems: a) the ratio of different types of aberrations as a function of radiation quality (search for biomarkers); b) the ratio between aberrations scored in interphase and metaphase as a function of radiation quality (role of apoptosis); c) differences between cytogenetic effects produced by different ions at the same LET (role of track structure).

b. Methodology

Biological systems were peripheral blood lymphocytes and murine C3H 10T1/2 cells. Lymphocytes are generally employed for biological dosimetry of absorbed radiation, while 10T1/2 cells represent an *in vitro* model of radiocarcinogenesis. Cells were exposed to accelerated charged particles at the facilities in Loma Linda (H), Naples (H), Brookhaven (Fe), and Chiba (C and Ne). Details of beam physics are described in Table I.

Table I. Characteristics of the different radiation types used in our experiments.

Radiation	Source	Energy (MeV)	Target	LET (keV/μm)	Doses (Gy)
γ-rays	^{137}Cs, Baylor Medical College	0.66	Lymphocytes	0.3	1, 3, 5, 7
Protons	Loma Linda Medical Center	250	Lymphocytes	0.4	1, 3, 5, 7
	Tandem TTT-3, Naples	0.86	C3H 10T1/2	31	1, 2, 3, 4.5
Carbon	HIMAC, Chiba	290/n	Lymphocytes	13, 42, 77	3, 5
Neon	HIMAC, Chiba	400/n	Lymphocytes, C3H10T1/2	31	1, 2, 3, 4.5, 7
Iron	Brookhaven National Laboratories	1000/n	Lymphocytes	140	0.5, 0.75, 1, 2

For PCC analysis, irradiated lymphocytes were fused to mitotic CHO cells following a 8 h-incubation interval at 37 °C to allow repair of radiation damage. Alternatively, lymphocytes were stimulated to grow *in vitro* in medium supplemented with PHA and harvested following 48 h incubation at 37 °C. Chromosome spreads were hybridized *in situ* by whole chromosome probes specific for chromosomes 2 and 4 (Vysis). Details of the experimental procedures for PCC induction and FISH-painting have been published [7-8].

Mouse 10T1/2 cells were exposed in plateau-phase, and subcultured immediately after exposure. Mitosis were accumulated in colcemid and collected after 28 h in culture. Spreads were hybridized by a DNA cocktail specific for mouse chromosomes 2 and 8 (Stratagene). These autosomes were quite stable in the 10T1/2 karyotype, with a modal number of 4 copies of each chromosome per cell.

c. Biomarkers of radiation quality

We have measured different chromosomal aberrations in PCC of human lymphocytes incubated 8 h following exposure to heavy ions. Results reported in figure 1 show that the ratios deletions/interchanges and complex/simple exchanges are higher, at the same dose, for densely ionizing radiation. These aberration ratios could be used as biomarkers of radiation quality for biodosimetry.
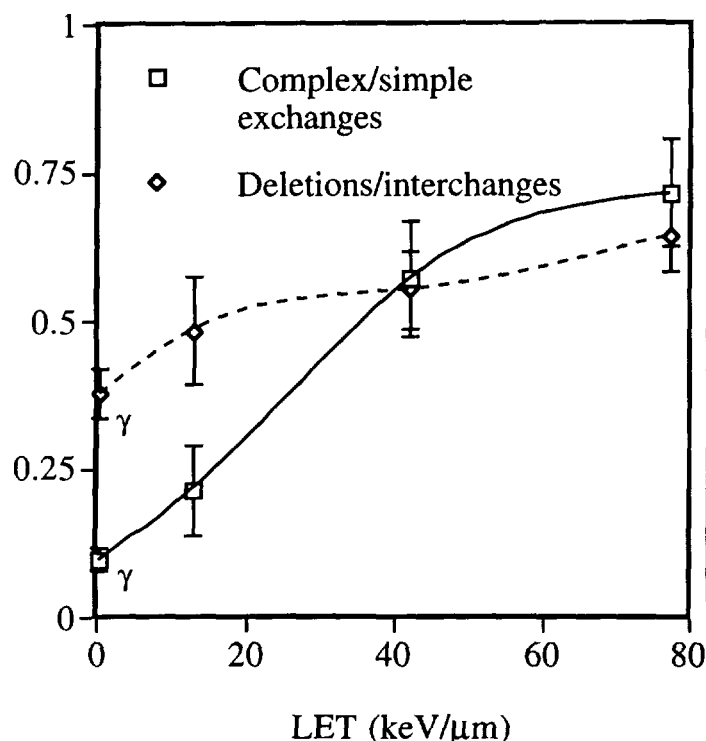

Figure 1. Ratios of different radiation-induced chromosomal aberrations in human lymphocytes. Isolated lymphocytes were exposed to 5 Gy of γ-rays or carbon ions. Following exposure, lymphocytes were incubated 8 h at 37 °C and then fused to mitotic CHO cells for PCC induction. PCC spreads were hybridized with a composite probe specific for human chromosomes 2 and 4, and observed at a fluorescence microscope. Deletions include all acentric fragments, such as interstitial deletions and incomplete exchanges. Complex exchanges include all aberrations involving >2 breaks on >1 chromosomes.

d. Interphase death induced by heavy ions

When γ-ray-induced chromosomal aberrations are compared in metaphase and interphase (following incubation for repair), approximately the same yield of aberrations is observed [8]. However, we found that more aberrations are scored in PCC than in mitotic chromosomes when human lymphocytes are exposed to heavy ions (figure 2). It is known that heavy ions produce efficiently cell-cycle delay and interphase death. Our results suggest that a selection of the population observed in metaphase is induced, and damaged cells appear to be selectively eliminated. These data are relevant for biodosimetry of mixed fields, where analysis in metaphase could lead to an underestimation of the high-LET component.

e. Track structure

The role of track structure has been investigated in 10T1/2 cells exposed to H and Ne ions at the same LET (30 keV/μm). We found that protons were generally more efficient than Ne ions in the induction of chromosomal aberrations (figure 3), but the difference was dependent upon the aberration type. Maximum difference was found for simple aberrations, but little variations were observed for complex exchanges. Complex exchanges are produced in inter-track mode, while simple aberrations can be induced in intra-track mode. Protons deposited all the energy in a volume below 100 nm, which is considered the critical volume for intra-track events [9]. On the other hand, about 20% of the energy released by 400 MeV/n is deposited outside the 100 nm volume. This physical difference in track structure could explain our experimental results.
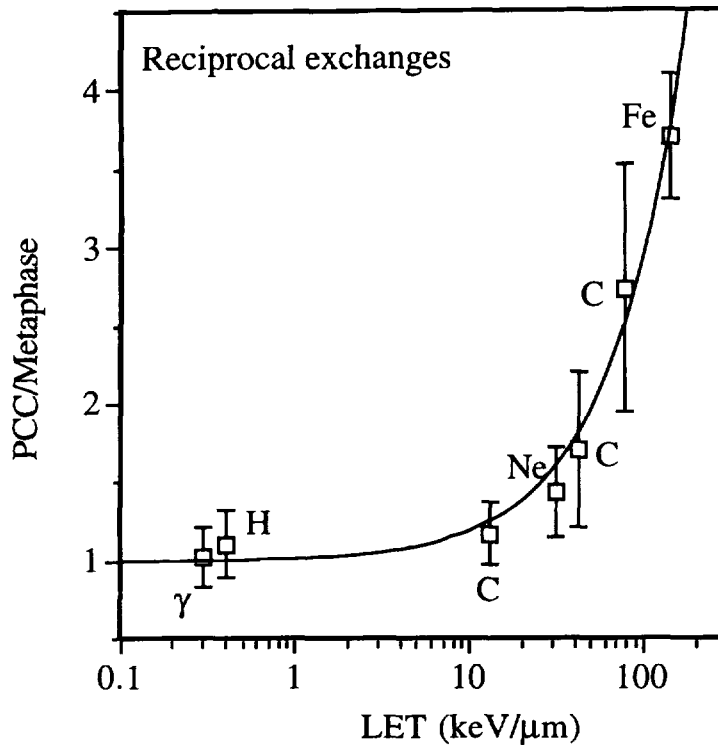
2

Figure 2. Ratio of chromosomal aberrations scored in interphase and metaphase. Human lymphocytes were exposed to charged particles and incubated thereafter at 37 °C. PCC were fixed following 8 h incubation, whereas metaphases were harvested after 48 h stimulation in medium supplemented with 1% PHA. PCC and metaphase spreads were hybridized with a composite probe specific for chromosomes 2 and 4. Reciprocal exchanges include dicentrics and translocations.
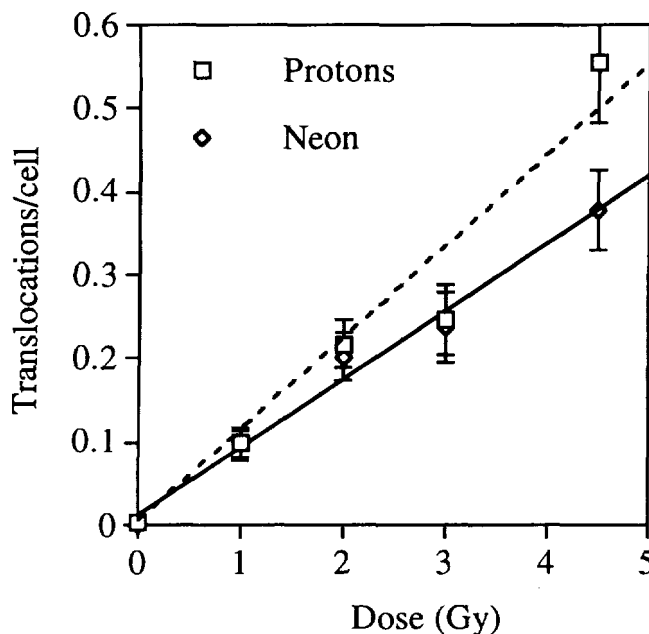
Figure 3. Yield of translocations induced by H or Ne ions at the same LET in chromosomes 2 and 8 of C3H 10T1/2 mouse fibroblasts. Aberrations were scored by FISH at the first mitosis following exposure.

Interestingly, qualitative differences were also observed in the complex exchanges induced by the two radiation types. Low-energy protons produced mostly insertions, while Ne ions induced a greater fraction of non-reciprocal exchanges (figure 4). These data also suggest that protons are more efficient in the induction of aberrations formed by closely-spaced DNA lesions.

0.4

☷ Protons

◺ Neon

D=4.5 Gy

0.3

Complex exchanges/cell

0.2

0.1

0

Non-reciprocal exchanges   Insertions

Figure 4. Different types of complex exchanges produced by H and Ne ions at the same dose and LET in chromosomes 2 and 8 of 10T1/2 cells.

f. References

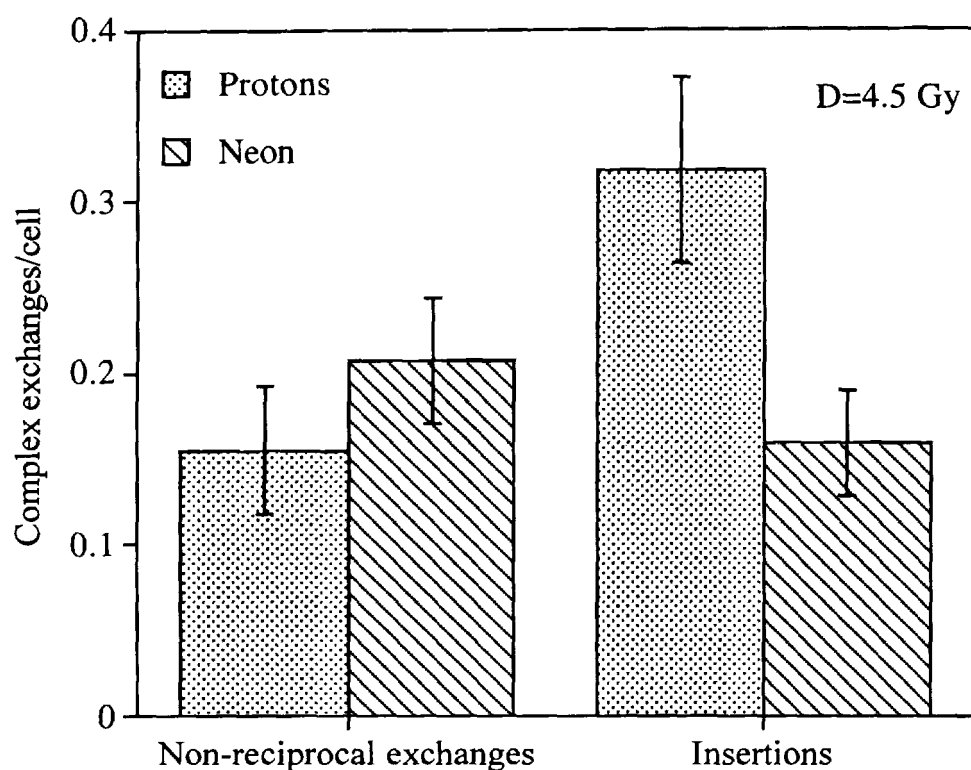1. Ritter, S., Kraft-Weyrather, W., Scholz, M., and G. Kraft, Induction of Chromosome Aberrations in Mammalian Cells After Heavy Ion Exposure, *Adv. Space Res.* **12**, 119 (1992).

2. Ritter, S., Nasonova, E., Kraft-Weyrather, W., and G. Kraft, Influence of Radiation Quality on the Expression of Chromosomal Damage, *Int. J. Radiat. Biol.* **66**, 625 (1994).

3. Ritter, S., Nasonova, E., Scholz, M., Kraft-Weyrather, W., and G. Kraft, Comparison of Chromosomal Damage Induced by X-rays and Ar Ions with an LET of 1840 keV/μm in G1-phase V79 cells, *Int. J. Radiat. Biol.* **69**, 155 (1996).

4. Suzuki, M., Watanabe, K., Suzuki, K., Nakano, M., and K. Matsui, Heavy Ion-Induced Chromosome Breakage Studied by Premature Chromosome Condensation (PCC) In Syrian Hamster Embryo Cells, *Int. J. Radiat. Biol.* **62**, 581 (1992).

5. Goodwin, E.H., Blakeley, E.A., and C.A. Tobias, Chromosomal Damage and Repair in G_1-Phase Chinese Hamster Ovary Cells Exposed to Charged-Particle Beams, *Radiat. Res.* **138**, 343 (1994).

6. Goodwin, E.H., Bailey, S.M., Chen, D.J., and M.N. Cornforth, The Effect of Track Structure on Cell Inactivation and Chromosome Damage at a Constant LET of 120 keV/μm, *Adv. Space Res.* **18**, 93 (1996).

7. Durante, M., George, K., and T. C. Yang, Biological Dosimetry by Interphase Chromosome Painting, *Radiat. Res.* **145**, 53 (1996).

8. Durante, M., George, K., Wu, H.-L., and T. C. Yang, Rejoining and Misrejoining of Radiation-Induced Chromatin Breaks. I. Experiments in Human Lymphocytes, *Radiat. Res.* **145**, 274 (1996).

9. Wu, H.-L., Durante M., Sachs, R.K., and T.C. Yang, A Random Walk Model for Interphase Chromosomes and the Relationship between Centric Rings, Acentric Rings and Excess Acentric Fragments Produced by Low-LET Radiation, *Int. J. Radiat. Biol.* **71**, 487 (1997).

Comparison of RBE for inactivation and chromosomal damage of high energy Carbon ions

K. Füssel, S. Ritter and G. Kraft

GSI, Biophysik, Planckstr. 1, D-64291 Darmstadt

Values of the relative biological efficiency (RBE) for cell inactivation and for chromosome damage were compared for 200 MeV/u Carbon-ions (LET is 16.2 keV/μm), which corresponds to the energy of ^{12}C-ions penetrating the healthy tissue of a patient in an heavy-ion radiotherapy. As chromosomal damage is a predecessor of radiogenic late effects like the development of solid tumours or leukemia it is of extreme interest to know RBE-values for the induction of chromosome aberrations in the surviving cells of a patient's healthy tissue.

Contact-inhibited cells of the human fibroblast line AG01522B were irradiated in G_0-phase and cell inactivation measured using the colony-forming assay. For 10 % cell inactivation the RBE is 1.3, thus agreeing with results of former investigations with Chinese hamster cells. Those had shown, that RBE values are above unity in the entrance channel of a therapeutic Carbon beam, but clearly increase to higher values in the range of the Bragg-peak (Scholz et al., 1997).

To investigate the induction of chromosome aberrations contact-inhibited fibroblasts were irradiated and samples taken in regular intervals up to 70 hours after irradiation.

Using fluorescence-plus-Giemsa (FPG)-staining of chromosome slides, the mitotic index (number of mitotic cells in the cell population) of cells in the first post-irradiation mitosis was measured. This examination showed a significant decrease in the maximum number of first cycle metaphases with dose (Figure 1), while the appearance of mitotic cells was not shifted to later times after irradiation. This suggests, that the number of cells, entering first mitosis is dose-dependently reduced.

To evaluate chromosome aberrations in cells of the first post-irradiation mitosis, the chromosomes number 4 and 8 were painted with the FISH-technique (pBS-4 and pBS-8 from J.W. Gray, San Francisco) and the amount of aberrant cells and of aberrations were scored in intervals of 4 hours between 30 and 55 hours after irradiation. The number of aberrations increased with sampling time as can be seen in Figure 2 for translocations and dicentric chromosomes, agreeing with data from Ritter et al., 1996. Interestingly, the induction of translocations always exceeded
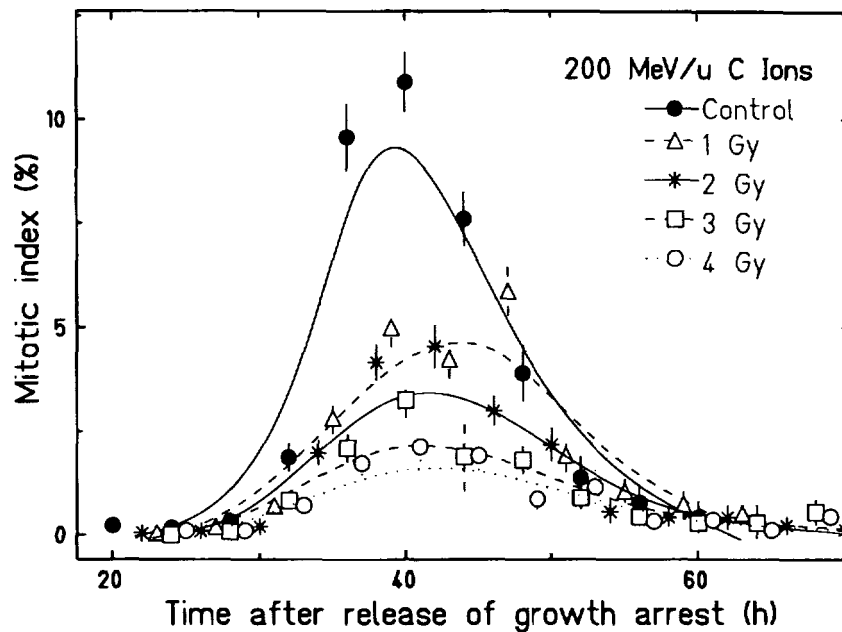
Figure 1: Time course of the appearance of first post-irradiation mitotic cells after exposure to 1, 2, 3 and 4 Gy ^{12}C-ions.

that of dicentric chromosomes, although both aberration-types are results of two rejoined chromosomes. The ratio translocations to dicentric chromosomes is 1.7 for irradiation with ^{12}C-ions and 2.4 for X-irradiation, but without significant difference between the radiation-types. No difference in the spectrum of chromosome lesions could be found for ^{12}C-ions and X-rays, as described by Ritter et al., 1996, for ^{40}Ar-ions with an LET of 1840 keV/μm.

RBE-values of 200 MeV/u ^{12}C-ions are 1.3 for 10, 20 or 30 % aberrant metaphases and between 1.2 and 1.5 for different types of chromosome aberrations (translocations, dicentric chromosomes and chromosome breaks). These data not only agree with RBE-values found for the cell survival of fibroblasts but also with the induction of DNA-double strand breaks measured by Heilmann et al., 1995.

As the composition of aberration types is the same for 200 MeV/u ^{12}C-ions and for 250 kV X-rays, and the RBE for the induction of aberrations corresponds with that for cell inactivation, no markedly increase of late effects in the healthy tissue caused by chromosomal aberrations can be expected, using ^{12}C-ions as a therapeutical beam.
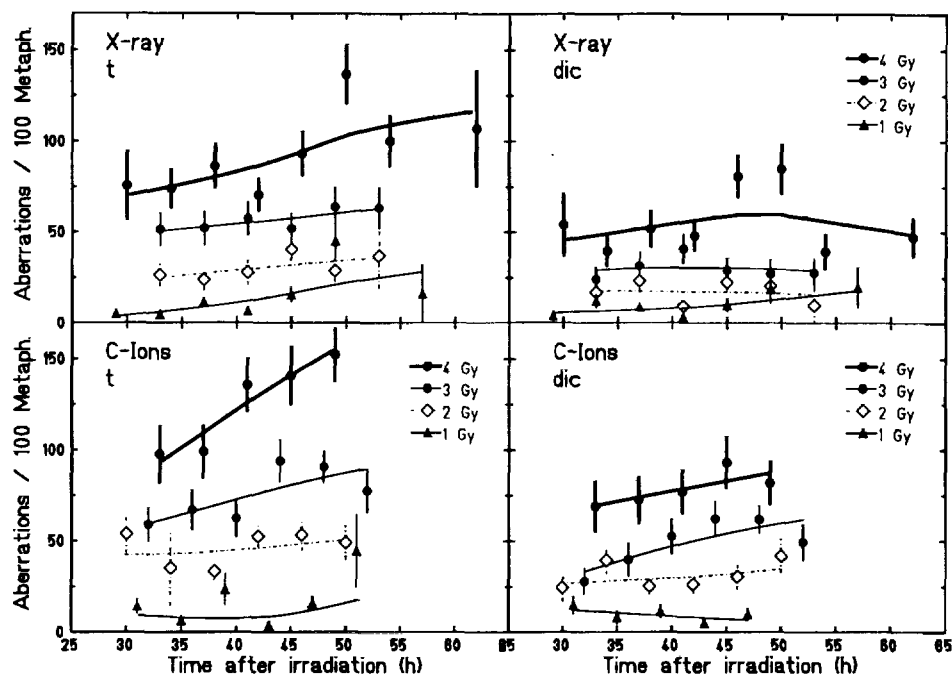
Figure 2: Number of translocations (t) and dicentric chromosomes (dic) detected in human fibroblasts after exposure to X-rays (upper panels) or 200 MeV/u ^{12}C-ions (lower panels). Aberrations were analyzed by the use of the FISH-technique painting chromosomes number 4 and 8.

References:

Scholz, M., A.M. Kellerer, W. Kraft-Weyrather, G. Kraft (1997). Computation of cell survival in heavy ion beams for therapy: The model and its approximation. Radiat. Environ. Biophys., 36:59-66.

Ritter, S., E. Nasonova, M. Scholz, W. Kraft-Weyrather and G. Kraft (1996). Comparison of chromosomal damage induced by X-rays and Ar ions with an LET of 1840 keV/μm in G$_1$ V79 cells. Int. J. Radiat. Biol., 69:155-166.

Heilmann, J., G. Taucher-Scholz and G. Kraft (1995). Induction of DNA double-strand breaks in CHO-K1 cells by Carbon ions. Int. J. Radiat. Biol., 68:153-162.

Mutation induction by heavy ions: cross sections, RBE and molecular analysis

J. Kiefer, F. Gutermuth, P. Schmidt, U. Stoll

Strahlenzentrum der Justus-Liebig-Universität

Giessen, Germany

Mutation induction by heavy ions at the HPRT locus was investigated in V79 Chinese hamster cells using both the UNILAC and the SIS accelerators at GSI, Darmstadt and the cyclotron at HMI, Berlin. Induction curves were (with few exceptions) linear, and cross sections were determined from their slopes. RBE values were calculated from them and initial slopes of the linear-quadratic induction curves obtained after 300 kV X-rays. All data are compiled in the following tables. It is already obvious and will be discussed in more detail during the presentation that no unique relationship exists between LET and neither mutation induction cross section nor RBE. The influence of ion energy is different with lighter and heavier ions: RBE decreases with energy in the first case demonstrating LET as the more important parameter while it remains constant or even increases with very heavy ions. This can be explained by the high density of energetic and thus far reaching electrons which contribute significantly to mutation induction. If the RBE data are compared with the function suggested by the ICRP (1991) for the dependence of quality factor on LET they are found to differ not gravely in the lower LET-range up to about 1000 keV/μm. It is noteworthy that according to our observations the ICRP recommendation does not underestimate the experimental values which may well reach a RBE around 30. With very high LET our determination demonstrate a steeper decline with LET than suggested by the ICRP-function.

Recently we started to analyse the molecular pattern of heavy ion induced mutations at the HPRT locus in Chinese hamster cells by using a multiplex polymerase chain reaction. There is tendency that the fraction of total gene deletions increases with ionisation density but there is still a certain fraction of so-called "wildtype" mutants representing either point mutations or deletions too small to be detected. Little variation is found with partial deletions. It is, however, obvious from the analysis that heavy ions do not only induce bulky damages but also quite a number of small deletions which again reflect the complexity of track structure.

Inactivation and mutation induction by accelerated heavy ions (Data from Stoll et al. 1995, 1996 and new measurements)

Ion	Energy MeV/u	LET keV/μm	Inactivation cross section μm²	Mutation induction cross section 10⁻⁴ μm²	RBE (mutation) (initial slope
Helium	0.9	110.0	31.0	9.8	32.8
	27.5	8.0		0.2	7.4
Carbon	265.0	12.0	1.0	0.3	8.9
	210.0	14.0	1.0	0.3	7.6
	93.0	25.0	2.5	0.5	6.6
Oxygen	1.9	754.0	71.2	11.4	5.6
	8.8	276.0	50.0	20.0	26.6
	10.7	238.0	49.5	9.5	14.7
	46.0	46.0	4.3	1.2	9.6
	396.0	18.0	1.3	0.2	3.5
Neon	8.0	452.0	45.0	21.3	17.3
	10.7	366.0	52.0	15.7	15.8
	12.0	335.0	42.0	15.0	16.5
	14.3	294.0	33.0	7.7	9.6
	65.0	91.0	12.5	2.7	10.9
	191.0	42.0	4.7	1.1	9.6
	395.0	28.0	2.1	1.0	13.1
Nickel	6.0	3190.0	61.0	9.1	1.0
	9.5	2517.0	65.0	8.3	1.2
	14.3	1961.0	87.0	5.7	1.1
	136.0	407.0	52.0	5.6	5.1
	387.0	218.0	39.0	5.5	9.3
	630.0	180.0	38.5	6.2	12.7

Inactivation and mutation induction by accelerated heavy ions (continued)

Ion	Energy MeV/u	LET keV/μm	Inactivation cross section μm^2	Mutation induction cross section $10^{-4} \mu m^2$	RBE (mutation) (initial slope
Gold	2.2	12895.0	57.0	4.1	0.1
	8.7	12568.0	90.0	8.3	0.2
Lead	11.6	11948.0		8.7	0.3
	15.2	10800.0	88.0	9.2	0.3
	150.0	3090.0	97.0	14.5	1.7
	500.0	1630.0	68.0	8.9	2.0
	980.0	1325.0	52.0	8.3	2.3

References:

ICRP 60. Recommendations of the International Commission on Radiological Protection. Ann. ICRP 21, No. 1-3, 1991

Stoll, U., A. Schmidt, E. Schneider, J. Kiefer. Killing and Mutation of V79 Chinese Hamster Cells exposed to accelerated O- and Ne-Ions. Radiat. Res. 142, 288-294 (1995)

Stoll, U., B. Barth, N. Scheerer, E. Schneider, J. Kiefer. HPRT-mutations in V79 Chinese hamster cells induced by accelerated Ni-, Au and Pb-ions. Int. J. Radiat. Biol., 70, 15-22 (1996)

ANALYSIS OF MUTATIONS IN THE HUMAN HPRT GENE INDUCED BY HEAVY-ION IRRADIATION.

Fumio Yatagai[1], Yasuhiro Kagawa[2], Nobuhisa Fukunishi[1], Naohito Inabe[1], Tuneo Shimazu[2], Shozo Kanai[2], Masahiko Hirano[2], Masao Suzuki[3], Kiyomi Kasai[3], Yoshiya Furusawa[3], Kouichi Tatsumi[3], Masami Watanabe[4], Takesi Kato[5], and Fumio Hanaoka[1].

[1]The Inst. Phys. Chem. Res., Saitama 351-01, Japan, [2]Toray Res. Center, Kanagawa 248, Japan, [3]Natl. Inst. Radiol. Sci. , Chiba 263, Japan, [4]Nagasaki Univ., Nagasaki 852, Japan, [5]Osaka Univ., Osaka 565, Japan.

Not only from the viewpoint of basic research on radiation biology but also from that of the application of heavy-ions in radiation therapy, it is interesting to study the characteristics of the mutations induced by heavy-ion irradiation. We have analyzed the hypoxanthine phosphoribosyl-transferase (hprt) mutations in human cultured cells. Both WI-L2-NS and TK6 are the human lymphoblastoid cell lines, derived from the same human spleen. The WI-L2-NS has a mutation in codon 237 of p53. For irradiation on these cells, the energies of C- and Ne-ions were adjusted so to irradiate the cells with three different LETs. For irradiation on these cells, the energies of C- and Ne-ions were adjusted so to irradiate the cells with three different LETs; one at the initial energy or so, one at the peak of Relative Biological Effectiveness (RBE), and one at the level just before the stop of the ions. The ion-beams were supplied by RIKEN Ring Cyclotron (Wako, Japan) except the 13 keV/μm C-ion beam by HIMAC (Chiba, Japan).

One of our current interests is to determine whether the difference in X-ray sensitivity between these two cell lines can still be seen even after irradiation of such heavy ions. A difference of the type and level of the p53 protein between these two cell lines has been reported to account for the differences in their X-ray sensitivities[1]. Another interest is whether the analysis of cDNA for the heavy-ion induced hprt mutant clones would provide a frequent recovery of exon skipping, because we often observed such type of hprt mutations in the human embryo (HE) cells iirradiated by 230 keV/μm C-ions[2]. Some knowledges on both questions were obtained as described below.

The survival curves were determined by limiting dilution method and

mutant clones were identified as resistance to 5 μg/ml of 6-thioguanine. The outline of these procedures are schematically illustrated in Fig. 1. Both survival-curves and mutation-frequencies for X-ray irradiation are shown in Fig. 2. These results were basically same as those reported by Amundson et al.[3]. As shown in Fig. 3, the difference in radiosensitivity for X-rays between these two cell lines were preserved at only low-LET (initial-energy) of C- and Ne-ions. Using the D10 dose for X-ray irradiation as a standard, the values of RBE were calculated and the result is shown in Fig. 4. The expected LET effect on cell killing was observed with both cell lines and this LET dependence was similar to that observed with human embryo cells in our previous experiment[4]. The hprt mutation frequencies at a certain survival level were also compared and the tendency of RBE for mutation seems to be similar to that for cell killing (data not shown).

Isolation of genomic DNA and mRNA from the mutant clones induced by HIMAC C-ions (13 keV/μm) were performed to identify the hprt mutation at the DNA sequence level. The strategy of analysis of mutation is shown in Fig. 1 (4), and the analyzed DNA-regions and the primers for PCR amplification and DNA sequencing were shown in Fig.5. The recovered mutant-clones were analyzed by the so-called multipex PCR for the genomic DNA. As can be seen in Table1, We have observed a significant difference in the mutational classes of TK6 cell-line between C- and Ne-ion at high LET obtained by ions just stopping. The majority of mutational event recovered from the the high-LET C-ions was a point-mutation in contrast to the very few recovery of such event by the high-LET Ne-ion beams. The frequent recovery of point mutations following the high-LET C-ion irradiation involved the exon-skipping event (data not shown) as observed in our previous experiment[2]. Further analyses for the genomic DNA and cDNA of the mutant clones are proceeded to confirm these tendencies together with other interesting results.

References

1) W. Zhen, C.M. Denault, K. Loviscek, S. Walter, L. Geng, and A.T.M. Vaughan: Mutat. Res. 346: 85-92 (1995).
2) Y. kagawa, F. Yatagai, M. suzuki, Y. Kase, A. Kobayashi, M. Hirano, T. Kato, M. Watanabe, and F. Hanaoka: J. Radiat. Res. 36: 185-195 (1995).
3) S.A. Amundson, F. Xia, K. Wolfson, and H.L. Liber: Mutat. Res. 286: 233-241 (1993).
4) M. Suzuki, M. Watanabe, M. Kanai, Y. Kase, F. Yatagai, T. Kato, and S. Matsubara: Adv. Space Res. 18: 127-136 (1995).
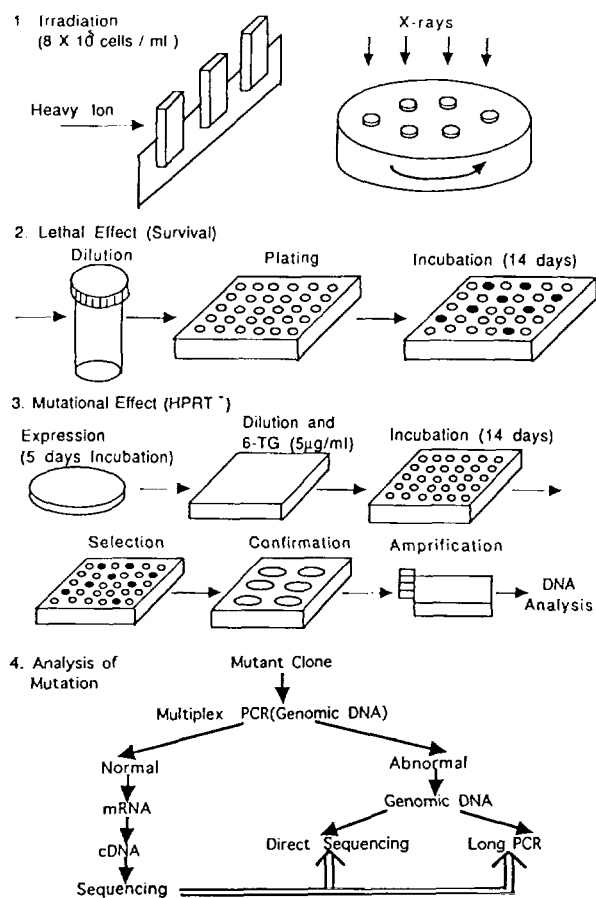
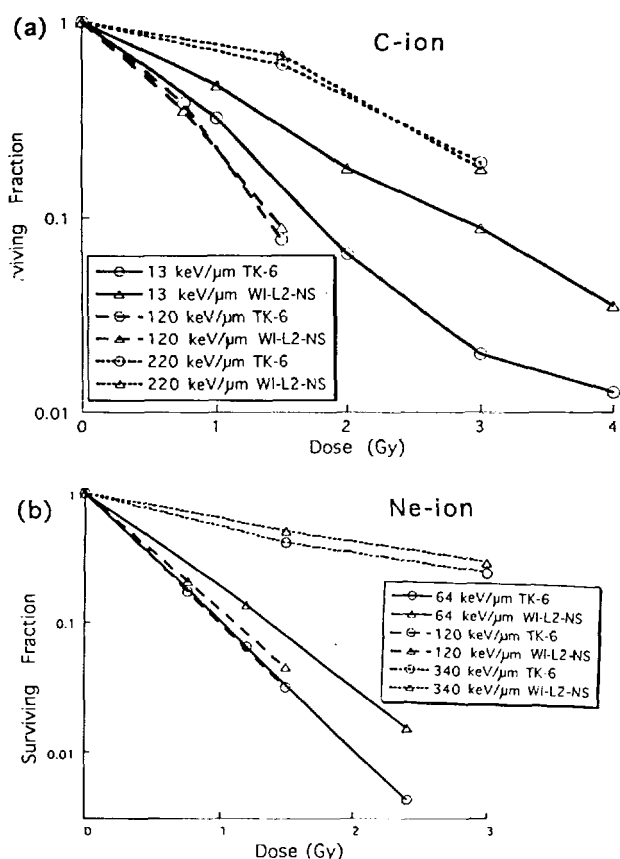## Fig. 1 A schematic illustration of experimental procedures

1. Irradiation
(8 X 10 cells / ml)

Heavy Ion →

X-rays

2. Lethal Effect (Survival)

Dilution → Plating → Incubation (14 days)

3. Mutational Effect (HPRT⁻)

Expression
(5 days Incubation) → Dilution and 6-TG (5μg/ml) → Incubation (14 days)

Selection → Confirmation → Amprification → DNA Analysis

4. Analysis of Mutation

Mutant Clone

Multiplex PCR(Genomic DNA)

Normal / Abnormal

mRNA / Genomic DNA

cDNA → Direct Sequencing / Long PCR

Sequencing

Survival Curves for X-rays
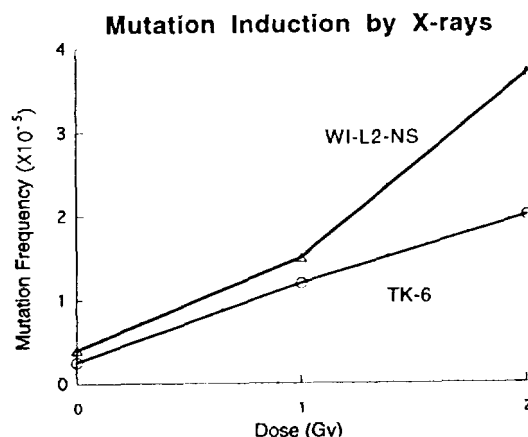
WI-L2-NS

TK-6

Mutation Induction by X-rays

WI-L2-NS

TK-6

Fig. 2 Effects of killing and mutability X-ray irradiation

Fig. 3 LET dependence of killing effect by irradiation of C-ions (a) and Ne-ions (b)

(a) C-ion

- 13 keV/μm TK-6
- 13 keV/μm WI-L2-NS
- 120 keV/μm TK-6
- 120 keV/μm WI-L2-NS
- 220 keV/μm TK-6
- 220 keV/μm WI-L2-NS

(b) Ne-ion

- 64 keV/μm TK-6
- 64 keV/μm WI-L2-NS
- 120 keV/μm TK-6
- 120 keV/μm WI-L2-NS
- 340 keV/μm TK-6
- 340 keV/μm WI-L2-NS
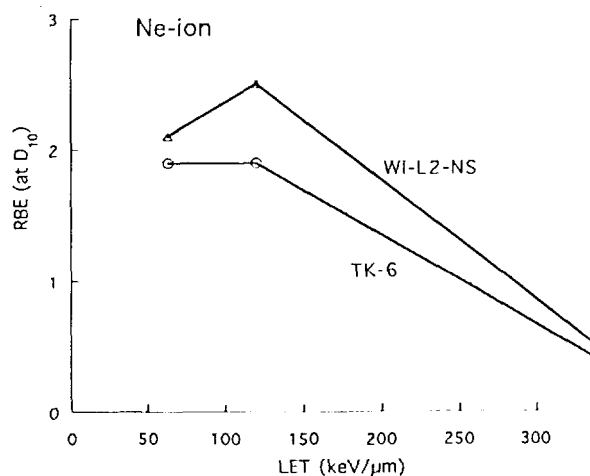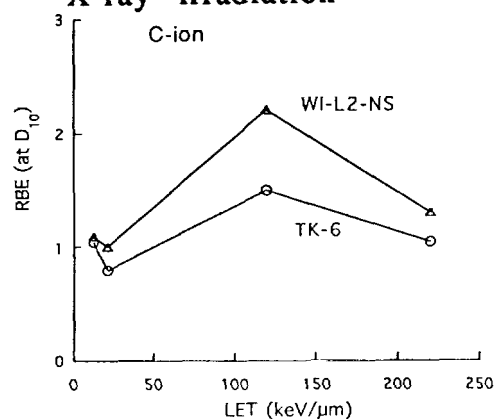
Fig. 4 RBE for a killing effect

C-ion

WI-L2-NS

TK-6

Ne-ion

WI-L2-NS

TK-6

3

HPRT Gene Locus

```
exons 1        2 3      4  5  6  789
      ├──────┤┼┼─────┼──┼──┼──┼┼┼──────────
        ├──────────┤  ├──────┤├────────────┤
             A         B          C
      0      1 0     2 0    3 0    4 0     5 0
      ├───────┼───────┼──────┼──────┼───────┤
```

kilobases
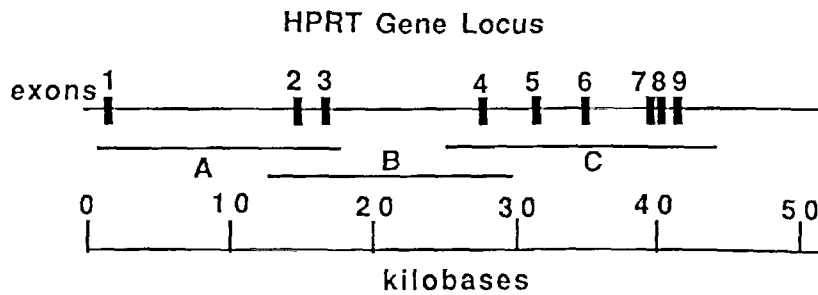
Long PCR

A	16.4 Kbp	S 1238	(35 mer)	~	A 17591	(35 mer)
B	16.4 Kbp	S 12965	(35 mer)	~	A 29298	(35 mer)
C	19.2 Kbp	S 24966	(35 mer)	~	A 44187	(35 mer)

Multiplex PCR

exon 2	393bp	S 14674	(27mer)	~	A 15066	(23mer)
exon 3	459bp	S 16519	(22mer)	~	A 16977	(24mer)
exon 4	332bp	S 27754	(23mer)	~	A 28085	(23mer)
exon 5	236bp	S 31500	(23mer)	~	A 31735	(24mer)
exon 6	280bp	S 34817	(25mer)	~	A 35096	(23mer)
exon 7,8	900bp	S 39596	(24mer)	~	A 40495	(25mer)
exon 9	794bp	S 41261	(21mer)	~	A 42054	(23mer)

cDNA(exons)

```
┌────┬──┬────┬──────┬───┬─┬───┬─┬───┬─┬─────┐
│    │ 1│ 2  │   3  │ 4 │5│ 6 │7│ 8 │9│     │
└────┴──┴────┴──────┴───┴─┴───┴─┴───┴─┴─────┘
-100   1        200        400       600
  └───┴────┴─────┴─────┴─────┴─────┴─────┴───┘
```
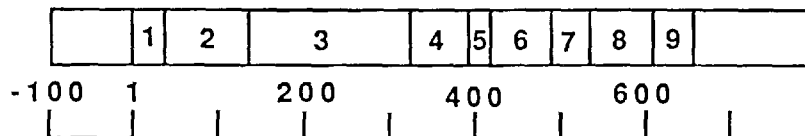
DNA Sequencing (Amplified by PCR)

PCR 1	810bp	S -59 (17mer)	~	A 751	(18mer)
PCR 2	756bp	S -46 (23mer)	~	A 710	(23mer)
PCR/Seq 1	757bp	S -36 (20mer)	~	A 721	(20mer)
PCR/Seq 2	718bp	S -17 (20mer)	~	A 701	(20mer)

Fig. 5 The analyzed DNA-regions and the used primers

Table 1 Analysis of mutational events of TK6
by multipex PCR for genomic DNA

Ion (LET, keV/μm)	Number of Mutant Clones		
	Whole Deletion	Partial Deletion	Point Mutation
C (250)	0	11	17
Ne (310)	5	24	5

4

HPRT-MUTATIONS IN V79 CELLS. TYPE OF LESIONS DEPENDENT ON LET.

H. Rink, D. Melchior, P. Marcoso, Y. Eryigit und K. Yeghjazaryan

Experimental Radiology and Radiation Biology, University of Bonn,

Sigmund Freud Straße 25, D-53105 Bonn, Germany

Introduction

The study of mutations induced by accelerated heavy ions was performed for two reasons. First, we wanted to get more insight into the quality and type of lesions produced in a distinct gene. Lesions of this type should obviously depend on the ion in question, its LET, its specific energy and on fluence. The simple question sounds : is the deleterious effect due to the target and its spur or does it depend on the number, the energy and the range of the produced delta electrons. On the other hand highly accelerated heavy ions, being part of the cosmic radiations, are of special interest in view of radiation protection during long-termed manned space missions as well as in cases of cancer therapy with heavy ions. To address these aspects, the mutational spectra of the hprt-gene (located on the X-chromosome, 36 kbp,9 exons) of male V79 Chinese hamster cells were analysed on a molecular level.

Materials and Methods

Heavy-ion irradiation has been performed at GSI (Gesellschaft für Schwerionenforschung) in Darmstadt, Germany. Beams had nearly the same flux rates ($3-4 \times 10^6$ particles/cm^2), but differed in ions, specific energies (MeV/u), LETs (keV/µm), spur diameters (µm) and doses (Gy). Table I compiles the different beam parameters.

Table I : **Physical Parameters of Radiation.**

Ion	Atomic number	Flux rate (10^6/cm^2)	LET (keV/µm)	Spec.Energy (MeV/u)	Spur dia- meter (µm)	Dose (Gy)
O	8	4.0	62	69.7	15.3	0.4
O	8	3.0	247	10.8	2.4	1.2
O	8	3.2	318	7.6	1.7	1.6
O	8	2.9	754	1.9	0.4	3.5
Ar	18	3.0	1104	11.4	2.5	5.3
Ca	20	3.1	2386	3.6	0.8	11.8
Au	79	3.0	13,223	8.8	1.9	63.5
U	92	1.0-8.0	15,580	8.8	1.9	25-200

Oxygen was used at different levels of specific energies. LET varied between 60 and 16,000 keV/µm, specific energies between 1.9 and 70 MeV/u and spur diameters between 0.4 and 15.3 µm. Within this work a total of 216 heavy-ion induced hprt mutants has been selected. Additionally 30 spontaneous mutations, which all exhibit point mutations, have been investigated so far.

The heavy-ion irradiated cells (BIBA, Kraft et al. 1980) were preincubated for 5 days in order to express the mutation. During this time period the preexisting hprt-mRNA and hprt-enzyme molecules will disappear. After this preincubation period cells were selected for hprt-mutants in a 6-thioguanine (6-TG) medium (10 µg/ml) over a 10 day period with change of medium every 3rd day. Wildtype cells with functional hprt-genes or enzymes are able to incorporate 6-TG into its DNA. The incorporated 6-TG in turn leads to a stop in DNA synthesis. By this way wildtype cells are killed, whereas hprt-mutants which cannot incorporate 6-TG survive and can be selected. The obtained mutant cells were cloned and further cultivated to get 5×10^7 cells per mutant clone. Genomic DNA was extracted from each of these mutant cell lines, purified (Quiagen kit) and digested by three different restriction enzymes (EcoR I, Pst I and Bgl II). The DNA-fragments obtained were separated by agar gel electrophoresis, denatured (converted to single-strand DNA), blotted to a nylon filter membrane, and hybridized with a radioactively labelled (P-32, primer extension kit, DuPont) hprt-cDNA. The hprt-cDNA (1.4 kbp) as an insert in the recombinant plasmid pHpt 12, containing the whole coding sequence of the hprt-gene, was kindly provided by John Thacker (Medical Research Council, Radiobiology Unit, Chilton, UK) This probe specifically recognizes the hprt-fragments separarted by agar gele electrophoresis (Southern Blot Technique, Southern 1975).

Results

Figure 1 gives the cross-sections for mutation induction (σ_m). These values agree well with data published by Thacker et al. (1979), Wulf et al. (1985) and Kranert et al. (1990). The σ_m values generally increase with LET, and exhibit ion specific hooks in the very high LET range, however, less pronounced as with σ_i values. A comparison of the various restriction patterns of the different mutants with the wild type pattern suggests a classification into three types of totally different mutations :

A) **Total Deletions**: the gene is totally absent, the cDNA probe does not recognize any homologous sequence.

B) **Partial Deletions**: the gene is partially absent, some bands are missing or its position (molecular weight) has changed.

C) **No Change Mutations**: compared to WT-pattern there are no detectable differences, (point mutations and minor alterations of up to 500 bp).
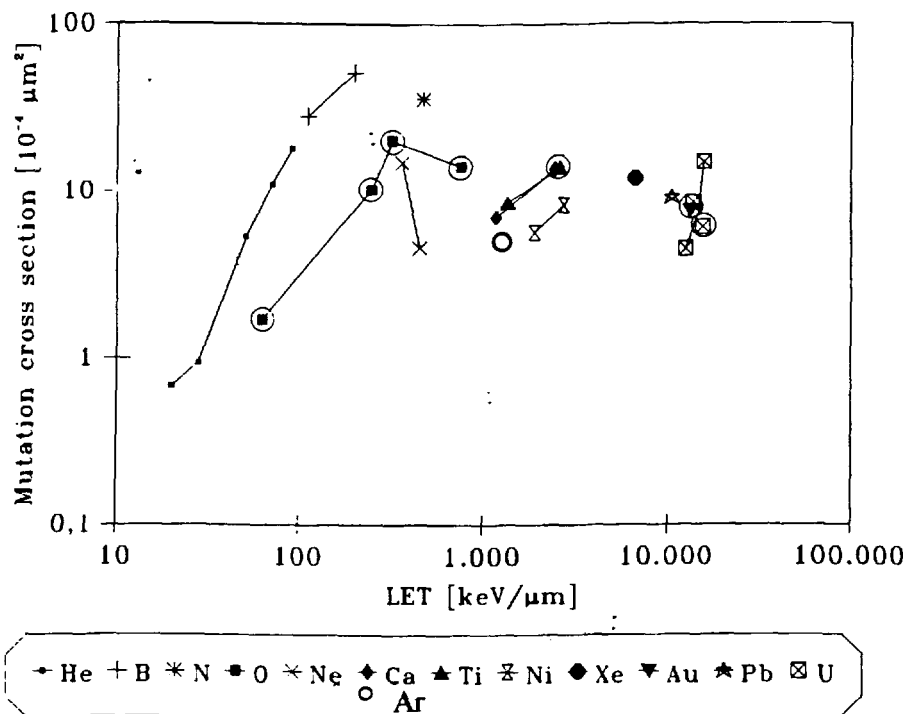
Figure 1:   Cross-sections of mutation induction dependent on LET with data of Thacker et al.
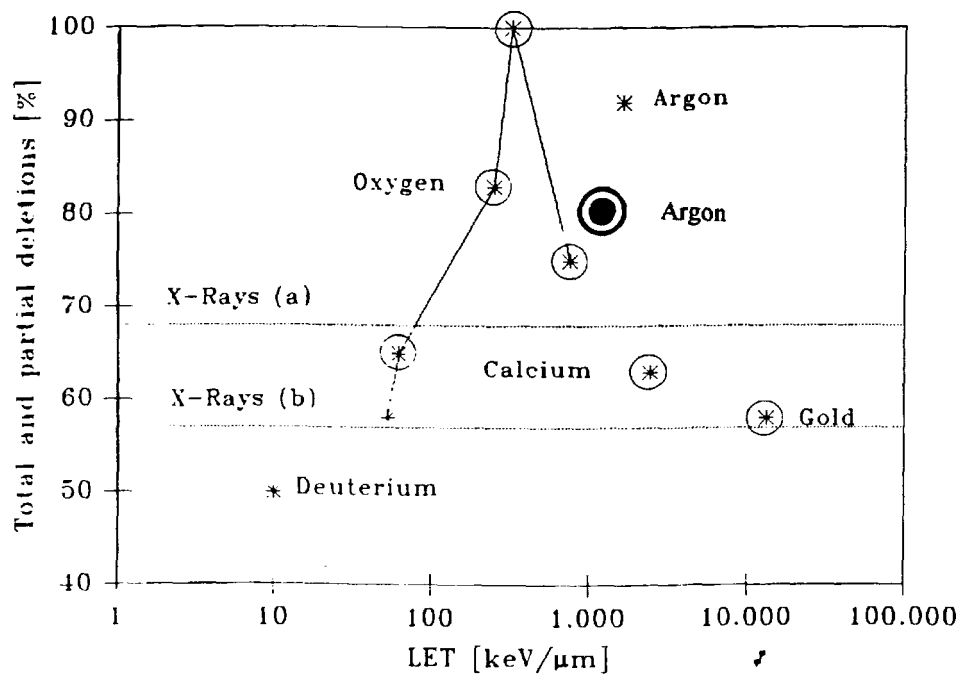(1979) and Kranert et al. (1990). Own data are indicated by circles.

Figure 2:   Sum of total and partial deletions dependent on LET. Data without circles are
taken from Stoll (1994, PCR-method). Dotted lines give the percent range for the
X-ray induced mutations (a: Jostes et al., 1994; b: Aghamohammadi et al., 1992).
Own data are indicated by circles.

The data of figure 2, which represent the severe gene deletions (total and partial deletions) show an initial increase of gene damage up to about 500 keV/μm, followed by a decrease for further increasing LET-values. For LET-values higher than 1,000 keV/μm the damage pattern becomes comparable to that obtained with sparsely ionizing radiations (X-rays).

Table II : **Localisation of DNA Break Sites in the hprt Gene**

Break Location Between	Number of breaks (%)
Exon 1 and 2	2 (3%)
Exon 2 and 3	5 (8%)
Exon 3 and 4	· 7 (11%)
Exon 4 and 7	**44 (71%)**
Exon 7 and 8	1 (2%)
Exon 8 and 9	3 (5%)

By comparing the different patterns in class B (partial deletions), we found that 70% of the damage was located between exons 4 and 7 (Table II). In this connection it should be mentioned that exon 5 is rather small, its sequence consisting of only 18 bp (Rossiter et al. 1991).

Discussion

The last mentioned result is probably due to so-called scaffold-attached regions of the DNA within the genome. These sites obviously prevent the action of repair enzymes. The data in figure 2 may explain why biological damage induced by accelerated heavy ions depends not only on LET, but also on other beam parameters as well, especially on spur diameter. With very high LET-values the specific energies decrease and this in turn results in smaller spur diameters, as described by the relation : $r = r_0 E/u$, with $r_0=0,219$ μm (constant).

Thus at LET-values above 1,000 keV/μm (small spur diameters) the probability that a cell will get hit directly by a particle (its spur) is rather low. On the other hand the probability that many cells will get hit by delta-electrons increases. The biological action spectrum of delta-electrons is comparable to that of the action spectrum induced by X-rays. In summary :

   i) The quality of biological damage increases with LET-values up to 500-1,000 keV/μm.

   ii) With LETs >1,000 keV/μm the damage is comparable to that of X-rays

   iii) The hprt gene is not damaged randomly, but mainly between exons 4 and 7 of the gene.

References.

Aghamohammadi et al., Mutation Research **269**: 1-7 (1992)

Jostes et al., Radiation Research **137**: 371-379 (1994)

Kraft et al., Nuclear Instrumentation Methods **168**: 175-179 (1980)

Kranert et al., International Journal of Radiation Biology **58**: 975-987 (1990)

Rossiter et al., Genomics **9**: 247-256 (1991)

Southern, Journal of Molecular Biology **98**: 503-517 (1975)

Stoll. Diss Nat. Fak. University of Giessen (1994)

Thacker et al.. International Journal of Radiation Biology **36**: 137-148 (1979)

Wulf et al. Radiation Research **104**: 122-134 (1985)

Structural Changes of DNA in Heavy Ion-Induced Mutants on *Arabidopsis*

S. Tano, N. Shikazono, A.Tanaka, Y.Yokota and H. Watanabe

Advanced Science Research Center, Japan Atomic Energy Research Institute,

1233 Watanuki, Takasaki, Gunma 370-12, Japan

Introduction

High LET radiation causes localized and dense ionization within cells compared to low LET radiation (Kraft et al. 1992). It is proposed that high LET radiation predominantly produces double strand breaks with damaged end groups which repairability may be low (Hagen 1994). Therefore, it may be said that high LET radiation could be able to generate large genetic changes more frequently than low LET radiation.

Effects of high LET radiation on living organisms at molecular level have been extensively investigated in mammalian cells. Many of them reported that the frequency of deletion was higher for high LET radiation than for low LET radiation (Schwartz et al. 1994, Stoll et al. 1995, Zhu et al. 1996, Suzuki et al. 1996). On the other hand, some researchers reported that no significant differences in the frequency of deletions were observed between high and low LET radiations (Thacker 1986, Aghamohammadi et al. 1992, Jostes et al. 1994, Bao et al. 1995,Yamada et al. 1996). Some investigations on the molecular nature of mutations by X-rays, gamma-rays and fast neutrons have been carried out along with the isolation of genes in plants. Although rearrangement types of mutations were observed in several genes, it was shown that these radiations frequently induced deletions whose length were larger than several thousand base pairs. Bruggemann et al. (1996) reported that 13 out of 18 long hypocotyl 4 (*hy4*) mutant of *Arabidopsis* induced by fast neutrons carried deletions larger than 5kb. However, there are few investigations in plants on the type of mutation induced by high LET radiations.

In order to investigate the frequency of structural changes induced by high LET radiation in plants, a comparison was made between DNA fragments amplified by the polymerase chain reaction (PCR) from C ion- and electron- induced *Arabidopsis* mutants at *GL* and *TT* loci.

Materials and Methods

Dry seeds of *Arabidopsis thaliana* , ecotype Columbia, were irradiated with 150Gy of C-ions (220MeV) and 750Gy of electrons (2MeV) and LETs of these radiations were calculated as 113keV and 0.2keV/μm, respectively. These doses were determined from the relative biological effectiveness of C-ions compared with that of electrons on the survival of the plants. M1 plants were raised from the irradiated seeds and selfed to obtain the M2 seeds. *gl* and *tt* mutants were selected from 52,407 M2 plants and these mutants were crossed to each tester for complimenta-tion analysis (induced *gl* mutants to *gl1-1*, *-2*, and *-3* : induced *tt* mutants to *tt3-1*, *tt4-1*, *tt6-1* and *tt7-1*).

Genomic DNA was extracted from the M3 mutants following procedure described by Konieczny and Ausubel (1993). Primers for PCR were designed using the computer software Genetyx Mac ver.7.3 (Software Development Co. Ltd., Japan). The amplified DNA fragments were analyzed by agarose gel electrophoresis and visualized by ethidium bromide staining.

In the present study, 4 mutant lines, composed of 2 *gl1* mutants and 2 *tt4* mutants, were induced by C-ions and 5 mutant lines, composed of 3 *gl2* mutants, 1 *tt3* mutants by electrons.

Based on the DNA base sequence of the *GL1* locus (3,614bp), 4 kinds of sense primers and 3 kinds of antisense primers were constructed as shown in Table 1. The electrophoretic patterns of PCR fragments from the wild type and the *gl1* mutant line induced by C-ions are representatively shown in Fig.1. In all combinations of primers, DNA fragments were amplified in the case of wild type (Panel A). In the case of *gl1* mutant (Panel B) the molecular weights of amplified DNA fragments were the same as those of the wild type for all primer combinations that included either primer 4 or primer 5. However, DNA fragments were not detected when primer 4 or primer 5 was excluded from the primer set.
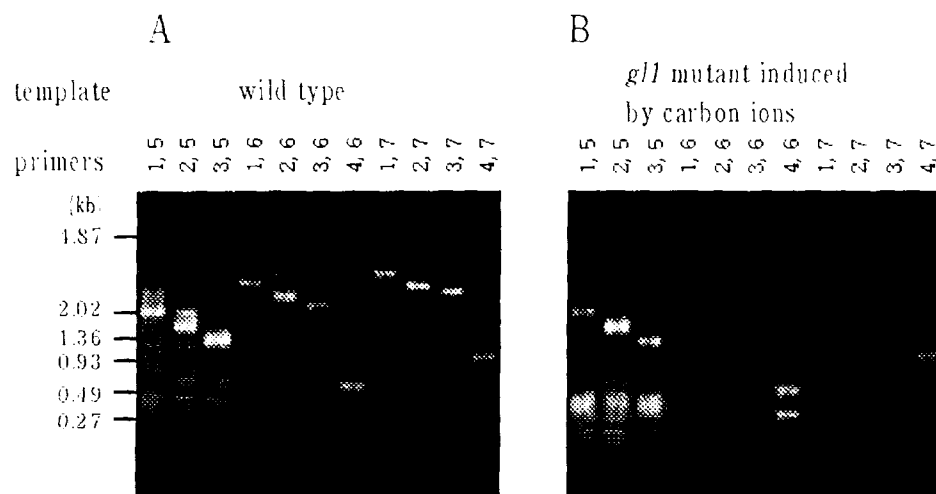

Fig. 1 Analysis of *gl1* mutation induced by C-ions by PCR. The primers used for each reaction are indicated at the top of each lane. The template DNA was from wild type (Panel A) or from C-ion induced *gl1* mutant (Panel B)

The results of PCR at the 4 induced mutant loci, are schematically shown in Fig.2. The result of the *gl1* mutant indicated that a break occurred at exon 3 between primer 5 and 4, and then either the upstream or downstream region was inverted or translocated (Fig.2A a). In the other *gl1* mutant line induced by C-ions, no DNA fragment was amplified (Fig.2A b). This result indicated that this mutant carried either a deletion larger than 3.1kb or a rearrangement. Fig. 2B show the results of 3 lines of *gl2* mutant induced by electrons. Two of these lines (a and b) showed no detectable changes in number or size of the amplified DNA fragments, suggesting that point-like mutations were induced in these mutants. However, it should be noted that deletions less than several tens of base pairs could not be detected in the present study due to the resolving power of the agarose gel. In the residual *gl2* mutant (c), the data indicated that a break occurred at exon 3 between primer 6 and 4. Fig. 2C shows the results of a *tt3* mutant induced by electrons. Since no detectable change

was observed, it was estimated that a point-like mutation occurred in this mutant. In the case of *tt4* mutant (Fig. 2D) induced by C-ions shown in panel a, it was revealed that a break occurred within exon 2 (between primer 7 and 8) and that either the upstream or downstream fragment underwent inversion or translocation. The residual *tt4* mutants (b and c), one induced by C-ions and the other induced by electrons, may both carry point-like mutations.

Further fine analysis of *gl1* mutant was performed by DNA sequencing the cloned fragments after digestion with several enzymes. From the result of this experiment, break point was 91bp upstream from the end of *GL1* exon 3 and 107bp unknown fragment existed at the upstream of this break point (Fig. 3).
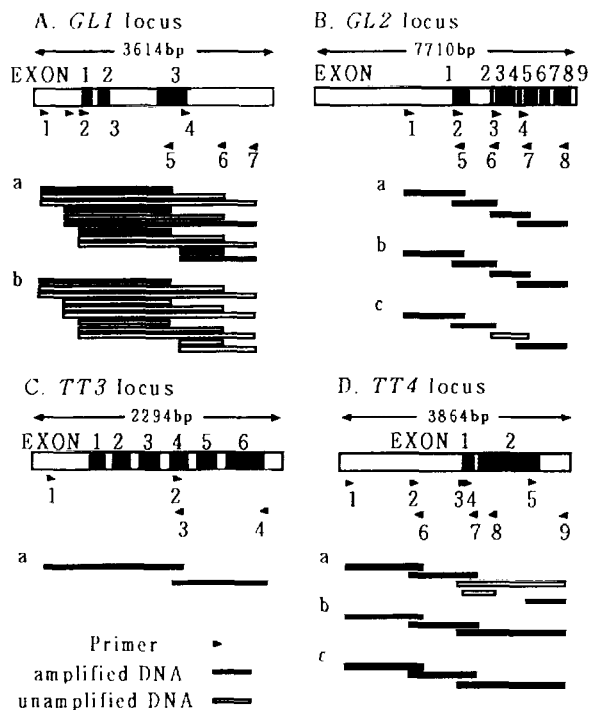

Figure 2. Schematic representation of the results of the PCR analysis of the mutants. The number of base pairs that was sequenced and the location of exons and primers are presented at each locus. DNA fragments which were amplified are shown as black boxes, whereas DNA fragments which were not are shown as white boxes. Panel A: *gl1* mutants induced by carbon ions (a, b); Panel B: *gl2* mutants induced by electrons (a, b, c); Panel C: *tt3* mutant induced by electrons (a); Panel D: *tt4* mutants induced by carbon ions (a, b) and by electrons (c).
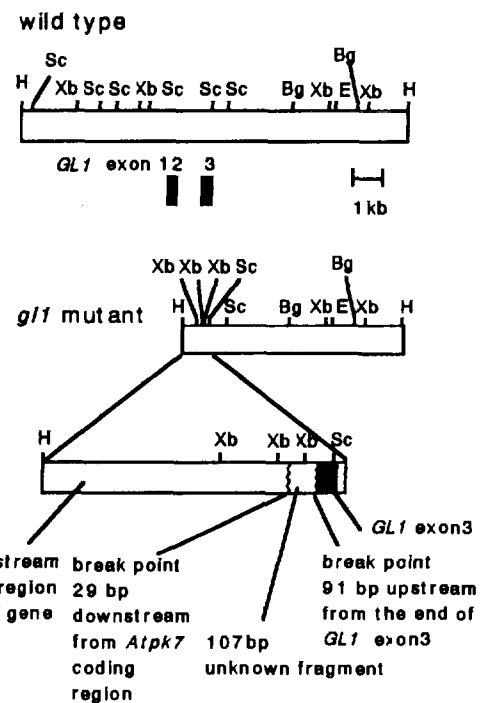

Figure 3. Schematic representation of the *GL1* locus in the wild type and in the carbon-induced mutant (Fig. 1, Panel A a). The position and size of the exons are shown beneath the wild type DNA fragment. The restriction enzyme sites are indicated. H=HindIII, Sc=ScaI, Xb=XbaI, Bg=BglII, E=Eco RI.

Discussion

The frequency of deletion is affected by the presence of a nearby essential gene. When a deletion occurred to extend beyond the essential gene, mutant can not be recovered. In this case, the segregation ratio of recessive mutants should be less than 0.25. *Arabidopsis* mutants induced by X-rays

or fast neutrons segregated with an average ratio of 0.215, a value lower than Mendelian expectation (Dellaert 1980, Koorneef et al. 1992). Therefore, this type of mutations are most likely a large deletion extending to an essential gene. In contrast, the segregation ratio of mutants induced by C-ions was 0.248 and fit to the Mendelian expectation. Therefore, one may conclude that C-ions would not induce such large deletions. It seems more likely to presume that the C-ion induced *gl1* mutant showing no detectable PCR fragments may have arisen from rearrangements. If this were the case, 3 out of 4 mutants induced by C-ions and 1 out of 5 mutants induced by electrons resulted from rearrangements. These results imply that, among mutants induced by C-ion irradiation in *Arabidopsis*, non-lethal rearrangements rather than large deletions are frequently generated.

The results obtained in *Arabidopsis* showed a clear contrast to the results of mammalian cells in which the majority of large genetic changes induced high LET radiation were deletions. Further analysis should be made to elucidate the molecular nature of the mutations induced by high LET radiations in plants.

References

Aghamohammadi, S. Z. et al. Mutat. Res. 269:1-7 (1992)

Bao, C-Y. Mutat. Res. 326:1-15 (1995)

Bruggemann, E. et al. Plant J. 10:755-760 (1996)

Dellaert, L. M. W. Theor. Appl. Genet. 57:137-143

Goodhead, D. T. Radiat. Environ. Biophys. 34:67-72 (1995)

Hagen, U. Radiat. Environ. Biophys. 33:45-61 (1994)

Jostes, R. F. et al. Radiat. Res. 137:371-379 (1994)

Konieczny, A. and Ausbel,F. M. Plant J. 4:403-410 (1993)

Koornneef, M. et. al. Mutat. Res. 93:109-123

Kraft, G. et al. Radiat. Environ. Biophys. 31:161-180 (1992)

Schwartz, J. L. et al. Mutagenesis 9:537-540 (1994)

Stoll, U. et al. Radiat. Environ. Biophys. 34:91-94 (1995)

Suzuki, M. et al. Adv. Space Res. 18:127-136 (1996)

Thacker, J. Mutat. Res. 160:267-275 (1986)

Yamada, Y. et al. Radiat. Res. 145:481-490 (1996)

Zhu, L. X. et al. Radiat. Res. 145:251-259 (1996)

Track Theory Estimates of Single Particle Traversals of Cell Nuclei

Robert Katz, University of Nebraska, Lincoln NE 68588-0111 and
F. A. Cucinotta, NASA Langley Research Center, Hampton VA,23665-5225

Acording to C. R. Geard[1] et al. single α particles (110 keV/μm) directed through cell nuclei in a charged particle microbeam apparatus has yielded the results that single α particles through cell nuclei cause death (60-85% cell survival) and cause oncogenic transformation of C3H10T1/2 cells (1×10^{-4}).

M. Pugliese et al.[2] report that the survival probability for a single 4.3 MeV α particle traversing the nucleus of a Chinese Hamster V-79 cell is 67 $\pm$ 10 %

We compare the findings of Geard et al. to calculations from Katz[3] theory. For this we require cellular radiosensitivity parameters for these two phenomena and some physical properties of α particles of this stopping power. We note from our table that in water: at $\beta = 0.04$, T=0.75 MeV/amu, z^{*2}/β^2=2290, LET=116 keV/μm, range = 17.1μm.

For Chinese hamster cells, aerobically irradiated, we have κ=1100 and m=3, so that $z^{*2}/\kappa\beta^2$=2.08 From track theory the probability of cell killing by a particle passing through its nucleus is given by $P = (1-\exp\{-z^{*2}/\kappa\beta^2\})^m$. We find that P = 0.67. Thus 33% of these cells would survive.

For T-1 kidney cells, aerobically irradiated, κ=1400 and m = 2.5. Then 42% of these cells would survive.

For T-1 kidney cells hypoxically irradiated κ=1900 and m = 2.5. Then 59% of the cells survive.

We compare the findings of Pugliese et al. to calculations from Katz theory at a slightly different energy of 1.167 MeV/amu, for which z^{*2}/β^2 is 1538. Taking values of κ and m for Chinese Hamster cells as before we find the surviving fraction to be 58%, in quite good agreement with the experimental finding.

Next we deal with the probability of causing an oncogenic transformation in C3H10T1/2 cells caused by an α particle which intersects a gene. Here κ =750 and m = 2. At 116 keV/mm 91% of the intersected genes are mutated, from the equation for P, above. But there is now a geometric factor because the microbeam's α particles are directed through the nucleus rather than through the gene. If we take the geometric factor to be the ratio of the values of σ_0 for cell killing and for transformation we find the geometric factor to be 1.15(-10)/ 5(-7)=2.3(-4).   Multiplying P by the geometric factor we find the fraction of C3H10T1/2 cells experiencing an oncogenic transformation to be 2.1×10^{-4}.

Subsequent data, by R.C. Miller et al.[4] lead them to conclude, from preliminary results, that one α particle traversal through a C3H10T1/2 cell is not carcinogenic since the transformation frequency for single traversals of alpha particles at 90 keV/micron is consistent with the spontaneous frequency of transformation.

In this connection we note a report by M. Tubiana[5], based on analysis of epidemiological data,that no carcinogenic effect has been observed from low doses of α particles.

Additionally we call attention to the theoretical conclusion, by Katz and Hofmann[6] in 1982, that transformation probabilities for α particles in the range 1-2 MeV/amu are so low as to suggest that more than 1 electron or α particle must interact with the nucleus of a cell to induce malignant transformation.

We must look more closely into our predictions of the outcome of microbeam experiments as more specific data become available. With presently available data the predictions made from Katz theory are in qualitative agreement with experiment, and possibly better .

We recall that this theory has represented, from the first, that its analysis of cellular survival at high doses of high LET particles enabled the prediction of the lowest possible doses of both low and high LET particles, that is single particle traversals of electrons[7] and high LET particles through cell nuclei.

Calculated "tracks" of high LET particles through the nuclei of T-1 kidney cells as simulated on a typewriter in 1979 from the above equation for P, are shown in the accompanying figure from Katz and Hofmann. In this simulation P leads to the random selection of the cell killed in a chosen path length interval . We hope that this will be suggestive for those contemplating additional single particle experiments.

References

[1]C.R.Geard ,R. Randers-Pehrson, T.K. Hei, R.C. Miller, L.J. Wu and D. J. Brenner, Microbeam Mediated Cellular Effects. Abstracts for 12'th Symposium on Microdosimetry, Oxford,1996 Friday Morning
[2]M. Pugliese, M. Durante, G.F. Grossi, F.Monforti, D. Orlando, A. Ottolenghi, P. Scampoli, and G. Gialanella, Effects of Single Alpgh-Particle Traversals: A Method Based on Nuclear Track Detectors, Abstracts for 3'rd International Workshop: Microbeam Probes of Cellular Radiation Response, 1997
[3]R. Katz, R. Zachariah, F.A. Cucinotta, and Chunxiang Zhang, Survey of Cellular Radiosensitivity Parameters, Radiat. Res. 140, 356-365(1994)
[4]R. C. Miller, G. Randers-Pehrson, D. J. Brenner, E. J. Hall, and C. R. Geard, Microbeams and Cellular Changes: Single Particle Induced Oncogenic Transformation, Abstracts for the 3'rd International workshop on Microbeam Probes of Cellular Radiation Response, Columbia University, 1997.
[5]M.Tubiana, Effets cancerogenes des faibles doses du rayonnement ionisant, Radioprotection (France) 31, 155-191(1996).
[6]R. Katz and W. Hofmann, Biological Effects of Low Doses of Ionizing Radiations, Particle Tracks in Radiobiology, Nucl. Instr. nd Meth 203, 433-442(1982).
[7]R. Katz and M.P.R. Waligorski, On the Linear Extrapolation to Low Dose. Radiat. Prot. Dosimetry 52, 197-199(1994).

PARTICLE TRACKS IN "CLOSE PACKED" T-1 HUMAN KIDNEY CELLS (AEROBIC)

in 1 mm segments

‡ indicates position of Bragg peak.
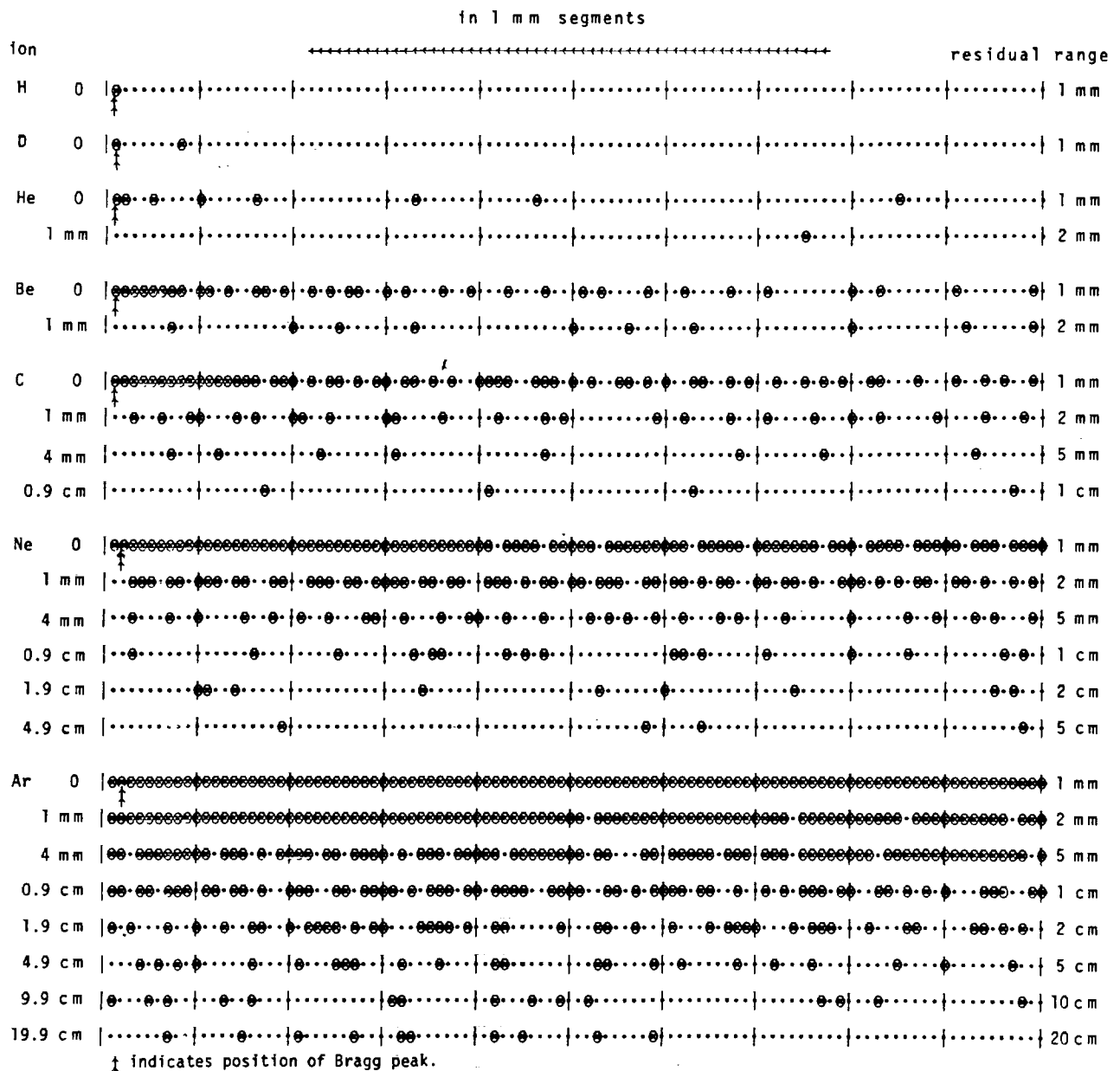
Each cell is taken to have a diameter of 10 microns, with the leftmost end of the first cell at the residual range indicated at left. Cells are close-packed and aligned along the ion's path.

⊖   indicates a cell killed by a heavy ion moving from right to left, in the "ion-kill mode".
·   indicates a cell whose nucleus has been intersected by the moving heavy ion and which experiences only sub-lethal damage.

R. Katz   19 October 1979

Molecular spectra of heavy-ion induced mutations

Paul Schmidt, Jürgen Kiefer

Strahlenzentrum der Justus-Liebig-Universität, Giessen, Germany

Chinese hamster V79 cells were exposed to carbon and titanium ions, ^{241}Am alpha particles and X-rays. Mutations at the HPRT locus were selected in 6-thioguanine containing medium. For each radiation type at least 30 clones were isolated and the gene structure analysed by multiplex polymerase chain reaction. In all cases except titanium, background mutants pre-existing in the unirradiated cell suspension were investigated in parallel. This turned out to be essential for a correct analysis since the background pattern varies considerably from experiment to experiment. The distribution of partial deletions was also studied. It could be noted that in unirradiated cultures clonal expansion occurs since mutants with the same deletion pattern are often present in large numbers. The same mutants can also be found to appear several times among the irradiated cells indicating the contribution of background mutants to the irradiated mutant deletion pattern distribution. Figure 1 shows the distribution of deletions for the different radiation types together with the distribution of background mutants pooled from several experiments.
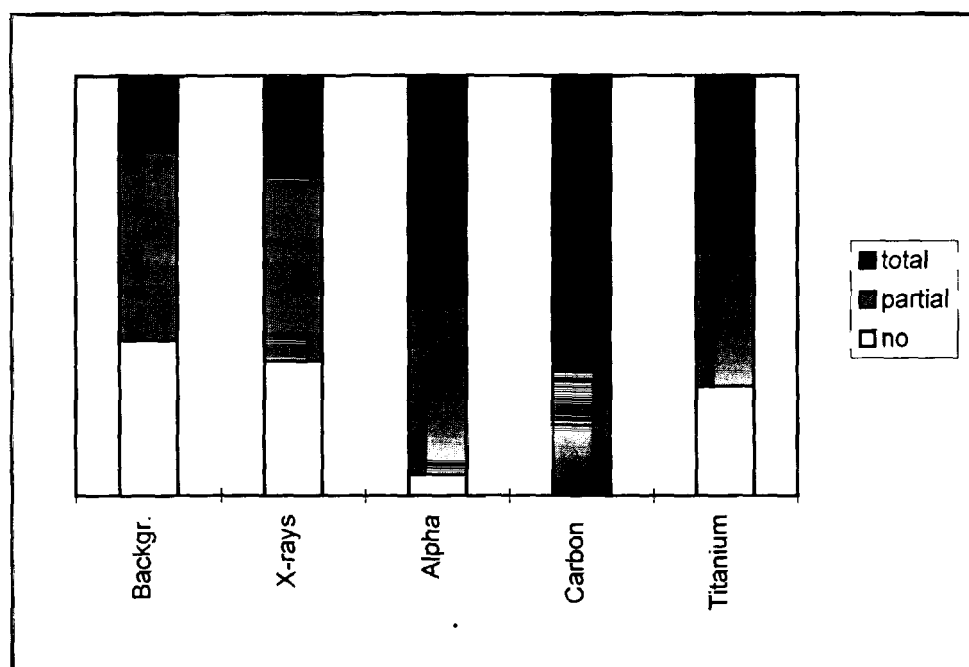

Fig. 1: Distributions of deletion types after background correction (except titanium)

It can be seen that the fraction of total deletions is larger for particle radiation than for sparsely ionising radiation suggesting more severe damage at the molecular level. This picture would not have emerged if the background had not properly been taken into account. Heavy particle induced mutants display also a special feature of partial deletions: While with X-rays or in unirradiated cells the deletions extend only over neighbouring exons, this is not always the case with alpha particles or heavy ions. There deletions are also found in well separated exons. We term this phenomenon, which may be a hallmark of the action of densely ionising radiations, "non-contiguous deletions". It may - if confirmed in further studies - serve as molecular marker of heavy ion action.
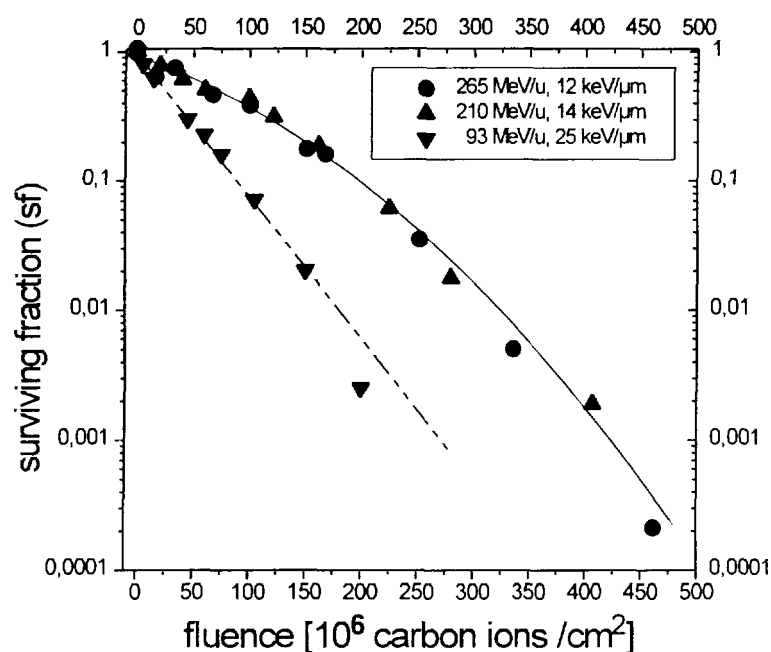

Fig. 2   Cell survival after carbon-ion irradiation:

sf = $e^{-\sigma_i \Phi}$ was the function used for fitting the 93 MeV/u data, yielding for σ_i, the inactivation cross section, 2.5 ±0.2 μm^2. The same type of fitting function resulted in σ_i = 1.0 ±0.5 μm^2 for 210 and 265 MeV/u, but did not fit the data well at high fluences, so that the alpha-beta model was also used and is shown here with α = 0.68 μm^2, β = 0,22 μm^4 .

In Fig. 1 it is surprising that the portion of "no deletion" vanishes for the carbon-ion induced mutants. Hence we want to focus here on mutation induction by carbon ions. Survival and mutation induction after three different energies (93 MeV/u, 210 MeV/u and 265 MeV/u reaching the cells) are shown in Fig. 2, the mutation-induction behaviour in Fig. 3.

The differences in cell kill are negligible between the two high energies (210 and 265 MeV/u), which also do not differ much in the associated LET (12 and 14 keV/μm, respectively). Considerably more efficient in cell killing are carbon ions at 93 MeV/u, where the LET is considerably higher (25 keV/μm). Accordingly, the differences in the mutation induction behaviour are also rather small for the two high energies. The mutation-induction cross section σ_i is $0.29 \pm 0.04 *10^{-4}$ μm^2 for 265 MeV/u, $0.30 \pm 0.06 *10^{-4}$ μm^2 for 210 MeV/u and $0.45 \pm 0.05 *10^{-4}$ μm^2 for 93 MeV/u carbon ions, as shown in Fig. 3.
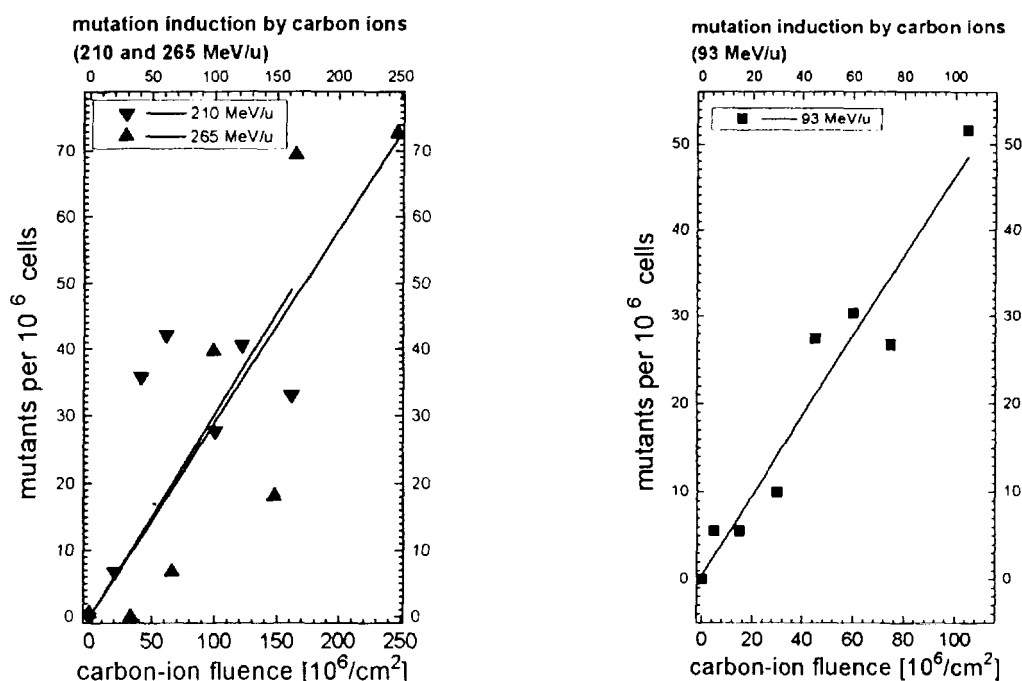

Fig. 3: Mutation induction by fast carbon ions

The molecular spectra of radiation induced HPRT mutants were analysed for the two high energies only. First the analysis was performed after 210 MeV/u, which - as shown in Fig. 1 - left no mutants with undetectable deletions (i.e. "no deletions" - also called "wild-type"

mutants) after subtraction of the background mutants. This was surprising, since one would expect the contribution of the large sparsely ionising penumbra present at these high energies to cause more very small deletions, which are typically caused by sparsely ionising radiation (e.g. X-rays). The second set of analysed carbon induced mutants, this time after 265 MeV/u, set this impression straight by revealing around 20% wild-type mutants after background correction (Fig. 4). The real portion of wild-type mutants caused by these fast carbon ions is probably somewhere between 0 and 20%.
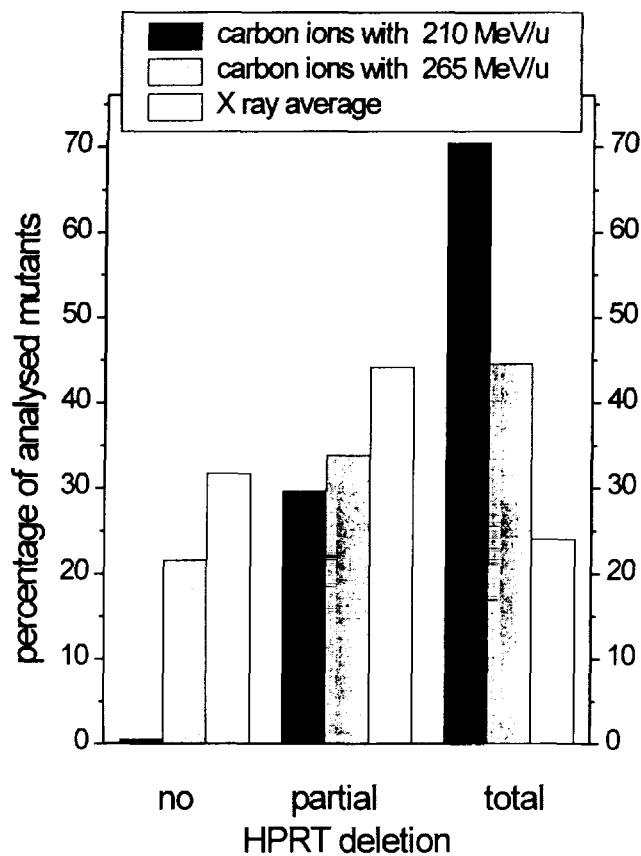

Fig. 4   Deletion-pattern distribution of the two carbon-ion experiments compared with the average of two X-ray experiments

D

Cell and Tissue Radiobiology

K. Ando (Chair)

Oral Presentations

1. Koichi Ando
(Nat. Inst. Rad. Science, Chiba, Japan)

   Mouse Skin Damages Caused by Fractionated Irradiation with Carbon Ions

2. Jürgen Debus
(Univers. Heidelberg, Germany)

   Conformal Radiotherapy with Volume-Scanned Carbon Ions - Relative Biological Effectiveness in the Rat Spinal Cord

3. Claudia Fournier
(GSI, Darmstadt, Germany)

   Human Fibroblasts as a Model for Healthy Tissue in Radiotherapy

4. Hiroshi Watanabe
(Jap. Atom. Res. Energ. Inst. , Takasaki, Japan)

   Influence of Penetration Controlled Irradiation with Charged Particles on Tobacco Pollen

5. L. Distel
(Univers. Erlangen-Nürnberg, Germany)

   First Biological Experiments at the Vertical Proton Beam

6. Milos Lokajicek
(Academy of Science, Prague, Czech Republic)

   Inactivation Mechanism of Different Radiation Kinds, Shapes of Survival Curves and Deviations from LQ Model

7. D. Choudhary
(Jawaharlal Nehru Univers., New Dehli, India)

   Effect of 45 MeV 7Li and 68 MeV ^{16}O Charged Particles on Biological Membranes

Posters

8. Martin Moosburger
(Ludwig-Max.-Univers. München, germany)

   Status of the Vertical Beam Facility at the Munich Tandem Accelerator

9. Mayank Srivastava
(Jawaharlal Nehru Univers., New Dehli, India)

   Effects of 45 MeV and 68 MeV Charged Particles on Microsomal Membrance Fluidity

10. A. Touati
(Univers. Paris 7 and 6, France)

    Experimental Determination of the Contribution of Carbon K-Ionizations to the RBE for Cell Inactivation by Ultrasoft X-Rays

11. Gianfranco Grossi
(Inst Sup. San. and INFN, Roma, Italy)

    Survival of Human Cells Exposed to Acute and Fractionated Doses of Low-Energy Protons

12. Daniel Zukowski
(Uni Mainz, Germany)

    Cellular Response of V79 Spheroids Exposed to High Energy Carbon Ions

13. Mirjam Fritsch
(Uni Erlangen, Germany)

    First Experiments at a Vertical Proton Beam

DE98F5447   *DE010813768*

Mouse skin damages caused by fractionated irradiation with carbon ions.

K.Ando[1], S.Koike, Chen YuJau, C.Ohira, K.Nojima, S.Ando, N.Kobayashi,
T.Ohbuchi, W.Shimizu and *T.Kanai
Space and Particle Radiation Science Research Group and *Division of accelerator
Physics, National Institute of Radiological Sciences, 9-1, Anagawa-4-chome, Inage-
ku, Chiba 263 Japan

Abstract
We have investigated carbon-dose responses of early and late skin damages after
daily fractionations to the mouse leg. Depilated legs were irradiated with 7
different positions within 290MeV/u carbon beams. Fractionation schedules were
1, 2, 4 and 8 daily fractions. Skin reaction was scored every other day for 32
days. Five highest scores in individual mice were averaged, and used as averaged
peak reaction. The isoeffect doses to produce an averaged peak skin reaction of
3.0 (moist desquamation) on dose-response curves were calculated with 95%
confidence limit. The isoeffect dose for control gamma rays constantly increased
with an increase in the number of fraction. The isoeffect doses in low LET carbon
ions of 14- and 20 keV/μm also increased up to 4 fractions, but did not increase
when 4 fractions increased to 8 fractions The saturation of isoeffect dose was
more prominently observed for 40 keV/μm in such that the isoeffect doses did not
change among 2, 4 and 8 fractions. The isoeffect doses for LET higher than 50
keV/μm were smaller than those for lower LET. However, the isoeffect doses for
50-,60-,80- and 100 keV/μm steadily increased with an increase in the number of
fraction and did not show any saturation up to 8 fractions. Relation between LET
and RBE was linear for all fractionation schedules. The slope of regression line in
4 fractions was steepest, and significantly ($P<0.05$) different from that in 1
fraction.

Materials and Methods
Mice
   C3H/He MsNrsf female mice aged 12-18 week old served for skin irradiation.
Animals were produced and maintained in the specific pathogen-free facilities.
Hairs on the right hind legs of mice were removed by applying a depilatory agent
(Shiseido, Tokyo) 7 to 8 days before irradiation. Mice irradiated
with γ rays were kept in the specific pathogen-free facilities while mice receiving
carbon beams were carried out to the accelerator facility shortly before irradiation.
Five mice for each irradiation scheme and a total of 1339 mice were used for whole
experiments.
Irradiation
   Carbon-12 ions were accelerated by HIMAC synchrotron up to 290 MeV/u.
Experiments were conducted in a room designed for biology experiments, using
horizontal beams with a dose rate of approximate 3 Gy/min. The beam was
perpendicularly spread by a thin lead and two wobbling magnets, which in turn
provided a uniform physical dose distribution for a circular field with a diameter
of 10 cm. For horizontal spread, an aluminum wedge filter designed by T.Kanai

(Radiation Research 147,78-85, 1997) was used and provided a 6-cm width SOBP. A physical dose declined to approximate 50 % when the irradiation position changed from the edge of proximal SOBP to distal SOBP. The LET of 290 MeV/u carbon ions was 14 keV/μm at the entrance of 6-cm SOBP, and gradually increased to 20 keV/μm along with 8-cm beam path. The proximal edge of the SOBP located at 9-cm path, and the LET at this position was 40 keV/μm. LET increased with beam path and reached to 200 keV/μm or over at 15-cm path that corresponded to distal falloff of SOBP. Irradiation field was made by simultaneous use of an iron collimator and a brass collimator. Depth position was adjusted by a Lucite range shifter. With pentobarbital anesthesia (50 mg per Kg) and taping, five mice were immobilized on a Lucite plate to place right hind legs in a rectangular field of 28- x 100-mm, and received either single or daily fractionated irradiation. The foot was excluded from irradiation field.

Reference beam was Cs-137 γ -ray with a dose rate of 1.6 Gy/min. FSD was 21 cm. A doughnut-shaped radiation field with 30 mm-rim was used to collimate the vertical beam. Daily fractionations employed an interval of 24$\pm$1 hours between fractions. Each fraction delivered an equal dose.

Endpoints and data analysis

Skin reactions of the irradiated legs were scored every other day according to a modified Aizawa's method, starting from Day 7 of initial irradiation up to Day 35. Scoring consists of 10 steps, ranging from 0.5 and 5.0. Five highest scores in an individual mouse were averaged. The averaged score was designated the averaged peak reaction. Relation between dose and the averaged peak reaction was fitted to a cubic polynomial. An isoeffect dose with 95% confidence limit was determined on a graph that possessed the averaged skin reaction on the x axis and dose on the y axis. An averaged peak reaction of 3.0 was used to calculate any isoeffect doses. For late skin damage measurement, two spots of Indian ink were intradermally tattooed prior to irradiation. Distances between the tattoo were measured once a month for up to one year. Percent shrinkage of skin was calculated by a formula 1- a/b where a and b were tattoo distance of post- and pre-irradiation, respectively.

Result

Animals were irradiated at 7 different positions within a carbon beam path, and therefore received 7 different LET. LET was adjusted for the skin at outer side of leg. LET ranging from 14- to 80 keV/μm completely penetrated the legs whereas 100 keV/μm stopped midway, leaving the inner side of leg skin intact. Skin reaction was detected as early as Day 7 of initial irradiation, and reached maximum between Day 14 and Day 25. Time course of skin reaction was similar to each other between 14 keV/μm and 100 keV/μm.

Dose responses for carbon ions and γ ray with 1, 2, 4 and 8 fractionated irradiation were obtained. The best fit to the dose responses was achieved by a cubic polynomial.

An isoeffect dose to produce skin score of 3.0 was calculated from these data, and plotted as a function of the number of fraction (Fig. 1). Isoeffect doses for γ ray increased with an increase in the number of fraction. Significant (p<0.05) difference was detected between any fractions; i.e., 1 versus 2 fractions, 2 versus 4

fractions, and 4 versus 8 fractions. Carbon ions of 14 keV/μm also increased its isoeffect dose when number of fraction increased from 1 to 2 as well as from 2 to 4 fractions ($p<0.05$). However, isoeffect doses of 14 keV/μm did not increase from 4 to 8 fractions and saturated, which was different from γ ray. Carbon ions of 20 keV/μm also showed the saturation of isoeffect dose between 4 and 8 fractions. Most prominent saturation was observed for 40 keV/μm in such that the isoeffect doses of 2,4 and 8 fractions were indistinguishable each other. In any LET stated above, the increase of fraction from 1 to 2 always increased ($p<0.05$) isoeffect doses. When LET further increased, the saturation of isoeffect dose disappeared. Isoeffect doses of 50 keV/μm increased with an increase in the number of fraction, and statistic significance ($p<0.05$) was detected between 1 and 4 fractions as well as between 2 and 8 fractions. In 60 keV/μm and 80 keV/μm, isoeffect doses significantly increased when the number of fraction increased from 1 to 2 as well as from 4 to 8. LET of 100 keV/μm showed a significant increase ($p<0.05$) of isoeffect dose between 4 and 8 fractions. For all LET except 50 keV/μm and 100 keV/μm, the isoeffect dose significantly increased when fractionation increased from 1 to 2. Significant increase of isoeffect dose from 2 to 4 fractions was observed only for γ ray, 14 keV/μm and 20 keV/μm.

Dose recovered during fractionation was calculated by (1) subtracting an isoeffect dose in the smaller number of fraction (i.e., Dm) from an isoeffect dose in the larger number of fraction (i.e., Dn), and (2) dividing the subtracted dose (i.e., Dn-Dm) by (n-m). Two fractions showed a peak at 40 keV/μm and the largest dependence on LET. The recovered dose in 4 fractions was largest for γ ray and decreased with an increase of LET. No peak was observed for 4 fractions. Eight fractions showed minimum recovered doses, and also the smallest dependence on LET.

RBE of carbon ions relative to γ ray was calculated for 1, 2, 4 and 8 fractions. Relation between LET and RBE was fitted to a linear regression. Correlation coefficient was 0.939, 0.986, 0.991 and 0.985 for 1, 2, 4 and 8 fractions, respectively. Slope of regression line was steepest for 4 fractions and shallowest for 1 fraction ($p<0.05$). Largest RBE was obtained at 4 fractions of 100 keV/μm (3.38) while smallest RBE was obtained at 2 fractions of 14 keV/μm (1.30).

- Data for late skin shrinkage will be presented in the workshop.

Discussion

It is unexpected that the isoeffect doses at low LET saturate between 4 and 8 fractions (Fig. 4). This implies that the survival curve of skin cells fit to the multitarget model that possess a shoulder at small doses. More puzzling is that the saturation disappears at higher LET of 50 keV/μm or over. The survival curves of skin cells may continuously bend downward with an increase of dose, a characteristic of linear-quadratic model. An alternative explanation for the increase of isoeffect dose is that skin cells irradiated with high LET repopulate during 8 days of fractionation. Skin cells do not repopulate during 4 days with a daily 3 Gy X ray, and that 0.5 Gy/fraction is required to compensate repopulation that occurs during 9 daily fractionation (Denekamp:Br.J.Radiol. 46, 381-387, 1973).

Fig.1
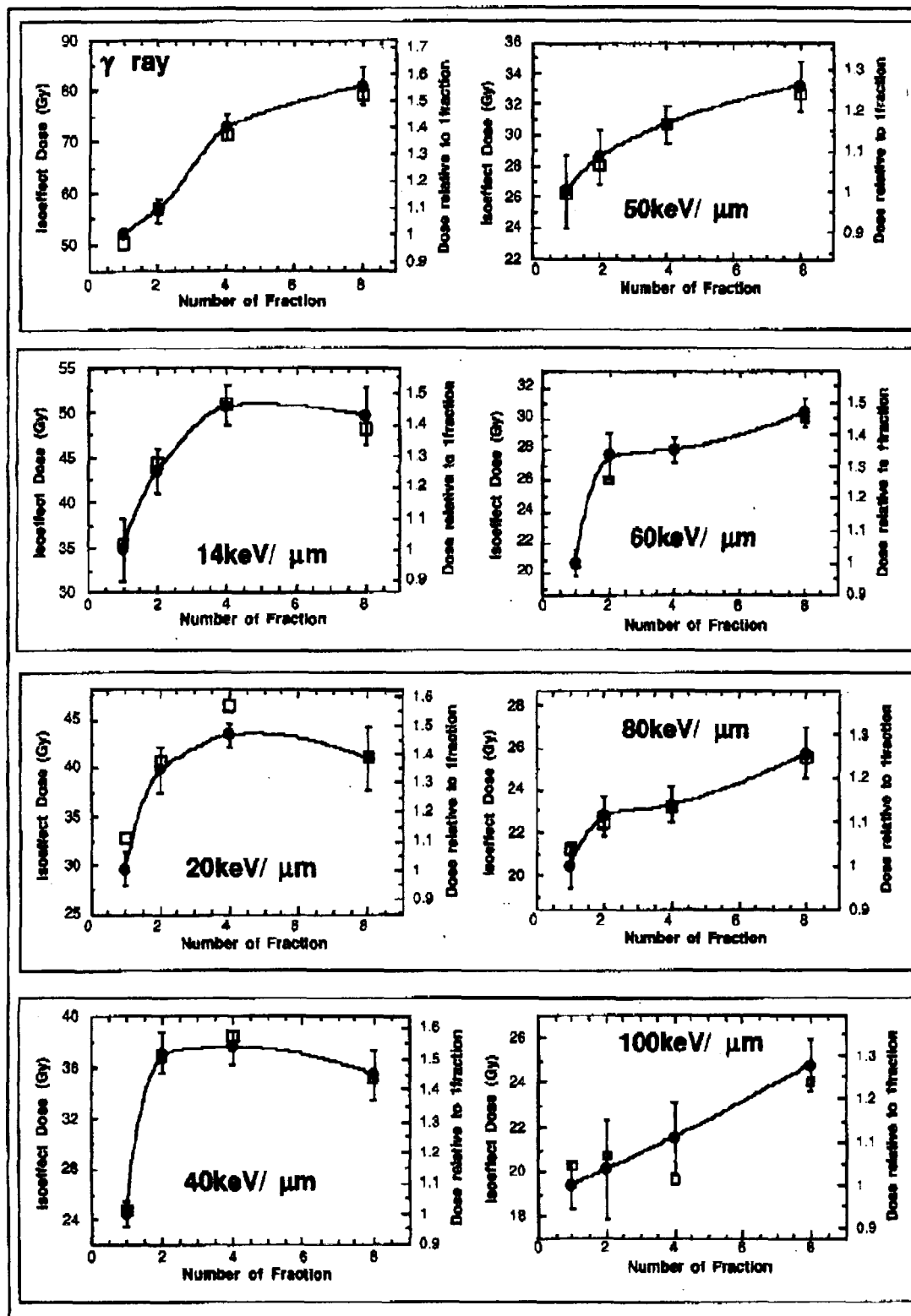
CONFORMAL RADIOTHERAPY WITH VOLUME SCANNED CARBON IONS - RELATIVE BIOLOGICAL EFFECTIVENESS IN THE RAT SPINAL CORD

Debus J*, Scholz M², Peschke P³, Jaeckel O³,
Haberer T, Hartmann G, Kraft G², Wannenmacher M*,

*University of Heidelberg, Germany and German Cancer Research Center, Heidelberg, Germany
²Gesellschaft für Schwerionenforschung, Darmstadt, Germany
³German Cancer Research Center, Department of Medical Physics, Heidelberg, Germany

Purpose / Objective: There are a number of facilites which plan to use conformal radiotherapy with three dimensionally scanned ions such as carbon ions. Comparative treatment planning has shown that this technique is capable to generate excellent physical dose distributions. The kowledge of the relative biological effectiveness (RBE) in different critical structures such as the spinal cord is essential for safe application of heavy ions. The RBE may be estimated by biological model calculation of heavy ion beam tissue interaction based on the known X-ray response. The aim of this study was to determine the RBE of carbon ion beams in the rat spinal cord and to examine the prediction of the biological model calculation.

Materials & Methods: All animals were treated with the beam delivery system which is used for clinical studies. The beam delivery for the heavy ions consists of a threedimensional raster scanning system with energy variation. Treatment planning was performed based on computed tomography data. A segment of 15 mm length of the upper cervical spinal cord was irradiated with 270 MeV/u carbon ions and in the mid of a 1 cm spread out bragg peak. We applied 1, 2 or 6 fractions on consecutive days under general anesthesia. The reference treatment was given with 15 MeV photons on a linear accelerator with the same field size. A total of 252 rats have been treated in five dose steps per treatment modality and six animals per group. The dose steps have been set according to the model calculations. Rats were followed up to 300 days after irradiation and scored for paresis. A logistic regression model was used to fit the observed tolerance data and to calculate the ED50 and corresponding RBE values.

Results: No acute deaths were observed. A slight weight loss was noted in the high dose groups as a consequence of radiation induced esophagitis. The median time to onset of paresis was 175 days and an earlier onset in animals treated with carbon ions was observed.
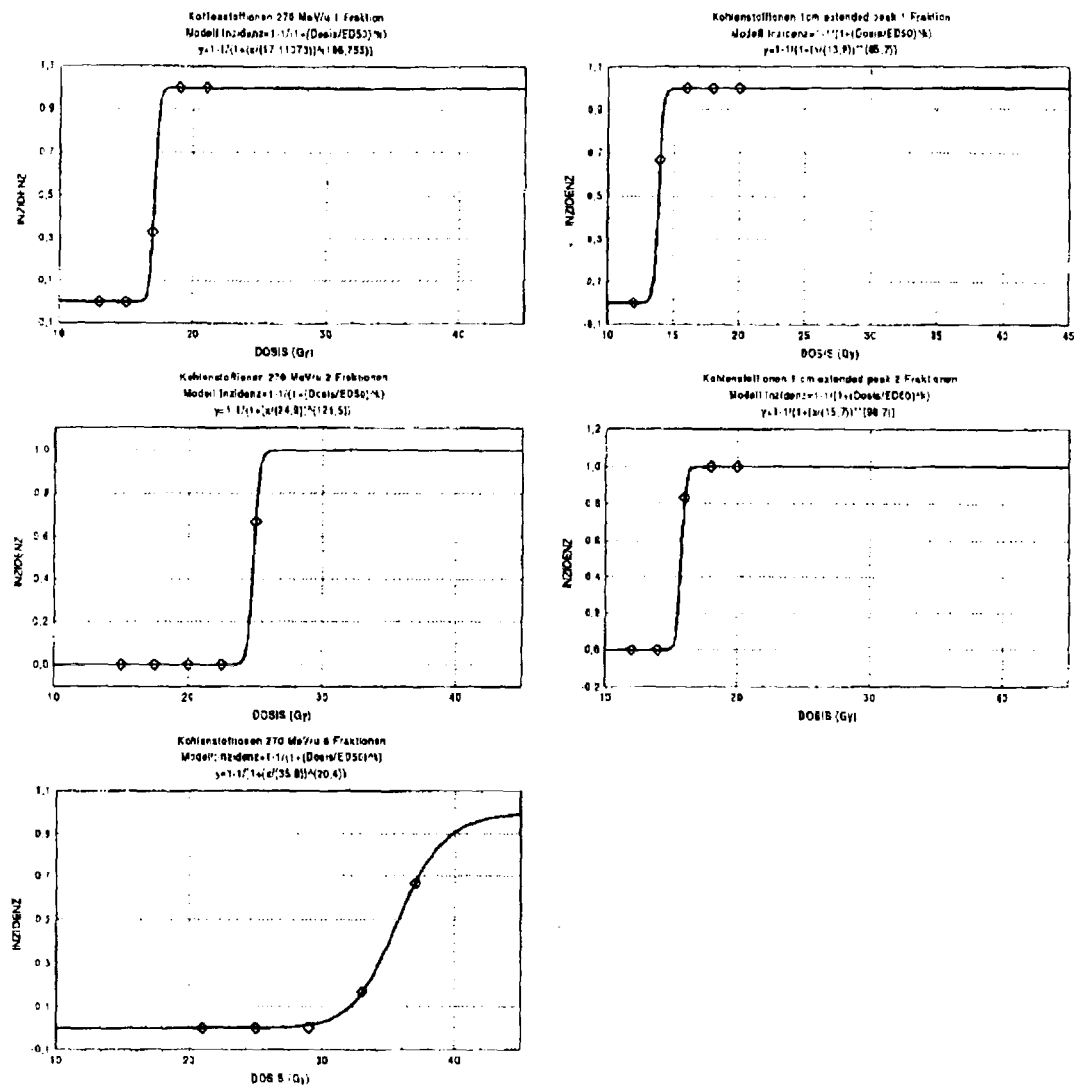
Fig. 1: Dose response for clinical myelopath for the different beam qualities.

Conclusion: The biological model calculation allows to estimate the carbon ion response of the ratspinal cord from photon sensitivity within the confidence limits of the experiment. A trend however can be detected for an underestimation of the RBE in the peak and an overestimation of the plateau region of the carbon ion beam. This results can serve as an guideline to set the RBE of the carbon beam of our clinical studies including patients with tumors at the base of skull. Furthermore we conclude from this experiments that the rasterscanning technique is feasible and reproducible.

DE98F5445

HUMAN FIBROBLASTS AS A MODEL
FOR HEALTHY TISSUE IN RADIOTHERAPY

C.Fournier, W. Kraft-Weyrather, G. Kraft

Gesellschaft für Schwerionenforschung, D-64291 Darmstadt

INTRODUCTION

The success of radiation tumortherapy is determinded by the relation of tumor inactivation and the amount of early and late damages in the healthy tissue.

In the context of a heavy ion tumortherapy, which will be realized at GSI- (Gesellschaft für Schwerionenforschung, Darmstadt) in cooperation with DKFZ (Deutsches Krebsforschungszentrum, Heidelberg) and Radiologische Klinik Heidelberg, human cells (a normal human foreskin-fibroblast strain AG 01522B, Coriell Institute, USA) were irradiated with carbon ions, which have been chosen for therapy. Human fibroblasts are a suitable model to investigate early and late radiation - induced damages because they are involved in any irradiation. They are not very specialized cells of the connective tissue and share many characteristics with other kinds of cells in the human body.

On the basis of survival experiments (x-ray, Carbon) the early damages of healthy tissue in the entrance channel of the beam and around the tumor are estimated. Increased differentiation and collagen secretion have been chosen to assess late effects. In vivo prematured differentiation as well as increased collagen secretion belong to a fibrotic reaction resulting after a stimulative response of tissue cells (1). Fibrosis is a late effect in several parenchymal tissues (lung, kidney, liver, skin). Fibrotic lesions often occur 3-12 months after exposure to radiation. Prematured differentiation was established by morphological features and increased collagen secretion was measured by labelling experiments.

SURVIVAL EXPERIMENTS

Contact-inhibited monolayer cell-cultures were irradiated in flasks and survival was deterimend in a colony-forming test. Experiments were performed with x-rays, carbon ions at high energy (200 MeV/u; LET 16.2 $keV/\mu m$) and at low energy (11 MeV/u; LET $153,5keV/\mu m$). Measured RBE_{10} values for carbon ions were 1.46 and 2.56 at energies of 200 MeV/u and 11 MeV/u, respectively (see fig.1).

In another experiment survival is determined by irradiating a stack of cell monolayers with carbon ions (max. 227 MeV/u) in a depth range from 0-150 mm. The tumor volume is supposed to be between 60-100 mm. In Fig. 2 dose and survival are shown as a function of penetration depth.

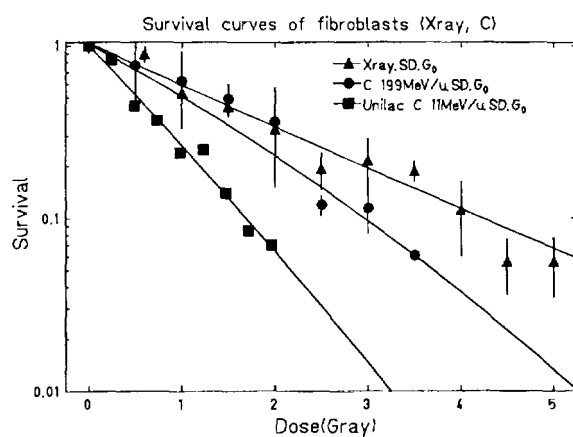Fig. 1   Survival curves of fibroblasts (G_0-cells) after irradiation with x-rays and carbon ions. Data are based on 2 experiments.
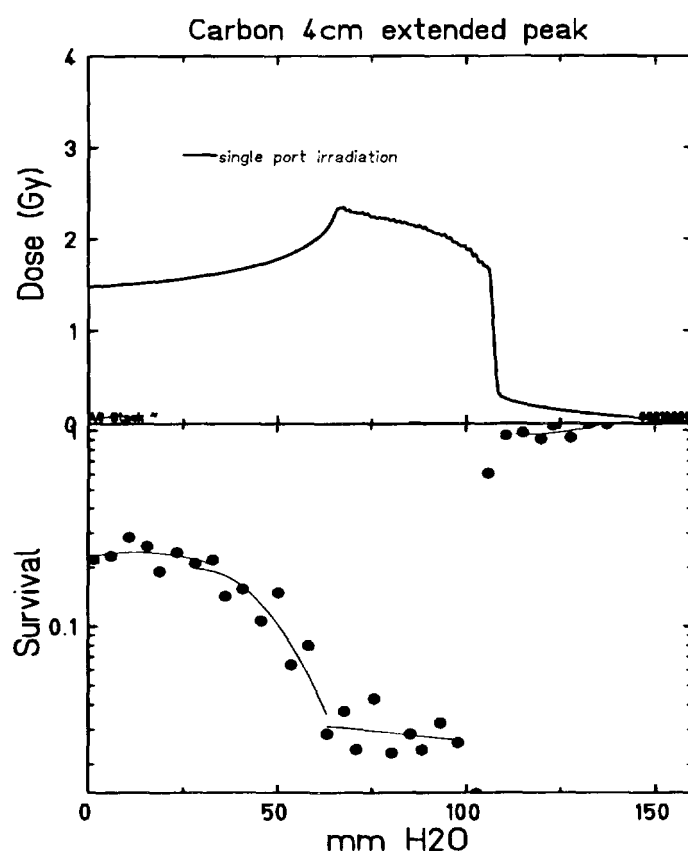

Fig.2   Survival of fibroblasts in relation to the penetration depth and the dose of carbon beam (max. 227 MeV/u).

MORPHOLOGICAL DIFFERENTIATION AND COLLAGEN SECRE-TION

Human skin fibroblasts differentiate in stages, which can be distinguished by morphological and biochemical features. They are divided into a mesenchymal stem cell-compartment, a mitotic progenitor-compartment (MFI, MFII, MFIII) and in a functioning fibrocyte compartment (PMFIV, PMFV, PMFVI). PMFVI is characterized by a specific capacity for the synthesis of interstitial collagen and other extracellular matrix components (2). Ionizing radiation has been shown to induce a premature terminal differentiation resulting in the enhanced acculmulation of postmitotic fibrocytes (3). The clinical manifestation of fibrosis corresponds to the increasing synthesis of interstitial collagen of PMFVI.

First experiments were performed with x-rays and low-energy carbon ions (11 MeV/u). Fibroblast cultures predominantly composed of progenitor-fibroblasts were seeded in sparse mass culture systems (8×10^2 cells per cm^2 for collagen secretion; 20 cells per cm^2 for morphological differentiation). 24h after seeding cells were irradiated. Total collagen synthesis was determined by the rate of incorporation of ^{35}S into pepsin resistant protein. Two weeks after irradiation cells show an increased collagen secretion correlating with prematured terminal differentiation.

REFERENCES

1. Rodemann, H.P. et al:*Kidney International* **49**, 32-36, 1996
2. Rodemann, H.P. et al:*J.Cell Sci.Suppl.* **10**, 115-130, 1988
3. Rodemann, H.P. et al:*Radiotherapy and Oncology* **35**, 83-90, 1995

INFLUENCE OF PENETRATION CONTROLLED IRRADIATION WITH CHARGED PARTICLES ON TOBACCO POLLEN

Hiroshi WATANABE[1], Atsushi TANAKA[2], Shigemitsu TANO[2] and Masayoshi INOUE[3]

1 *Department of Radiation Research for Environment and Resources, Japan Atomic Energy Research Institute, Takasaki, Gunma 370-12, Japan*
2 *Advanced Science Research Center, Japan Atomic Energy Research Institute, Takasaki, Gunma 370-12, Japan*
3 *Faculty of Agriculture, Kyoto Prefectural University, Kyoto 606, Japan*

Abstract

To investigate the effect of local irradiation on biological systems, an apparatus for penetration controlled irradiation with charged particles was set up. By comparison of ranges of 1.5 MeV/u He^{2+} between the theoretically calculated ranges and the practical ranges using RCD dosimeter, it was demonstrated that the range of particles could be controlled linearly by changing the distance from the beam window in the atmosphere to a target. In addition, the penetration controlled irradiation of tobacco pollen increased the frequency of 'leaky pollen'. The increased frequency of the leaky pollen suggests that a damage in the pollen envelope would be induced at the range-end.

Introduction

It is of great interest to understand the biological effects of low energy charged particles at the near end of particle range, especially for cell inactivation, mutagenesis and cell membrane damage. Concerning the energy deposition and the biological effects of charged particles, it has been reported that low energy particles were more effective for the inactivation of enzyme [1] or cells [2] where an increase of 10 to 30 % of cell inactivation was observed at the energy of around 100 keV/u. Furthermore, a gene transfer into rice cells, probably resulted from the increased permeability of cell membrane, was enhanced by shallow irradiation with 20-30 keV Ar ions [3]. Recently, W.Li et al. and H.Xie et al. reported that the inhibition of germination and survival of wheat seeds resulting from the implantation was stronger than those from the penetration [4,5]. Thus, the low energy charged particles appear to have specific features on the biological effects. Therefore, to investigate more detailed biological effects of the penetration controlled irradiation, we have constructed a new system for penetration controlled irradiation in the atmosphere, and established the technique of irradiation. From the irradiation of tobacco pollen, we found a characteristic effect of low energy charged particles on the envelop damage of pollen. This paper deals with the technique of irradiation and the biological effects of low energy charged particles penetrating partially to pollen.

Experimental

Irradiation system

An irradiation system was specially designed and installed on a beam line of 3MV tandem accelerator (TIARA, Takasaki). Fig. 1 shows a schematic diagram of the irradiation system. Ion beams are scanned at more than 6 X 100 mm by X-scanner. After passing through a slit of 5 X 90 mm, the scanned beams go out of the vacuum chamber through 6 X 101 mm beam window made of a kapton film of 7.5 μm thickness. Whole beam currents after the slit are

monitored by Faraday cup. Biological samples are irradiated on a hexagonal sample holder column which can be positioned at a given distance of 5 mm to 48 mm by 1 mm stepwise from the beam window. Uniform irradiation of sample was performed by moving up and down the sample holder column at a speed of 35 mm/sec.
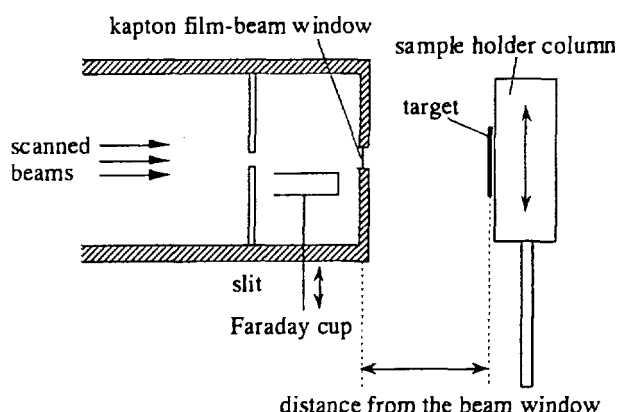

Fig.1 Schematic diagram of irradiation system connected to a beam line of 3MV tandem accelerator

Irradiation methods and samples

1.5 MeV/u He^{2+} ions were used in the experiment. Fluence estimated from beam currents was in accord with that measured by CR-39 film track detector (100 μm thickness) with an error of $\pm$ 3 %. Theoretical energy loss of ion beams was calculated by ELOSS code[6].

Tobacco dry pollen (*Nicotiana tabacum* L. cv Bright Yellow 4) was monolayered on a plastic plate and irradiated with He ions at the different distances from the beam window. The irradiated pollen was stained with 1 % aceto-carmine solution, and a frequency of leaky pollen whose cytoplasm leaked out due to the destruction of the envelope, was measured under an optical microscope. 300-900 pollen was used for each measurement. For the sectional observation of pollen envelope, dry pollen put on an adhesive tape was cut with a fine razor, shadowed with golden, and observed by the scanning electron microscope.

Results and Discussion

Penetration control

To estimate the range of He^{2+} ions, the energies and the stopping powers as a function of distance from the beam window were calculated by the ELOSS code. The maximum range in the atmosphere was estimated to be 39.7 mm. The range of ions at each distance from the beam window was ascertained experimentally by Radiochromic dosimeter (RCD, 51 μm thickness)
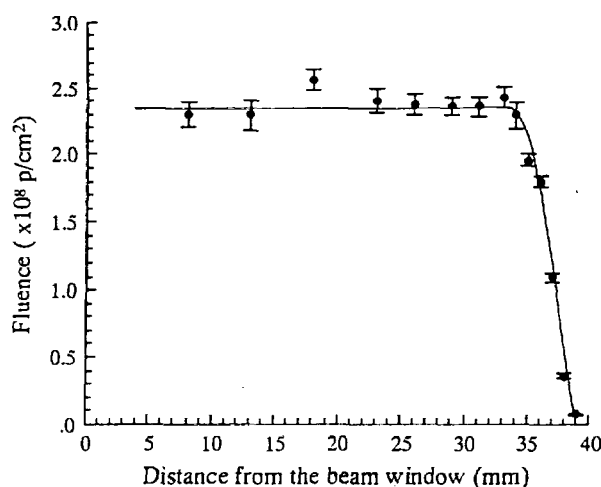

Fig.2 Change of the fluence as a function of distance from the beam window measured by CR-39 track detector Error bars are the standard errors.

which could detect even low energy radiation with several eV. The maximum range of He ions in RCD film was 40 μm and the each range at the different distances agreed with the calculated value. The fluence as a function of distance from the bean window was measured by CR-39. As shown in Fig.2, the constant fluence was observed up to 34 mm-distance from the beam window, but the fluence decreased at the near end of the range. The maximum range obtained from the results of CR-39 was 1 mm distance shorter than the calculated range, because it was difficult to detect the ion tracks by CR-39 when

the beam-range in CR-39 is shorter than 1 μm that corresponds to roughly 1 mm-distance in the atmosphere. Thus, using this system, the penetration depth of ions can be controlled by 1 μm accuracy in a range of 1 to 30 μm depth.

Effect of penetration controlled irradiation on pollen

Tobacco dry pollen is 20.2 ± 1.5 μm in diameter and has the envelop of 1.0 ± 0.1 μm thickness. When the irradiated dry pollen was stained with the aceto-carmine solution, so-called 'leaky pollen' was observed. Fig.3 shows a typical leaky pollen of which the internal substance leaks out through an opening of the envelope. To examine the effect of penetration-depth on the
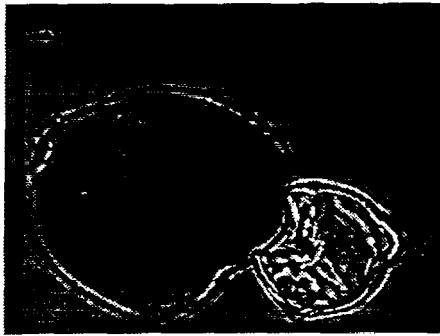

Fig.3 A typical leaky pollen stained with the aceto-carmine solution
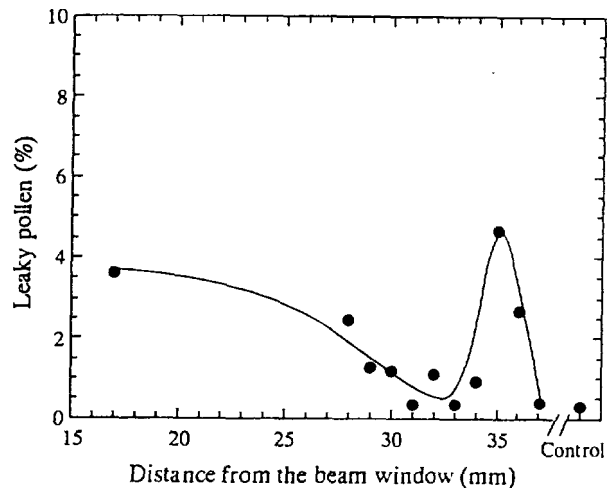
Fig.4 The leaky pollen induced by ion beam irradiation as a function of distance from the beam window
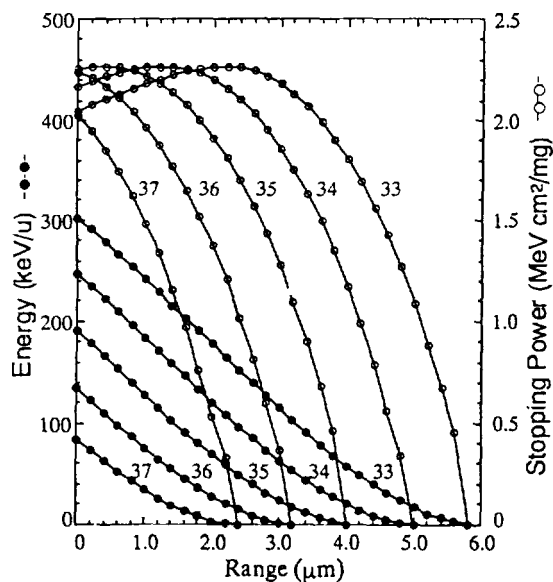
Fig.5 Changes of the energies and the stopping powers of 1.5 MeV/u He2+ in the biological target calculated by ELOSS code at given distances (numbers in figures; mm) from the beam window

induction of the leaky pollen, pollen was irradiated with He ions by changing the distance from the beam window (Fig.4). The frequency of the leaky pollen decreased with increasing the distance from 17 mm to 32 mm, whereas a peak of the frequency was observed at a distance of 35 mm. If it is assumed that the formation of the leaky pollen depends on the total energy deposited in the pollen, no any peak should be observed in the frequency of leaky pollen as a function of the distance from the beam window, since the total energy deposited in pollen decreased with increasing distance as shown in Fig.5. In addition, the energies deposited in pollen envelope (about 1 μm thickness) are similar among the distances at 33, 34 and 35 mm. Therefore, this specific phenomenon cannot be accounted for due to the total energy deposited in pollen and pollen envelope, suggesting that any factor(s) other

than the electron stopping may contribute to the breakage of the pollen envelope. A peak of nuclear stopping at 35 mm distance is in 3.8 μm depth from the pollen surface, and the overlap of each peak at 34 and 36 mm is not observed, although the depth is over the thickness of pollen envelope. Thus it is difficult to explain the sharp peak of leaky pollen due to only the contribution of nuclear stopping. Therefore, we should consider the combined action of electron stopping and nuclear stopping. Since the energy deposition due to electron stopping is much larger than that due to nuclear stopping, the pollen envelope would be primarily damaged by the energy deposition due to electrons. The damaged envelope might be disrupted efficiently by the action of nuclear stopping as a trigger.

Table 1 Survival and variation of plants derived from the crosses with pollen irradiated by He ions at 4 μm depth

Experiment	Fluence (p/cm^2)	Fertile capsules / crossed flower	Seeds / capsule	Survival rate (%)	Variation rate (%)
Control	0	4 / 4	320	94	8
He-1	3.8x10^9	5 / 5	85	93	12
He-2	1.1x10^{10}	10 / 10	66	90	11

Table 1 shows the biological effects of depth controlled irradiation. A number of seeds per capsule decreased significantly with irradiation, while the survival rate was not so influenced. In addition, the variation rate was 40-50 % higher than non-irradiation, suggesting that the particle irradiation at 4 μm depth may induce genetic change directly or indirectly. Concerning the biological effect of low energy particles, many problems remain unsolved. The new apparatus presented in this paper will be available to investigate the biological effects of the controlled penetration of charged particles.

References

[1] H.M.A. Al-Shaibani and D.E. Watt, Proc. 6th Symp. on Microdosimetry, eds J.Booz and H.G. Ebert (Brussels:CEC) (1978) p. 949

[2] E. Schneider, M. Kost and M. Schäfer, Radiat. Prot. Dosimetry 31(1/4) (1990) 291.

[3] Z.Yu, J.Yang, Y.Wu, B.Cheng, J.He and Y.Huo, Nucl.Instr.Meth. B 80/81 (1993) 1328.

[4] W.Li, Z.Wei, H.Xie, Q.Li, G.Han, B.Dang, G.Zhou, H.Yang, L.Wang and Q.Gao, J. Radiat. Res. & Radiat. Proces., 13(3) (1995) 167

[5] H.Xie, Z.Wei, W.Li, Q.Li, B.Dang, G.Han, J.Zhang and Y.Hu, J. Radiat. Res. & Radiat. Proces., 14(1) (1996) 50

[6] K. Hata and H. Baba, JAERI-M, (1988) 88

First biological experiments at a vertical proton beam

L. Distel, B. Distel, B. Rößner, G. Schwotzer, R. Sauer
Klinik für Strahlentherapie, Universität Erlangen-Nürnberg

W. Eyrich, M. Fritsch, A. Teufel
Physikalisches Institut, Universität Erlangen-Nürnberg

J. Besserer, J. de Boer, M. Moosburger, P. Quicken
Sektion Physik, Ludwig-Maximillian-Universität München

Abstract:

At the tandem accelerator laboratories in Munich and Erlangen vertical beamlines were installed last year. The advantage of a vertical beamline is that cells can be irradiated in a medium at 37°C and with simultaneous gassing, therefore also in physiological conditions.

First experiments were carried out at the accelerator in Munich with a proton energy of 25MeV. Chinese Hamster cells B14 were irradiated in Petri dishes where the base was of 1mm polystyrol or 2μm hostaphan foil.

The cell survival was measured by the cell survival assay and the repopulation of the colonies by the total colony volume.

A solution of DNA with protein was irradiated to study DNA double strand breaks by constant field gel electrophoresis and DNA protein crosslinks by the nitrocellulose filter assay.

For cell survival, total colony volume and DNA double-strand breaks X-rays and protons gave corresponding results, while with protons, higher yields of DNA-protein crosslinks were observed than with X-rays.

Introduction:

At the present time a limited (1-5) set of cell survival data and the relative biological effectiveness in dependence of the linear energy transfer (LET) is provided. All investigations were carried out at horizontal beamlines. A disadvantage of the horizontal beamline is that it is not possible to irradiate cells under physiological conditions, because the flasks (1), petri dishes (2-5) or membranes with adsorbed cells (6,7) have to be put in a vertical position and the cells can't be in a medium during irradiation.

We investigated the effects induced by a 25MeV proton beam in comparison to X-rays. Generally it is accepted, that a beam of this energy induces a similar effect to X-rays. Therefore, we measured the cell survival and the total colony volume in a cell survival assay.

Address for correspondence: L. Distel, Klinik für Strahlentherapie of the University Erlangen-Nürnberg, Universitätsstr. 27, 91054 Erlangen, Germany

DNA double strand breaks and DNA-Protein crosslinks were measured in a highly reproducible in vitro system, where DNA was irradiated in solution together with protein. The excess of the protein was 10 times the mass of DNA and scavenged most of the radicals. In these conditions it should be possible to find out slight differences between the effects of 25 MeV protons and X-rays.

Materials and Methods:

Beam. A vertical beamline with an exit window of 6 cm was used (fig. 1). The samples were irradiated with 25MeV protons $(2.2\text{keV}\cdot\mu\text{m}^{-1})$. Details are described in an accompanying abstract (8)

Cell survival assay. Asynchronous Chinese Hamster B14 cells were grown in MEM medium with Hanks salts containing 10% newborn calf serum. Cells were seeded 4 hours prior to irradiation in petri dishes with a base of 1mm polystyrol or 2μm hostaphan foil. In the petri dishes with a polystyrol base the cell survival was done directly. In petri dishes with hostaphan foil 50000 cells per dish were seeded, cells were irradiated and a serum free medium was added for 14 hours. Afterwards cells were trypsinysed and seeded in polystyrol petri dishes at appropriate numbers.
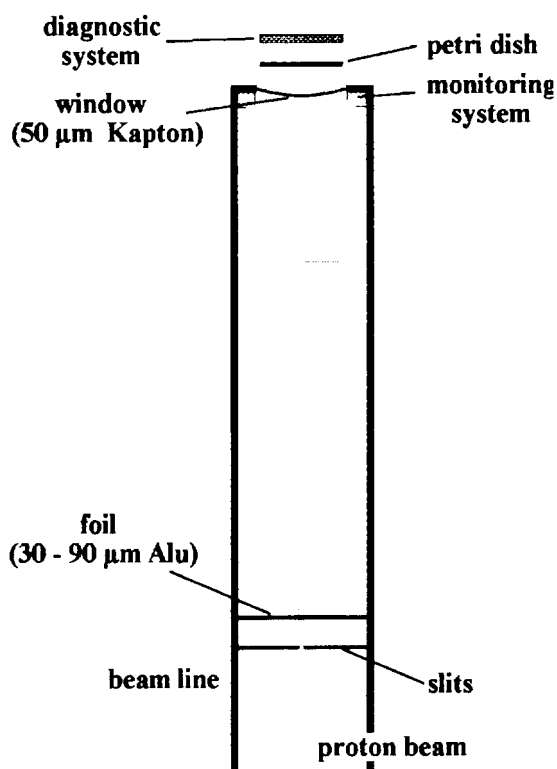
figure 1: Drawing of the beamline

Automatic colony analysing machine (ACAM). Before analysing the colonies were dyed for 30 minutes by methylene blue and washed 3 times with tap water followed by a washing step with deionized water. The petri dishes were dried in air and placed into the ACAM, where the petri dish was illuminated by LED's and photographed by a CCD camera. The data were transferred to a PC and analysed by software developed by the Institut für Nachrichtentechnik of the University Erlangen (9).

The ACAM does the scoring of the colonies and analyses the total volume of all colonies. The total colony volume (TCV) is the cell survival combined with the change of the numbers of cells in the colonies and is the same as the average volume of the colonies (10). The TCV is a measure of the repopulation of the colonies combined with the reproductive death of the cells.

Colonies which lay very close together or have grown in the same region, have to be separated for the scoring. For the analysing of the total colony volume the optical density of the colonies has to be integrated.

DNA double-stand breaks and DNA-protein crosslinks 0.1mg/ml highly poly-merized double stranded DNA from calf thymus with an average molecular weight of 16×10^6 Da from Calbiochem (Bad Soden, Germany) and $1mg \cdot ml^{-1}$ lyophilized bovine serum albumin (BSA) (Boehringer GmbH, Mannheim) or $0.1mg \cdot ml^{-1}$ histones from calf thymus (Sigma, St. Louis) were irradiated (200kV, 20mA and 2mm Al) in 10^{-2} mol·dm^{-3} phosphate buffer pH 7. Double-strand breaks were measured by constant field gel electrophoresis described in (11).

Nitrocellulose filter assay. The DNA- protein (500µl) samples were diluted with 5500µl of 1mol dm^{-3} NaCl, 10mmol dm^{-3} Tris and 10mmol dm^{-3} EDTA at pH7.2. Then 2 ml of the diluted sample were pipetted onto the filter and drained slowly into test tubes. The optical density of the filtrates and references were measured at 260nm and thus the DNA contents of the filtrates were determined. The binding of the protein to the filter was proved by testing the filtrate with Coomassie Brilliant Blue G-250.

Mathematical model for DNA-protein crosslinks. A binomial distribution of crosslinks on one DNA-molecule was assumed. By the high number of DNA-protein crosslinks(v) induced by dose (D) and the relatively low probability for a DNA-protein crosslink per DNA-molecule $\left(\frac{1}{m}\right)$, the binomial distribution was approximated by a Poisson distribution.

$$(1) \qquad P(X \geq 1) = 1 - \exp\left(-\frac{v \cdot D}{(\alpha \cdot D + \beta \cdot D^2 + 1) \cdot m}\right)$$

Since the number of double-strand breaks is measured by electrophoresis ($Z_{DSB} = \alpha \cdot D + \beta \cdot D^2$) and DNA-protein crosslinks are estimated by the nitrocellulose filter assay, the DNA-protein crosslinks (v) per dose can be calculated according to equation 1 (11).

Results:

Cell survival. The cell survival curves were fitted according the linear quadratic equation $S = \exp -(\alpha \cdot D + \beta \cdot D^2)$. The survival (S) of the cells irradiated with protons (α=0.166, β=0.027) was quite similar to the survival of cells irradiated with X-rays (α=0.157, β=0.027). The cells irradiated on Mylar folie and plated after a time delay of 14 hours were identical radiosensitive (α=0.166, β=0.029). The total colony volume (TCV) decreased more than the cell survival, especially at higher doses.

DNA double-stand breaks and DNA-protein crosslinks The yield of the DNA double-strand breaks induced by protons were identically with the yield of X-rays.

However the formation of DNA-protein crosslinks was about twice as high as for X-rays.
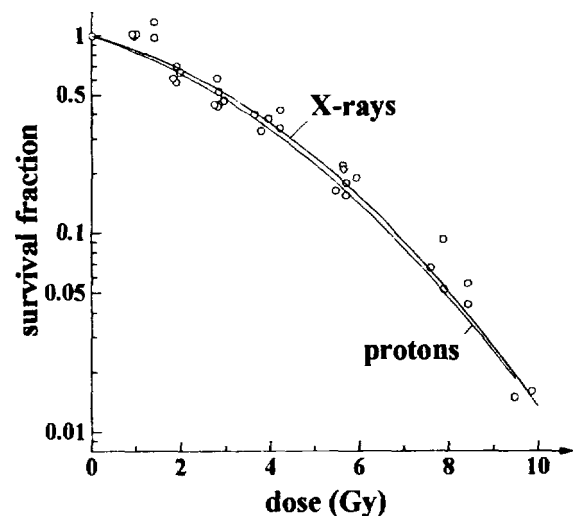

figure 2: cell survival, each point represents one petri dish

Discussion:

The vertical beam provides a good method to irradiate cells with protons under physiological conditions. The survival of cells and the TCV after proton irradiation were according to the values expected in the range of X-rays (1). The relative biological efficiency (RBE) was for cell survival and TCV 1. The cells plated with a delay of 14h had a similar survival to the cells without plating.

We did find comparable yields of proton and X-ray induced double-strand breaks. If double strand breaks are measured by the constant field gel electrophoresis, the broken DNA pieces are detected. But the gel electrophoresis has only a limited resolution of the DNA length. We have a high resolution from 50kBp to about 500Bp. We cannot detect short DNA pieces of some Bp until about 100Bp . So by our method it is not possible to assess the quality of the double strand breaks or two double strand breaks close together.

The proton induced DNA-protein crosslinks were about double the yield of the X-ray induced double-strand breaks. We propose that the DNA-protein crosslinks are formed by radical-radical reactions. A precondition to get crosslinks in the presence of air is that the DNA and protein lay very close together and that both molecules are attacked by radicals at the same time. Further the radical-radical reaction must be faster than the reaction of oxygen with the molecules. The 25MeV protons, are only slightly denser ionising than X-rays and induce such an increased yield of DNA-protein crosslinks.

We conclude that even at a proton energy where the cell survival and the total colony volume corresponds very well with X-ray effects, basic effects like DNA double-strand breaks and DNA-protein crosslinks may be changed. Whereby it is not clear in this study whether the double strand breaks are unchanged or changed in a way which could not be detected by the method used.

References:

1.   Bettega D. et al., Relative Biological Effectiveness for Protons of Energies up to 31 MeV, Radiat. Res. 1979, 77, 85

2.   Perris et al., Biological effectiveness of low energy protons. I. Survival of Chinese hamster cells, Int. J. Radiat. Biol., 1986, 50, 6, 1093

3.   Belli M. et al., Inactivation and mutation induction in V79 cells by low energy protons: reevaluation of the results at the LNL facility, Int. J. Radiat. Biol., 1993 63, 3, 331

4.   Goodhead D. et al., Direct comparison between protons and alpha-particles of the same LET: I. Irradiation methods and inactivation of asynchronous V79, HeLa and C3H 10T½ cells, Int. J. Radiat. Biol.,1992, 61, 5, 611

5.   Distel et al., Biological effectiveness of protons on mammalian cells, in Advances in Hadron Therapy edited by U. Amaldi, B. Larsson and Y. Lemoigne, Elsvier Science, Amsterdam, (in press)

6.   Folkard M., Inactivation of V79 cells by low-energy protons, deuterons and helium-3 ions Int. J. Radiat. Biol., 1996, 69, 6, 729

7.   Prise et al., The irradiation of V79 mammalian cells by protons with energies below 2 MeV. Part II. Measurement of oxygen enhancement ratios and DNA damage, Int. J. Radiat. Biol., 1990, 58, 2, 261

8.   Moosburger et al., Status of the Vertical Beam Facility at the Munich Tandem Accelerator, this report.

9.   Ficker M., Thesis Uni. Erlangen Automatische Erkennung und Auswertung von Zellkolonien am PC, 1992

10.   Distel L u. H. Schüssler, Koloniegröße und Gesamtzellvolumen als empfindliche Low-dose-Parameter, Strahlentherapie und Onkologie, 1995, 171, I, 52

11.   Distel L. and H. Schuessler, The effect of serum albumin on the radiolysis of DNA studied by constant field electrophoresis and compared to alterations caused by low molecular weight OH scavengers, Int. J. Radiat. Biol. 71, 401-412, (1997)

12.   Distel et al, Oxygen decides: double-strand breaks or DNA-protein crosslinks, Proceedings of Radiation Damage to DNA, in Press.

12 HUG. '97 11:05 4228212?

DE98F5441

Cell and Tissue Radiobiology D6

Inactivation mechanism of different radiation kinds, shapes of survival curves and deviations from LQ model

M. Lokajíček, J. Polák, K. Prokeš
Institute of Physics, Academy of Sciences, CZ-18040 Praha 8, Czech Republic
Department of Oncology, Charles University, CZ-12008 Praha 2, Czech Republic

Cumulative radiation effect (in fractionation radiotherapy) is given by two factors: inactivation efficiency to individual cells and proliferation ability of corresponding tissue. Rather detailed knowledge of both these factors for concerned tumour and normal cells and tissues is required if radiotherapy approaches in individual treatment cases are to be actually optimized.

The problem may be, however, hardly solved until a sufficiently detailed model simulation of corresponding processes is not found. Main deficiency in all contemporary attempts may be seen in that they are generally based on the so called linear-quadratic (LQ) model; i.e., the survival cell ratio is practically always assumed to be represented by a simple parabolic dependence in a semi-logarithmic graph:

$$s(d) = e^{-h(d)} \tag{1}$$

where

$$h(d) = \alpha d + \beta d^2 . \tag{2}$$

The positive parameters α and β have been related as a rule to one-hit and two-hits effects according to the interpretation proposed earlier e.g. in Ref. [1] for low-LET radiation kinds. However, many facts indicate that there are significant deviations of survival curves from such a simple behaviour practically for all kinds of radiation.

Then of course, the use of the LQ model in simulating cumulative radiation effect in tissues may be misleading. And any efficient optimization of fractionation courses in radiotherapy may be practically impossible until more detailed characteristics of survival curves in different cases are found.

First we will show with the help of a theoretical analysis that significant deviations from the LQ model must necessarily exist for any radiation of higher LET, e.g, in the range region of protons and other ions: Let us assume that the LET quality of radiation is characterized by average number h of hits in individual cells at a unit dose; i.e., the average number of hits in a cell at a dose D is given by

$$n_h = hD . \tag{3}$$

The higher LET the less is the value of h. The probability of hitting a given cell just k-times equals then

$$P_k = \frac{n_h^k}{k!} e^{-n_h} . \tag{4}$$

as the distribution of hits over a cell population may be regarded as Poissonian.

Let us assume now that the probability of inactivation at different hit numbers equals p_k. It is then possible to write

$$h(d) = -lg(1 - \Sigma_k P_k p_k) = \alpha d + \beta d^2 + \gamma d^3 + ... \tag{5}$$

where

$$\alpha = hp_1 , \tag{6}$$

$$\beta = \frac{h^2}{2}(p_2 - 2p_1) , \tag{7}$$

$$\gamma = \frac{h^3}{6}(p_3 + 3(p_1 - p_2)) , \tag{8}$$

1

and similarly for higher terms in the given Taylor series (5).

It is immediately evident that the LQ model may be justified only if

$$p_2 \gg p_1 \tag{9}$$

and higher terms in the series may be neglected. However, if one assumes that it holds for all $k > 0$

$$p_{k+1} \geq p_k \tag{10}$$

and further

$$p_k \leq 1 \tag{11}$$

significant deviations from the LQ shape must exist when

$$p_1 > 0.5 . \tag{12}$$

In such a case the even terms in the Taylor series should be mostly negative.

The experimental data concerning the survival curves in different parts of Brag peaks of protons and other ions (see e.g. [2, 3]) seem to agree with the preceeding theoretical analysis. However, there are other experimental data showing important deviations from the LQ model, too.

As shown in recent experiments (see e.g. [4]) significant deviations exist in the region of small doses for low-LET radiation; smaller doses may be more effective than some a little higher doses. This phenomenon may be interpreted as a consequence of the fact that the cell repair system must be triggered by hitting another part of a given cell; otherwise, it does not work. The survival curve may be then expressed in the form

$$s(d) = e^{-v_i d} e^{-V d} + (1 - e^{-v_i d}) e^{-v d} \tag{13}$$

where v_i characterizes the volume of a triggering center and V, resp. v, the sensitive volumes for inactivation without, resp. with, working repair system.

Significant deviations from the LQ formula have been evident also in experiments performed already earlier with negative pions [5] as it was reported for the fist time in [6]. In the given experiments the cumulative effect of pions on mouse skin was studied under different fractionation schemes; see Fig. 1.

It is necessary to assume that the final effect of negative pions consists of two components: the effect of heavy nuclear fragments and that of secondary electrons hitting also more distant cells. The resulting survival curve may be then written as

$$s(d) = 1 - A_f - A_e + A_f A_e \tag{14}$$

where

$$A_f = (1 - e^{-h_f d})(1 - s_f(d)) , \tag{15}$$

$$A_e = (1 - e^{-h_e d})(1 - s_e(d)) \tag{16}$$

and h_f (resp. h_e) is the average number of cell hits (at unit dose) by fragments (resp. by electrons). The functions $s_f(d)$ and $s_e(d)$ represents then survival ratios corresponding to individual radiation kinds.

The original analysis [6] were performed under some limiting conditions as individual survival curves were allowed to exhibit very smooth behaviour only. The preceding theoretical analysis as well as the behaviour of low-LET radiation at small doses require, however, to use more general

formulas, which has been respected in a new more detailed analysis of the mentioned experiments with negative pions.

In this analysis the survival curves for nuclear fragments has been described with the help of formula

$$\nu(d) = e^{-(\alpha d + \beta d^2 + \gamma d^3 + \delta d^4 + \varepsilon d^5)} \tag{17}$$

and survival curves for electrons by the formula (13). By fitting the corresponding experimental data the following numerical values of individual free parameters have been obtained. For nuclear fragments:

$$\alpha = 0,225, \quad \beta = -0,0041, \quad \gamma = 0,0062,$$
$$\delta = -0,49.10^{-3}, \quad \varepsilon = 0,11.10^{-4}; \tag{18}$$

for secondary electrons:

$$\nu_c = 0,110, \quad V = 0,300, \quad v = 0,0040. \tag{19}$$

Fitted theoretical curves together with experimental points are shown in Fig. 1. The corresponding survival curves are represented in Fig. 2. However,the survival ratios for electrons do not correspond to doses indicated in the graph but is much smaller doses corresponding to the fraction of energy transferred by these particles. Similar behaviour should be expected in Brag regions of protons and especially of heavier ions.

It follows from the preceding analysis that the survival curves may differ from the LQ shape rather significantly. These deviations cannot be neglected if one should understand an actual role of proliferation processes in influencing the cumulative biological effect in fractionated irradiation (see e.g. [7]).

References

[1] K.H.Chadwick, H.P.Leenhouts: A molecular theory of cell survival; Phys. Med. Biol. 13 (1973), 78-87.

[2] M.Belli et al.: Inactivation and mutation induction in V79 cells by low energy protons: re-evaluation of the results at the LNL facility; Int. J. Radiat. Biol. 63 (1993), 331-7.

[3] M.Belli et al.: Inactivation Induced by deuterons of various LET in V79 cells; Radiation Protection Dosimetry 52 (1994), 305-10.

[4] B.Marples, M.C.Joiner: The response of chinese hamster V79 cells to low radiation doses: Evidence of enhanced sensitivity of the whole cell population. Rad. Research 133 (1993), 41-51.

[5] D.J.Chaplin et al.: Int. J. Radiation Oncology Biol. Phys. 12 (1987), No. 8, 1199-208.

[6] M.Lokajíček: The shape of survival curves for pions and X-rays in a living tissue; research report F19-89-239, JINR, Dubna 1989.

[7] M.Lokajíček et al.: Deviations of survival curves from the LQ-shape and cumulative effect in fractionation; Advances in Hadron Therapy (eds. U.Amaldi et al.), Elsevier Science B.V., in press.

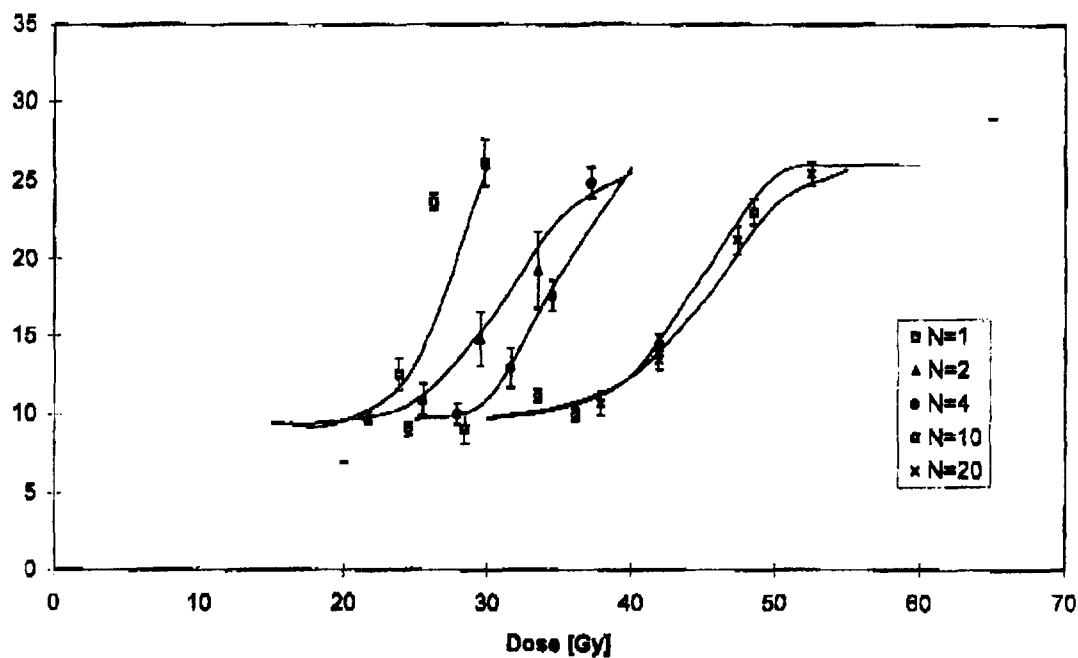**Fig. 1:** Mouse skin irradiated by negative pions.
Experimental data taken from [5]; full lines represent theoretical fits
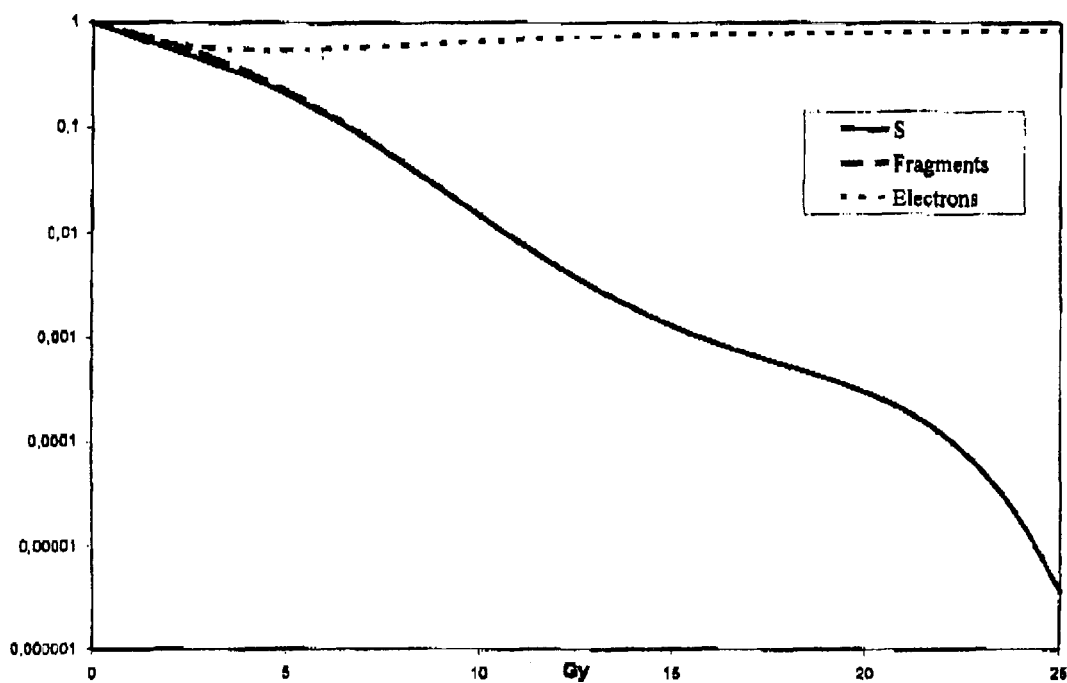for parameter values given in text.

Fig. 2: Survival curves derived from experimental data shown in Fig. 1.

Effect of 45 MeV ^{7}Li and 68 MeV ^{16}O charged particles on biological membranes

D. Choudhary[1], M. Srivastava[1], A. Sarma[2] and R. K. Kale[1]

[1]Radiation Biology Laboratory, School of Life Sciences
Jawaharlal Nehru University, New Delhi 110067, INDIA
[2]Nuclear Science Centre, Aruna Asaf Ali Road
New Delhi 110067, INDIA

There is growing interest in the radiobiological studies with high LET radiation due to its application in radiation therapy of cancer and importance in radioprotection especially in manned space flights. Extensive work has been carried out in DNA damage to understand the detrimental effect of high LET radiation. However apart from DNA, cellular membranes are also considered to be critical targets of radiation actions (Alper, 1968; Obioha et al., 1984). It has been suggested that the damage to membrane organization is an initial step in triggering cell death (Kerr et al., 1972). A good correlation has been observed between impaired membrane damage and loss of colony forming ability in cells, the breakdown of nuclear membrane and chromosomal condensation and damage to the organization of mitotic spindles, interphase death in nonproliferating cells and the disorganization of membrane system (Sato and Yonei, 1987). Although, cellular membranes are vital elements and their integrity is extremely essential for the viability of the cells, yet very little information is available about the effects of high LET radiation on the membranes. Therefore, in the present work an attempt has been made to understand the membrane damage by high LET radiation using 45 MeV ^{7}Li ions and 68 MeV ^{16}O ions having maximum LET value as 354 keV/μm and 1130 keV/μm respectively.

Lipid peroxidation is an important effect of ionising radiation on cellular membranes and induces a plethora of lesions (Leyko and Bertosz, 1986; Kale and Sitaswad, 1990; Gupta and Kale, 1996). Therefore, the lipid peroxidation induced by high LET radiation was studied using microsomal membranes prepared from liver of rat. Since, the membrane-active property of CPZ, conformation or association of lipids in membranes and lipid peroxidation are likely to be interlinked (Shenoy and Singh, 1985; Raleigh, 1988), an attempt was made to study the effect of CPZ on ^{7}Li and ^{16}O ions induced lipid peroxidation. In addition to this, we have also studied heavy ion induced

hemolysis of erythrocytes. Microsomes (0.6 mg protein/ml) and rabbit erythrocytes (1×10^7 cells/ml) prepared from liver of rats were irradiated with ^{7}Li ions of energy 45 MeV and ^{16}O ions of energy 68 MeV having maximum LET value as 354 keV/μm and 1130 keV/μm respectively (Fig. 1a). ^{7}Li and ^{16}O-induced microsomal lipid peroxidation was found to increase with fluence. The enhancement of peroxidation persisted even in post-irradiation period (Fig. 1b). ^{16}O ions were relatively more effective than ^{7}Li ions which could be due to difference in the dose delivered by them (Fig. 1c). These findings suggested that the biological membranes could be peroxidized on exposure to high LET radiation. The inhibition of lipid peroxidation was observed in presence of a membrane active drug - chlorpromazine (CPZ) which could be due to scavenging of free radicals (Fig. 1d). The extent and pattern of protective effect of CPZ was found to be almost the same against ^{7}Li and ^{16}O ions (Fig. 1e). The increase in erythrocytes hemolysis with time was of a sigmoidal pattern type and found to be function of the fluence. The higher fluences were relatively more effective. The relative effectiveness of ^{7}Li and ^{16}O is shown in figure (1f) in terms of time taken for 50% hemolysis (T-50) at a particular fluence.

The peroxidation of microsomes perhaps reflected the involvement and importance of molecular oxygen in membrane damage caused by high LET radiation. High LET induced microsomal lipid peroxidation was inhibited by CPZ. However, when viewed in terms of the effects of LET, the difference between action of both the ions are not as significant as one would expect given that the LET_{max} of ^{16}O is about three times that of ^{7}Li. The small change in the effect could perhaps be related to 30% difference in their dose imparted to the system. Since membranes are also considered to be critical targets of radiation action, these findings may have significance in understanding the radiobiological effects of high LET radiation.

References

Alper T (1968) Low oxygen enhancement ratios for radiosensitive bacterial strains and the probable interaction of two types of primary lesion. Nature 217:862-863

Gupta M, Kale RK (1996) Paradoxical influence of Ca^{2+} on lipid peroxidation. Ind J Exp Biol 34:1071-1076

Kale RK, Sitaswad SL (1990) Radiation induced lipid peroxidation in liposomes. Radiat Phys Chem 36, No.3:361-364

Kerr JFR, Willie AH, Currie AR (1972) Apoptosis: A basic biological phenomena with wide ranging implications in tissue kinetics. Br J Cancer 226:239-257

Leyko W, Bartosz G (1986) Membrane effects of ionizing radiation and hyperthermia. Int J Radiat Biol 49:743-770

Obioha FI, Gillies NE, Cullen BM, Walker HC, Alper T (1984) Constants of the Alper and Howard-Flanders oxygen equation for damage to bacterial membrane, deduced from observations on the radiation induced penicillin-sensitive lesion. Int J Radiat Biol 45:427-437

Raleigh JA (1988) Radioprotection of membranes. Pharmacol Therapeut 39:109-113

Sato C, Yonei S (1987) Membrane changes. In: ed by Potten CS, Perspectives in mammalian cell death. Oxford University Press, , pp 1-17

Shenoy MA, Singh BB (1985) Temperature dependent modification of radiosensitivity following hypoxic cytocidal action of chlorpromazine. Radiat Environ Biophys 24:114-117
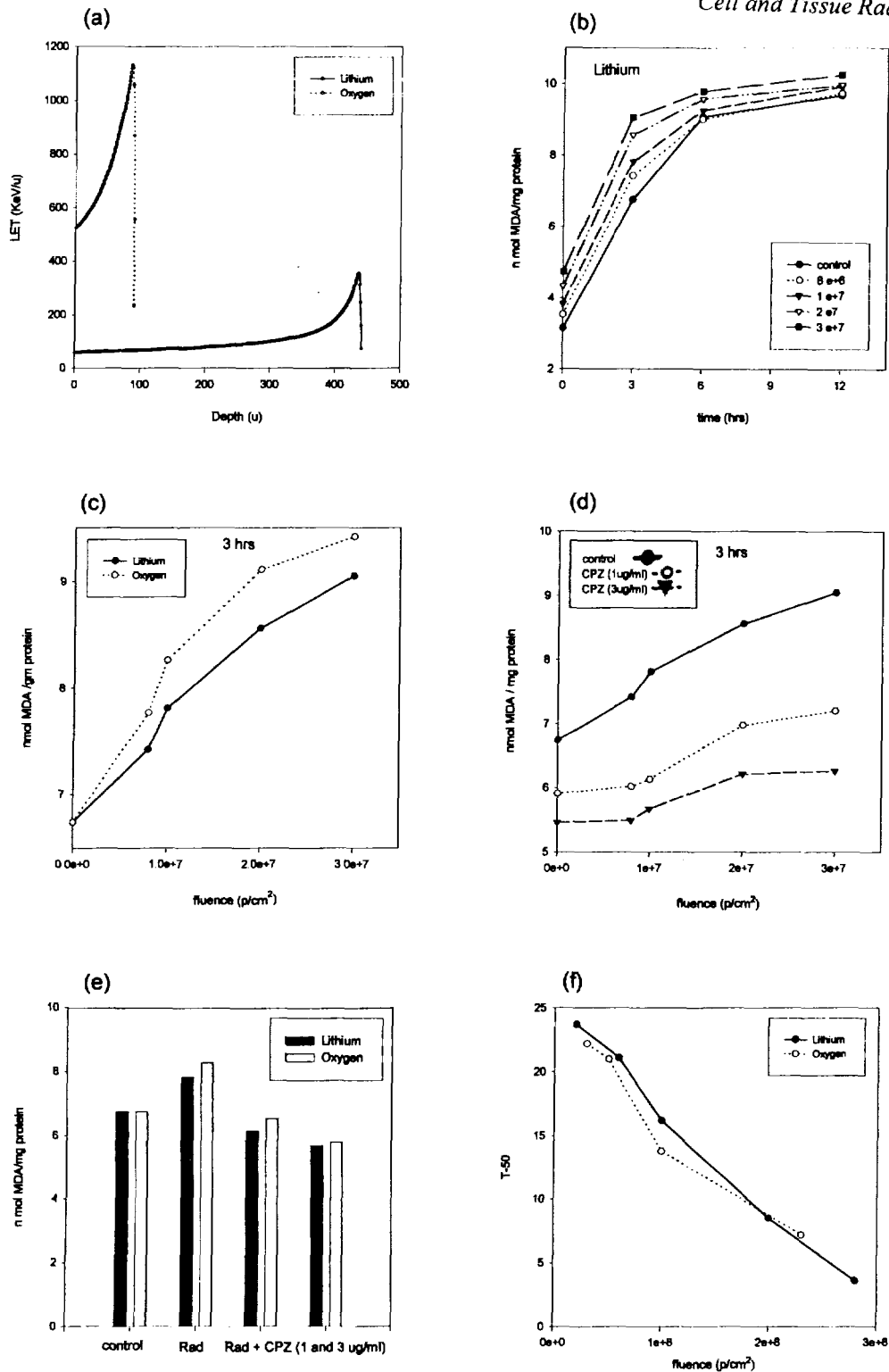
Figure 1. (a) LET-depth profile of 45 MeV ^{7}Li and 68 MeV ^{16}O charged particles; (b) effect of various fluences of 45 MeV ^{7}Li on lipid peroxidation in microsomes;(c) comparison of effect of ^{7}Li and ^{16}O charged particles on microsomal lipid peroxidation at 3 hrs post-irradiation time; (d) effect of CPZ on ^{7}Li-induced microsomal lipid peroxidation; (e) relative effectiveness of CPZ against ^{7}Li and ^{16}O induced lipid peroxidation at 2x10^7 p/cm^2 and 3 hrs post-irradiation time; (f) relative effectiveness of various fluences of ^{7}Li and ^{16}O on T-50 of rabbit erythrocytes.

Status of the Vertical Beam Facility at the Munich Tandem Accelerator *

J. Besserer, J. de Boer, M. Dellert, M. Moosburger, P. Quicken
Sektion Physik, Ludwig–Maximilians–Universität München,
85748 Garching

L. Distel, H. Schüßler
Klinik für Strahlentherapie, Universität Erlangen–Nürnberg,
91054 Erlangen

W. Eyrich, M. Fritsch, A. Teufel
Physikalisches Institut, Universität Erlangen, 91058 Erlangen

Radiobiological investigations using proton or heavy–ion accelerators are of fundamental importance in radiobiology because of the increasing use of ion beams in tumor therapy [1, 2]. The main problem in such experiments is the precise determination of the applied dose and the simultaneous maintenance of a suitable biological environment for the sensitive "live" targets under irradiation.
A vertical beamline allows cells or cell material to be irradiated in the medium or in solution through the thin bottom of a petri dish. Specified temperatures or gas atmospheres can easily be maintained.

Therefore at the Tandem Accelerator Laboratory of the Ludwig–Maximilians University and the Technical University Munich a vertical beam facility was installed [3]. As presented in Fig. 1 the particle beam is deflected into the vertical direction using a 90° bending magnet. It leaves the beam tube through a thin exit window with a diameter of 60 mm. At a height of 4 m a platform around the vertical part of the beamline allows access to the irradiation table

---
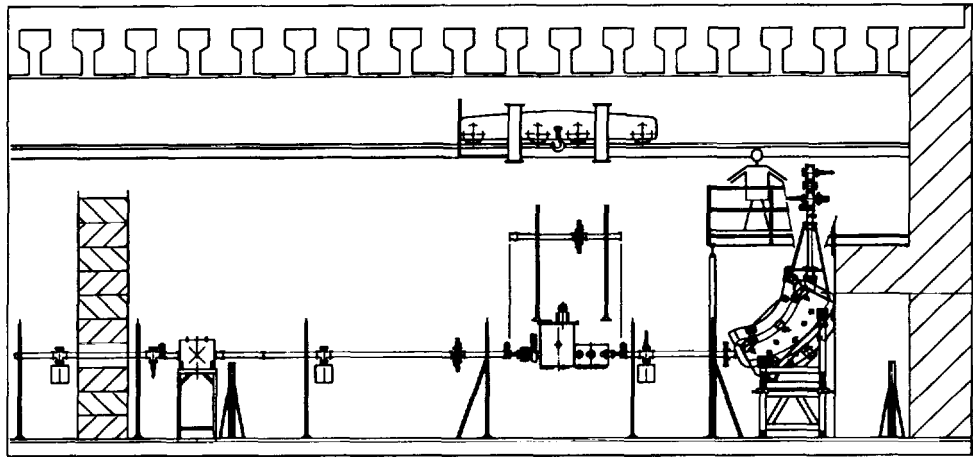
Figure 1: The vertical beamline with the 90° magnet and the platform for experiments at a height of 4 m

with the computer–controlled sample changer from all sides.

For the cultivation of biological targets like cell samples and DNA–solutions a rudimentary cell–culture laboratory has been installed in the adjacent building including a sterile flow box, an incubator and a microscope.

The beam is spread passively by thin scatter foils in front of the 90° magnet and dynamically by a system of electromagnetic bending coils in the vertical part of the beamtube. To measure the intensity distribution of the radiation field a plate of plastic scintillator material was irradiated by the spread–out beam and observed by a CCD camera. The intensity profile of Fig. 2 shows the good homogeneity of better than 95 % of the radiation field above the exit window. The dose rate can be widely adjusted to fit the requirements of the irradiation experiments.

For dosimetry the flux of particles is measured by a two dimensional array of silicon pin–diodes with fast read–out electronics. Additionally the dead time of the electronic system is monitored. For an irradiation the fluence of particles is calibrated to the count rate of four additional pin–diodes installed within the vacuum tube around the exit window. The field detector is then
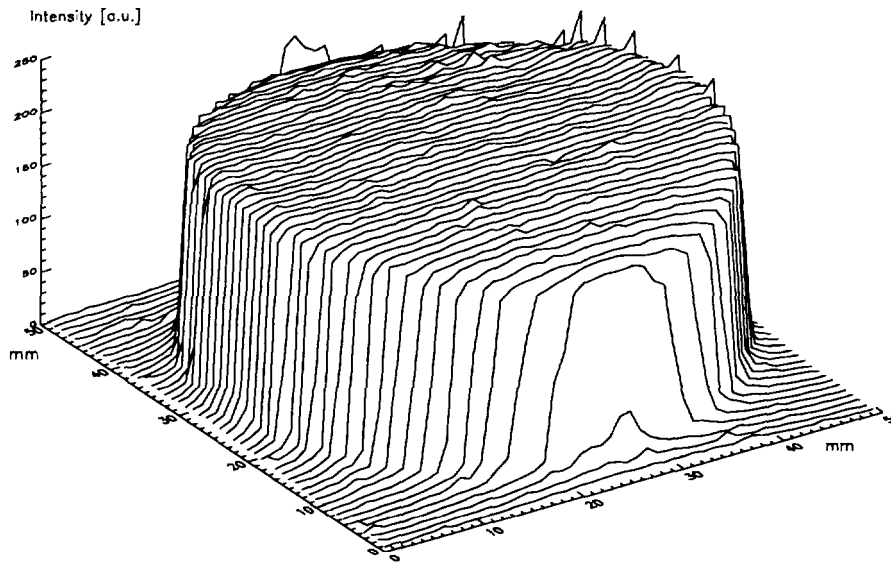
Figure 2: Homogeneity of the dose distribution above the exit window

replaced by the sample, which is irradiated according to a presettable sum of monitor counts. The dose must be calculated from the fluence of particles and their linear energy transfer (LET). The count rate of the monitor diodes is stored every 10 ms, which allows to control the beam intensity during irradiation. The symmetric installation of the monitor counters allows also to observe a possible drift of the beam position.

In order to check the accuracy of the dosimetry system, thermoluminiscence crystals were irradiated with a wide range of doses. The TLD response shows good agreement with the predicted dose value from our single–proton counting system as can be seen in Fig. 3a. As an alternate test Fricke solution was irradiated as a chemical dosimeter. The gain of Fe^{3+} ions after irradiation is plotted in Fig. 3b against the applied dose. The solid line line respresents the amount of ions calculated with parameters for a high–energy electron beam. The small discrepancy may be due to a slightly different dose response for protons. The use of a standard ionization chamber for dosimetry is planned

3
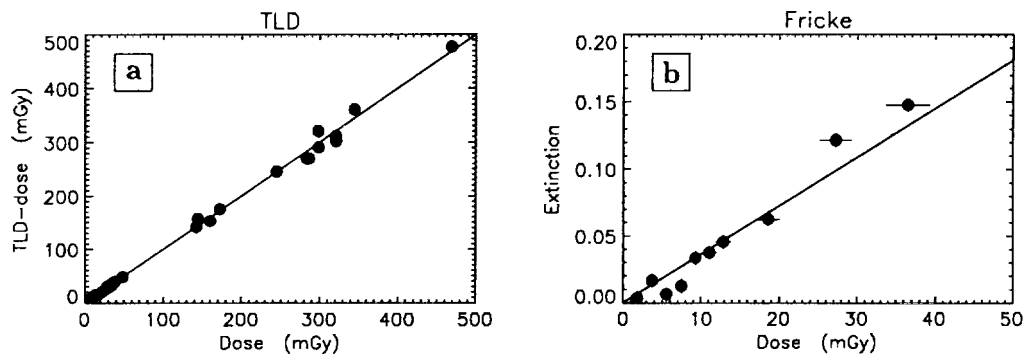
Figure 3: Dose verification with TLD and Fricke dosimeter

for additional dose verification.

In summary an absolute dose determination with an uncertainty of ±6 % was achieved. The relative dose accuracy is still higher.

In first experiments the feasibility of radiobiological experiments at the new vertical beam facility of the Munich Tandem Accelerator was demonstrated. The results show the reliability of the irradiation apparatus and the dosimetry system [4].

References

[1] E.A. Blakely, in *Ion Beams in Tumor Therapie*, Ed. U. Linz, (Chapman, Weinheim, 1995), 63.

[2] L. Distel et al., Proceedings of the Second International Symposium on Hadrontherapie, PSI/CERN, (1996).

[3] J. Besserer et al., Annual Report Accelerator Laboratory Munich, 113 (1996).

[4] L. Distel et al., this report.

4

Effect of 45 Mev ^{7}Li and 68 Mev ^{16}O charged particles on microsomal membrane fluidity.

M. Srivastava, D. Choudhary, A.Sarma* and R.K. Kale

School of Life Sciences, Jawaharlal Nehru University,

New Delhi, INDIA

*Nuclear Science centre, New Delhi 110067, India

The cellular membranes are vital elements and their integrity is extremely essential for the viability of the cells. The fluorescence polarization and anisotropy changes has proven to be among the most sensitive, reproducible and convenient means of probing the fluidity and organization of membrane (Friefelder 1986). Therefore we have tested the possibility of change in the fluidity by using the DPH probe which localizes in the fatty acyl side chain region of lipid bilayer (Patel and Block 1988). Microsomes prepared from the liver of Sprague-dawley rats (200-250 gms body weight)were irradiated with 45 MeV ^{7}Li and 68 MeV ^{16}O and fluorescence polarization and anisotropy changes were measured after irradiation.

The results of present findings are shown in Table 1. When microsomes irradiated with 45 Mev ^{7}Li and 68 Mev ^{16}O charged particles (8×10^6 - 3×10^7), the fluorescence polarization was found to increase with the fluence of ^{7}Li and ^{16}O ions (Table 1).Since the fluorescence polarisation is inversely proportional to the fluidity of the membrane, our findings suggests that the high LET radiation caused more close packing of membranes making them more rigid probably as a result of peroxidative damage which is known to shorten the fatty acyl chain, induces peroxides and aldehydes in the hydrocarbon region, removes unsaturation and induces cross linking among the lipid as well as protein molecules. These changes cause the membrane to pack more closely making the membrane more rigid resulting in increase in fluorescence polarization.It was also found that^{16}O charged particles induced more changes in the membrane characteristics than ^{7}Li ions. More effectiveness of ^{16}O ions than ^{7}Li would probably be attributed to their differences in

the energy distribution profile   which showed that LET of ^{16}O ions was three times more than that of ^{7}Li.

We also studied the change in the flourescence polarisation at 0,3,6 and 12 hours post irradiation period (Table 1). ^{7}Li and ^{16}O ions induced change in the fluidity was seen to increase further with time which was suggestive of persistence of the radiation effect even in the post irradiation period. It might be mentioned that the post irradiation effect was also more in case of ^{16}O ions than ^{7}Li ions.

A characteristic change related to the fluidity was also confirmed by the measurement of anisotropy. Anisotropy was also enhanced with the fluence of 45 Mev ^{7}Li and 68 Mev ^{16}O charged oparticles and post irradiation time (Table 2). The increase in the anisotropy reflected the more highly constrained motion of hydrophobic interior and lowered fluidioty of the membranes (Purohit et al.). Relatively more change in the anisotropy was also observed with ^{16}O as compared to ^{7}Li ions which could be due to the difference in their LET values.

In conclusion, our results suggest that exposure to the 45 Mev ^{7}Li and 68 ^{16}O charged particles lead to the change ¢in the fluidity. This change in the membrane property increased with post irradiation time. It is quite possible that these high LET radiations might have induced close packing and highly constrained motions of hydrophobic interior of membrane leading to decrease in its fluidity. As importance of high LET radiation in cancer therapy and estimating the risks associated with space flight, thes findings may have significance from the radiobiological studies point of view.

References:

1. Patel,J.M. and Block,E.R.(1986):Free Rad. Biol. Med.;4: 121-134.

2. Freifelder,d in Physical biochemistry, W.H. Freeman and Company, New York.(1982): pp 537-572.

3. Purohit, S.C., Bisby, R.H and Cundall, R.H.: Int. J. Rad. Biol.;38:147-158.

Table:1.

Fluence (p/cm^2)	Time (hrs)			
	0	3	6	12
^{7}Li				
Control	0.145	0.162	0.197	0.200
8x10^6	0.154	0.180	0.200	0.210
1x10^7	0.155	0.185	0.206	0.217
2x10^7	0.160	0.189	0.205	0.218
3x10^7	0.165	0.190	0.205	0.218
^{16}O				
Control	0.145	0.162	0.197	0.200
8x10^6	0.201	0.206	0.210	0.263
1x10^7	0.207	0.214	0.216	0.271
2x10^7	0.208	0.217	0.218	0.275

Table 2. Effect of 45 MeV ^{7}Li and 68 Mev ^{16}O charged particles on anisotropy in microsomal membranes

Fluence (p/cm^2)	Anisotropy			
	Time (hrs)			
	0	3	6	12
45 MeV ^{7}Li				
Control	0.101	0.114	0.140	0.141
8x10^6	0.108	0.127	0.141	0.151
1x10^7	0.108	0.131	0.143	0.156
2x10^7	0.112	0.134	0.147	0.157
3x10^7	0.116	0.135	0.147	0.157
68 MeV ^{16}O				
8x10^6	0.143	0.147	0.151	0.192
1x10^7	0.148	0.153	0.155	0.199
2x10^7	0.149	0.156	0.157	0.202
3x10^7	0.156	0.167	0.162	0.205

EXPERIMENTAL DETERMINATION OF THE CONTRIBUTION OF CARBON K-IONIZATIONS TO THE RBE FOR CELL INACTIVATION BY ULTRASOFT X-RAYS

A. TOUATI[1] , M.A HERVE DU PENHOAT[1] , I.DESPINEY-BAILLY[2] , F.ABEL[1], B.FAYARD[1], A.LHOIR[1], L.SABATIER[3] , A.CHETIOUI[1] , D.STEVENS[4] , M.HILL[4] , D.T.GOODHEAD[4].

(1) Groupe de Physique des Solides, Universités Paris 7 et Paris 6,(CNRS URA 017, CEA LRC N° 6), Tour 23, 2 place Jussieu, 75251 Paris cedex 05.
(2) CEA/DSV/DRR/, Lab de Radiotoxicologie, BP.1291680 Bruyères le Chatel, France.
(3) CEA/DSV/DRR/, Lab de Radiobiologie et Oncologie, BP.6, 92265 Fontenay aux Roses cedex, France.
(4) Radiation and Genome Stability Unit, Medical Research Council, Harwell, Didcot,Oxfordshire, OX11 0RD, U.K.

INTRODUCTION.

Recent questions on the possible role of K-ionization in the biological effect of heavy ions (Chetioui *et al* , 1994) show that there is a strong need of a systematic study of the biological effect of a K-electron removal in C,N,O atoms of the DNA.

A method to study selectively the effect of a K-ionization consists in comparing biological effects of X-ray irradiations at energies before and after the K-ionization threshold. X-ray induced K-ionizations have probably a less severe effect than ion-induced ones since the latter are usually accompanied by multiple outer shell ionizations in the same atom and additional ionizations along the ion-track. Nevertheless, the lethal effectiveness of X-induced K-ionizations provides a lower limit of that of ion-induced ones.

To test the feasibility of experiments at the K-threshold of the various atoms and to determine an appropriate range of irradiation energies, we have performed a simple calculation of the RBE of X-rays around K-edges, assuming the same lethal effectiveness for the K-ionizations of C,N and O atoms of DNA.(For a first trial a uniform 1% value has been chosen) This calculation is performed in the framework of the model of critical size events of Goodhead *et al* (1979) : track clusters (clusters of more than 100 eV in 2nm-size volumes occuring at the track end of secondary electrons) and clusters from K-ionization are both considered to contribute to the lethal effect.

The results of the calculation (Du Penhoat *et al*, submitted to Radiation Research -1997) display a strong increase of RBE (by a factor of ~ 2) just above the C-K threshold , followed by a less pronounced increase above the N-K threshold and then a decrease above the O-K threshold since O-K ionizations occur mostly outside the DNA.These results have motivated an experimental study of the lethal effectiveness of C-K ionizations (Threshold energy : 284 eV)

EXPERIMENT and METHODS.

Because of the strong absorption of ultrasoft X-rays, a comparison of the effect of two radiations at different energies can only be significant if their attenuation in the cell is the same. The isoattenuation criteria has been fullfilled by using radiations of well defined energies: 250 and 340 eV respectively. The experiment was performed with monochromatized synchrotron radiation at the LURE facility in Orsay close to the super ACO storage ring.

The entrance dose to a cell was evaluated from the X-ray fluence. Two separate measurements of the intensity were performed by an X-ray Si photodiode with a 20 mm^2 active area, and by a commercial parallel plate extrapolation chamber with modified window.

When comparing radiations with isoattenuation, the mean dose within the cell nucleus is an appropriate parameter to correlate with the cell survival. Consequently the attenuation within the cell must be known. For this purpose measurements of the thickness of cytoplasm and nucleus of cells under study have been performed using confocal microscopy.

Study of cell survival was performed with a V79 chinese hamster cell line. Cells were grown as monolayers on 0.9 µm thick mylar foil and allowed to attach to the film and flatten for 48 hours. In these conditions, the mean dose inside the nucleus was about 15% of the entrance dose

RESULTS and DISCUSSION.

The survival curve for the 250 eV radiation display a linear quadratic shape. When plotted against the average dose, the coefficients of the quadratic fit are : $\alpha = 0.40$ Gy^{-1}, $\beta = 0.54$ Gy^{-2} ,very near those obtained in the experiment of Goodhead *et al* (1979) with carbon K-X rays (278 eV) : $\alpha = 0.43$ Gy^{-1}, $\beta = 0.62$ Gy^{-2} .

At 340 eV, the survival curve present a much steeper decrease as a function of dose: at 250 eV, the dose for 10% survival is about twice the one at 340 eV. This enhanced lethality is the consequence of the production of **concentrated energy depositions around the C-K ionizations which mostly take place on the DNA.**

In the framework of the calculation described in the introduction, one can extract from the survival curve at 250 eV a 1.8% value for the lethal yield of track clusters overlapping DNA, close to that -1.9%- which can be extracted from the survival curve of Goodhead *et al* (1979). From the survival curve at 340 eV, a lethal yield of the order of 2% is obtained for C-K ionization clusters overlapping DNA.

This value is high since it is comparable to the yields measured for major events such as K disintegrations of incorporated ^{125}I nuclides .

The knowledge of the RBE of X-rays at various energies provides - in the frame of the above model- some information about the lethal yield of C,N,O K-vacancies generated by heavy ions and their role on the overall ion lethality.

REFERENCES.

Chetioui A, Despiney I, Guiraud L, Sabatier L and Dutrillaux B (1994). Possible role of inner
shell ionization phenomena in cell inactivation by heavy ions. *Int.J.RadiatBiol.* **65** 511-522.

Goodhead D.T, Thacker J Cox R (1979). *Int.J.Radiat.Biol.* Effectiveness of 0.3 keV carbon
ultrasoft X-rays for the inactivation and mutation of cultured mammalian cells. **36**, 101-104.

Acknowledgements.

Survival of human cells exposed to acute and fractionated doses of low-energy protons

M. Belli[1], D. Bettega[2], P. Calzolari[2], F. Cera[3], R. Cherubini[3], M. Dalla Vecchia[3], M. Durante[4], S. Favaretto[3], G. Gialanella[4], G. Grossi[4], A.M.I. Haque[3], R. Marchesini[5], G. Moschini[3], A. Piazzola[2], M. Pugliese[4], O. Sapora[1], P. Scampoli[4], G. Simone[6], E. Sorrentino[1], M.A. Tabocchini[1], L. Tallone[2] and P. Tiveron[3]

1 Istituto Superiore di Sanità and INFN-Sezione Sanità, Roma, Italy

2 Dipartimento di Fisica, Università di Milano, and INFN-Sezione di Milano, Milano, Italy

3 Laboratori Nazionali di Legnaro INFN, Padova, Italy

4 Dipartimento di Scienze Fisiche, Università "Federico II", and INFN-Sezione di Napoli, Napoli, Italy

5 Fisica Sanitaria, Istituto Nazionale dei Tumori, Milano, Italy

6 Istituto FRAE-CNR, Bologna and INFN-Sezione Sanità, Roma, Italy

I. Introduction

Use of proton beams for radiation therapy has shown a remarkable increase in the past few years. Protons are attractive for tumor therapy because of their favorable ballistic properties, but detailed measurements of the RBE, especially in proximity of the Bragg peak, are lacking. A collaborative research program, involving different Italian Institutes, is aimed to investigate the biological effectiveness of low-energy protons. Four human cell lines have been selected for inactivation studies, namely tumor epithelial (SQ20B and SCC25) cell lines, and normal epithelial (H184B5 F5-1 M/10) and fibroblast (HF19) cell lines.

We have recently reported preliminary dose-response curves for inactivation of the above cells exposed to γ-rays and to accelerated protons in the energy range 0.6-5 MeV and in the dose range 0-14 Gy [1]. Updated measurements of the RBE-LET relationships will be presented here.

In addition, we started to investigate the effect of proton dose fractionation on cell survival. Therapeutic doses are delivered in multiple fractions, and it is well known that fractionation produces a better tumor control for a given level of normal tissue toxicity than a single acute exposure. While fractionation regimens for γ-rays have been investigated in detail both *in vitro* and *in vivo* [2], less information is available for protons. We will compare the effect of split-doses of protons and γ-rays in the above mentioned *in vitro* normal and tumor human cell lines. Preliminary results are discussed below.

II. Methodology

The SCC25 and SQ20B tumor cell lines [3] were kindly provided by Dr. E. Blakeley and were grown in D-MEM:F12 (75:25) supplemented with 0.4 µg/ml hydrocortisone and 20% fetal calf serum (FCS). The M/10 cells are a subclone of the immortal human mammary epithelial line H184B5, originally isolated by Dr. M. Stampfer [4], and were kindly donated by Dr. T.C. Yang. Cells were

grown in α-MEM supplemented with 10% FCS. The HF19 lung fibroblast cell line was maintained in culture using Eagle's MEM supplemented with 10% FCS.

Log-pahse cells were irradiated with monoenergetic protons at the radiobiological facilities installed at the 7 MV Van der Graaf CN accelerator in Legnaro (SSC25, SQ20B, and HF19) or at the 3 MV TTT-3 Tandem accelerator in Naples (M/10). Cells were irradiated as monolayers attached to thin mylar foils. Details of irradiation facilities and methods have been reported elsewhere [1, 5, 6].

For acute dose experiments, the cells were tripsinized, diluted, and plated at the appropriate concentration for survival determination. Colonies were fixed and stained after about two weeks incubation. For split-dose experiments, cells were incubated at 37 °C for different times (1.5-4.5 h) between fractions, and finally harvested after the last exposure.

III. RBE of low energy protons

Survival curves for each proton energy and cell line were obtained from 3 to 6 indipendent experiments. Data were fitted by a linear-quadratic function. A remarkable difference in sensitivity among different cell lines was observed. SQ20B cells were resistant to γ-rays, surviving fraction after 2 Gy being about 4-times higher than survival of HF19, M/10 or SCC25 cells. The RBEs of low energy protons are reported in Table 1. RBE was evaluated as the ratio 2 Gy/D_p, where D_p is the proton dose producing the same survival level as 2 Gy γ-rays. Although SQ20B was the most resistant cell line also to proton exposure, their RBE was higher than those measured in the radiosensitive lines, especially at the highest LET. These results suggest that the use of protons in radiation therapy might influence the effectiveness of treatment of radioresistant tumors.

Table 1. RBE of low energy protons for the inactivation of different human cell lines. The RBE was evaluated at the survival level produced by 2 Gy γ-rays. The LET is calculated at the proton energy incident on the cell monolayer.

Proton LET (keV/μm)	HF19	M/10	SCC25	SQ20B
7.7			0.98	0.96
10	0.93	1.03		
20		1.09	1.43	2.50
28	1.05		1.43	7.5
32		1.39		

IV. Split-dose experiments

It is known that mammalian cells can repair part of the radiation-induced damage. As a consequence of the repair processes, survival following an acute exposure is generally lower than after a fractionated exposure. In the linear quadratic model (under the assumption of total repair of sublethal damage between fractions) $R = \exp(2\beta d^2)$, where R is the ratio between survivals in fractionated and

acute exposure at the same total dose, d is the dose per fraction, and β is the quadratic coefficient of the survival model. Dose-survival relationships measured in the previous experiments demonstrate that the β coefficient is small in our cell lines exposed to low-energy protons. Therefore, high doses were used in fractionated experiments, corresponding to survival levels around 5%. Due to the different radiosensitivity, the cell lines were irradiated with total doses ranging from 5 to 12 Gy. Gamma radiation was used for comparison. Fractions were separated by 1.5, 3 or 4.5 h time intervals.

Preliminary results are shown in figure 1, where survival is plotted vs. time interval between fractions. In these first experiments, a proton LET of about 8 keV/μm was used for all cell lines, and the same dose was delivered either in a single exposure or in two equal fractions, separated by a time interval at 37 °C. Surviving fraction increases as a function of time, and appears to reach a plateau around 3 h. Following 3 h incubation, R values between 2 and 4 were found for the different total doses and cell lines. For a given cell line, the recovery seems to be more pronounced at high doses. More experiments are under way to measure R for the different cell lines.
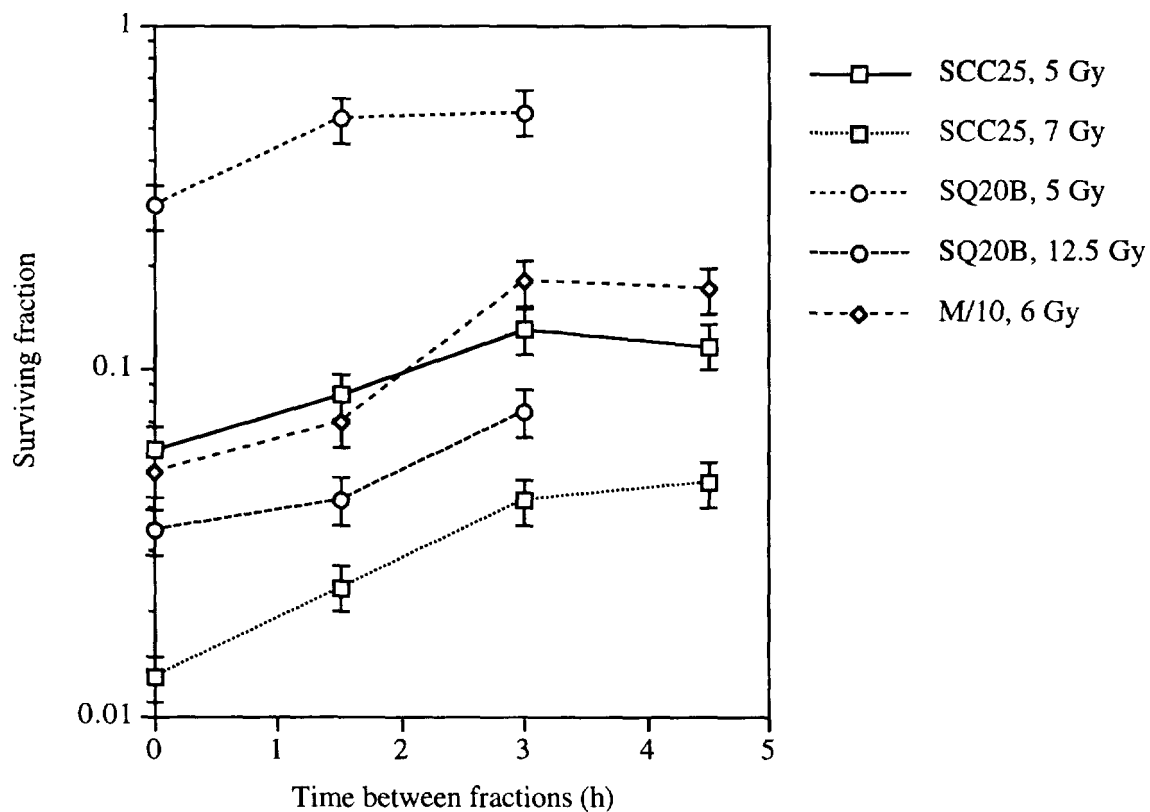

Figure 1. Survival of different human cell lines exposed to protons (LET around 8 keV/μm). Radiation doses were delivered in two equal fractions.

3

V. References

1. M.Belli, A.Ascatigno, D.Bettega, P.Calzolari, F.Cera, R.Cherubini, M.Durante, S.Favaretto, G.Gialanella, G.Grossi, A.M.I.Haque, F.Ianzini, R.Marchesini, G.Moschini, A.Piazzolla, M.Pugliese, O.Sapora, P.Scampoli, G.Simone, E.Sorrentino, M.A.Tabocchini, L.Tallone, P.Tiveron. RBE for inactivation of tumoural and normal cell lines of human origin irradiated with low energy protons. In: *Proceedings of the 2nd Symposium on Hadrontherapy*, Switzerland, September 9-13, 1996.

2. E.J. Hall, Nine decades of radiobiology: is radiation therapy any the better for it? *Cancer* **71** (1993) 3753-3766.

3. R.R. Weischelbaum, M.A. Beckett, J.L. Schwartz, A. Dritschilo, Radioresistant tumor cells are present in the head and neck carcinomas that recur after radiotherapy. *Int. J. Radiat. Oncol. Biol. Phys.* **15** (1988) 575-579.

4. M.R. Stampfer and J.C. Bartley, Induction of transformation and continuous cell lines from normal human mammary epithelial cells after exposure to benzo(a)pyrene. *Proc. Natl. Acad. Sci. USA* **82** (1985) 1394-1398.

5. M. Belli, F. Cera, R. Cherubini, A.M.I. Haque, F. Ianzini, G. Moschini, O. Sapora, G. Simone, M.A. Tabocchini and P. Tiveron, Inactivation and mutation induction in V79 cells by low energy protons: re-evaluation of the results at the LNL facility. *Int. J. Radiat. Biol.* **63** (1993) 331-337.

6. M.Napolitano, M.Durante, G.F.Grossi, M.Pugliese and G.Gialanella, Inactivation of C3H 10T1/2 cells by monoenergetic high-LET α particles. *Int. J. Radiat. Biol.* **61** (1992) 813-820.

Cellular response of V79 multicellular spheroids exposed to high energy carbon ions

D. Zukowski, M. Scholz[1], G. Kraft[1] and W. Mueller-Klieser

Institute of Physiology and Pathophysiology, University of Mainz, D-55099 Mainz, Germany
and [1]GSI, Planckstr. 1, D-64291 Darmstadt, Germany

SUMMARY

To quantify the effectiveness of heavy ion beams at a cellular level, V79 spheroids of $200 \pm 30 \mu m$ ($\pm$ SD) in diameter were irradiated either with high-energy carbon ions ($^{12}C^{+6}$, 227 meV/u) in small spinner flasks under different oxygen tensions or in sealable glass vessels on a gyratory shaker for x-ray irradiation. Subsequently, spheroids were assayed for dose-dependent volume growth, clonogenicity and cell cycle distribution. V79 spheroids of this size contain no detectable fraction of hypoxic cells and showed similar survival rates when irradiated with an oxygen pressure of 147 mm Hg or 688 mm Hg. A RBE value of about 1.6 was calculated in relation to standard x-ray irradiation. Under acute strictly hypoxic conditions (0 mm Hg) a dominant hypoxic shoulder could be observed reflecting an OER of about 2.4. For irradiation at 40 mm Hg an OER of 1.25 could be determined, representing a theoretical hypoxic fraction of 12 %. Volume growth curves of spheroids irradiated with heavy ions exhibited a biphasic behavior with an intermediate dose-dependent growth recovery at the third to ninth day after irradiation. For spheroids irradiated under hypoxic conditions these volume growth characteristics were even more pronounced. Spheroids irradiated with x-rays showed a less obvious phasic growth recovery. For higher doses an exponential regrowth at the seventh to ninth day after irradiation could be observed leading to a transient saturation of the relative growth delay time as a function of dose. Cell cycle analysis documented a dose- and oxygen-dependent accumulation of cells in the G_2/M-phase with this effect being more pronounced with heavy ions compared to x-rays. For the chosen particle energy no dramatic differences between high energy carbon ion and standard x-ray irradiation could be demonstrated, but it can be expected that significant differences in the oxygen effect occur, if carbon ions with lower energy are used.

RESULTS AND DISCUSSION

All presented survival curves of irradiated V79 spheroids comprise at least three independent experiments with each minimum five determinations of relative survival per dose ($N/N_0 \pm$ SEM). The data were mathematically modeled according to the Linear Quadratic model (LQ-model) to obtain the corresponding α- and β-values.

Determination of the Relative Biological Effectiveness

To determine the relative biological effectiveness (RBE) of 227 meV/u $^{12}C^{+6}$-ions in relation to standard x-ray irradiation V79 spheroids were irradiated in carbondioxide equilibrated air (pO_2= 147 mm Hg, pCO_2= 14 mm Hg) either with carbon ions or with 250 kV x-rays. As indicated in *figure 1*, a RBE of 1.64 ± 0.05 ($\pm$ SEM) could be demonstrated revealing the slightly higher Linear Energy Transfer (LET) of high energy charged particles in comparison to x-ray radiation.

The corresponding α- and β-values of the LQ-model were determined to α= 0.079, β= 0.026 (x-ray) and: α= 0.326, β= 0.041 (227 meV/u $^{12}C^{+6}$).
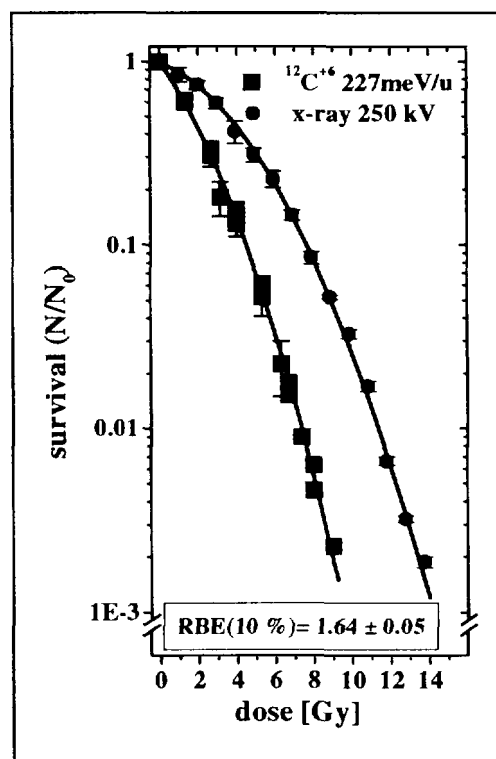

figure 1   Dose response curves of V79 spheroids of $200 \pm 30 \mu m$ ($\pm$ SD) in diameter irradiated with either 227 meV $^{12}C^{+6}$-ions or x-rays at pO_2= 147 mm Hg demonstrating the RBE at the level of 10 % relative survival.

Evaluation of the Oxygen Effect

To demonstrate the effects of oxygen present during irradiation, spheroids were gassed either with carbon dioxide equilibrated air (pO_2= 147 mm Hg, pCO_2= 14 mm Hg) or different gas mixtures equilibrated with carbon dioxide (pCO_2= 14 mm Hg) for two hours prior to
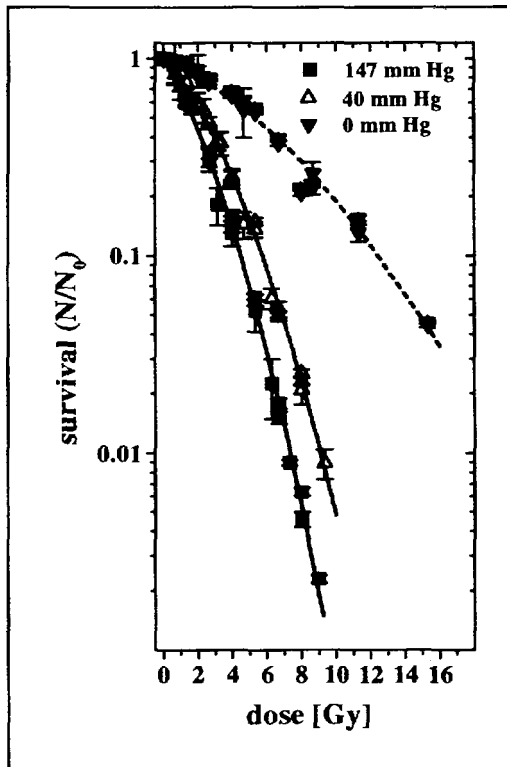

figure 2   Dose response curves for V79 spheroids 200 ± 30 μm in diameter irradiated with 227 meV/u $^{12}C^{+6}$-ions at different oxygen tensions.

irradiation (pO_2= 40 mm Hg and pO_2= 0 mm Hg). For pO_2= 40 mm Hg a moderate oxygen effect with an OER of 1.26 ± 0.05 (± SEM) could be observed (*figure 2*). For a pO_2 of 0 mm Hg the OER was drastically increased to 2.4 ± 0.07 (± SEM). The OER obtained at pO_2= 0 mm Hg is slightly lower than that for x-ray irradiation (OER 2.8 ± 0.1) which mirrors the higher RBE of carbon ions. A decrease of the external pO_2 from 147 mm Hg to 40 mm Hg, a value near the pO_2 of venous blood, is associated with an increased survival which reflects a substantial oxygen effect including a calculated hypoxic fraction of 12 ± 1 %. The corresponding α- and β-values were calculated to α= 0.216, β= 0.032 (pO_2= 40 mm Hg) and α= 0.089, β= 0.0076 (pO_2= 0 mm Hg), respectively. Unexpected hypoxia during irradiation at pO_2= 147 mm Hg was ruled out by irradiation at pO_2= 688 mm Hg showing similar results in relative survival.

Volume growth characteristics of irradiated V79 spheroids

For dose-dependent volume growth curves the volume of at least 50 individual spheroids was determined for every given dose and time point (V(t) ± SD [10^{-5} cm^3]). To obtain the corresponding theoretical volume growth, the data were mathematically modeled by the Gompertz function. The dose-dependent relative growth delay $T_{Dr}(V_i)$ expressed in percent was calculated by dividing the volume difference between treated and untreated spheroids $T_D(V_i)$ by the initial volume doubling time dt_S of the corresponding controls. This was done for spheroid volumes that correspond to 4-times and 16-times the initial spheroid volume of controls. This procedure represents a normalization under consideration of the individual variability in the initial volume growth. Volume growth curves of spheroids irradiated at a size of 200 ± 30 μm in diameter at various oxygen tensions showed a dose-dependent growth alteration (*figure 3*). Spheroids irradiated at pO_2= 147 mm Hg exhibited a shrinkage at doses higher than 7 Gy with subsequent exponential regrowth at day seven after irradiation. Spheroids irradiated at pO_2= 0 mm Hg with doses below 9 to 10 Gy exhibited only a retardation of growth without a phase of regression, as shown by the decreased slope of the Gompertzian fit (*figure 3*). Spheroids irradiated at pO_2= 147 mm Hg showed an intermediate growth behavior as indicated by the relative growth delay $T_{Dr}(V_i)$. For the chosen oxygen pressures distinct differences in relative growth delay could only be observed at doses higher than 3 Gy (*figure 4*).

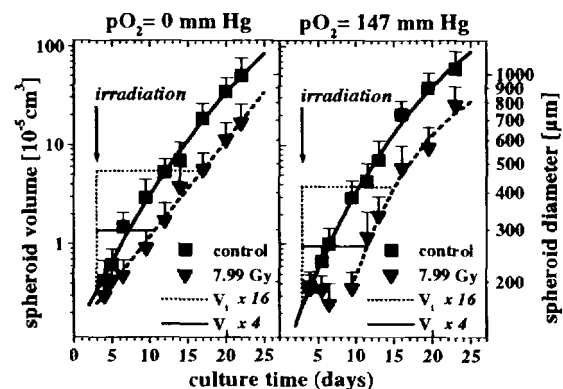*figure 3*   Representative volume growth curves for V79 spheroids irradiated with 227 meV/u carbon ions at pO_2= 147 mm Hg and pO_2= 0 mm Hg at the third day after initiation of spinner culture (see arrow) having a size of 200 ± 30 μm (± SD). The dose-dependent increase in relative growth delay $T_{Dr}(V_i)$ is indicated by the horizontal lines (16- and 4-times the volume at the time of irradiation).
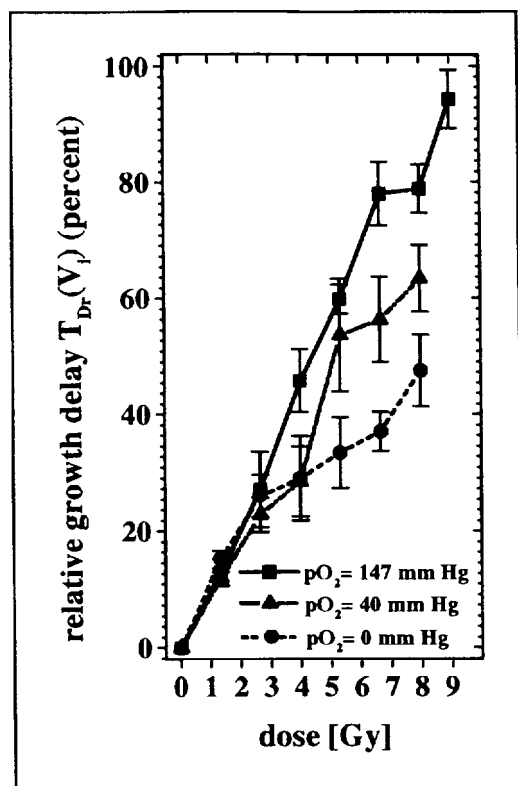
figure 4 Relative growth delay $T_{Dr}(V_i)$ of V79 spheroids irradiated with $^{12}C^{+6}$-ions. Relative growth delay was calculated for a 4-fold increase in the initial spheroid volume of the corresponding control population. This represents the dose dependent time delay to achieve two volume doublings.

If volume growth of irradiated spheroids ($200 \pm 30 \, \mu m$) is plotted relatively to the control population (= 1), a phasic growth recovery is observed (*figure 5*) peaking at days 3 and 8 to 9 after irradiation for spheroids irradiated at $pO_2= 147$ mm Hg. Spheroids irradiated with 227 meV/u carbon ions under anoxia
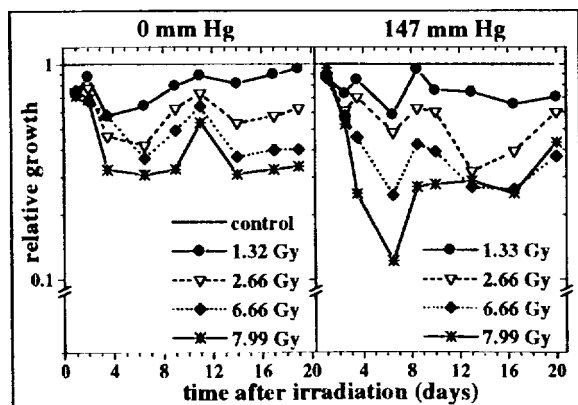
figure 5 Relative growth (control population = 1, dashed and dotted line) of V79 spheroids ($200 \pm 30 \, \mu m$) irradiated with 227 meV/u heavy carbon ions. A phasic growth recovery is observed.

($pO_2= 0$ mm Hg) showed a more pronounced phasic behavior with local volume growth maximums at days 2 and 11 after irradiation. Spheroids treated with x-rays exhibited a similar phenomenon which is less obvious (data not shown).

Analysis of cell cycle distribution
For analysis of cell cycle distribution spheroids were trypsinized, washed and stained with standard propidium iodide/RNase after ethanol fixation and subsequently investigated by flow cytometry. The obtained data of propidium iodide fluorescence were mathematically modeled to obtain the cell cycle distribution.
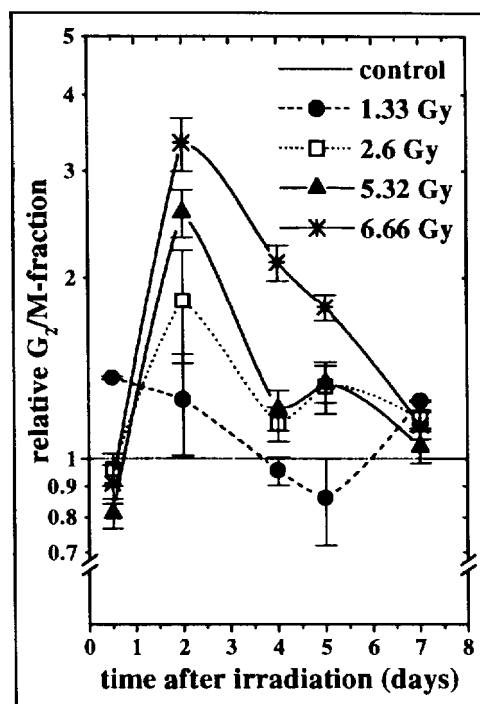
figure 6 Relative cell cycle distribution (control population = 1, dashed and dotted line) of V79 spheroids irradiated at a diameter of $200 \pm 30 \, \mu m$ and at $pO_2= 40$ mm Hg showing a more than 3-fold increase in G_2/M-fraction for a dose of 6.66 Gy.

As indicated in *figure 6*, a dose-dependent accumulation of G_2/M-phase cells occurred for high energy $^{12}C^{+6}$-irradiation of V79 spheroids. Irradiation at $pO_2= 147$ mm Hg showed a more pronounced G_2/M increase. The cell cycle distribution after irradiation also exhibited a phasic behavior especially for the G_2/M-fraction being much more pronounced for spheroids irradiated at $pO_2= 40$ mm Hg. The G_2/M-fraction peaks in a time interval of about two to three days. This might reflect a radiation induced cell cycle synchronization that also could correlate with the observed phasic growth behavior.

E

1. A.Kellerer (Introduction)
   (LMU, Munich, Germany)
2. Michael Scholz
   (GSI, Darmstadt, Germany)
3. Alessandro Campa
   (Inst Sup. San. and INFN,
   Roma, Italy)
4. Andrea Ottolenghi
   (Uni. Milano, INFN, Italy)

5. Robert Katz
   (Univers. of Nebraska, USA)

6. Nina Tilly
   (Uni. Stockholm, Sweden)

Treatment Planning I: The Role of Clinical RBEs
A. Kellerer (Chair)

Oral Presentations
Accounting for Radiation Quality in Heavy Ion Therapy

Estimation of Clinical RBE for Carbon Therapy

RBE evaluation of Therapeutic Proton Beams in Computer Simulations

Analysis of a Slowing down 150 MeV Proton Beam in Water: Physical Characteristics and Effectiveness in Inducing DNA Clustered Damage
Treatment Planning Problems with Range Modulated Heavy Ion Beams

Posters
The Contribution by Inelastic Nuclear Interactions to the RBE of Protons

Accounting for Radiation Quality in Heavy Ion Therapy

A. M. Kellerer, Radiobiological Institute, LMU, Munich
and Institute for Radiation Biology of the GSF - National Research Center for Health and Environment

This introductory contribution outlines the need for models and their use in radiotherapy dose planning. The linear-quadratic dose relation is now predominantly used in therapy dose planning. In Section I it is linked to the earlier quantitative scheme for conventional radiotherapy. In Section II two major approaches are presented in a form that makes them comparable; the section can be read by itself, if this comparison alone is of interest. Models for therapy planning are tools, largely of empirical character; they do not need to elucidate unknown mechanisms of radiation action. The emphasis is, therefore, on the computational scheme, not on its interpretation.

I. The Ellis formula and the linear-quadratic dose dependence

Dose planning in conventional radiation therapy has developed through clinical experience, not through models. But as clinical practise became more complex, quantitative methods were needed to determine *iso-effect* treatment plans. Formulae to compute *effective doses* - first as empirical equations then as radiobiological models - have, thus, come into use to integrate and unify clinical experience. When entirely new radiation modalities - such as neutrons and, subsequently, heavy ions - were introduced, the quantitative schemes assumed added importance, because they were required to translate gradually acquired clinical experience into a form that can support the introduction of these new treatment modalities. The subsequent considerations will explore common traits in this quantification.

The notion of an effective dose

In one of the first quantitative attempts to quantify iso-effect treatment schemes, Magnus Strandqvist (1) formulated an effective dose to the skin as the product of total dose times the total treatment duration (in days) to the power -0.22. In his formulation he did not separate between the influence of the number, N, of dose fractions and the treatment duration, T. Ellis (2,3) has subsequently refined the approach and has introduced the iso-effect relation:

$$NSD = D \, N^{-q} \, T^{-p} = d \, N^{(1-q)} \, T^{-0.11} \quad \text{with } q=0.24 \text{ and } p=0.11 \tag{1}$$

N is the number of fractions (presumed to be separated in time by one or a few days), and T is the total duration in days. d is the dose per fraction, and $D= N \, d$ the total dose. *NSD* - originally called the *nominal standard dose* but later also termed *effective dose*, C - is a measure of the effectiveness to the normal tissue of the treatment schedule. Since this discussion is concerned with the principle of the approach, there is no need to consider here the further complexities, such as the modified formulation for the effective dose to the tumor, the accounting for hypoxic tissues, or the influence of irregular or interrupted fractionation schemes.

The Ellis formula accounts for the reduced efficiency of fractionation, i.e. of the subdivision of the total dose into N fractions, on the one hand, and for the reduction of the effect due to a longer total treatment time, T. The first factor is understood in terms of the curved dose dependence of cell survival. It is more important than the second term, the dependence on T, that accounts for repopulation in the tissue. While the Ellis formula was, at least in some aspects, an oversimplification and had always been considered as such, it served well to elucidate the influence of the different factors that determine the effect of the treatment, and it can, specifically, elucidate how radiation quality is ac-

counted for. To simplify the presentation, the term in T will subsequently be disregarded, since it is not related to the dose dependence.

The implicit dose dependence for single fractions

There is no reference to radiation quality in the Ellis formula, since it relates only to x-rays or γ-rays with little assumed difference of effectiveness. But implicitely radiation quality is accounted for through the factor $N^{-0.23} D$, as has earlier been demonstrated (4) by linking the Ellis formula to the familiar interpretation of the tolerance of normal tissue or the tumor eradication probability in terms of cell killing. Assume that each of the individual dose fractions reduces the logarithm of cell survival by the decrement *ln S(d)*. The logarithm of the survival level after N fractions is then:

$$ln\ S = N\ ln\ S(d) \qquad (2)$$

Setting *S(d)* proportional to $d^{\,p}$,

$$ln\ S(d) = c\ d^{p} \qquad \text{with } p = 1/(1-q) = 1.32, \qquad (3)$$

results in Eqs(1):

$$NSD^{\,p} = N\,d^{\,p} \quad \text{or} \quad NSD = N^{(1-q)}\,d = N^{-q}\,D \qquad (4)$$

This shows that the Ellis formula corresponds implicitely to a cell survival curve that is, on the logarithmic scale, a simple power function in dose:

$$S(d) = exp(-\,c\,d^{\,p}) \qquad \text{with } p = 1.32 \qquad (5)$$

For brevity, the added term T^{-p} is here disregarded since it is unrelated to the dose dependence.

Substitution by the linear-quadratic dose dependence for use with densely ionizing radiation

The proportionality of the logarithm of cell survival to a single power ($p > 1$) of dose disagrees with radiobiological experience. It would imply an unlimited increase of total dose as the number of fractions is increased beyond the conventional treatment schedules, for example in hyperfractionation; this conflicts with clinical experience. The Ellis formula and the implied dose dependence are, thus, merely an approximation that is adequate for the conventional magnitude of doses per fraction (say 1.5 Gy to 6 Gy of photons or electrons).

In view of this fact the dose dependence (Eq(3) with $c=1$ (in the dose unit Gy) has been replaced by the more meaningful linear-quadratic relation:

$$ln\ S(d) = \alpha\,d + \beta\,d^2 \approx c\,d^{\,p} \qquad \text{with } \alpha = 0.98/Gy \text{ and } \beta = 0.138/Gy^2 \qquad (6)$$

which led to the modified Ellis formula (5), $NSD = (\alpha\,d + \beta\,d^2)\,N^{-q}\,T^{-p}$, which is here merely cited in passing to indicate the link of the current approaches in terms of the linear-quadratic relation to the accustomed formalism in treatment planning. The modification is for conventional treatment schedules equivalent to the Ellis formula. But it has the advantage that it remains applicable also for different schedules with small doses per fraction.

The linkage of the linear-quadratic dose dependence to the Ellis formula is helpful, because it connects the improved and more generally applicable computations for new treatment schemes to established radiological experience. The linear-quadratic relation had actually been introduced into dose

planning formulae (6-9), before the linkage to the conventional formalism had been pointed out. It, too, must be seen as an approximation, but its use is by now established.

An important issue in the present context is, that the linear-quadratic formula can be applied with other radiation qualities, such as neutrons or heavy ions, to obtain the tolerance dose of a treatment schedule. To this purpose one merely needs to determine the coefficients α and β of the dose relation that apply to this radiation. This would be fairly easy in those cases where the radiation quality is constant throughout the treatment field. Experiments with cell cultures could then provide the values α and β for γ-rays and the actual radiation quality, such as neutrons. The comparison of these parameter pairs would make it possible to translate the values α and β that apply to conventional treatment to the parameter pair for the radiation actually used in the treatment. Any derivation of radiotherapy parameters from radiobiological findings is, of course, tentative and needs to be fine-tuned in terms of gradually accumulated clinical observations. However the linkage to radiobiology and, specifically, to cell studies is essential, as has been seen in the tragic failure of the first attempts to use neutron therapy; successful application of this therapy became possible only much later, when cell culture work had brought out the marked differences in the sigmoid survival survival curves for photon radiation and the more linear dependences for densely ionizing radiations, such as neutrons.

Experimental radiobiological observation being more certain than the results of theoretical models, these would not be required and experimental determinations would suffice, if one dealt with one fixed radiation quality throughout the irradiation volume. In actuality, however, whenever densely ionizing radiations are employed, one encounters markedly different radiation quality throughout the field of irradiation. This complicates treatment planning, because correct parameters α and β must then be used for each point in the irradiation field. While radiobiological input from cell work remains the basis for this complicated computational task, the use of models can support it.

II. Two algorithms to account for radiation quality

The use of the models in heavy ion therapy

If ions heavier than protons are used in therapy, the radiation quality varies markedly throughout the irradiation volume. Accounting for radiation quality is, therefore, essential. In treatment with carbon ions one encounters, apart from the primary ions, only a limited number of fragmentation products. In principle, it is therefore managable to derive the coefficients of the cell survival curve directly from experiments; for the commonly invoked linear-quadratic relation these are the values $\alpha(E,i)$ and β (E,i) in dependence on ion type, i, and energy, E, per atomic mass unit. In terms of these values one must then derive appropriate average values α and β for the spectrum of particles and particle energies at any point in the irradiation field.

While this may appear as a computationally cumbersome, but otherwise fairly straightforward task, it does involve some difficulties, with the resultant need to employ models. One purpose of the models is interpolation and consistency checking of the parameters $\alpha(E,i)$ and β (E,i) that are inferred from cell and tissue studies. A second purpose is the determination of the proper averaging procedures of the parameters $\alpha(E,i)$ and β (E,i) over the particle and energy spectrum at any point in the irradiation volume. The averaging of $\alpha(E,i)$ is straightforward; a mere dose weighted average needs to be performed over particle types and energies, and this is likely to apply to all sensible models. The proper averaging of the parameter β (E,i) is a more difficult issue. *A priori* it is unclear whether one needs to employ a dose weighted averaging of the parameter β (E,i) (dimension: Gy^{-2}) or of the parameter $\beta(E,i)^{0.5}$ (dimension: Gy^{-1}), or whether a more complicated procedure must be applied. Explicit model calculations and their comparison to experimental investigations with a few suitably chosen mixed radiations may suggest answers. Such computations may not need to be repeated in all actual dose determinations or optimizations, since they can be a guide to simpler pragmatic rules. Beyond this particular issue, one must streamline the numerical procedures to achieve sufficiently rapid computations for dose optimization.

There will be two presentations in this session that relate to specific models for dose planning. The more recent treatment by Scholz and Kraft (10,11) that has been adopted for the heavy ion therapy project of the GSI and the earlier established approach of Katz (12,13) are similar, but they are also significantly different. The common basic idea - introduced by Katz - is, the utilization of the distribution of *radial doses* around the heavy ion tracks as the physical characterization of the spatial patterns of energy deposition and, based on this representation, an algorithm to convert the shape of the cell survival curve into a predicted dose dependence for heavy ion irradiation. The conversion algorithms are different in the two models and they will here be intercompared.

The concept of the *radial dose* may seem somewhat loose, but could be given a formal definition in the style of ICRU. One would then speak of a *conditional absorbed dose given the localisation of the ion trajectories, their type and their energy*. This conditional absorbed dose - for brevity the term local dose, δ, will here be used - is a random function in the irradiated medium with pronounced microscopic variations. On the track core, i.e. in the immediate vicinity of the ion trajectories, δ exhibits extremely high values; apart from the trajectories it decreases, roughly with the square of the distance. One could speak of an extended *continuous slowing down approximation* (*CDA*) that is more elaborate than the familiar concept of infinitely narrow lines, because it accounts, in addition, for the average lateral energy dispersion. Since the fine structure of energy loss straggling of the δ-rays is disregarded, the term *amorphous track model* has been used (14), with no critical connotation, since electron straggling is, in fact, nearly irrelevant in the interior of the tracks of densely ionizing heavy ions.

Since the subsequent presentations by Katz and by Scholz need to be brief - and also because somewhat different terminology is used - it is desirable to outline in condensed and comparable form their computational procedures, i.e. the conversion algorithm from the observed survival curve, $S_x(D)$, for photons to the predicted survival curve, $S_I(D)$, for heavy ions. Being well familiar with the approach by Scholz et al., but less certain about the computational method of Katz, I welcome subsequent clarifications or corrections.

Comparison of the approach for the GSI therapy program and the method of Katz

The algorithm of Katz (12):

<u>*Conversion formula:*</u>

Let $S_y (D)$ be the cell survival after a photon dose D. The survival after a heavy ion exposure with dose D is then modelled as:

$$S_I (D) = exp(- P \, \sigma_0 \, \phi) \; S_Y ((1-P) \, D) \tag{7}$$

$$P = [\, 1 - exp(- (z^2/\beta^2) / \kappa) \,]^m \tag{8}$$

> z: effective charge of the ion
> β: velocity of the ion divided by speed of light
> (z^2/β^2 is proportional to the *radial dose* at specified distance from the track)

With fluence, ϕ, in cm^{-2}, dose, D, in Gy, and linear energy transfer, L, in keV/μm one has:
$\phi = 6.25 \; 10^8 \; D / L$,   and the initial slope: $\alpha = 6.25 \; 10^8 \; \sigma_0 \, P / L$

Free parameters in the conversion formula:

σ_0 (typical value: $5 \cdot 10^{-7}$ cm^2), κ (typical value: 500)

(m is a parameter in the assumed survival curve for γ-rays, see below)

Assumed dose dependence for γ-rays:

$S_\gamma(D) = (1 - exp(-D/D_0))^m$ (the socalled *m-target dose* dependence)   (9)

Typical values of the parameters from cell studies:

$D_0 = 1.95$ Gy; $m = 2.5$

The typical values refer to mammalian cells (*Skarsgard et al* cited in (12)). For added data see (12).

The algorithm of Scholz et al (11):

Conversion formula:

Let $S_\gamma(D)$ be the cell survival after a photon dose D. The survival after a heavy ion exposure with dose D is then modelled as:

$S_I(D) = mean (exp(<lnS>))$ with $<lnS> = \int ln(S_\gamma(\delta)) \, dV/V$ (10)

where δ is the dose dependent random function *local dose* in the cell nucleus, V, which is approximated by a cylinder of radius $5\mu m$ (with axis parallel to the particle tracks). The symbol *mean (.)* stands for the expectation value which is determined by repeated random simulations of the exposure of V.

Free parameters in the conversion formula:

$D_t = 30$ Gy :   *threshold dose*, not derived from the photon irradiation experiments and, therefore,
part   of the conversion algorithm

$r = 5$ μm :   radius of the assumed critical volume, V, (not an entirely free parameter, since V
repre-   sents the cell nucleus).

Assumed dose dependence for γ-rays:

$- ln S(D) = \alpha_\gamma D + \beta_\gamma D^2$ for $D <= D_t$ (assumed constant slope for $D >= D_t$)   (11)

Typical values of the parameters from cell studies:

$\alpha_\gamma = 0.18$/Gy , $\beta_\gamma = 0.028$/Gy^2 (CHO-cells (11)).

Properties of the algorithms:

Both algorithms - although they differ substantially - have been reported to give good agreement with observed radiobiological data (11,12). They are both phenomenological, i.e. suitable to describe, interpolate and - within some limitations - predict dose dependences for complex radiation fields.

- The approach of Katz models the survival curve for heavy ion exposure as the product of a survival according to the γ-ray dependence and an exponential term. The fraction P of the dose is assigned to the exponential term (*'ion kill'*), the fraction (1-P) to the γ-ray dependence (*'gamma-*

kill'). *P depends merely on the parameter z^2/β^2 which determines the energy density within the track, i.e. at radial distances considerably less than the maximum δ-ray range. The formulae are here given for a particle of specified energy, but summation over a mixed field is straightforward, since no integrations over distributions of local dose are required.*

- Scholz models survival curves for heavy ions by an approach that averages the γ-ray response - in terms of the logarithm of the survival, *ln S_γ (δ)* - over the actual random values of local dose, δ, in a cell nucleus. The survival probability of the cell is linked to this average value. The formulae are given in general form, not linked to a particular analytical representation of the radial dose distribution. They require integrations which can be perfomed rapidly by suitable sampling procedures (11). Routine calculations can use precalculated parameters $\alpha(E,i)$ and $\beta(E,i)$ of the resulting linear-quadratic dose dependences for ions of type *i* and of energy *E* per atomic mass unit.

Scholz et al have followed Katz in linking - in terms of the radial dose distribution around heavy ion tracks - observed γ-ray survival curves to predicted dose dependences for heavy ion exposure. But different functional dependences of the γ-ray survival curve are utilized:

- The approach by Katz is related to a particular equation for the survival curve for γ-ray exposure. The reason is that the conversion formula itself contains elements - specifically the parameter *m* - , of this equation, the classical *m-target* formula with zero initial slope. The vanishing initial slope for photon exposure is inconsistent with cell studies and with clinical experience from hyperfractionation. But this may well be uncritical in computations with large doses per fraction, and it may also be uncritical for heavy ion exposures where a substantial linear component is introduced through the exponential term.

- The approach by Scholz is not *a priori* linked to a particular representation of the radial distribution and of the survival curve for γ-ray exposure. The conversion formula, and the the survival curve for γ-ray exposure are independent. The linear-quadratic dose dependence is chosen, because it accords well with the results of cell studies and because it agrees with current dose quantification schemes in radiation therapy.

If one considers the assumed radius 5μm of the cell nucleus as a free parameter, the number of parameters is the same in both approches. In both procedures two parameters are directly taken from the γ-ray survival curve. Two other parameters are determined otherwise. The approach of Katz has been applied to a wider range of radiobiological observations, and - even for mammalian cells - all four parameters have been varied. In the approach by Scholz two of the parameters, *r* and D_t , are seen as constants.

Models to account for radiation quality are essential for heavy ion therapy where one deals with varying types and varying energies of particles at any point in the irradiated volume. The two models that have here been considered are both empirical. They do not imply specific mechanisms, and - for the purpose of dose planning in heavy ion therapy - they need to be seen as mere computational tools. The two models vary considerably in their formalism, and it is, therefore, of interest whether they lead to roughly the same conclusions when applied to the same input data, i.e. the same photon survival curve determined for a specific cell line. The presentation that has here been given may motivate and facilitate such numerical comparisons.

References

1   Strandqvist M (1944) Studien über die kumulative Wirkung der Röntgenstrahlen bei Fraktionierung. Acta radiol. Suppl. LV
2   Ellis F (1969) Dose, time and fractionation: A clinical hypothesis. Clin. Radiol. 20, 1
3   Ellis F (1971) Nominal standard dose and the ret. Br. J. Radiol. 44, 101
4   Kellerer AM (1977) Grundlagen der Ellis-Formel. Strahlentherapie 153, 384-392
5   Kellerer AM (1984) Verallgemeinerung des NSD-Konzeptes auf Multifraktionierung, sowie intrakavitäre und interstitielle Therapie. Medizinische Physik, Proc. Symp., 97-108
6   Fowler JF, Stern BE (1963) Dose-time relationships in radiotherapy and the validity of cell survival curve models. Br. J. Radiol. 36, 163
7   Cohen L (1968) Theoretical 'iso-survival' formulae for fractionated radiation therapy. Br. J. Radiol. 41, 522-528
8   Cohen L (1983) Biophysical models in radiation oncology. CRC Press, Inc., Boca Raton, Florida
9   Orton C, Ellis F (1973) A simplifaction in the use of the NSD concept in practical radiotherapy. Br. J. Radiol. 46, 529-537
10 Scholz M, Kraft G (1994) Calculation of heavy ion inactivation prohabilities based on track structure, X-ray sensitivity and target size. Radiat. Prot. Dosim. 52, 29-33
11 Scholz M, Kellerer AM, Kraft-Weyrather W, Kraft G (1997) Computation of cell survival in heavy ion beams for therapy. Radiat. Environ. Biophys. 36, 59-66
12 Katz R, Ackerson B, Homayoonfar M, Sharma SC (1971) Inactivation of cells by heavy ion bombardment. Radiat. Res. 47, 402-405
13 Katz R, Dunn DE, Sinclair GL (1985) Thindown in radiobiology. Radiat. Prot. Dosim. 13, 281-284
14 Kellerer AM (1976) A survey of approaches to radiation biophysics. Microdosimetry. Proc. Symp. 409-438, EUR 5452 d-e-f, Euratom

Estimation of clinical RBE values for application in charged particle tumor therapy

M. Scholz

Gesellschaft für Schwerionenforschung, Planckstraße 1, D-64291 Darmstadt

Radiol. Klinik der Univ. Heidelberg, Im Neuenheimer Feld 400, D-69120 Heidelberg

In order to fully exploit the potential biological advantages of heavy charged particles in tumor therapy, the estimation of clinical RBE values represents an important step within the therapy planning procedure. This is a complex task, because RBE depends on the composition of the charged particle field, the dose level and the biological endpoint. In particular the dependence of RBE on the biological endpoint represents a major challenge for the estimation of clinical RBE values. It becomes evident from this tissue dependence, that RBE values obtained from *in vitro* cell survival experiments cannot be directly applied to therapy planning. However, *in vitro* experiments represent the only tool to determine the systematics of RBE values with high precision, and *in vivo* experiments mainly serve to check the estimated RBE values for selected cases. Therefore, the question raises how to link *in vitro* and *in vivo* RBE values to clinically applicable RBE values.

Within the GSI project, we have chosen an approach based on model calculations, which are tested using *in vitro* as well as *in vivo* experiments. The model calculations are based on the low-LET dose response curve, the radial dose distribution around the particle track and the target size. The model has been shown to successfully describe the complex dependencies of inactivation probabilities as a function of LET, energy and particle type in the case of mammalian cell survival [Scholz and Kraft 1996]. The computational rapidity can be considerably increased by application of certain approximations [Scholz et al. 1997], so that an application within the framework of therapy planning becomes feasible. But most important, it could be shown that the same type of calculations can be also applied to *in vivo* effects like e.g. normal tissue complications [Scholz 1996].

If e.g. for normal tissue complications α_X and β_X values, describing the photon dose response, are available from a direct analysis of experimental or clinical data, they can be used as input for the calculation as in the case of cell inactivation. Furthermore, it could be shown that even if absolute values for α and β are not available, the ratio α/β is sufficient to estimate RBE values. This is due to the fact, that according to the model calculations RBE is expected to depend mainly on the size of the shoulder of the X-ray dose response curve, i.e. on the ratio α_X/β_X. This finding is in line with experimental and clinical data, as e.g. the decreased RBE of repair deficient cell lines with correspondingly decreased shoulder of the survival curve or the higher RBE of late normal tissue complications compared to early effects for neutron therapy. In contrast, only a weak dependence on the absolute values of α and β is expected, when the ratio α_X/β_X stays constant.

The major advantage of the approach is that the calculations are closely related to the biological endpoint under investigation and that via their dependence on the photon dose response parameters they explicitly include cell- and tissue specific RBE values.

Comparing predicted RBE values with experimental data from the literature for normal tissue complications, in general agreement is found for different endpoints and treatment conditions [Scholz 1996] (Fig. 1). The model has therefore been used for estimation of RBE values for animal experiments performed in preparation of the heavy ion therapy project at GSI, as e.g. irradiation of the skin and lung of minipigs or the rat spinal cord. For the pig skin and rat spinal cord irradiation, sufficient agreement has been found [Zacharias et al. 1996, Debus 1997], whereas for the pig lung RBE values were slightly overestimated. However, due to the limited number of animals per dose group no detailed quantitative analysis could be performed in the latter case. Based on the model calculations, the influence of different tissue compositions and their respective radiobiological characteristics on the effective depth-dose profile has been determined. A compilation
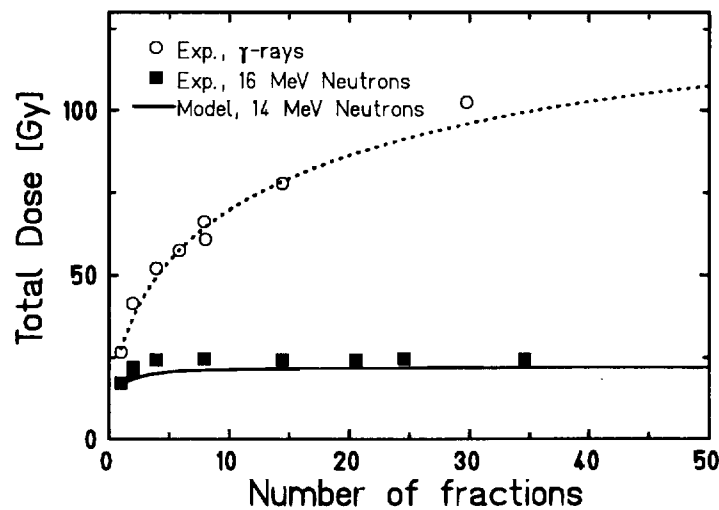
Figure 1: Comparison of model calculations and experimental results for neutron irradiation of the rat spinal cord. The induction of ataxia in 50% of the animals was chosen as endpoint. Experimental data were taken from [Hornsey 1991]. Calculations were based on α/β=6.6 as determined from a fit of the Douglas-Fowler plot of the photon data.

of the results, which are based on a tumor extension from 6 to 10 cm depth and a simulation of a two port irradiation with carbon ions, is shown in Fig. 2. Physical doses were adjusted so that in each case a photon dose equivalent of 2 Gy is delivered to the tumor. Due to the higher RBE, the physical dose corresponding to an effective photon dose of 2 Gy is considerably smaller in the case of the smaller α/β-ratio. Depending on the biological characteristics of the surrounding tissue, quite different therapeutic ratios D_{eff}(Tumor)/D_{eff}(Normal Tissue) are obtained, thus clearly demonstrating the remarkable influence of the tissue composition.

The comparison emphasizes the need for a biologically oriented treatment planning for the optimization of charged particle tumor therapy and a realistic comparison with proton and photon irradiation techniques.

1. Debus, J., 1997, personal communication

2. Hornsey, S., Experimental central nervous system injury from fast neutrons. In: Gutin, P.H., Leibel, S.A. and Sheline, G.E. (eds.), *Radiation Injury to the Nervous System*. Raven Press, New York (1991), 137-148

3. Scholz, M. and Kraft, G., 1994, Calculation of heavy ion inactivation probabilities based on track structure, X-ray sensitivity and target size. *Radiation Protection Dosimetry* 52, 29-33

4. Scholz, M., 1996, Calculation of RBE for normal tissue complications based on charged particle track structure, *Bull. Cancer/Radiother.* 83 Suppl. 1, 50s-54s

5. Scholz, M., Kellerer, A.M., Kraft-Weyrather, W. and Kraft, G., 1997, Computation of cell survival in heavy ion beams for therapy - The model and its approximation, *Radiat. Environ. Biophys.* 36, 59-66

6. Zacharias, T., Dörr, W., Enghardt, W., Haberer, Th., Krämer, M., Kumpf, R., Röthig, H., Scholz, M., Weber, U., Kraft, G. and Herrmann, Th., 1997, Acute response of pig skin to irradiation with ^{12}C-ions or 200 kV x-rays, accepted for publication in Acta Oncologica, GSI preprint 97-24
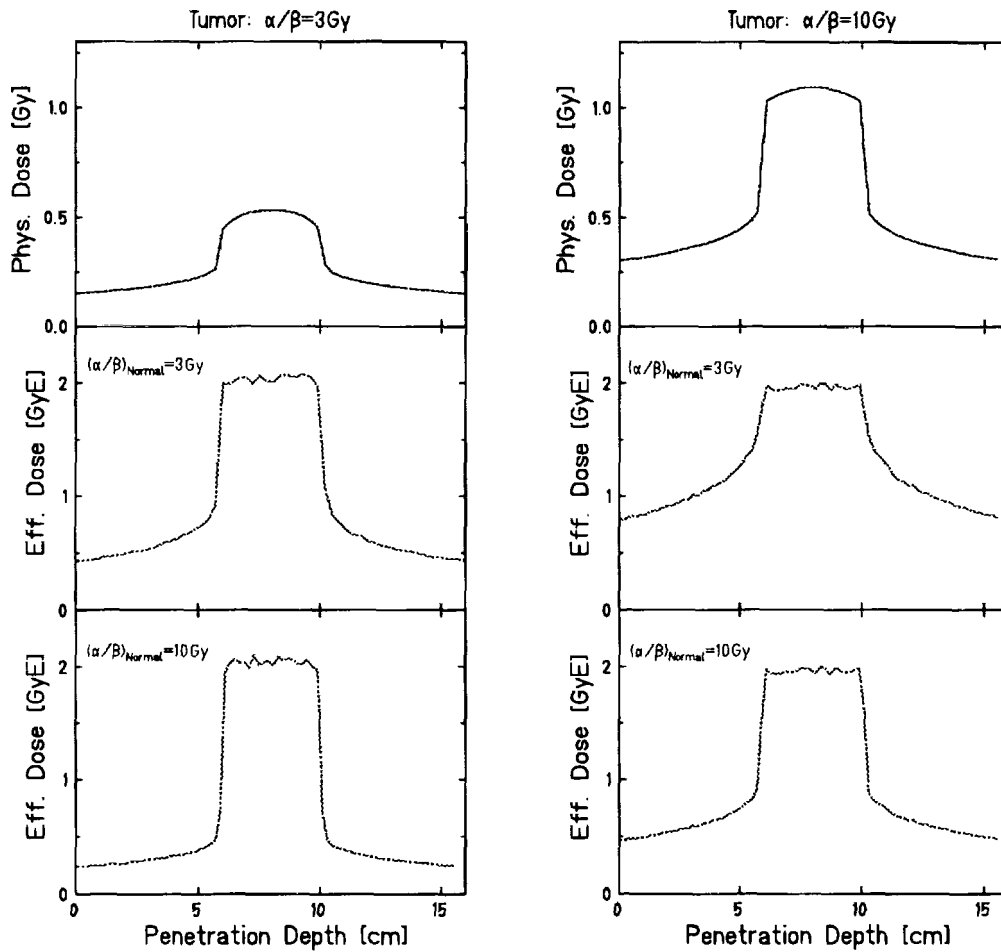
Figure 2: Comparison of physical dose profiles and biologically effective dose profiles as a function of the biological characteristics of the tumor and normal tissue, i.e. the α/β-ratio. The tumor is assumed to extend from 6 to 10cm depth, and irradiation with carbon ions was simulated. As a first approximation, the simulation is based on the effects of primary particles, because for the illustrative purposes to be considered here the influence of fragmentation is expected to be of minor importance compared to the variations due to the different tissue characteristics.

E

RBE EVALUATION OF THERAPEUTIC PROTON BEAMS IN COMPUTER SIMULATIONS

M. Belli, A. Campa and I. Ermolli[*]

Physics Laboratory, Istituto Superiore di Sanità, and INFN - Sezione Sanità, viale Regina Elena 299, 00161 Roma - Italy

The therapeutic applications of proton beams needs a better knowledge of their relative biological effectiveness (RBE). Along the path through the tissues, the energy depositions by the protons causes not only the degradation of the beam energy, but also, even in the case of originally monochromatic beams, the spreading of the energy distributions of the protons delivering a dose in any particular point. The RBE of protons is a function of their energy, in such a way that the knowledge of the dose alone, without knowing the energy of the protons that delivered the dose, is not sufficient to determine the biological effect. Therefore it is clear that, when a dose is delivered by protons distributed according to an energy distribution, the biological effect depends on the distribution; in other words, fixing the reference dose with respect to which one computes the RBE, this is a functional of the energy distribution.

We have already devised a method to compute the RBE of any given proton energy distribution, that starts from the experimental determination of the survival curves for monoenergetic protons, and uses a semi-empirical approach to obtain the desired RBE [1]. The aim of this communication is to show how, during the simulation of a proton beam that goes through a tissue, one can compute, following our method, the RBE in any given point traversed by the beam, without determining and storing the proton energy distributions that are present in the different points.

---

[*] Present address: Astronomical Observatory, viale Mellini 84, 00136 Roma, Italy

First we give a short summary of the method described in detail in [1].Considering as biological ending point the cell inactivation, we use the experimental information on its energy dependence [2,3,4]. The experimental data provided the parameters α and β of the linear-quadratic survival curve for monoenergetic protons of different energies in the range between about 0.5 MeV and about 5 MeV. In order to obtain α and β for all the energy values that are present in the proton energy distributions, we have defined, by fitting the experimental data, two functions of the energy, $\alpha(E)$ and $\beta(E)$, with the condition that at high energy they tend asymptotically to the value of α and β for X-rays, also provided experimentally.

Suppose to run a simulation of a proton beam traversing a tissue (we have used Geant in [1], that is particularly suitable to simulate also complex geometries). If at a given point the beam is composed by N_p protons distributed according the normalized energy distribution $n_0(E)$, the dose delivered is given by:

$$D = KN_p \int_{E_1}^{E_2} n_0(E)L(E)dE \tag{1}$$

where $L(E)$ is the unrestricted LET as a function of the energy, and K is a factor of proportionality. $L(E)$ can be obained, e. g., from the Tables of the ICRU Report 49 [5]. Extending the usual relation for monoenergetic protons, we have made the hypothesis that the survival S can be written as:

$$\ln S = -KN_p \int_{E_1}^{E_2} \alpha(E)n_0(E)L(E)dE$$
$$-K^2 N_p^2 \int_{E_1}^{E_2} \int_{E_1}^{E_2} \beta(E_a,E_b)n_0(E_a)L(E_a)n_0(E_b)L(E_b)dE_a dE_b \tag{2}$$

For the "interaction" term $\beta(E_a,E_b)$ we have chosen the definition:

$$\beta(E_a,E_b) = \sqrt{\beta(E_a)\beta(E_b)} \tag{3}$$

obtaining:

$$\ln S = -KN_p \int_{E_1}^{E_2} \alpha(E)n_0(E)L(E)dE - K^2 N_p^2 \left(\int_{E_1}^{E_2} \sqrt{\beta(E)}n_0(E)L(E)dE \right)^2 \tag{4}$$

2

It is now possible to compute the RBE of a beam of protons distributed according to $n_0(E)$. To this aim one can proceed as follows. Taking the X-rays reference dose D_x one computes the surviving fraction S_x for this dose (alternatively, one computes the reference dose D_x if one chooses directly the reference surviving fraction S_x). Then one puts $S=S_x$ in eq. (4) to obtain a quadratic equation for KN_p. The result is substituted in (1), thus finding D, and therefore the desired RBE.

We now show how it is possible to make the calculation of the RBE practically for as many points as desired, in spite of the fact that the RBE is, as already noticed, a functional of $n_0(E)$, and therefore in principle one should store a whole histogram for each point of interest. This possibility is a direct consequence of our definition (3), that makes the double integral in (2) factorizable, as shown in (4). We note that (1) can be written as:

$$D = N_p \int_{E_1}^{E_2} dD(E) \tag{5}$$

where $dD(E)=Kn_0(E)L(E)dE$ is the (infinitesimal) fraction of dose released at energies between E and $E + dE$. With this notation (4) can be rewritten as:

$$\ln S = -N_p \int_{E_1}^{E_2} \alpha(E)dD(E) - N_p^2 \left(\int_{E_1}^{E_2} \sqrt{\beta(E)}dD(E) \right)^2 \tag{6}$$

Although a functional of $n_0(E)$, with our expression (6) one can compute the RBE in many different points during the simulation, without the heavy storage of energy distributions. For a given chosen reference survival level, if one can compute on line the two integral terms in (6) for the points of interest, this is sufficient to obtain the RBE, since from their value one has the solution of the quadratic equation and therefore, through (5), the dose D and the RBE. The two integral terms can be computed in the following way. For a given point one can choose a small volume containing it. For any proton traversing the small volume, the difference between the incoming energy and the outcoming energy gives (neglecting the factor of proportionality depending on the mass of the volume, that at the end of the calculation would cancel out) a contribution to $dD(E)$; the energy E can be taken as the average between the incoming and the outcoming energies. In this way, using the functions $\alpha(E)$ and $\beta(E)$, one can build during the

simulation the two integral terms in (6), and besides, when they have stabilized, one can be confident that the statistics is sufficient. Let us call for brevity I any one of the two integral terms in (6), e. g. the one depending on α. If, after the passage of N protons the value of I is $I(N)$, then, at the passage of the $(N+1)$-th proton we have:

$$I(N+1) = \frac{1}{N+1}\left(N \bullet I(N) + \alpha\left[\frac{1}{2}(E_{in} + E_{out})\right] \bullet (E_{out} - E_{in})\right) \qquad (7)$$

In this way, for each point of interest we can determine, during the simulation, the value of the RBE, using the energy of the protons traversing the tissue.

REFERENCES

1 M. Belli, A. Campa and I. Ermolli, A semi-empirical approach to the RBE evaluation of therapeutic proton beams: the methodological framework, submitted to *Radiat. Res.*

2 M. Belli, F. Cera, R. Cherubini, A. M. I. Haque, F. Ianzini, G. Moschini, O. Sapora, G. Simone, M. A. Tabocchini and P. Tiveron, Inactivation and mutation induction in V79 cells by low energy protons: re-evaluation of the results at the LNL facility. *Int. J. Radiat. Biol.* **63**, 331-337 (1993).

3 M. Belli, F. Cera, R. Cherubini, A. M. I. Haque, F. Ianzini, G. Moschini, O. Sapora, G. Simone, M. A. Tabocchini, and P. Tiveron, The RBE of protons for cell inactivation: the experience with V79 cells. In *Hadrontherapy in Oncology* (U. Amaldi and B. Larsson, Eds.), pp. 702-705. Elsevier, Amsterdam, 1994.

4 R. Cherubini, F. Cera, M. Dalla Vecchia, S. Favaretto, A. M. I. Haque, G. Moschini, P. Tiveron, M. Belli, F. Ianzini, O. Sapora, M. A. Tabocchini and G. Simone, Biological effectiveness of light ions for cell inactivation and mutation induction on V79 cells. In *Proceedings of the Fifth Workshop on Heavy Charged Particles in Biology and Medicine* (G. Kraft, Ed.), pp. 73-76. GSI-Report-95-10, Darmstadt, 1995.

5 ICRU Report 49, *Stopping powers and ranges for protons and alpha particles.* International Commission on Radiation Units and Measurements, Washington D. C., 1993.

ANALYSIS OF A SLOWING DOWN 150 MEV PROTON BEAM IN WATER: PHYSICAL CHARACTERISTICS AND EFFECTIVENESS IN INDUCING DNA CLUSTERED DAMAGE

A. Ferrari, M. Merzagora and A. Ottolenghi

Dipartimento di Fisica, Università di Milano and INFN, sezione di Milano, Via Celoria 16, 20133 Milano, Italy

1. Introduction

Charged-particle beams offer several potential advantages for the treatment of localized tumors, due to their ability to conform the dose distribution. The number of centers around the world using charged-particle beams for radiotherapy is increasing, together with the research activity to improve their effectiveness. In particular, there is a strong need for a better understanding of the physical characteristics of the particle beams and the biological effectiveness as a function of depth.

It has been suggested (Goodhead, 1994) that clustered damage to DNA plays a major role in determining biological effects of radiation. In this perspective, particle fields should therefore be characterized by their capability of inducing clusters of ionizations in biological targets (Ottolenghi and Merzagora, 1997).

In previous works (Ottolenghi et al, 1997) we have simulated the induction of complex lesions (cl, operatively defined as two or more double strand breaks within 30 base pairs) by protons, alpha particles and electrons of various energies, using the track structure simulation code Mocal5 by Wilson and Paretzke (Paretzke, 1987) and a technique originally proposed by Charlton et al (1989). The results tended to support the assumption of a strict connection between the dependence of biological effectiveness on radiation quality and the induction of ionization clusters. Indeed, simulations of typical radiobiological experiments were able to reproduce the main features of inactivation RBE vs LET and particle type found experimentally (Grossi et al 1997).

Some of the contributors to this workshop have been asked to calculate the effectiveness for inactivation along a particle beam of 15 cm penetration depth. In this work we report an analysis of the physical characteristics and the effectiveness in inducing clustered lesions of a 150 MeV proton beam (15.8 cm CSDA range), 2 cm diameter and $\Delta p/p = 1\%$ (FWHM). The aim of the calculations was to investigate the effects of protons of different energies and of secondary hadrons along the particle beam, under the assumption that clustered DNA damage is a fundamental step in the process leading to cell inactivation.

2. Physical characteristics of a 150 MeV proton beam in water.

The basic code used for this simulation is FLUKA. A description of the physics of the code as well as benchmarks against experimental data on hadron production and particle transport can be found in Ferrari and Sala, 1997 and Fassò et al, 1997.

In Fig. 1 the absorbed dose deposited by the different beam components (primary protons together with secondary electrons of energy lower then 10 keV, electrons ($E \geq$ 10 keV), secondary hadrons including ions) is plotted as a function of depth (integrated over 1 cm radius). The recoil and inelastic reaction product component accounts for approximatively 8% of the dose even in the proximity of the surface, and it disappears at the Bragg peak.

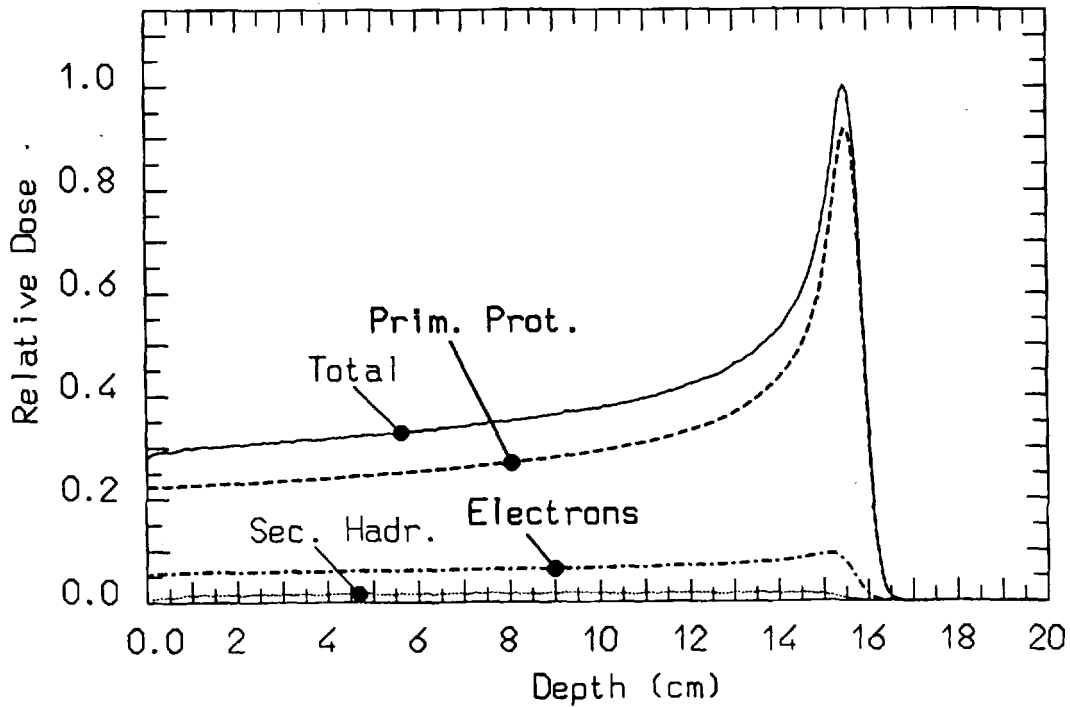**Fig. 1:** Depth-dose curve for a 150 MeV proton beam. Dose deposited by the different components of the beam are also reported. See text for details.
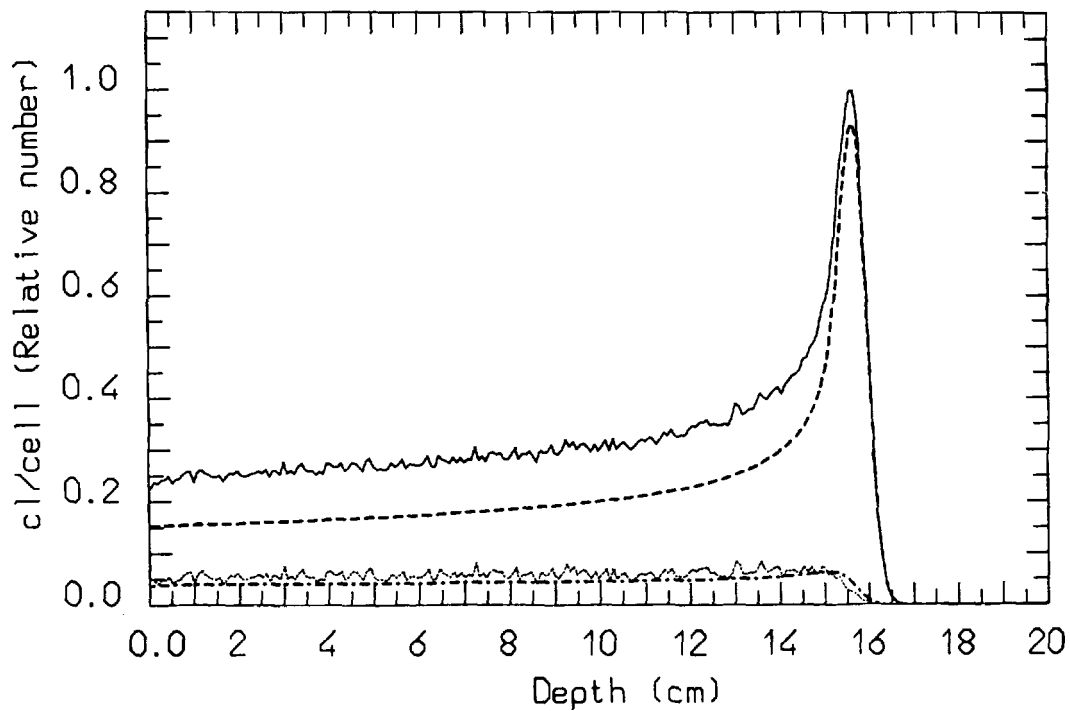

Fig. 2: Relative number of complex lesions per cell as a function of depth, induced by a 150 MeV proton beam. The separate contributions of the components of the beam are also reported. Line styles are as in figure 1. See text for details.

2

3. Clustered lesion induction along the beam

The Fluka code is able to calculate the energy deposited by the different components of the beam. We have modified the code to obtain the number of cl per dalton (or, after proper renormalization, per cell) along the beam by multiplying the dose deposited by each particle (primary or secondary) by the number of cl/Gy/dalton obtained in the simulations described in the introduction. The yields of complex lesions used as input (see Ottolenghi et al, 1997 for details) ranged from $1.5 * 10^{-13}$ cl/Gy/dalton at 4 MeV to $1.2 * 10^{-12}$ cl/Gy/dalton at 0.3 MeV for protons and from $3.6 * 10^{-13}$ cl/Gy/dalton at 5 MeV/u to $2.5 * 10^{-12}$ cl/Gy/dalton at 0.3 MeV/u for α-particles. A linear decrease with energy down to zero was assumed for energies lower than 0.3 MeV/u. For electrons, γ, protons of $E > 9$ MeV and α of $E > 50$ MeV/u a constant value of $1.0 * 10^{-13}$ was used. In this exercise, the effectiveness in inducing clustered lesions of slow heavier ions, such as oxygens, was assumed equal to the highest value for α-particles, i.e. $2.5 * 10^{-12}$ cl/Gy/dalton, although this question deserves a deeper understanding in the future.
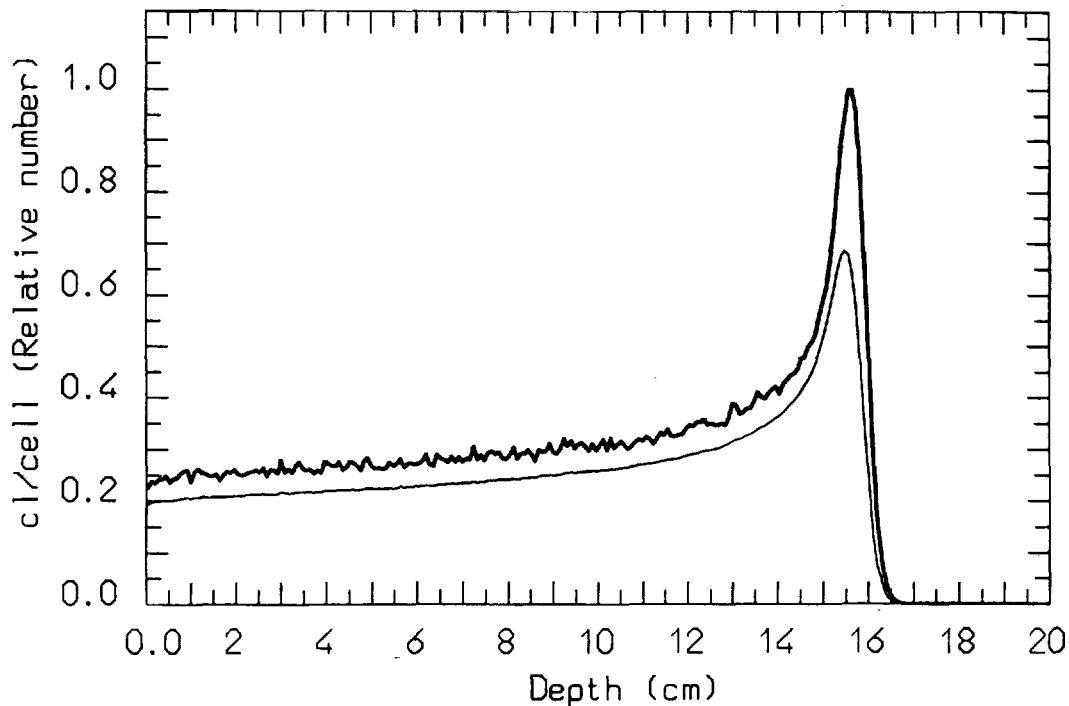
Fig. 3: Relative number of complex lesions per cell as a function of depth induced by a 150 MeV proton beam. Upper curve: the different effectiveness of the components of the beam are taken into account (same as continuous line in fig. 2). Lower curve: a constant effectiveness equal to that of γ rays is assumed.

Results of calculations are reported in Fig. 2, where the relative yield of cl/cell is reported as a function of depth, including the different contributions of the components of the beam (the same as for dose, in Fig. 1). The Bragg peak for the induction of cluster lesions is more pronounced than in the depth-dose curve, and the relative contribution of recoil and inelastic scattering products becomes more relevant.

In Fig. 3, the total yields of cl obtained taking into account the different effectiveness of the components of the beam is compared with the same yield obtained assuming a fixed effectiveness equal to that of γ rays $(1.0 * 10^{-13}$ cl/Gy/dalton). The increase in effectiveness is of a factor of ≈ 1.2 at the entrance, due to the presence of secondary particles. At the Bragg peak, the effectiveness increases to a factor of ≈ 1.5, and the peak appears slightly shifted toward larger depths; this is mainly due to the presence of low energy protons, expecially beyond the peak. The factor 1.5 is much lower than the factor ≈ 12 found by comparing the yields of complex lesions of low energy protons and of γ rays. This is due to the presence, in the Bragg peak, of a large variety of proton energies.

4. Conclusions and future developments

The calculations described in this work have to be considered as an exercise, with the only purpose of giving a rough estimation of the effects of the different components of a proton beam as a function of depth. Even so, some simple conclusions can be drawn, together with some indications for more detailed studies: a) at higher energies (before the Bragg peak) there is a significant role of secondary hadrons that give rise to an increase of a factor of 1.2 of the biological effectiveness, compared with γ rays or electrons; b) the Bragg peak of the yield of DNA cluster lesions is more pronounced than the depth-dose peak, even if the greater effectiveness of low energy protons is moderate by the simultaneous presence of low LET protons; c) the Bragg peak of the yield of DNA cluster lesions is slightly shifted to a larger depth, compared to the depth-dose Bragg peak.

These results highlight the need of a more precise and accurate knowledge of cross sections for nuclear reactions and of the biological effectiveness of ions of different types and velocities. A more precise and reliable description of RBE for inactivation requires a better knowledge of the molecular nature of relevant DNA lesions and a detailed description of the biochemical processes governing the conversion of initial lesions into observable biological end-points.

References

Charlton DE, Nikjoo H, Humm JL (1989) Int J Radiat Biol, 56, 1-19

Goodhead DT (1994) Int J Radiat Biol, 65, 7-17.

Grossi GF, Durante M, Gialanella G, Merzagora M, Monforti F, Pugliese M, Ottolenghi A (1997) In: Proceedings of the 12th Symposium on Microdosimetry. Thomas Graham House. Cambridge. In press.

Fassò A, Ferrari A, Ranft J and Sala PR (1997) In: Hirayama H (ed), KEK report Proceedings 97-5, p. 32.

Ferrari A and Sala PR (1997) In: Proceedings of the "Workshop on Nuclear Reaction Data and Nuclear Reactors Physics, Design and Safety", World Scientific, in press.

Ottolenghi A and Merzagora M (1997) In: Proceedings of the 12th Symposium on Microdosimetry. Thomas Graham House. Cambridge. In press.

Ottolenghi A, Merzagora M, Paretzke HG (1997) Radiat Environ Biophys, 36, 97-103.

Paretzke HG (1987) In: Freeman GR (ed) Kinetics of Nonhomogenous Processes. Wiley, New York, pp 89-170

Draft for Baverno, Italy, on Heavy Ion Therapy   1997

Treatment Planning Problems with Range Modulated Heavy Ion Beams

Robert Katz , University of Nebraska, Lincoln NE 68588-0111 USA
F. A. Cucinotta, NASA Langley Research Center, Hampton VA 23681-0001 USA

Range modulated beams for heavy ion therapy pose a number of special problems which become more serious the higher the atomic number of the beam of choice, both from the point of view of physics and from the point of view of biology.

From the viewpoint of physics we must know the particle-energy spectrum within the beam at every point within the patient, including fragments from the projectile and the target[1]. We must know particle trajectories which take scattering into account as well as energy loss. Isodose profiles are useless, except possibly for proton beam, but even there fragment production in the irradiated tissue, especially near the end of the range renders ineffective the use of dose as a measure of response[2] .

But knowledge of the physics alone is not enough. The radiosensitivity parameters of the cellular components of irradiated tissue vary with stage in the cell cycle, with cellular identity, with the degree of oxygenation. Even with a radiobiological model of demonstrated predictive value, such as the Katz model for which radiosensitivity parameters for many cell lines and for both oxic and hypoxic cells (but not for variations with stages in the cell cycle) are known from experiment[3], our knowledge is incomplete. Earlier work has shown that isodose profiles are not isoeffect profiles, that one can only obtain isoeffect profiles for both oxic and hypoxic cells with symmetric irradiation from opposite directions. Physiological constraints may make it impossible to achieve this symmetry. We have discussed these points earlier when our beam models had only limited validity for lack of knowledge of fragment structure[4]. Now, the study of nuclear fragmentation by the NASA Langley group can yield a superior beam model. Nevertheless it is clear that the use of RBE for treatment planning in a mixed radiation field is a basic error which cannot help but lead to difficulties. It has sometimes been suggested that one use a weighted average of RBE for different components of the beam to obtain the RBE for the mixed field. Such a procedure is only valid for 1 hit detectors, as Katz has shown, and is not valid for cells[5].

But there is another problem which has not yet been addressed, that of fractionation in a mixed radiation field of low and high LET components. In different parts of the field the ratio of gamma kill dose to ion kill dose, as described by the Katz model, will vary. We must expect that fractionation will affect the response of tissue to the gamma kill dose fraction, but not the ion kill dose fraction, just as the oxygen effect is displayed in gamma kill, but not in ion kill. We have known for many years that the variation of OER with LET parallels the fraction of the dose in the gamma kill mode[6], that at high LET the OER equals one. The RBE passes through a maximum when the gamma kill dose is about half the total dose, in a monoenergetic ion beam. This is because a further increase in the ion kill component results in overkill, hence in a loss of effectiveness.

We do not know how to adjust fractionation for maximum effectiveness with heavy ion beams. Design for fractionation will be more difficult for beams of heavier

particles. Calculations of the variation of dose in the treatment volume for range modulated heavy ion beams must be supplemented by calculation of cell killing for both oxic and hypoxic cells using appropriate cellular radiosensitivity parameters, and by calculation of the gamma kill dose across the treatment volume for both oxic and hypoxic cells using parameters now established for several cell lines as the basis for estimating the response of different cellular populations in the treatment volume. Note that if an isoeffect region is obtained by asymmetric irradiations corrected on different days by use of opposing beams to simulate effect symmetry, an additional problem will arise because of fractionation, because cells in the first day's asymmetric irradiation will repair and recover differently from the second day's irradiation.

These problems are minimal for proton therapy and increase with increasing atomic number of the heavy ion beam, where projectile and target fragmentation also pose more difficult problems.

References

[1] J. L. Shinn, R.Katz, F.A.Cucinotta,J.W. Wilson,and Duc M. Ngo, Cellular Track Model for Study of Heavy Ion Beams, NASA Technical Paper 3351, August 1993.

[2] F.A.Cucinotta, R. Katz, J. W. Wilson, L. H. Townsend, J. Shinn amd F. Hajnal, Biological Effectiveness of High Energy Protons: Target Fragmentation. Radiat. Res. 127, 130-137(1991)

[3] R. Katz, R. Zachariah, F.A. Cucinotta, and C.X.Zhang, A Survey of Cellular Radiosensitivity Parameters, Radiat. Res. 140, 356-365(1994)

[4] R. A. Roth and R.Katz, Heavy Ion Beam Model for Radiobiology, Radiat. Res. 38, 499-510(1980)

[5] R. Katz, Relative Effectiveness of Mixed Radiation Fields, Radiat. Res. 133,390(1993)

[6] R. Katz and S. C.Sharma, Response of Cells to Fast Neutrons, Stopped Pions and Heavy Ion Beams, Nucl. Instr. Meth. 111,93-116(1973)

The contribution by inelastic nuclear interactions to the RBE of protons

Nina Tilly*[1,2], Anders Brahme[1], Erik Grusell[2] and Bengt Glimelius[2]

[1] Department of Medical Radiation Physics, Karolinska Institutet and Stockholm University, P. O. Box 260, S-171 76 Stockholm, Sweden

[2] Department of Oncology, Akademiska sjukhuset, Uppsala University, S-751 85 Uppsala, Sweden

The dominant energy loss mechanism for protons in matter is through electromagnetic Coulomb interactions with electrons of the medium. However, nuclear interactions are important because it has been shown that the loss of primary protons considerably reduces the peak-to-plateau ratio (Medin and Andreo 1997).

For high energy protons, RBE values of 1.1-1.2 *in vitro* and *in vivo* have been reported (Tepper *et al.* 1977, Hall *et al.* 1978, Raju and Carpenter 1978, Urano *et al.* 1980). Since the spatial and energy distributions of electrons from low-LET protons and gamma rays are similar, the nuclear interactions might be the reason for the higher RBE of plateau protons compared to ^{60}Co γ-rays.

In this work, proton transport in tissue was Monte Carlo simulated to obtain charged particle energy distributions at different positions in the depth dose curve. The Monte Carlo code used was LAHET (Prael and Lichtenstein 1989) with the Bertini intranuclear cascade model (Bertini 1963). RBE calculations were performed using the Katz track structure model (Katz *et al.* 1971, Katz and Sharma 1973, 1974). This model has two different modes of cell killing. Gamma-kill is the result of accumulation of sub-lethal damage from delta-rays from more than one ion path. The summed, radially, effect of a single ion including its delta-rays is called ion-kill.

At higher doses where intertrack effects are important, target fragmentation is the cause of the slight increase in proton RBE from unity. Single proton tracks dominate at lower doses and the proton RBE increases due to ion kill from both primary protons and nuclear fragments (Cucinotta *et al.* 1991).

Proton RBE calculations were done for V79 Chinese hamster cells and the results were compared to experimentally obtained RBE values for similar proton beams and cell systems.

References

Bertini, H. W. Low-energy intranuclear cascade calculation Phys. Rev. 131: 1801, 1963

Cucinotta, F. A., Katz, R., Wilson, J. W., Townsend, L. W., Shinn, J. and Hajnal, F. Biological effectiveness of high-energy protons: Target fragmentation. Radiat. Res. 127: 130-137, 1991

Hall, E. J., Kellerer, A. M., Rossi, H. H. and Lam, Y. M. P. The relative biological effectiveness of 160 MeV protons-II Biological data and their interpretation in terms of microdosimetry. Int. J. Radiat. Oncol. Biol. Phys. 4: 1009-1013, 1978

Katz, R., Ackerson, B., Homayoonfar, M. and Sharma, S. C. Inactivation of cells by heavy ion bombardment. Radiat. Res. 47: 402-425, 1971

Katz, R. and Sharma, S. C. Response of cells to fast neutrons, stopped pions and heavy ion beams. Nucl. Instr. Meth. 111: 93-116, 1973

Katz, R. and Sharma, S. C. Heavy particles in therapy: An application of track theory. Phys. Med. Biol. 19: 413-435, 1974

Medin, J. and Andreo, P. Monte Carlo calculated stopping-power ratios, water/air, for clinical proton dosimetry (50-250 MeV). Phys. Med. Biol. 42: 89-105, 1997

Prael, R. E. and Lichtenstein, H. User Guide to LCS: The LAHET Code System Group X-6 MS B226 Los Alamos National Laboratory, 1989

Raju, M. R. and Carpenter, S. G. A heavy particle comparative study; Part IV: acute and late reactions. British Journal of Radiology, 51:720-727, 1978

Tepper, J., Verhey, L., Goitein, M., Suit, H. D. and Phil, D. In vivo determinations of RBE in a high energy modulated proton beam using normal tissue reactions and fractionated dose schedules. Int. J. Radiat. Oncol. Biol. Phys.2: 1115-1122, 1977

Urano, M., Goitein, M., Verhey, L., Mendiondo, O., Suit, H. D. and Koehler, A. Relative biological effectiveness of a high energy modulated protom using a spontaneous murine tumor in vivo. Int. J. Radiat. Oncol. Biol. Phys. 6: 1187-1193, 1980

F

Treatment Planning II: Dose Optimization and Inverse Planning

M. Benassi (Chair)

Oral Presentations

1. Oliver Jäkel
   (DKFZ, Heidelberg, Germany)
2. Michael Krämer
   (GSI, Darmstadt, Germany)
3. Yoshihisa Takada
   (Uni. Tsukuba, Japan)
4- Uli Weber
   (GSI, Darmstadt, Germany)
5. Enzo Menapace
   (ENEA, Bologna, Italy)
6. Dieter Schardt
   (GSI, Darmstadt, Germany)
7. Ivan Petrovic
   (Vinca, INS, Belgrade, Yugoslavia)

Treatment Planning for Heavy Ion Irradiation I

Treatment Planning for Heavy Ion Irradiation II

SOBP Formation by Two-Dimensional Array of Cone Filter
Bragg-Peak Widening Using a Ripple Filter

The Role of Nuclear Constants for Applications Related to the Proton Radiotherapy
Nuclear Fragmentation of 270 MeV/u ^{12}C Ions in Water
SRNA: A Monte Carlo Code for Proton Transport Simulation

Poster

8. Angela Mitaroff
   (GSI, Darmstadt, Germany)

Investigation of Treatment Planning Using Biological and Thermoluminescence Detectors

DE98F5428

Treatment Planning for Heavy Ion Irradiation I

O. Jäkel[1] and M.Krämer [2]

[1]*Deutsches Krebsforschungszentrum, FS Radiologische Diagnostik und Therapie*
INF 280, 69120 Heidelberg, Email: o.jaekel@dkfz-heidelberg.de
[2]*Gesellschaft für Schwerionenforschung (GSI)/Biophysik, Darmstadt, Email: M.Kraemer@gsi.de*

1 Introduction

Ions in general offer the advantage of a depth dose distribution with a pronounced maximum at large penetration depth in contrast to the exponential dose deposition of photons or the broad maximum generated by electrons. The energy dependent position of the maximum together with their charge enables an active beam delivery system, using magnetic deflection and energy variation. Light ions like ^{12}C offer further advantages over protons (or lighter charged particles): First, the lateral scattering in tissue is reduced roughly by a factor of 3. This factor arises from Highland's parametrization of Molier's scattering [1], where the projectile's charge Z and momentum p enter as $\frac{Z}{\beta pc}$. Second, they have an increased relative biological effectiveness (RBE), especially in the stopping region known as the Bragg peak.

In order to investigate if these advantages of heavy ions are clinically relevant, a clinical heavy ion therapy facility has been installed at the German Heavy Ion Research Center (GSI) during the last 3 years. The installation at GSI realizes for the first time a unique combination of a two dimensionally scanned beam [2] with an active energy variation of the accelerator. Therefore no passive beam shaping devices are necessary and the installation makes full use of all the specific properties of heavy ions.

Conformal three-dimensional treatment of deep seated tumors with this irradiation method requires an adequate selection of the beam energy and intensity for each raster point. The beam delivery thus inherently implies intensity modulation of the treatment fields. Due to the numerous parameters that cannot be fixed manually by a trial-and-error method an inverse planning procedure is used for optimization of the parameters. For photon beams computer-based planning is common practice in radiotherapy and numerous commercial and research prototype packages exist. Commercial inverse planning packages for intensity modulated photon fields are available [3]. However, due to the different interaction of heavy ions with matter and due to the special beam delivery system there are substantial differences in the planning procedure for heavy ions. Therefore new methods had to be applied to solve the inverse problem for charged particles. Packages for the graphical user interface and the handling of patient images, used for photon therapy can be adapted. A universal environment for radiotherapy planning in research and routine environments, called VOXELPLAN, has been developed [4] at the German Cancer Research Center, DKFZ. VOXELPLAN, which is mainly used for photon and electron beams was modified and is now interfaced to a package that handles heavy ion specific tasks: The newly developed GSI computer code TRiP (**TR**eatment planning for **P**articles) models the specific physical and biological properties of heavy ions and links it with the existing solutions of treatment planning and CT processing of VOXELPLAN.

In this contribution we will outline briefly the GSI beam delivery system and the qualitative differences in the methods used for inverse planning arising from it. We will describe the planning package, consisting of VOXELPLAN and TRiP and show some results for first test cases.

2 Treatment planning for Intensity Modulated Fields

The principle aim of radiation therapy is to eradicate a tumor without causing significant damage to the adjacent normal tissue, especially to organs at risk. In general a better dose conformation to the tumor increases the probability of successful treatment.

The first approach to achieve an improved dose conformation to the tumor was the application of multiple irregular fields without intensity modulation: techniques with up to 14 fields, dynamic methods including gantry rotation and multiple source techniques like the Gamma-knife. This kind

of three-dimensional therapy planning is, however, not able to conform the dose to concave shaped target volumes, e.g. tumors growing around an organ at risk. This drawback can be circumvented using intensity modulation. It can be achieved statically, using custom made irregular compensators or static multileaf collimators. With the development of dynamic multileaf collimators and scanning beam techniques a dynamic and therefore more economic application of intensity modulated fields became possible [5, 6, 7, 8, 2, 9]. Intensity modulation allows the conformal treatment not only of convex but also of concave shaped target volumes with only a few beam ports (typically 3 to 7). Examples are tumors near the rectum (e.g prostate carcinoma), near the spinal chord (e.g. lymphoma) or tumors of the brain near the eyes (e.g. meningeoma).

2.1 The inverse problem

The rationale for using intensity modulated fields for radiation treatment is given by a mathematical analysis of the so called inverse problem. We briefly outline here the case of a multiple photon field irradiation, as it is presented in detail in the literature (see e.g [10]): A two dimensionally intensity modulated radiation field k is thought of as being composed by a number of small pencil beams with different intensities. It can be described as a vector $\vec{x}^k$, the components $(x_0^k, x_1^k, \ldots, x_p^k)$ being the intensities of the p pencil beams. The contributions of q different fields can again be put into one single vector with $N = q \times p$ components. In addition the patient model, consisting of CT data, is split into voxels. If a CT scan consists of j slices with the size $l \times l$ then the dose in these voxels can be arranged as another vector $\vec{d}$ with $M = j \times l \times l$ elements:

$$\vec{x} = (\vec{x}^1, \vec{x}^2, \ldots, \vec{x}^q); \quad \vec{d} = (d_1, d_2, \ldots, d_M). \tag{1}$$

Since each pencil beam i is contributing to the dose in each voxel j with a certain weight, D_{ij}, the dose at each point can be written as:

$$d_i = \sum_{j=1}^{N} D_{ij} \cdot x_j. \tag{2}$$

This linear relation between dose and pencil beam intensity results from the linear superposition principle for dose. It is important to know that it breaks down for biological effective dose that does in general not vary linearly with dose. The matrix D_{ij} includes the complete dose calculation method. The task of finding the set of intensities x_i to achieve a prescribed dose distribution d_j (e.g. a dose of 100% within the target volume and 0 outside) is then equivalent to finding the inverse of the matrix D_{ij}. There are, however, a number of obstacles that prevent this straightforward solution of the inverse problem: First, the matrices involved are in general not quadratic and the inverse is then not well defined. Even if D is in a quadratic form, it has to be a nonsingular matrix, which also is not the case in general. Second, even if the inverse matrix D_{ij}^{-1} is mathematically well defined, it may contain negative weights, that are physically not meaningful. Finally, due to the size of the matrix it is difficult to handle them in a computer: In a typical case of 5 beams each described by 1000 pencil beams and a target consisting of 10000 voxels, the matrix size is (5000 × 10000). Thus, the inverse problem can in general not be solved and one has to find approximative solutions using optimization methods. The objective function F_1 is defined by demanding, that the mean square deviation of the dose d_i in each point i of the target T from the prescribed (constant) dose p is a minimum:

$$F_1 = \sum_{i \in T}(d_i - p)^2 = \sum_{i \in T} \left(\sum_{j=1}^{N} (D_{jk} \cdot x_j) - p \right)^2 \stackrel{!}{=} \min. \tag{3}$$

The techniques to derive a solution to this problem use different iteration methods (e.g. the Newton gradient method or stochastic methods like simulated annealing) and in addition imply additional constraints to the solution regarding the dose in normal tissue or biological effects. The different strategies are described in the following section.

2.2 Intensity modulated fields of photons and charged particles

Clinical application of intensity modulation for photon fields is currently practiced using dynamic multileaf collimators [5] and the tomotherapy method, where a nonuniform fan beam is rotated around the patient and the dose is delivered slice by slice [6]. Both techniques allow the application of multiple beams that lead to a uniform dose to the target only when they are superimposed. Due to the physics of radiation transport they provide a 2-dimensional intensity modulation for the single fields, because the depth dose behavior cannot be changed.

There are currently two major lines which are followed in order to optimize the beam weights: The first is oriented solely on physical criteria (see e.g. [11]). It uses a modified objective function where for example dose volume constraints for the organs at risk are imposed so that certain regions in a dose volume plot are excluded or absolute dose limits are set for sensitive structures like the spinal chord. Another idea is to imply biological models to directly achieve the maximum tumor control probability without normal tissue complications [12] [13] [14]. Obviously, a biological objective function is more directly connected to the aim of radiation therapy. At present, however, this approach suffers from the incomplete database for the models.

Various methods exist for modulated charged particle fields. First attempts used a broad beam with a defined spread out Bragg peak generated by modulator wheels. The field is shaped by patient specific passive devices like collimators and compensators to match the tumor in beams eye view. A compensator for charged particles does not influence the intensity of the beam, but only its range. To achieve a homogeneous spread out bragg peak the intensity of the beam has to be adequately modulated as a function of depth. This technique thus implies a 1-dimensional intensity modulation. The application of a dynamical multileaf collimator would offer 2-dimensional intensity modulation as for photons. A major drawback of this broad beam technique, however, is that the dose can not be tailored to the proximal end of the target volume, so that substantial dose is delivered to the adjacent normal tissue.

If multiple fields are used they should be optimized simultaneously. In practice, however, they are usually optimized to result in a homogeneous target dose for each single beam or in the case of patched fields covering only parts of the target volume. The number of fields used is in general smaller than for photons.

The beam scanning technique for charged particles to achieve an intensity modulated field for clinical use was investigated at NIRS (1980, [7]), Loma Linda (1990, [8]) and PSI (1991, [9]) for protons and at LBL (1989, [15]) and GSI (1993, [2]) for light ions. Together with a fast energy variation this results in a three-dimensional intensity modulation, as the number of ions can exactly be defined for each beam position and each energy. With this method a better conformation can be achieved [16], in particular at the proximal end of the target volume, where the dose in the adjacent normal tissue is substantially reduced compared to the broad beam technique. Due to this high degree of conformation that is obtained already with a single beam, 2-3 fields are sufficient for an optimal conformation. So far the single fields are optimized independently. The simultaneous optimization of several three-dimensionally modulated fields will be an important direction for future developments. The problem is that the number of optimization parameters that for each field is much higher than for two dimensions.

Compared to photon treatment planning the following issues are of special importance:

- a 3-dimensional intensity modulation as solution of the inverse problem is mandatory for charged particles;

- tissue inhomogeneities have to be accounted for more precisely than for photons;

- the quality of CT imaging is essential for the range calculation of the particles;

- for broad beams compensators have to be designed

- the rapid distal dose fall-off is potentially more dangerous in the sense of an underdosage of the tumor

In addition, for heavy ions a changing biological efficiency plays an important role. RBE in general is not a linear function of dose, i.e. the linear superposition principle in eq. (2) is no longer valid. Therefore a different iteration method has to be developed.

3   Treatment planning with VOXELPLAN

Due to the special beam delivery system used at GSI and the high flexibility needed for the planning program we decided to develop a separate package to handle the heavy ion specific aspects and interface our new software to existing products for the graphical user interface and CT processing tasks.

At the German Cancer Research Center (DKFZ) an environment, called VOXELPLAN, was developed. An important feature of VOXELPLAN [4] is that it is flexible enough to be used for treatment planning with different kinds of beams. It includes tools to guide all basic steps in treatment planning and provides formats for data exchange and an interface to dose calculation algorithms. VOXELPLAN consists of two major modules, which we will outline briefly.

3.1   Setup of the patient model

The imaging of the patient is routinely done in a CT-scanner and - in most cases - also in an MR-scanner. While the CT-data is mandatory to obtain quantitative tissue information for the range calculation, the MR-data is used to help the therapist in defining the target volume. For treatments of the head and neck region a fixation of the patient in a thermoplastic mask attached to a stereotactic ring is used. During imaging, fiducial markers are attached to the frame, thus establishing a stereotactic coordinate system that can be localized in each slice.

The data are then converted to a standard VOXELPLAN file format. After the conversion the fiducial markers are detected automatically and stereotactic coordinates are defined for each slice. This is done in the module TOMAS (TOol for MAnual Segmentation). The contour definition is then done within the same module. It is supported by a correlation of CT- and MR-images, where contours are simultaneously shown in the same slice of the two different modalities. The contour definition has to be done manually in each slice resulting in a three-dimensional patient model. The correlation technique together with the use of a stereotactic coordinate system ensures a highly accurate target definition. During positioning a stereotactic guiding frame is attached to the stereotactic ring, while the patient is still fixed by the mask. The guiding frame is used to align the target point in the patient with the reference point of the treatment room using wall mounted lasers.

As a position verification check for each individual patient, an X-ray of the patient in treatment position is done for each fraction. Thus the position of the target point can be monitored over the complete treatment, which may last over 3 - 4 weeks.

3.2   Definition of planning parameters and dose calculation

The huge parameter set of the beam delivery system requires an automatic inverse planning technique. Therefore, only the angle of the patient couch has to be defined manually and optimized by an iteration of dose calculation and graphical display of the results. This is done in the VOXELPLAN module VIRTUOS [17] (VIRTUal radiOtherapy Simulator). The selection of the table angle is supported by the beams-eye-view, where the three-dimensional patient model as seen from the beam can be rotated. Furthermore the coordinates of the target point are defined, either manually or automatically, using the center-of gravity of the target volume.

Treatment plans can also be defined to be more complex, consisting of any number of beams with different weights, to allow crossfire techniques. These plans, however, are then optimized separately and the dose is simply summed according to the weights given.

If a plan is defined, it can be saved and different dose calculations can be invoked from within VIRTUOS, to allow either optimization of physical dose or biological dose equivalent. If the dose calculation is started, the plan information is passed to a UNIX shell script which starts the heavy ion
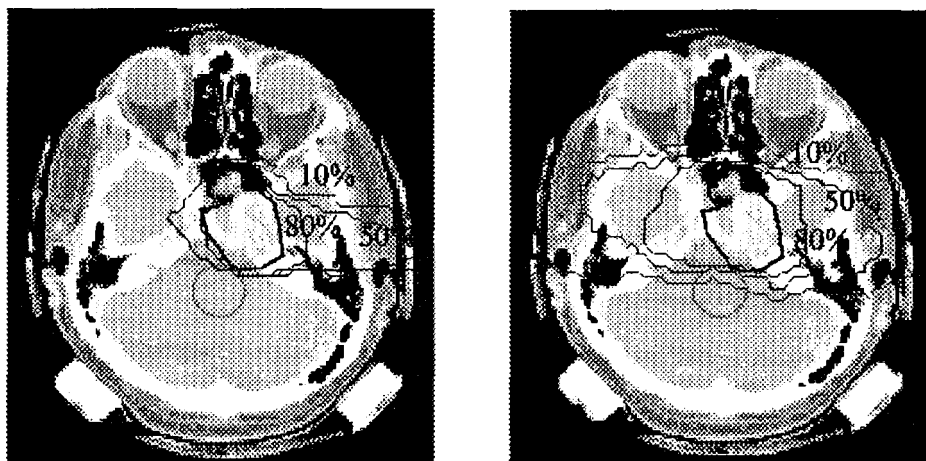
Figure 1: Treatment plans for a patient with a clivus chordoma. Dose distributoin resulting from a single field heavy ion plan (left) and three irregular fields of photons (without intensity modulation; two lateral and one anterior field). Shown is the 10%, 50% and 80% isodose line together with the contour of the target and the brain stem.

package with the desired options. This package TRiP (**TR**eatment planning for **P**articles) contains the dose algorithm and was developed at GSI.

TRiP uses the VOXELPLAN cube handling routines to generate the dose cube, so that this dose cube can be read back to the VOXELPLAN environment. TRiP also reads the contour information provided by the module TOMAS.

The dose cube can then be assessed by the therapist using the VIRTUOS result mode. To support this procedure, a set of graphical tools are available, like colourwash display of dose distributions, isodose distributions etc.

If a dose distribution is considered not to be optimal, the couch angle can be changed and the dose has to be calculated anew, possibly using different values for the primary beam width or the spacing of the scanner positions.

Fig. 1 gives a comparison of a single field heavy ion plan and a photon plan with three irregular fields of photons (without intensity modulation). It demonstrates clearly the better dose conformation
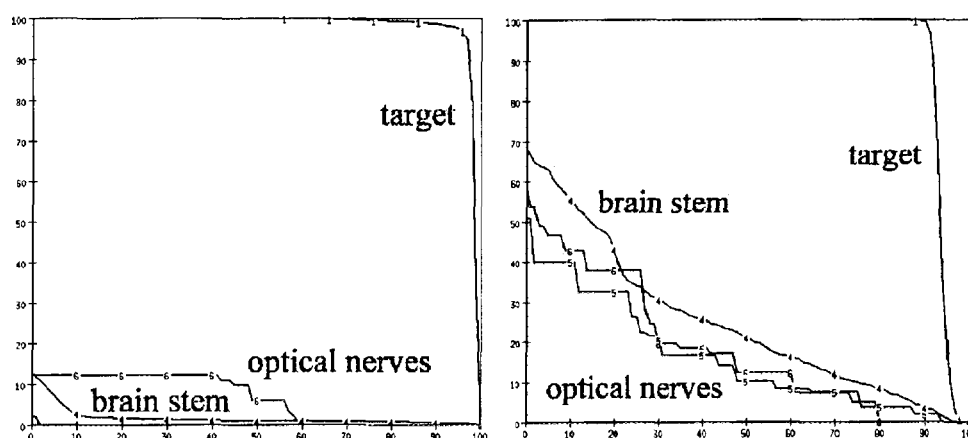

Figure 2: Dose volume histogram for the plans in fig. 1. Shown is the target, the brain stem and the optical nerves.

even of a single heavy ion field against conventional 3D treatment planning. This is also reflected in the dose volume histograms shown in fig. 2.

References

[1] V.L. Highland, Some practical remarks on multiple scattering, Nucl. Inst. Meth. 129, 1975, p.497 and 161, 1979, p. 171.

[2] Haberer Th. et al., Magnetic scanning system for heavy ion therapy, Nucl. Instr. Meth. 1993, A330, p.296-305.

[3] KonRad Inverse Planning Tool, MRC Systems GmbH, Heidelberg, Germany.
PEACOCK, NOMOS Corporation, Sewickley (PA), USA.

[4] Gademann G. et al, Dreidimensionale Bestrahlungsplanung - Untersuchungen zur klinischen Integration, Strahlentherapie und Onkologie 169, 1993, p. 159-167.

[5] C.C. Ling et al., Conformal radiation treatment of prostate cancer using inversly-planned intensity-modulated photon beams produced with dynamic multileaf collimation, Int. J. Rad. Oncol. Biol. Phys. 35, 1996, p. 721-730.

[6] T.R. Mackie et al, Tomotherapy: a new concept for the delivery of dynamic conformal radiotherapy, Med. Phys. 20, 1993, p. 1709-1719.

[7] T. Kanai et al., Spot scanning system for proton radiotherapy, Med. Phys. 7(4), 1980, p. 365-369.

[8] G. Coutrakon et al., A beam intensity monitor for the Loma Linda cancer therapy proton accelerator, Med. Phys. 18(4), 1991, p.817-820.

[9] M.H. Phillips et al., Effects of respiratory motion on dose uniformity with a charged particle scanning method, Phys. Med. Biol. 37, 1992, p. 223-234.

[10] Th. Bortfeld et al , Three dimensional solution of the inverse problem in conformation radiotherapy, Advanced radiation therapy tumor response monitoring and treatment planning, ed. A. Breit, Springer 1992, Berlin-Heidelberg, p. 503-508.

[11] Th. Bortfeld, J. Stein and K. Preiser, Clinically relevant intensity modulation optimization using physical criteria, In: Proc. of the XIIth ICCR, May 27-30 1997, Salt Lake City, ed. D.D. Leavitt and G. Starkschall, Medical Physics publishing, Madison, WI 1997.

[12] A. Brahme, Treatment optimization using physical and biological objective functions, In: Smith A. (ed.); Radiation Therapy Physics, Berlin Springer 1994.

[13] A. Niemierko, M. Urie and M. Goitein, Computer optimization of 3D radiation therapy plans with biological models of tissue response; Int. J. Radiat. Oncol. Biol. Phys. 1990, 19 Suppl. 1, p. 208.

[14] X.-H. Wang et al., Optimization of intensity modulated D conformal treatment plans based on biological indices, Radiother. Oncol. 37, 1995, p. 140-152.

[15] T.R. Renner et al., Preliminary results of a raster scanning beam delivery system, IEEE Part. Accel. Conf. Chicago, 1989, p. 672-674.

[16] M. Goitein and G. Chen, Beam scanning for heavy charged particle radiotherapy, Med. Phys. 10(6), 1983, p.831-840.

[17] R. Bendl et al., Virtuelle Therapiesimulation, Dreidimensionale Strahlentherapieplanung, DKFZ Workshop April 1995, Heidelberg 1995.

Treatment Planning for Heavy Ion Irradiation II

M.Krämer[1] and O. Jäkel[2]

[1] *Gesellschaft für Schwerionenforschung (GSI)/Biophysik, Darmstadt, Email: M.Kraemer@gsi.de,*
[2] *Deutsches Krebsforschungszentrum, FS Radiologische Diagnostik und Therapie*
INF 280, 69120 Heidelberg, Email: o.jaekel@dkfz-heidelberg.de

1   The GSI beam delivery system

The general idea of the GSI beam delivery system is to use completely active volume shaping in three dimensions. This can be achieved by magnetic deflection of the ^{12}C beam in lateral direction and by energy variation of the GSI SIS synchrotron to cover different depths in order to spread out the dose across the target volume.

The SIS accelerator provides heavy ion beams from protons to Uranium. For radiotherapy only carbon ions from 80 MeV/u to 430 MeV/u are used, corresponding to a range in tissue between 20 mm and 330 mm, respectively. The ion energy can be switched from pulse to pulse, i.e. within $\approx$ 5 seconds and thus different depths can be reached without the need of additional absorbers. The magnetic scanning system deflects the ion beam in lateral (x,y) direction across a field size of 200$\times$200 mm. The number of ions delivered at a certain position is monitored by transmission ionization chambers, thereby compensating for fluctuations in beam intensity. The computer control system is designed for a maximum number of N_E=64 energy slices and a grand total number of $N_E \times N_x \times N_y$ =524288 raster points. The irradiation time for typical cases is in the order of a few minutes.

The combination of an active energy variation with a scanning beam results in a better dose conformation compared to conventional passive beam shaping devices not only at the distal, but also at the proximal end of the target volume.

2   The heavy ion package TRiP

2.1   Requirements and design principles

The treatment planning procedures for ^{12}C ions have to account for the unique properties of the ion species (compared to e.g. protons or photons) as well as for the unique capabilities of GSI's irradiation facility.

The first requirement makes it necessary to describe the transport of ^{12}C ions in tissue in a way suitable for fast treatment planning. This rules out Monte Carlo techniques which are popular in other areas of physics. Moreover, methods developed for protons are not well suited due to projectile fragmentation and reduced lateral scattering. Last but not least the RBE dependence on particle charge and energy prohibits an optimization based on physical dose alone. It is not possible to apply the RBE as a global factor afterwards.

The second requirement forces the implementation of techniques similar to "inverse planning" in photon therapy. That is, the irradiation intensity is determined from the desired dose distribution by some optimization procedure. However, whereas in photon therapy only a few irradiation fields have to be considered the GSI scanner requires several hundreds of single scanner positions to be optimized.

2.2   Physical beam model

The most important input to the dose calculation is the depth dose $d(E_{beam}, z)$ generated by a heavy ion beam of energy E_{beam} in water or water-equivalent material at depth z. Due to energy loss straggling and projectile fragmentation the depth dose is generally different from the single particle Bragg curve. The depth doses for the various beam energies are obtained by model calculations [1] based on semi-empirical descriptions of fragment production and well-established energy loss tables [2]. The absorber under consideration (water) is divided into approximately 70 slices with thicknesses varying from 0.1 to 0.001 times the expected Bragg peak position. Within each of these material slices

the linear energy loss and the yield of outgoing particles from nuclear fragmentation of the incoming particles are computed. All fragments are propagated to the next slice and contribute to the energy loss and the next fragment generation. The calculations finally do not only yield the depth dose values but also the energy and charge distributions $\frac{dN}{dEdZ}(E_{beam}, z, Z, E)$ of the nuclear fragments as a function of depth. These spectral distributions are needed as input for the RBE calculation described later. The model calculations have been verified experimentally at several selected energies with ionization chambers in combination with variable water columns.

2.3 Physical dose calculation

For the dose calculation in first order it is sufficient to use one-dimensional dose distributions $d(E_{beam}, z)$ because the lateral beam scattering is negligible compared to the initial beam width as delivered from the accelerator. Within the target volume the overlapping of neighbouring beams compensates for the crude approximation of a gaussian profile by a delta function.

For a given particle fluence $F(E_{beam}, x, y)$ the computation of the dose $D(\vec{x})$ thus reduces to:

$$D(\vec{x})[\text{Gy}] = 1.602189 \times 10^{-7} \times d(E_{beam}, z)[\frac{\text{MeV}}{\text{mm}}] \times F(E_{beam}, x, y)[\text{mm}^{-2}]/\rho[\text{gcm}^{-3}] \qquad (1)$$

At the edges of the target volume, however, the finite width of the single beam spots has to be taken into account. After the optimization of the dose $D(\vec{x})$ the result is convoluted with the beam profile in order to obtain a realistic dose distribution for the assessment of a given plan.

2.4 Calculation of biological equivalent dose

A main advantage of heavy charged particles is their increased RBE which is due to increased local ionization density on the level of the cell nucleus. The basis for our RBE calculation is the model of Scholz [3] which converts the x-ray damage to particle damage using the radial dose distribution inside a particle track.

Due to the nonlinearity of the dose effect curve the RBE itself is dose dependent which makes it impossible to use an overall factor. The dependence of the RBE on charge and energy of the traversing particle requires the knowledge of the respective distributions in three dimensions. Fig. 1 shows a comparison of the measured and calculated survival of CHO cells as a function of depth after irradiation with 195 MeV/u ^{12}C. The very good agreement gives us high confidence in the validity of the model.

2.5 Optimization of dose

For the heavy ion therapy at GSI dose optimization means finding an optimum set of accelerator energies, E_{beam}, to cover the whole depth range and for each energy and scanner position (x, y) the corresponding particle fluences $F(E_{beam}, x, y)$ to achieve the prescribed dose. This represents a least squares minimization with fluence values $F(E_{beam}, x, y)$ as adjustable parameters:

$$\chi^2 = \Sigma_z \Sigma_{E_{beam}} W(\vec{x})(D_{prescribed} - D(\vec{x}))^2, \quad \partial\chi^2/\partial F = 0. \qquad (2)$$

with appropriately chosen weight factors $W(\vec{x})$ and the dose $D(\vec{x})$) as given by Eq. 1. Because the parameters $F(E_{beam}, x, y)$ enter linearly into Eqs 1,2 it could in principle be solved analytically. However, we are forced to use an iterative procedure, due to the obvious constraint of non-negative fluences. Even more important, the inclusion of the dose-dependent RBE, where the physical dose D is replaced by a biological dose equivalent

$$D_{eff} = RBE \times D = f(D) \times D \qquad (3)$$

introduces a nonlinear dependence of the optimization function on the optimization parameters.

Typically $\approx$ 20-30 beam energies are necessary to obtain a reasonably flat dose distribution within a volume of 2-4 cm diameter.

2.6 Inhomogeneous targets

The algorithms and procedures described so far are based on the assumption of water targets. However, biological tissues, e.g. lung and bone, have densities which differ considerably from 1 g/cm^3. The basic idea to account for it is to transform the voxels of the CT system as seen by the heavy ion beam into a water-equivalent system.

The water-equivalent path length for heavy ions has to be derived from the CT Hounsfield numbers. There is no direct functional dependence between Hounsfield number and equivalent path length because the chemical composition affects both quantities but cannot be retrieved from the knowledge of the CT number alone. However, a scatter plot of measured path length versus CT number reveals a piecewise linear relation at least for tissue equivalent materials.

3 Quality assurance

In the framework of the technical commissioning of the complete facility a quality assurance program had to be established for the treatment planning procedure. It covers acceptance tests and constancy checks, that have to be performed on a regular basis. Software checks ensure that a consistent and up-to-date dataset is used and that a proper management of programs during development is achieved. To ensure a proper program management, we introduced version control and version release for the software. Checks on the imaging devices and the positioning allow to test that position and form of anatomical structures are correctly transferred from imaging to planning computers. In addition the calculation of the target point coordinates is checked by comparing X-ray images in treatment position versus digitally reconstructed radiographs.

For a direct verification of dose calculations, measurements are done in different phantoms, to check the accuracy of the algorithm. The measurements are performed with a multichannel dosimeter (max. 24 channels), using small cylindrical ionization chambers (0.03cm^3 sensitive volume). These tests have to be performed as acceptance tests as well as regular constancy checks before each treatment period. The phantoms used are a homogeneous phantom (a water tank), an inhomogeneous phantom (a hemisphere containing certain disks and rings of lung, bone and other phantom material and a irregular phantom (Alderson head phantom). In addition very valuable information on the range of the carbon ions in tissue can be gained by measuring the activity of radioactive isotopes induced by nuclear fragmentation of the carbon ions. Using positron emission tomography, the three dimensional activity distribution in the patient can be reconstructed accurately within a few minutes. For this purpose a PET-camera has been installed in the treatment room by a group from the research center Rossendorf [4].

4 Results

The heavy ion package TRiP has already been used for the past two years stand-alone as well as in combination with VOXELPLAN for the planning of numerous irradiation experiments including inhomogeneous phantoms, TL dosimeters, cells and animals such as mini-pig lungs and the spinal chord of rats. Fig. 1 shows a real treatment plan for rat's spinal chord. An additional absorber was added in front in order to shift the range of the beam.

TRiP has been included in the VOXELPLAN environment, so that there is now a complete treatment planning package available for routine treatment planning with heavy ions. In addition, a complete set of test procedures has been developed to establish a complete quality assurance program for treatment planning. All the above mentioned tests have been performed during the technical commissioning phase of the facility in May and June 1997. Overall we observed a very good agreement of calculations and measurements.
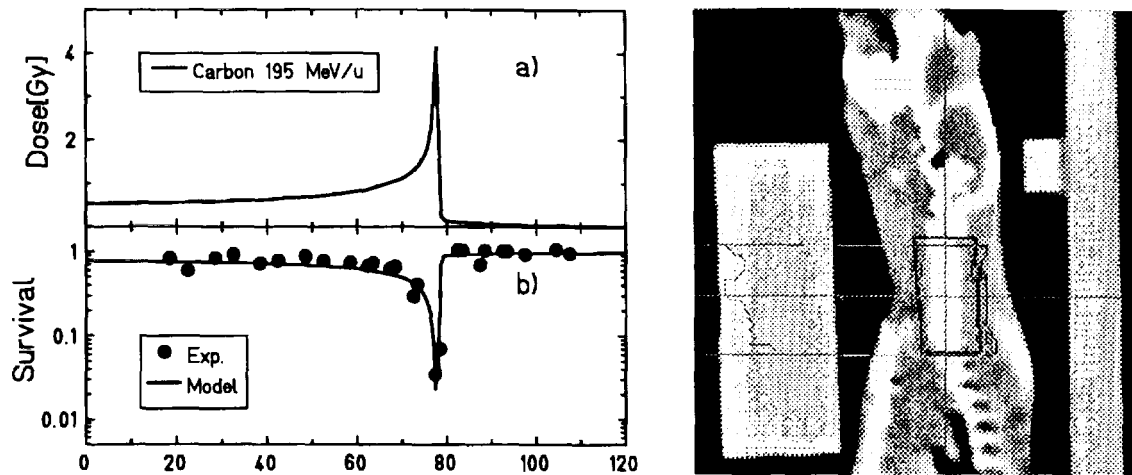
Figure 1: Left hand side: (a) Calculated depth dose, (b) measured [5] and calculated survival of CHO cells irradiated with 195 MeV/u ^{12}C. Right hand side: ^{12}C treatment plan for the rat spinal chord

References

[1] Haberer Th, Entwicklung eines magnetischen Strahlführungssystems zur tumorkonformen Strahlentherapie mit schweren geladenen Teilchen, GSI-report 1994; 09.

[2] Heinrich W, Wiegel B, Kraft G, β, Z_{eff}, dE/dx, range and restricted energy loss energy loss of heavy ions in the region $1 \leq E \leq 1000$ MeV/u GSI-report 1994; 09.

[3] Scholz M, Kraft G, Track structure and the calculation of biological effects of heavy charged particles, Adv. Space Res. 1996; 18 1/2; 5-14.

[4] J. Pawelke et al., Phys. Med. Biol. 41, 1996, p. 279.

[5] Kraft-Weyrather W, private communication.

Bragg-Peak-Widening using a Ripple Filter

U.Weber and G.Kraft (GSI Darmstadt)

The ripple filter was constructed for the improvement of the heavy-ion therapy with the raster scan system [1]. This irradiation technique combines a lateral beam scanning with a stepwise variation of the beam energy by the accelerator for a 3D conformal irradiation of deep seated tumours with a homogeneous dose distribution (or a homogeneous biological effect). Therefore the step size of the different energies has to be small enough, so that the superposition of the corresponding Bragg-curves results in a smooth extended Bragg-peak (see fig. 1).

Fig. 1: Superposition of 50 Bragg-curves for an extended Bragg-peak with a nearly constant dose in a depth range from 30 to 50mm (only the 8 deepest Bragg-curves are shown).

Especially for a low entrance depth (2-5 cm), the narrow width of the Bragg-peaks would require a large number (>100) of different energies to irradiate a tumour of average size with an homogeneous dose. This would result in an undesirable long irradiation time (1 energy step ≙ 5 s). The treatment time could be strongly reduced by widening the Bragg-peak by 1-2 mm.

The ripple (fig. 2) filter was especially constructed to solve this problem. It is a passive element for widening the Bragg-peak of a heavy ion beam and it consists of a thin plate of
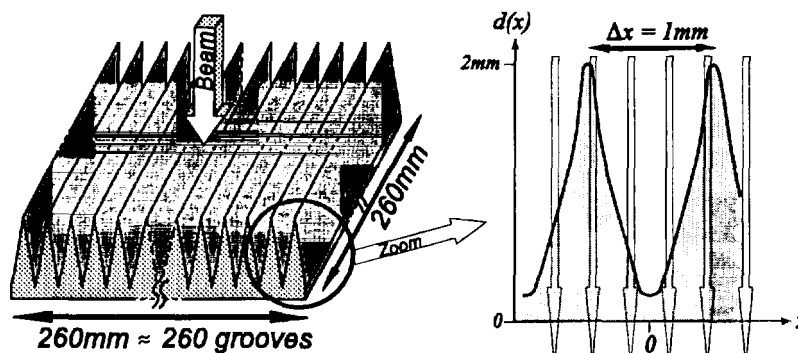
Fig. 2: Dimensions and periodical shape d(x) of the grooves of a ripple-filter.

plexiglas (PMMA) of 2 mm thickness with a periodic structure of fine grooves with a distance of typically 1 mm (fig. 2). Using a CNC-machine the grooves were precisely formed with a cutter.

Unlike the conventional rotating or oscillating range modulators, the ripple filter is motionless installed in a fixed distance of 65 cm from the patient position. A heavy ion beam passing through the ripple filter gets range modulated and the Bragg-peak width increases by 2 mm (fig. 3). The modulation effect can be described by equation 1:

$$b_{mod}(z) = \frac{2}{\Delta x} \int_0^{\Delta x/2} b(z + d(x))\ dx \qquad (1)$$

$b_{mod}(z)$ and $b(z)$ are the modulated and the original Bragg-curves. The characteristics of the ripple filter are described by the shape $d(x)$ and the distance Δx of the grooves (see fig. 2).
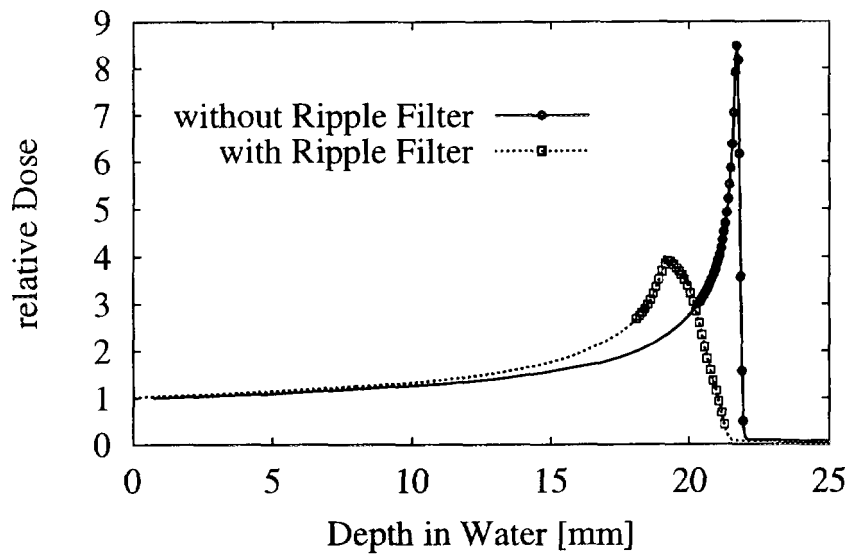
Fig. 3: Measurement of Bragg-peak widening of a heavy ion beam (^{12}C, 90 MeV/u) using the ripple filter. The shape $b_{mod}(z)$ of the modulated peak is defined by the shape $d(x)$ of the grooves of the ripple filter and the unmodulated Bragg-curve $b(z)$ (see equ. 1).

The form $d(x)$ of the grooves was designed, so that the peak of the resulting modulated Bragg-curve is nearly gaussian shaped. This gives best conditions for a smooth superposition to an extended Bragg-peak. The periodic structure of the ripple filter does not induce a lateral inhomogeneity of the dose in the target, because the structure is completely washed out due to the lateral coulomb scattering.

Using the ripple filter the number of energy steps for a superposition to a desired smooth depth dose profile can be strongly reduced in comparison to a superposition of unmodulated Bragg-curves (compare fig. 4 and fig. 1). A ripple filter with the dimensions shown in figure 1 is therefore permanently installed at the therapy unit at GSI.
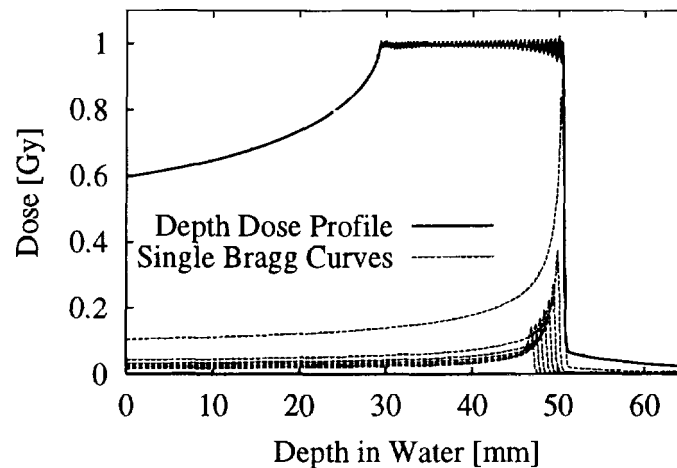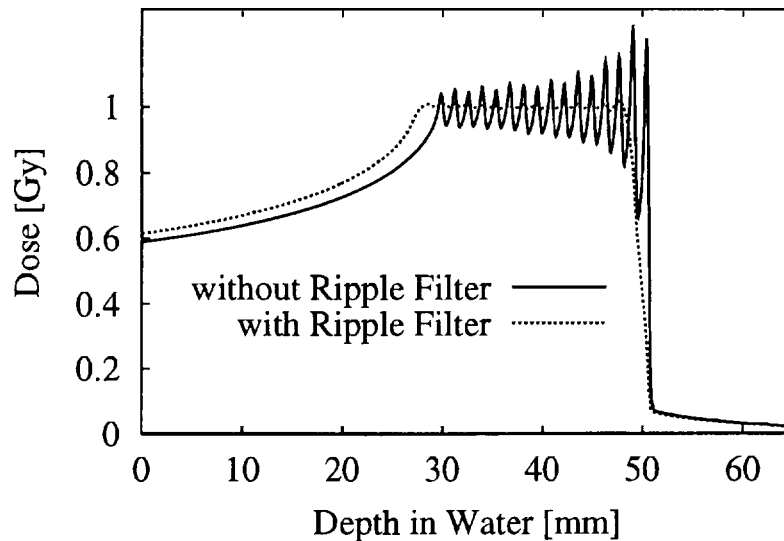

Fig. 4: Superposition of 16 Bragg-curves for an extended Bragg-peak with a constant dose in a depth range from 30 to 50mm. The depth-dose profile modulated by the ripple filter is much more homogeneous than the unmodulated one. Without the ripple filter more than twice the number of energy-steps would be required to achieve the same homogeneity (compare fig. 1).

Reference:
[1] Th. Haberer er al., NIM A330 (1993) 296-305.
[2] U. Weber, Ph.-Thesis, Hochschule Kassel (1996).

DE010813982

DE98F5425

"The Role of Nuclear Constants for Applications Related to the Proton Radiotherapy."

By E. Menapace

Abstract.

A review is presented on the exigencies and the state of the art and on the recent progresses, concerning the most important nuclear constants of interest for the present studies on the proton radiotherapy and on the related diagnostics through PET analyses.

In particular, major results on the matter are illustrated as deduced from activities in the framework of recent initiatives and Working Groups organized by the NEA-Nuclear Science Committee and by the IAEA, with the active participation by the author .

Selected topics are presented, as from direct experience, of main impact on computational simulations (typically by Monte Carlo approach) related to dosimetry and radiobiology studies, and also to shielding calculations and to simulations for treatment plannings . Moreover, the relevance of the nuclear constants is shown to the activation estimate for crucial components of the facilities.

Accordingly, typical results are reviewed, of specific impact on the present programmes for the proton radiotherapy and the related diagnostics .

Nuclear Fragmentation of 270 MeV/u ^{12}C Ions in Water

D. Schardt[1], D. Aleksandrov[2], L. Chulkov[2], M. Golovkov[2], G. Kraus[1]

[1] *Biophysik, Gesellschaft für Schwerionenforschung, Darmstadt, Germany*

[2] *Kurchatov Institute Moscow, Russia*

Beams of light ions like ^{12}C in the energy range of 50 - 400 MeV/u offer excellent conditions for the treatment of deep seated tumors because of their favourable depth-dose profile (Bragg curve) and an enhanced biological efficiency at the end of range. The slowing-down process of the beam particles is governed by continuous interactions with the atomic shell of the target nuclei (tissue), however nuclear reactions may cause a significant alteration of the radiation field and the dose distribution. In peripheral fragmentation collisions, which occur most frequently at these energies, the beam particles may loose one or several nucleons but continue travelling with nearly the same velocity and direction. This leads to an attenuation of the primary beam flux and a build-up of lower-Z fragments with increasing penetration depth. These fragments in general have longer ranges ($R \sim A/Z^2$) and therefore the depth-dose profile of light-ion beams exhibits a characteristic fragment tail beyond the Bragg peak (Fig.1, left). The transverse beam profile is superimposed with the fragment profiles which are considerably broader for the lightest fragments like hydrogen or helium (Fig.1, right). As the dose contributions scale with Z^2, this has little effect in the central part of the transverse dose profile, but gives broad low-dose tails at large penetration depths. Furthermore, the biological efficiency of the fragmentation products is different from the primary ions and therefore the composition of the particle field as a function of penetration depth has to be included in the calculation of the biological effects.
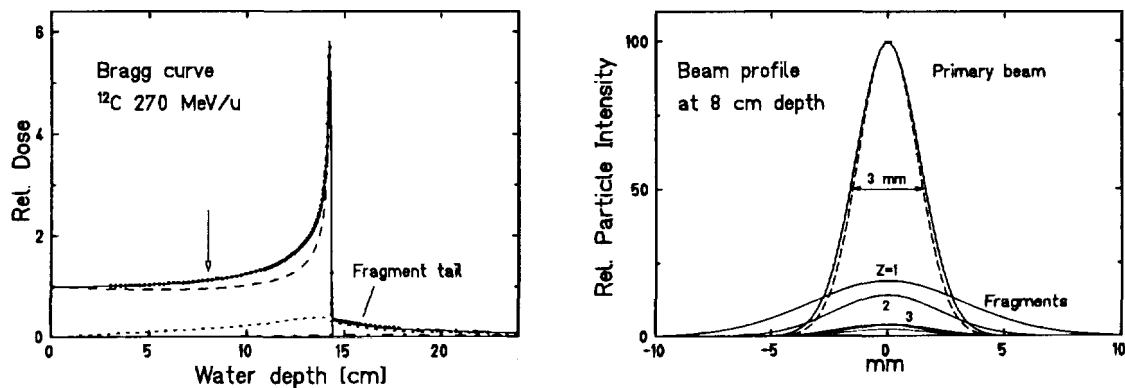
Fig.1: Left part: Bragg curve for 270 MeV/u ^{12}C ions in water measured at GSI with large parallel-plate ionization chambers. The data points are compared to a model calculation [1] (solid line). The dashed and dotted lines show the calculated contributions from the primary particles and from fragments originating from nuclear collisions, respectively. Right part: Illustration of the transverse beam profile at 8 cm water depth, based on earlier measurements at GSI [2] and this work. The primary ^{12}C beam entering the water absorber with an initial width of 3 mm FWHM (dashedline) is only very slightly broadened, whereas the lower-Z fragments show larger widths. The areas below the fragment profiles correspond to their yields at 8 cm water depth.

In previous experiments [3] at GSI the fragmentation characteristics of various light ion beams in the energy range between 200 and 670 MeV/u using water as a tissue-equivalent material was investigated. Elemental yields for projectile fragments down to Z=5 and total and partial charge-changing reaction cross sections were obtained. In continuation of these studies we present here an analysis of longitudinal and transverse momentum distributions of projectile fragments which were produced by a primary ^{12}C beam in thick water absorbers. The experimental set-up was designed for the detection of low-Z fragments including helium and hydrogen.

The arrangement of beam detectors, water absorber, and fragment detectors is shown in Fig.2. The 270 MeV/u ^{12}C beam delivered by the heavy-ion synchrotron SIS passed through a thin vacuum exit window (0.2 mm steel) and a beam counter (plastic scintillator 1.5 mm thick) which gave the start signal for time-of-flight (TOF) measurements. A multiwire proportional chamber (MWPC) was used for beam alignment. The water absorber consisted of one or two thin-walled plastic bottles, corresponding to 4.26 or 8.52 g/cm² of water. This means about 0.17 or 0.34 interaction lengths for the primary carbon beam. The projectile fragments were detected in two large scintillator arrays which are parts of the TOF-wall of the ALADIN spectrometer at GSI and were available for these measurements. They were placed about 3.4 m downstream, covering forward emission angles from 3° to 19° (array 1) and from 26° to 43° (array 2) in the laboratory frame. These detectors gave information on the fragments nuclear charge Z_f (via energy loss signal ΔE), the emission angle (detected position), and the fragment velocity (TOF).
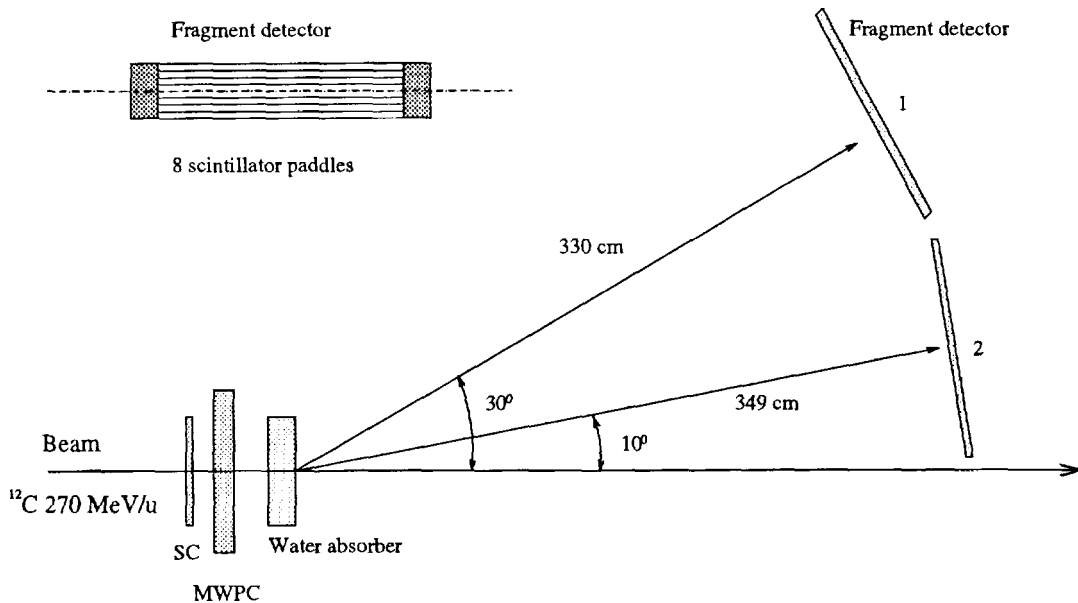

Fig.2: Experimental set-up used for fragmentation measurements. Passing through a scintillation counter (SC) and a multiwire chamber (MWPC), the ^{12}C beam hit a thick water absorber. The emerging projectile fragments were detected in two large position-sensitive scintillator arrays. The velocities of the fragments were obtained from time-of-flight measurements.

The position spectra which were measured with the scintillator arrays were transformed to angular distributions of the fragments in the laboratory frame. The effect of multiple scattering of fragments in the target material does not play a significant role for the absorber thicknesses used here and was not taken into account. The longitudinal momentum distributions of the fragments were obtained from the measured TOF-spectra. The overall TOF resolution of 0.5 ns FWHM corresponds to 17 MeV/c/u in the momentum (velocity) scale and does not significantly affect the widths of the measured longitudinal momentum distributions.

As an example, the measured angular distribution of helium fragments and the longitudinal momentum distributions of fragments with nuclear charges Z=1 to Z=5 are shown in Fig.3. For the helium fragments we find that both transverse and longitudinal momentum distributions are well described by two Gaussians in the rest frame of the projectile. This behaviour is not understood, but a similar picture has been observed for beryllium and boron isotopes in fragmentation of carbon beams on boron, carbon and silver targets [4].
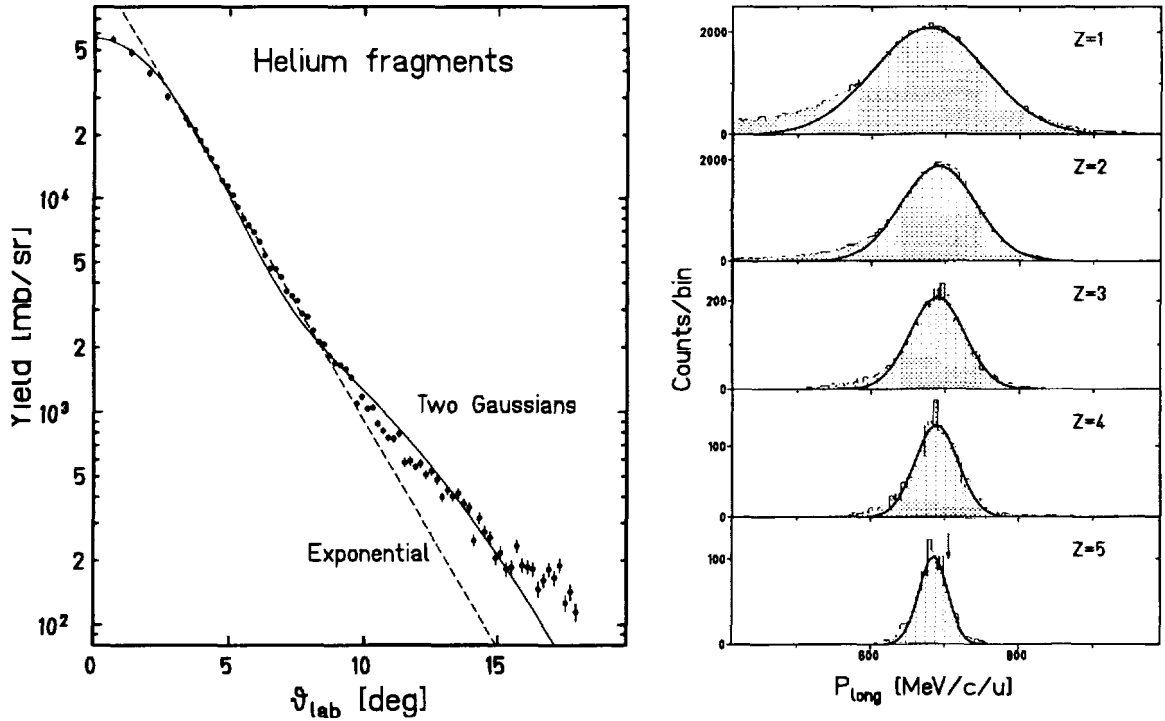
Fig.3: Measured angular distribution of helium fragments produced by an incidident 270 MeV/u ^{12}C beam after penetration of 4.26 g/cm^2 of water (left part). Data from earlier measurements at small angles ($\vartheta_{lab} < 4^0$) are included. Longitudinal momentum distributions obtained from time-of-flight data are shown for lower-Z fragments with nuclear charges Z=1 to Z=5 (right part). The arrow indicates the initial momentum of the primary ^{12}C ions.

The elemental fragment yields for a 4.26 g/cm^2 water absorber are shown in Fig.4. They are defined here as the total number of fragments with a given nuclear charge normalized to the number of incoming beam particles and were obtained by integration of the measured angular distributions. The highest yields were observed for hydrogen (0.24) and helium fragments (0.12). The comparison with predictions of the NUCFRG2-code [5] shows reasonable agreement except for hydrogen, where the calculated yield is a factor of 2.5 higher.
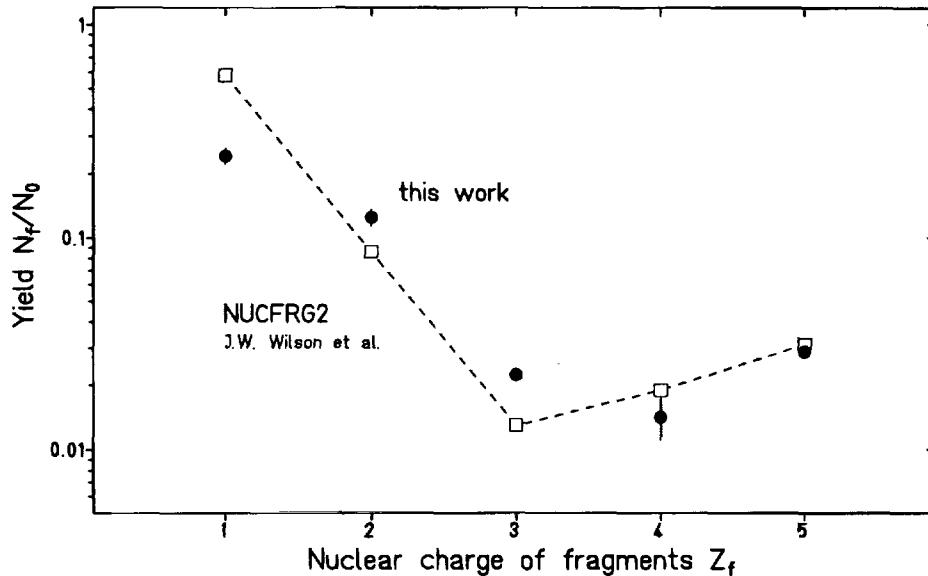
Fig.4: Yields of lower-Z fragments from a 270 MeV/u ^{12}C beam passing through a water absorber of 4.26 g/cm^2 thickness. The data are compared to predictions (open squares) of the NUCFRG2-code [5].

Our fragmentation measurements were intended as a contribution to an experimental database for the physical models used in therapy planning codes. Such data are of particluar importance for the planning and verification of 3D-irradiation profiles using pencil-like ion beams with fast scanning techniques.

[1] L. Sihver, D. Schardt, T. Kanai: A model for calculating depth-dose and fluence distributions, GSI Scientific Report 1994, 221 (1995)

[2] U. Weber: Volumenkonforme Bestrahlung mit Kohlenstoff-Ionen zur Vorbereitung einer Strahlentherapie, Thesis, Darmstadt 1996

[3] I. Schall et al.: Charge-changing nuclear reactions of relativistic light-ion beams (5≤Z≤10) passing through thick absorbers, Nucl. Instr. and Meth. B 117, 221-234 (1996)

[4] C. Guet: Nucl. Phys. A 400, 191c-220c (1983)

[5] J.W. Wilson et al.: NUCFRG2: An evaluation of the semiempirical nuclear fragmentation database, NASA Technical Paper 3533 (1995) and R.K. Tripathi, private communication

SRNA: A Monte Carlo Code for Proton Transport Simulation

Radovan Ilić and Ivan Petrović

VINČA Institute of Nuclear Sciences
P.O. Box 522, 11001 Belgrade, Yugoslavia

1. INTRODUCTION

The SRNA code is being developed for the simulation of the proton transport using the Monte Carlo method for numerical experiments in dosimetry, radiation protection, radiation therapy and other numerical experiments with protons. The creation of this code represents the continuation of an earlier work dedicated to the development of the FOTELP code designed for the transport of photons, electrons and positrons using the Monte Carlo techniques. The SRNA code is in operation for the three-dimensional (3D) geometry with the arbitrary proton spectrum coming from the source where the geometry of a material medium can be described with the surfaces up to the second order. The transport of protons is based on the theory of condensed history, i.e., on the model of multiple scattering on the step-length of the proton range. Along the step-length of the range the average energy loss is determined while the corresponding fluctuations are obtained from the Vavilov's distribution. The proton deflection angle is evaluated from the Molière's distribution based on the multiple scattering condition. According to dimensions of the absorber corresponding algorithms are applied for the energy absorption in 3D geometry including corrections of proton trajectories. The current version of the code is operational for the proton energy range being from 100 keV to 250 MeV for water, and under 100 MeV for materials of arbitrary composition ($Z=1$ to $Z=92$). The SRNA code calculates the probabilities for the proton to be transferred from one state of the phase space to another. Further development of this code will include nuclear reactions as well as the transport of secondary particles created in these reactions. The work on this additional development of the SRNA code coincide, not without reason, with the terminal phase of construction of the VINCY Cyclotron which is the main part of the TESLA Accelerator Installation in the VINČA Institute of Nuclear Sciences. Thus, the code should serve in planning and interpretation of experiments as well as therapy with protons.

2. PROBABILITY CALCULATIONS

According to the theory of condensed history[1], on the step-length Δs, a proton looses the average energy ΔT. The proton step-length Δs is evaluated by integrating the stopping-power over energy from ΔT to $T+\Delta T$, while the stopping-power is calculated according to the model and the data used in the code TRIM[2]. The fluctuations of the average energy loss are described by the Vavilov's distribution[3]. The SRNADAT module of the SRNA code prepares the inverse Vavilov's distribution for which a new approach of numerical integration has been developed[4]. To prepare probabilities for the transfer of protons from one point of the phase space to another the logarithmic scale of energy decrease (the continuous slowing-down approximation) $T_{n+1}=T_n/2^{I/m}$ has been adopted, where the values of m are from 8 to 32 depending on the geometry resolution of the proton transport simulation. At each proton step-length Δs the inverse Vavilov's distribution is calculated for several hundreds preselected probabilities.

When using the Monte Carlo simulations of the charged particle transport usually Molière's[5] or Goudsmit-Saunderson[6] angular distributions are employed. In the model applied in this code the preparation of probabilities is performed using the Molière's angular distribution including the Fano's correction[7]. In the SRNADAT module for each proton step-length Δs the inverse angular distribution as a function of cos ϑ is evaluated for about 100 values of preselected probabilities.

In all applications of the Monte Carlo techniques the central position belongs to the methods for preparation of the probabilities for the transfer of protons from one point of the phase space to another. That is why in the development of the SRNADAT module special attention has been dedicated to this problem. For numerical experiments given in this paper the logarithmic energy scale has been chosen with energies being from 0.1 MeV to 250 MeV and having 452 points. The inverse angular distribution has been prepared for 452 x 361 values, while the energy loss by ionization for 452x801 points. Using these data and cross sections for scattering on nuclei (non-nuclear reactions) it was possible to verify the quality of the probabilities.

3. SIMULATION TECHNIQUE

The RFG module[8] provides an efficient geometrical support of the SRNA code. It calculates in 3D geometry and for each segment of the proton trajectory the intersection of the straight line (which is collinear with the particle velocity) with the surfaces of the first and second order. The index of the corresponding zone and the shortest distance to the next zone provide geometrical tracking of the proton history in the space. In such geometry the proton energy, its initial coordinates and its velocity unit vector are chosen from corresponding distributions in the reference coordinate system. The proton energy loss is calculated along the proton trajectory at each step-length Δs, while its fluctuation is determined from the Vavilov's distribution. The energy lost along the step-length Δs is assumed to be uniformly absorbed. The random cos ϑ of the scattered proton is chosen from the Molière's inverse angular distribution and the proton having reduced energy is shifted to the end of the path Δs. Whenever the proton changes the zone the simulation is performed with the probabilities corresponding to that zone. If Δs is greater than the shortest distance l to the boundary of the following zone the loss of energy is weighted by the ratio $l/\Delta s$, thus the proton enters into the following zone with the energy reduced precisely by this weighted energy loss. This kind of modeling enables a physically more accurate treatment of the influence of different material media at their zone boundaries. The proton history ends when it leaves the material zones or when its energy reaches the chosen cut-off energy.

The number of protons coming from the source is divided into at least 20 batches in order that the Central Limit Theorem could be applied to estimate the statistical error. The proton energy loss, i.e., the absorbed energy is recorded in the channels of the geometrical mesh. When all proton histories are brought to an end one obtains the space distribution of absorbed energy. During the simulation other values necessary for the estimation of the fluence at the zone boundaries and of the proton leakage fluence are registered as well.

3. NUMERICAL EXPERIMENTS

The SRNA code has been tested on a water phantom using proton beams of 26.4 MeV, 62 MeV and 160 MeV. The beam of 5000 protons penetrates the half space which simulates an semi-infinite phantom. In numerical experiments the absorbed energy in the phantom has been simulated with the statistical error being smaller than 1%. The history of each proton has been followed from the initial energy to the cut-off energy of 100 keV. The simulation of the proton

10. G. Cuttone, Private communication, INFN-LNS, Catania, Italy (1997)
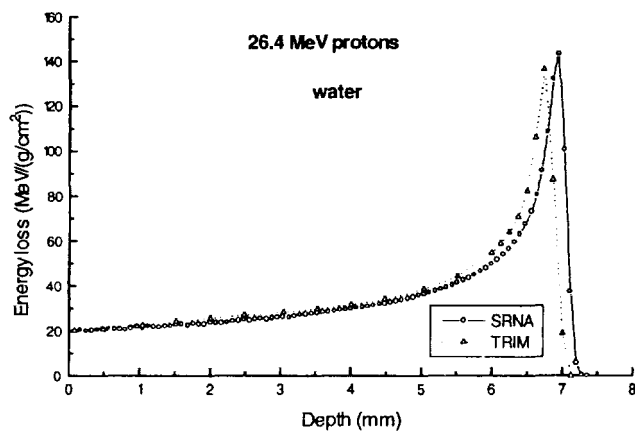11. A. Fasso, A. Ferrari, P. Sala and J. Ranft, FLUKA-94/95, CERN, TIS-RP (1995)
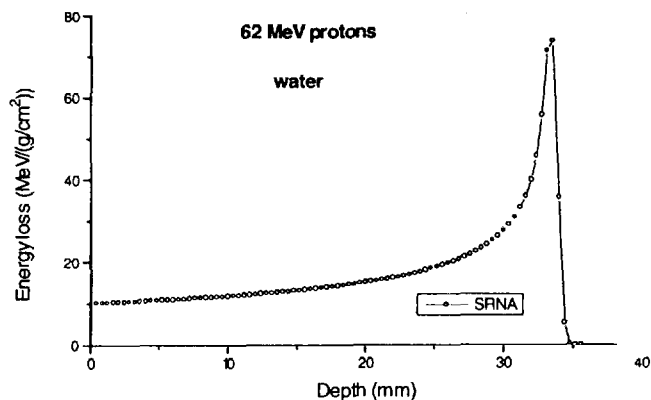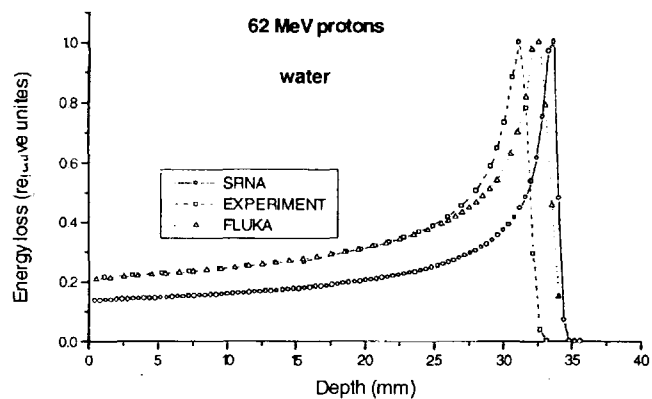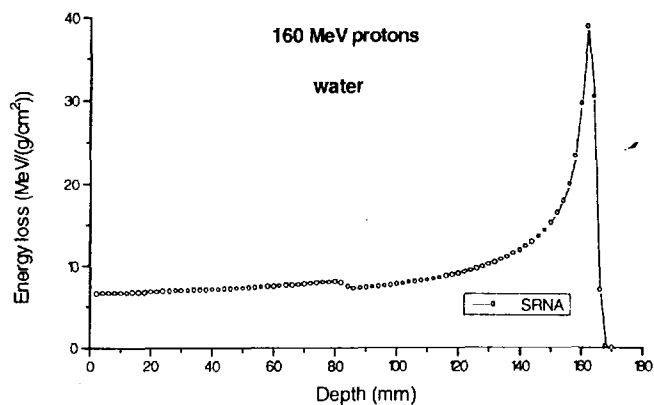

Figure 1.

Figure 2.

Figure 3.

Figure 4.

transport has been carried out with 20 batches. The proton energy loss distribution as a function of depth has been given in Figures 1 to 4.

In Figure 1. the comparison of the proton energy loss distributions, corresponding to incident protons having energy of 26.4 MeV, obtained by the codes TRIM[2,9] and SRNA show certain discrepancy that increases with the depth and is most important at the Bragg's peak. This might be explained by the fact that the energy mashes and cut-off energies used by two codes were not the same. Figure 2. gives the energy loss distribution as a function of depth obtained by the SRNA code for the incident protons of 62 MeV. In Figure 3. this distribution has been compared with the distributions obtained by an experiment[10] and by the FLUKA code[10, 11] where previously all distributions have been normalized to their maximum values. Although this normalization could hide some effects certain comments can still be made. Here one can notice that the energy loss distribution obtained by the SRNA code differs from two other distributions along the whole depth. This is mostly the consequence of the fact the SRNA code does not take into account nuclear reactions and the transport of secondary particles which become important approximately at 60 MeV. In addition the explanation given in the previous case is valid here as well. Figure 4. gives the energy loss distribution as a function of depth obtained by the SRNA code for the incident protons of 160 MeV. One can notice again certain problems that have already been mentioned.

4. CONCLUSION

Numerical comparisons performed here show that an additional work has to be done to improve the SRNA code. Especially, further development of this code will include nuclear reactions as well as the transport of secondary particles created in these reactions. The SRNA code will be probably used in the near future for planing and interpretation of the experiments and therapy with protons, since the TESLA Accelerator Installation includes, apart from the VINCY Cyclotron, a number of experimental channels. Two of these channels will be using proton beams. The experimental channel for radiation physics, radiation chemistry and radiation biology will be using proton beams with the energy up to 30 MeV, while the channel for proton therapy will be using proton beams with the energy of about 75 MeV.

REFERENCES

1. M. J. Berger, Monte Carlo calculation of the penetration and diffusion of fast charged particles, in Methods in computational physics, Vol I, p.135, Accad. Press, N.Y. (1963)
2. J. P. Biersack and L. G. Hoggmark, A Monte Carlo Computer Program for the Transport of Energetic Ions in Amorphous Targets, Nucl. Instr. and Methods, 117, p.257 (1980); J. F. Ziegler, TRIM, Version 95.4.
3. P. V. Vavilov, Ионизационнье потери тяжелнх частицбольшнх энергий, ЖЭТФ, Т.32.внп.4, с.920 (1957)
4. R. D. Ilić, Vavilov's Distribution Data Preprartion for Heivy Charged Particles Transport by Monte Carlo, XLI ETRAN Conference, Zlatibor, Yugoslavia, Jun 3-6, 1997
5. G. Moliere, Theorie der Streuung schneller geladener Teilchen II: Mehrfach - und Vielfachstreuung, Z.Naturforsch 3a, p.78 (1948); H. A. Bethe, Moliere's theory of multiple scattering, Phys. Rev., 89, p.1256 (1953)
6. S. Goudsmit and J. L. Saunderson, Multiple scattering of electrons, Phys. Rev. 57, p.24 (1940)
7. U. Fano, L.V. Spencer and M. J. Berger, Penetration and diffusion of X-rays. in Encyclopedia of Physics, Vol 38/2, 660, Springer, Berlin (1959)
8. D. V. Altiparmakov and P. Beličev, An efficiency study of the R-function method applied as solid modeler for Monte Carlo calculations, Progres in Nuclear Energy, vol.24, p.77 (1990)
9. L. Torrisi et all., Energy loss measurements of 27 MeV protons irraditing water-equivalent materils (to be published in Nuc. Instrum. Methods)

DE010814012

Investigation of Treatment Planning using Biological and Thermoluminescence Detectors

A. Mitaroff, W. Kraft-Weyrather, G. Kraft

Gesellschaft für Schwerionenforschung, Planckstr. 1, D-64291 Darmstadt

Introduction

As a consequence of the different spatial energy distribution particle radiation inactivates cells more effectively than photon radiation. The RBE - Relative Biological Efficiency - is defined as the ratio of the heavy ion dose to the dose of the reference radiation for the same biological effect (in our case 250 kV X-Rays are taken as a reference). Experiments[1] and model calculations[2] have shown that the RBE is a function of LET and energy. Carbon ions have their maximum of RBE nearby the Bragg Peak. By overlaying many Bragg curves an enhanced RBE all over the extended target volume can be reached. The aim of cancer therapy is inactivating cancer cells to a certain surviving level, this means getting an isoeffect in the extended target volume. For irradiation of each point in this volume with the raster-scanner system[3] the knowledge of the number of particles per raster-point is required. Complex calculations taking into account RBE and fragmentation spectra are necessary[4, 5] to get this appropriate particle distribution. We wanted to verify the predictions of these calculations and the beam quality using Chinese Hamster Ovary - CHO - cells as biological detectors. Additionally we measured the physical dose distribution and the beam quality using Thermoluminescence Detectors - TLDs.

In certain respects Thermoluminescence materials react similar to biological systems. Due to the different spatial distribution of ionisation events the dose response of the TLDs differs between low and high LET radiation which can be expressed in analogy to the biological RBE,

$$RBE = \frac{D_{HI}}{D_{ref}}\bigg|_{isoeffect} \qquad \text{as the efficiency:} \qquad \eta = \frac{(TL/D)_{HI}}{(TL/D)_{ref}}$$

the ratio of TL light output per dose for heavy ions to TL light output per dose for a reference radiation (for example 250 kV X-Rays). The efficiency is a function of heavy ion energy and charge. Our dosimetry measurements base on the model of M. Krämer and O. Geiß which calculates the TL efficiency for a wide range of energy and ions[6]. That has been verified in former experiments[6].

Experimental Setup for Biological Dosimetry

Chinese Hamster Cells CHO K1 were grown as monolayers on slides - 52mm length, 9mm width, 1mm thickness - made of polymethylpentene submerged in Pan's F12 medium supplemented with 10% fetal calf serum, 1% glutamine, 0.5% penicillin and streptomycin. Under these conditions the cells have a doubling time of 12 hours and a plating efficiency of about 90%. Immediately before irradiation the slides were put into the phantom filled with Pan's F12 medium supplemented with 0.5% penicillin and streptomycin only . The phantom is a cylindric container made of acrylic glass. It is 200mm high, has 5mm thick walls and can be closed watertight. Both ends of the slides were fixed vertically on a plastic frame lattice so that the slides could not disarrange. Figure 1 shows a plan view of the phantom. The lattice consists of 33 rows - between 2 and 12 slide positions per row - in beam direction. Two neighboured rows are moved against each other by the half distance to extend the resolution. Thus we get a resolution of 5mm in beam direction and 7.5mm perpendicular the beam direction. The irradiations were carried out with

carbon ions in the medical Cave of our facility. We treated various target volumes in different depths. After irradiation the slides were trypsinized, diluted with fresh medium, counted with a Coulter counter and plated at the appropriate concentration for cell survival. After 7 days of incubation at $37°C$ the cells were stained and the colonies were scored for survival evaluation.
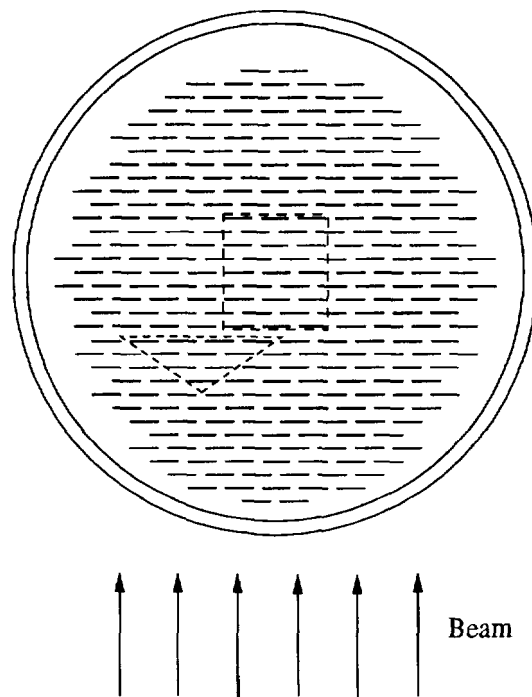
Figure 1: a plan view of the experimental setup

Experimental Setup for TLD Dosimetry with LiF Chips

For comparison with the biological dosimetry we used the same experimental setup for physical dosimetry. But instead of biological cells and medium we took small LiF chips - 3x3x0.38mm^3 and water. We sealed the chips in transparent film to avoid chemoluminescence of LiF with water. After irradiation, readout of the TLDs was done with a Harshaw Series 8800 system. The chips were heated to a temperature of $300°C$ with a constant heating rate of $25°C/s$. The chips were held at this temperature for 20s, following by a $400°C$ annealing for 20s.

Results

Two different volumes have been irradiated, yet: A cube and a prisma with triangular base. Figure 1 shows the positions of these volumes in our phantom. The cube was placed centric in order to compare our results with former stack experiments[7]. The prisma was positioned acentric to get the curvature of the phantom into the calculations. In both cases survival level of about 12% were planed. The curve in Figure 2 shows the appropriate calculated TL response[6] of the isoeffect cube for a cut through the isocentre in beam direction. The symbols are our measured TL responses with TLDs. The curve in Figure 3 shows the calculated survival[4, 5] of the prisma for a cut through the isocentre, again. The symbols here are our experimental data

with CHO cells from one experiment. The error bars shown in Figure 2 are estimated from the knowledge of cell behavior known from former survival curves.
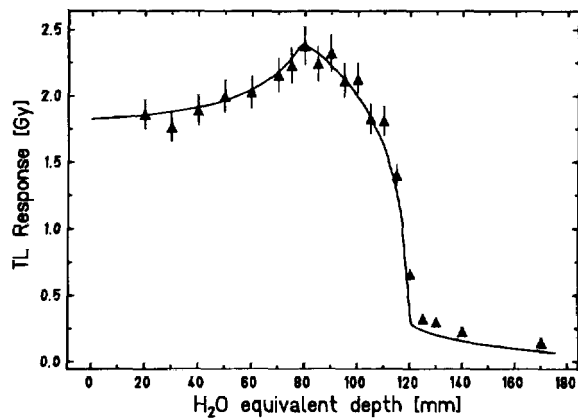
Figure 2: TL light output as a function of depth   Figure 3: Survival as a function of depth
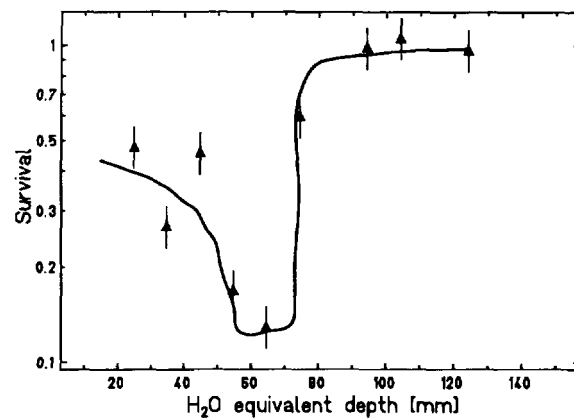
Some of our experiments are not in such a good agreement with the calculated data as the experiments above: The measured TL responses are too low between 10% to 15% . The measured cell survival are up to 30% too high. A possible reason for these results can be too low real fluences during irradiation. To exclude this possibility future experimental setups will measure the fluence with CR39 additionally. Another problem we experienced was the dose fall off smeared at the edges of our volumes. In future experiments the irradiation plans have to be corrected according to the measured dose.

References

[1] G.W.Barendsen, Int. J. Radiat. Biol.,1979, vol. 36, no. 1, 49-63

[2] M.Scholz and G. Kraft, Adv. Space Res.,1996, vol. 18, no. 1/2, 5-14

[3] Th.Haberer, GSI Report, June 1994

[4] M.Scholz, A.M.Kellerer, W.Kraft-Weyrather, G.Kraft, Radiat. Environ. Biophys., 1997, vol. 36, 59-66

[5] M.Krämer, see this book of absracts

[6] O.Geiß, Dissertation, 1997, Uni Kassel and references there

[7] W.Kraft-Weyrather, M.Scholz and G.Kraft, GSI Report, October 1995

G

Dosimetry Kanai/Goitein (Chair)

Oral Presentations

1. Tatsuaki Kanai
   (Chiba, Japan)
   Three-Year Experiences of Heavy-Ion Dosimetry at HIMAC
2. Adolf Coray
   (PSI, Villingen, Switzerland)
   Monitoring the Dose Delivery for the Spot Scanning at PSI
3. S. Onori
   (Ist. di San., Rome, Italy)
   Recent Developments in the Measurement of Dose Distributions in the Framework of the Top Project
4. Maurizio Rosetti
   (ENEA, Rome, Italy)
   Proton Energy Determinations in Water and in Tissue-Like Material
5. Günter Hartmann
   (DKFZ Heidelberg, Germany)
   Carbon Ion Dosimetry at GSI Using Ionization Chambers

6. Marco Donetti
   (INFN, Torino, Italy)
   First Results on Magic Cube 3-D Dosimeter

7. Oliver Geiss
   (GSI, Darmstadt, Germany)
   TLD Dosimetry of Heavy-Ion Beams

8. R.F. Laitano
   (ENEA, Rome, Italy)
   Effects of Thermal Conduction and Convection on Temperature Profile in a Water Calorimeter for Proton Beams

9. Antonio Guerra
   (ENEA, Rome, Italy)
   Water Calorimetry with Thermistor Bridge Operated in DC and AC Mode: Comparative Results

Posters

10 Belinda Bathelt
   (GSI Darmstadt, Germany)
   Film Dosimetry with Heavy-Charged Particles

11 G.C. Bonazzola
   (INFN, Torino, Italy)
   A VLSI Circuit for the Charge Measurement of a Strip Ionization Chamber

12 Caterina Brusasco
   (GSI Darmstadt, Germany)
   A Detection System for the Verification of 3-D Dose Distributions in light-ion Radiotherapy

13 E. Casnati
   (Uni. Ferrara and INFN, Italy)
   Effects of the Inhomogeneity between Wall and Gas in Ionometric Proton Dosimetry

14 E. Gargioni
   Effects of Thermal Conduction and Convection on Temperature Profiles in a Water Calorimeter for Proton Beams

15 Peter Heeg
   (Uni. Klin. Heidelberg, Germany)
   Development and Application of an Initial Quality Assurance Program for Dosimetry at GSI

16 Marija Radojcic
   (VINCA Belgrade, Yugoslavia)
   Absorbed Dose Distribution Measurements in Radiotherapy

17 Ulla Ramm
   (Uni. Klin. Frankfurt, Germany)
   Heavy-Ion Dosimetry with Magnetic Resonance Imaging of Polymer Gels

Three-year experiences of heavy-ion dosimetry at HIMAC

Tatsuaki Kanai, Masahiro Endo, Shinichi Minohara, Nobuyuki Miyahara, Hiroko Koyama-Itoh, Hiromi Tomura,

Naruhiro Matsufuji, Yasuuki Futami, Akifumi Fukumura, Takeshi Hiraoka, Yoshiya Furusawa, Koichi Ando, Masao

Suzuki, Fuminori Soga. and Kiyomitsu Kawachi

National Institute of Radiation Sciences,

9-1, Anagawa 4-chome, Inage-ku, Chiba-shi, 263 CHIBA JAPAN

1. Introduction

A clinical trial of the heavy-ion radiotherapy at HIMAC (Heavy-Ion Medical Accelerator in Chiba) has been performed since June 24 of 1994 after three and half months of pre-clinical experiments. In these three years, over 300 patients were treated using carbon beams of 290, 350 and 400 MeV/u. Three clinical treatment rooms (room A, B and C) are used for the clinical trial of heavy-ion radiotherapy. A wobbler system is used for the beam broadening. In this method, a scattered beam is wobbled and draws a circle at the irradiation site to make a uniform field. The irradiation fields are made by the multi-leaf collimator or the patient collimator. About one tenth of the accelerated beam is used for the patient irradiation and rest of the beam is blocked by the collimators in the typical case of the irradiation fields.

In these three years of the heavy-ion treatments, the physical characteristics of the beam delivery system were measured and new technologies for the irradiation of the heavy-ion beams are developed. A synchronized irradiation technique was developed for the irradiation synchronized with patient respiration, for a three dimensional irradiation and also for a multiple-radii wobbler method.

A rehearsal by the patient, the check of the range and monitor calibration of the treatment are usually performed just before the treatment. In order to treat patients safely and efficiently, systematic calibration procedures were developed at HIMAC.

In this paper, the new developments of the irradiation system are described. Dosimetry and the physical characteristics of the heavy-ion beam are also discussed.

Dose calibration procedure at HIMAC

Standard procedure of the dose calibration using the above system is as follows;

1) Depth dose distribution of a spread-out Bragg peak (SOBP) which has 6 cm width is measured by a standard

dosimeter.   The standard dosimeter is a parallel-plate ionization chamber, which is fabricated by Far West Technology, Co.   We use a binary filter to change a depth in water in the measurements of the depth dose distributions.   Inserting PMMA plates of various thicknesses in the beam course, the target thickness is changed.   The thickness of the PMMA is transferred to water equivalent thickness.

2) The measured dose distribution is compared with a calculated depth dose distribution.   From the comparison, variations of the residual range of the carbon beam at the irradiation site and absolute values of the output of the standard chamber are recorded for the check of the energy and the sort of ions of the accelerated beam and for the check of the irradiation system.   Usually the variation of the range of the carbon beams is less than 2% of the average value. The variation of the dose at zero absorber position in the measurement of the depth dose distribution is also less than 2% of the average value.

3) The information of the treatments, (for example, the excitation current of the wobbler magnets, thickness of the scatterer, sort of the ridge filter, thickness of the range shifter and so on) are send to the irradiation control computer. And the devices are adjusted according to the transferred information.   The thickness of the binary filter is adjusted so that the ionization chamber is set at the center of the SOBP.   The thickness of the binary filter is given by the treatment planning system.   Dose calibration of the monitor chamber is again performed under this treatment condition several times.   These calibration factors are used for the real exposure to the patient.   This dose calibration measurement for the each patient condition is performed only at the first treatment.   The ratio of the dose calibration factor to the entrance dose of the depth dose distribution of the standard SOBP beam is recorded and used for the next treatments. The dose calibration factor for the later treatment is obtained by the ratio times the entrance dose of the depth dose distribution of the standard SOBP beam at that day.

From this simplified procedure of the dose calibration, it is possible to shorten the calibration time without making the accuracy of the dose calibration worse.

Depth dose measurements using a water bath and the binary filter

Due to a beam divergence, the depth dose distributions measured by the binary filter and the water bath are different.   In the depth dose distributions measured by the binary filter, the ionization chamber is always placed at the irradiation site.   The chamber is not moved and the PMMA absorbers are inserted at up-stream of the chamber.   On the other hand, the depth dose distributions using the water bath are measured by scanning the ionization chamber in the water bath.   The measurements using the water bath simulate practical situations of the beam irradiation to the patients much more than the dosimetry by the binary filter.   It is, however, not so easy to adjust the position of the center of the

SOBP in various conditions of the patient irradiation to the irradiation site in case of the water bath. At the center of the SOBP, the difference of the dose is very small.

Dose dependency on the field size of the collimated beam

For small irradiation fields, edge-scattered beams come into the field and increase the dose several percent near the surface. At the deeper region more than 5 cm, the dose for the small field size are smaller than the dose for the large field size due to the effect of the diffusion by the irradiation system.

Dose leakage from the brass collimator

For the case of the small irradiation fields, we use the patient collimator made of brass. The brass collimator for the 290 MeV/nucleon beam usually was 5 cm in thickness. In that case, the leakage from the collimator was less than 2 % of the peak of the physical dose distribution. Considering the RBE of the carbon beam, the contribution of the biological dose at the blocked region was less than 1 % of the target dose. After the collimator is used for the treatments, the collimator was usually activated. Typically the radiation from the activated collimator is less than $20\mu Sv$ at 10 cm apart from the collimator. The decay curve of the activation shows that they have two components, one of which have decay constant of 25 minutes, and the others has 90 minutes.

Absolute dosimetry of the heavy-ion beams

An ionization chamber method was adapted for the dosimetry of the heavy-ion beam. From the Bragg-Gray theory of the ionization in the cavity, the absorbed dose of tissue irradiated with the heavy-ion beam can be obtained as follows;

$$D = \frac{Q_{IC}}{M_{IC}} W S_{t/g} K$$

where K is a correction factor for temperature, pressure of the gas in the cavity, ion recombination and so on. Q_{IC}, M_{IC}, $S_{t/g}$ and W in the equation are the ionization charge collected by the chamber, mass of the gas in the cavity chamber, stopping power ratio of tissue to gas and W value of the chamber gas for the heavy-ion, respectively. The W value of the air for the heavy-ions are assumed to be 35.2 eV, which is the same as that for high-energy protons.

The absorbed dose measured by the ionization chamber method was compared by a fluence measurement method. The dose measured by the fluence method was about 5 % smaller than the dose obtained by the ionization chamber method. Near the surface of the material, the dose increases gradually about 5 %. These phenomena may be

explained by build up of secondary particles or target fragmentation due to nuclear interactions between the projectile and the target materials.

Decrease of response of the ionization chamber

The depth dose measurements were usually measured twice a day by the ionization chamber. The ionization chambers were used every day and were irradiated repeatedly. For these three years, the response of the ionization chamber decreased over 10 %. It may be due to the radiation damages of the heavy-ion beams.

Improvement of the irradiation system

By using the technique of RF knock-out extraction of the accelerated beam from the synchrotron[1], we can control the beam on and off in milliseconds. A synchronized irradiation with patient respiration is realized by this RF knock-out beam extraction technique.

In the three-dimensional irradiation with broad beam[2], the width of the multi-leaf collimator and the thickness of the absorber are controlled during the irradiation. In order to irradiate precisely, it is better to stop the irradiation during the multi-leaf collimator and the absorbers are moving. In this case, we also use the technique of the synchronized irradiation.

For the large irradiation fields of over 20 cm in diameter, the scatterer thickness becomes very large and the dose rate becomes very low. Then for the radiation fields over 20 cm in diameter, a beam wobbling with multiple radii is adapted. In this case, it takes about several tens milliseconds to change the wobbler radius. It is necessary to stop the beam during this transient time by the technique of the synchronized irradiation. By this technique, the dose rate for the large field was improved tremendously.

References

1. K. Noda, M. Kanazawa, A. Itano, E. Takada, M. Torikoshi, N. Araki, J. Yoshizawa, K. Sato, S. Yamada, H. Ogawa, H. Itoh, A. Noda, M. Tomizawa and M. Yoshizawa: Slow beam extraction by a transverse RF field with AM and FM. Nucl. Instrum. Methods in Phys. Res. A (1996) .

2. T. Kanai, K. Kawachi, H. Matsuzawa and T. Inada, Broad beam three-dimensional irradiation for proton radiotherapy. Medical Physics **10**, 344-346 (1983).

Monitoring the Dose Delivery for the Spot Scanning at PSI

A. Coray, T. Böhringer, M. Grossmann, S. Lin, T. Lomax, G. Munkel , E. Pedroni, *Department of Radiation Medicine, Paul Scherrer Institute, CH-5232 Villigen PSI, Switzerland.*

With the spot scanning technique at PSI, a sequence of discrete dose spots are delivered to the patient at predefined positions. During the scanning, a dedicated system, the „Dose Controller" measures dose and position of each spot and checks the values against a table of nominal values. If the given tolerance limits are exceeded the treatment is stopped and all spot parameters are printed out. During the scanning the relevant dose and position values for each spot are continuously written to a log file. At the end of the scanning the logged data are analyzed. Data about the variation of the spot-dose and -position during the treatment will be presented.

RECENT DEVELOPMENTS IN THE MEASUREMENT OF DOSE DISTRIBUTIONS IN THE FRAMEWORK OF THE TOP PROJECT

P. Fattibene and S.Onori

Laboratorio di Fisica - Istituto Superiore di Sanità - Rome (Italy)

Introduction

The Italian TOP (short for Terapia Oncologica con Protoni) project [1] is finalized to the design and realization of a Center for proton cancer therapy adopting a compact LINAC as accelerating machine. The available proton energy will be up to 200 MeV. In such a framework, one of the objectives is the development and construction of dosimetry systems for therapy proton beams including basic, clinical and transfer dosimetry. A problem which deserves special attention and proper solution is the dosimetry verification in homogeneous water phantom. To this purpose different relative dosimetry systems such as alanine, gel-Fricke, TLD, diode, scintillator are under study. The suitable systems are required to meet proper sensitivity and precision, tissue equivalence, energy independence, proper spatial resolution and independence of response from the beam time structure (DC or pulsed) and from the beam delivery mode (passive scattering or dynamic systems). The present contribution will deal only with the alanine/EPR (electron paramagnetic resonance) dosimetry system set up at the Istituto Superiore di Sanità (ISS) in Rome, summarizing the main results achieved and the problems still to be solved. The work done is part of the TOP project and was also partially supported by the Italian Institute of Nuclear Physics (INFN, ATER project).
The results here presented were obtained thanks to the close and active collaboration with E.Egger and B. Schaffner (PSI, Villigen, Switzerland), R.Cherubini (LNL-INFN, Legnaro, Italy), F.d'Errico (University of Pisa), I.Janovski (NRI, Rez, Check Republic) and C.de Angelis (ISS, Roma, Italy),

In phantom measurements

Alanine-based pellets and films were used. The pellets, 4.9 mm in diameter and 1,2 mm in length were manufactured at ISS with L-alpha alanine (80% by weight) and paraffin (20% by weight)[2]. The films were produced at the Nuclear Research Institute (NRI, Czech Republic) with L-alpha alanine (30% by weight) and polyethylene-vinyl-acetate (70% by weight)[3]. Irradiations were performed 1) at the INFN Legnaro National Laboratories (LNL) with a 7 MV Van de Graaff accelerator, 2) at the 62 MeV entrance energy proton beam of PSI (OPTIS) and 3) at the recently available 200 MeV dynamic beam at PSI.

Figs.1 and 2 show an example of depth-doses as measured with alanine and Markus ionization chamber for unmodulated proton beams of 62 MeV and 200 MeV entrance energy, respectively. Figs.3 shows an example of depth-dose in the 200 MeV modulated proton beam. Fig.4 reports a comparison of dose-profiles calculated and measured with alanine pellets for a treatment planning in an Alderson phantom using 200 MeV protons. Results obtained for the 62 MeV beam are well established[4,5,6], while those for the 200 MeV protons are to be considered as preliminary. Nevertheless, from the results reported in Figs.1 to 4 some general conclusions can be drawn:

1) alanine doses were calculated using a cobalt-60 calibration provided by NPL (UK). The quantitative agreement between alanine and Markus doses implies that there are no significant differences in alanine sensitivity between cobalt-60 beam and 62-200 MeV protons;

2) no energy dependence in the alanine response can be inferred both in an unmodulated beam down to the Bragg peak region and along the spread-out Bragg peak;

3) alanine does not perturb the dose distribution in a water phantom and the depth-dose in alanine can be scaled to the depth-dose in water with a density correction factor;

4) alanine response is insensitive to the beam delivery system adopted (passive scattering or dynamic system).

Since depth-dose measurements do not provide definitive evidence on energy dependence, some other measurements were taken using monoenergetic proton beams in the 2-7 MeV energy range available at LNL. Preliminary results have not shown significant differences in alanine response in the 2-7 MeV energy range.

Future work

The results obtained so far clearly show the suitability of alanine/EPR dosimetry for therapeutic proton beams. Nevertheless, some other information and improvements are needed for a definitive judgment. In particular:

1) Fig.5 shows depth-doses measured in a stack of 1 mm alanine pellets inserted in a solid water phantom. A dose tail is clearly evident behind the distal region which was tentatively ascribed to a misalignment of dosimeters in the stack. Extended simulation and experimental verification are needed to clarify the problem that could be of relevance when performing *in phantom* measurements.

2) The proton energy range used for testing alanine response should be extended to monoenergetic proton beams in the 7-20 MeV energy range.

3) The precision of alanine pellets decreases at low doses. At present 2% precision is obtained for doses over 5 Gy. Work is in progress to lower this limit through the use of a new generation of alanine-based pellets with polyethylene as binding material.
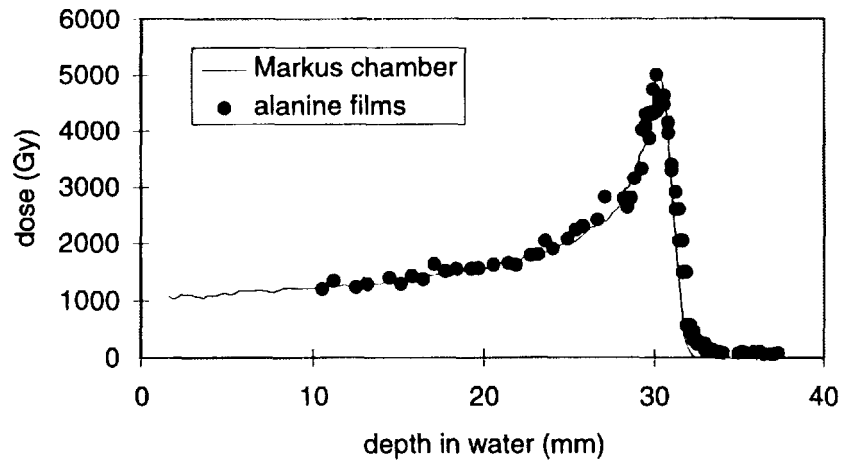
Fig. 1 Depth dose measured in the 62 MeV proton beam.
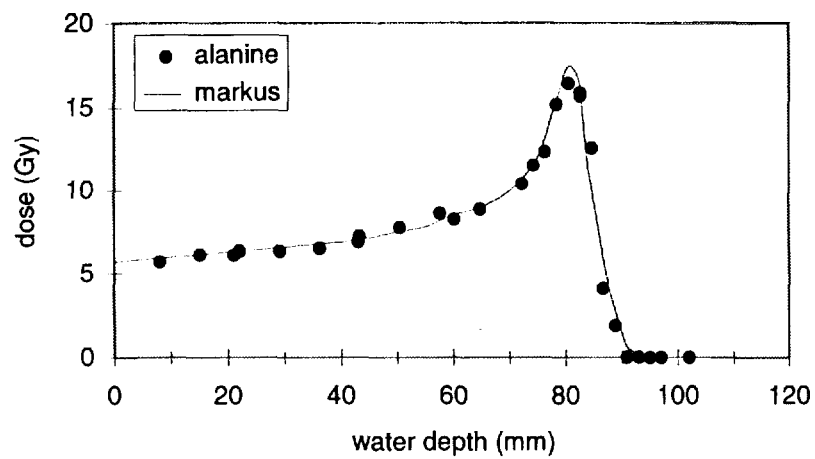
Fig.2 Depth dose measured in the 200 MeV proton beam.
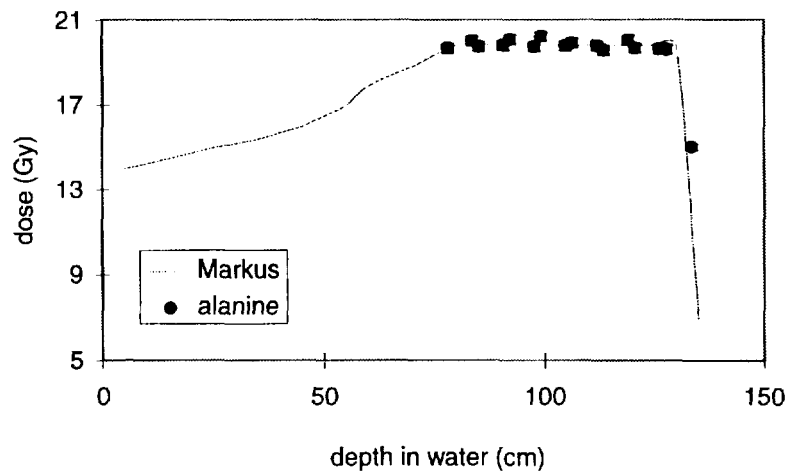
Fig. 3 Depth dose measured in the 200 MeV modulated proton beam.
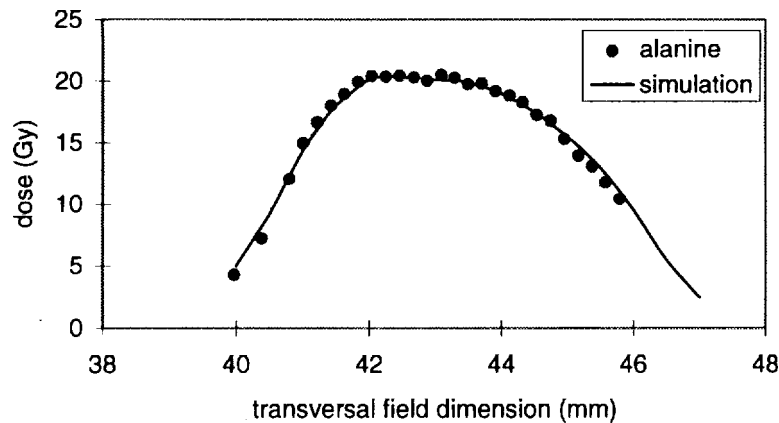
Fig.4 Dose profile measured with alanine pellets in a transversal plane of an Alderson phantom in the 200 MeV proton beam.
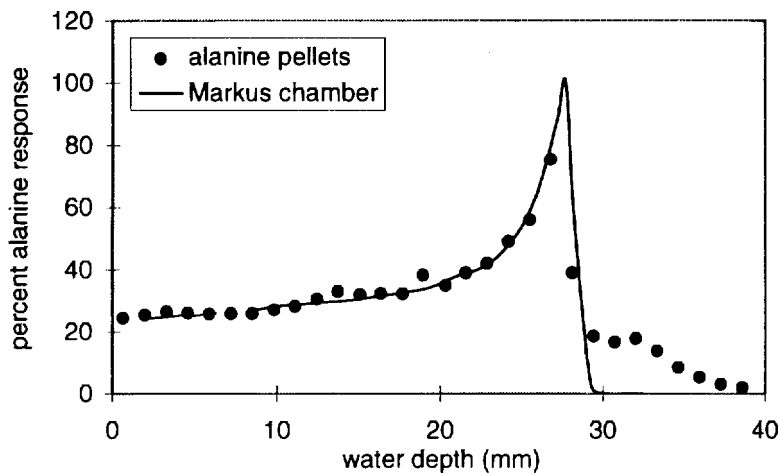
Fig.5 Depth dose distribution measured with a stack of 1mm alanine pellets in the 62 MeV proton beam.

References

(1) "The RITA network and the design of compact proton accelerators", U.Amaldi, M.Grandolfo and L.Picardi (Eds.), Frascati INFN Publisher, Italy, 1996

(2) P. Fattibene, S. Onori, "EPR/Alanine Dosimetry", TERA 94/1 TRA 11, 1994

(3) I. Janovsky, "Progress in alanine film/ESR dosimetry," *Proc. Int. Symp. on High Dos. Radiat. Processing*, (IAEA, Vienna, 1990) IAEA-SM-314/47, 173-187 (1991)

(4) S. Onori, F. d'Errico, C. De Angelis, E. Egger, P. Fattibene, and I. Janovsky. *Alanine Dosimetry of proton therapy beams*. Med.Phys. 24, 3, 447-453 (1997).

(5) P. Fattibene, A. Calicchia, F. d'Errico, C. De Angelis, E. Egger and S. Onori. *Preliminary Assessment of LiF and Alanine Detectors for the Dosimetry of Proton Therapy Beams*. 66, 1-4, 305-309 (1996)

(6) S. Onori, F. d'Errico, C. De Angelis, P. Fattibene, E. Egger, I. Janovsky. *Proton response of alanine based pellets and films*. Appl. Radiat. Isot. 47, 11/12, 1201-1204 (1996)

PROTON ENERGY DETERMINATIONS IN WATER AND IN TISSUE-LIKE MATERIAL

R. F. Laitano° and M. Rosetti*

°Istituto Nazionale di Metrologia delle Radiazioni Ionizzanti,
ENEA, C. R. Casaccia, c.p. 2400, Roma (Italy)
* Divisione di Fisica Applicata, ENEA, Bologna (Italy)

Abstract

The mean energy of proton beams in water and in a tissue substitute, respectively, were determined as a function of SOBP width, beam size and initial energy spread. Then an analytical expression to obtain the proton mean energy as a function of phantom depth and initial energy was established. This expression differs from the analogous ones reported in some current dosimetry protocols in that it accounts for the nuclear interaction effects in determining the mean energy. The preliminary results of the calculations referred to above are reported together with some comments on the specification of the the proton beam quality for clinical dosimetry.

1. Introduction

To characterize proton fluence or absorbed dose measurement in dosimetric water phantom (or in other tissue-substitute material) the proton mean energy at given depths in the reference medium is needed. For proton incident energies above 100 MeV the occurrence of nuclear interactions may influence the energy spectrum at any phantom depth, because of the production of lower energy secondary protons. In the recent years considerable efforts were made to develop Monte Carlo codes, as for example PTRAN [1], FLUKA [2], and PETRA [3], in the energy range of interest for radiotherapy (i.e. from 50 to 250 MeV).

In a recent study [4] the effects of nuclear interactions on proton mean energies in a tissue-like material were quantitatively assessed using the FLUKA code. That study was then extended in the present work to analyse, by means of the same code, the role of the above effects on the proton mean energy in both tissue and water as a function of: width of the spread-out Bragg peak (SOBP), beam radius, beam divergence and initial energy spread of the incident beam. Moreover a formula for determining the mean energy as a function of depth and initial energy was fitted to meet the needs in practical dosimetry.

2. Least-square fit for the mean energy expression

An expression to calculate the proton mean energy was obtained by a least-square fit of the mean energies calculated by the FLUKA code. This expression, given by the formula (1) below, is valid at depths outside the Bragg peak, in particular at depths not greater than 0.7 R, in the incident energy interval from 100 to 250 MeV and for a beam radius of 5 cm. The accuracy of this fit is about 0.3% in the above energy range.

$$E(z,R) = a_1 F^{a_2} + a_3 F^{a_4} + a_5 F^{a_6} + a_7 R^{a_8} + a_9 \left[(z/R)^{-1} + a_{10} R^{a_{11}} \right]^3 +$$

$$+ a_{12} \left[(z/R)^{-1} + a_{10} R^{a_{11}} \right]^2 + a_{13} \left[(z/R)^{-1} + a_{10} R^{a_{11}} \right] + a_{14} \qquad (1)$$

where:
z is the depth along the beam axis, F and R are the residual range and the range, respectively, of the proton beam in water or tissue. The parameters a_i referring to water are:

a_1 = 31.3596478	a_2 = 0.5318228	a_3 = 0.5034249	a_4 = 0.7509853
a_5 = 0.3778917	a_6 = 1.1038477	a_7 = -0.0078352	a_8 = 1.6607157
a_9 = -0.0180944	a_{10} = -0.0132526	a_{11} = 1.4147791	a_{12} = 0.2489916
a_{13} = -0.6432207	a_{14} = -0.1550280		

whereas the parameters a_i referring to tissue are:

$a_1 = 31.2441006$ $a_2 = 0.5319116$ $a_3 = 0.4855778$ $a_4 = 0.7679694$
$a_5 = 0.3731426$ $a_6 = 1.0886235$ $a_7 = -0.0053131$ $a_8 = 1.7285337$
$a_9 = -0.0186592$ $a_{10} = -0.0292664$ $a_{11} = 1.1557502$ $a_{12} = 0.2564629$
$a_{13} = -0.6625866$ $a_{14} = -0.2473501$

The above parameters were determined, using the range values, R, and the tissue composition reported in [5] and[6], respectively. A more simplified expression was also fitted from the Monte Carlo calculation. The simplified expression, less accurate than the formula (1), is not yet optimised and will be reported in a subsequent work.
The proton mean energy at the Bragg-peak depth was fitted by the expression (2) reported below:

$$E_p(E_0) = a_1 + a_2 E_0 + a_3 E_0^2 + a_4 E_0^3 \qquad (2)$$

where E_0 is the incident energy of the proton beam and the parameters are given for water by:

$a_1 = 0.134594 *10^2$ $a_2 = -0.139148$ $a_3 = 0.121528*10^{-2}$ $a_4 = -0.217771*10^{-5}$

and for tissue by:

$a_1 = -0.479915*10$ $a_2 = 0.232372$ $a_3 = -0.103042*10^{-2}$ $a_4 = 0.196657*10^{-5}$

The expressions (1) and (2) account for nuclear interactions and in this respect give results rather different, even more than 3%, from the analogous expressions [e.g. ref. 7] in which the nuclear interactions are not considered.

3. Mean energies at the SOBP depths

Proton mean energies were calculated at the depths corresponding to the SOBP for different maximum energies and SOBP widths. This Monte Carlo simulation was made with and without accounting for nuclear interactions both in water and tissue. Some preliminary results referring to water are shown in Table 1. The mean energies in the second column are lower than those in the third column because of the effect of secondary protons [4]. Mean energies vary appreciably in the spread-out peak and this should be properly accounted for in dosimetry. Most data referring to these calculations will be reported elsewhere. It is worth noting that, as expected, these data show that the mean energy at a given depth in the SOBP depends just on the depth and on the maximum proton energy, but not on the SOBP width.

Table 1. Mean energies at depths inside a 10 cm wide SOBP in a proton beam with maximum energy $E_0 = 250$ MeV. In the first column the depths are expressed also in terms of the percent width of the SOBP. $E(z)_{NI}$ and $E(z)$ are the mean energies determined with and without accounting for nuclear interactions. The percentage difference between $E(z)_{NI}$ and$E(z)$ is reported in the last column.

depth in water (cm)	$E(z)_{NI}$ (MeV)	$E(z)$ (MeV)	$\Delta (E(z)_{NI} / E(z))$ (%)
27.51 (0%)	97.39	99.76	2.4
28.51 (10%)	92.00	94.24	2.4
29.51 (20%)	86.33	88.36	2.4
30.51 (30%)	80.39	82.18	2.2
31.51 (40%)	74.16	75.79	2.2
32.51 (50%)	67.55	68.98	2.1
33.51 (60%)	60.43	61.68	2.1
34.51 (70%)	52.68	53.78	2.1
35.51 (80%)	43.96	44.90	2.1
36.51 (90%)	33.68	34.44	2.3
37.51 (100%)	20.29	20.62	1.6
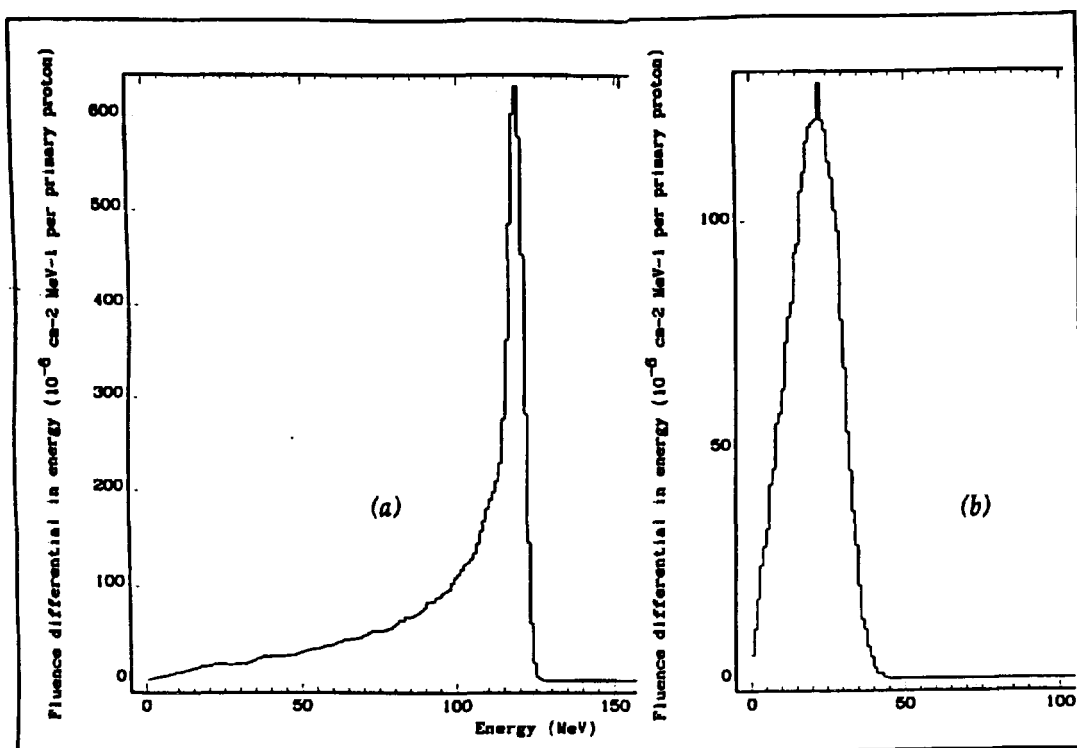
Fig. 1. Two proton energy distributions (a) and (b), occurring at the two extreme regions (proximal and distal points, respectively) of the SOBP in water. The width of the SOBP is 10 cm and the maximum proton energy is 250 MeV.

The proton energy distributions vary appreciably with the depth in the spread-out peak. As an example some preliminary results in this respect are shown in Fig. 1. The energy spectra (a) and (b) at the extreme points of the SOBP, respectively, are not only different in mean energies but also in shape.

4. Energy dependence on the initial energy spread

The effect of the incident beam energy spread on proton mean energies at various depths in water was also evaluated. The spread considered in this analysis was just the intrinsic spread due to the accelerator characteristics. The results reported in Table 2 for a 200 MeV proton beam show that varying the energy spread, $\pm\Delta E_0$, from 0.15% to 0.5% changes appreciably the mean energy. This change occurs however only at depths in the descending region of the peak. This effect, which is up to about 20%, is due to those protons with incident energy $E_0 + \Delta E_0$ which can travel distances longer than the range R at which the majority of the protons have near zero energy. Accordingly even a small initial spread $\pm\Delta E_0$ can appreciably change the mean energy near the end of the proton range.

5. Energy dependence on beam radius and divergence

The primary protons travel substantially along of the beam axis whereas the lower-energy secondary protons generated from nuclear interactions are emitted all over the solid angle. Accordingly a dependence of the proton mean energy $E(z)$ on beam field size is expected. Moreover this dependence is expected to increase with the nuclear interaction rate of the primary proton beam in the medium considered. The variation of $E(z)$ with the beam radius resulting from the present calculation, is not very large but not negligible. Changing from 5 cm to 1 cm the beam radius for a 250 MeV proton beam in water, results in a 2.8% mean energy increase. From the variation of $E(z)$ with the beam field size, also a dependence of $E(z)$ on beam divergence can be quantitatively assessed.

Table 2. Mean energy E(z) at the depth z in water for proton beams with incident energy E_0 = 200 MeV and initial spread $\pm\Delta E_0$. $\Delta E(z)$ is the variation of E(z) due to the spread $\pm\Delta E_0$. Three ΔE_0 values (0, 0.15 and 0.5%, respectively) are considered.

depth in water z/R (1)	E(z) (ΔE_0 = 0)	E(z) (ΔE_0= $\pm$0.15%)	$\Delta E(z)$ (%)	E(z) (ΔE_0= $\pm$0.5%)	$\Delta E(z)$ (%)
0.1	184.1	184.26	---	184.2	- - -
0.2	170.2	170.31	---	170.36	- - -
0.5	127.5	127.39	---	127.40	- - -
0.7	92.9	92.99	---	92.88	- - -
0.88 (2)	47.9	48.01	---	47.93	- - -
0.95 (3)	16.7	16.79	0.7	17.99	7.9
0.97 (4)	10.6	10.92	3.0	12.87	21.4

(1) The range R is defined here as the the intercept, on the z axis, of the depth dose curve as determined by the Monte Carlo calculation. (2) Depth at peak half maximum on the rising side. (3) Depth at peak maximum . (4) Depth at peak half maximum on the descending side

6. Mean energies in water and tissue substitute

The mean energies E(z) of a proton beam at the same depth z in water and tissue, respectively, differ from each other by a quantity $\Delta E_{w,t}$ because the differences in the csda stopping powers of the two media are not negligible [5]. If $E_{w,t}$ denotes the ratio of E(z) at the same depths in water and tissue, respectively, and $(E_{w,t})_{NI}$ the same ratio obtained by accounting for nuclear interactions (N.I.) in proton energy determination.,the results for a 200 MeV proton beam show that, at any depth before the Bragg peak, the N.I. change practically by the same factor the proton mean energy E(z) in water and tissue, respectively . At those depths in fact the ratio $(E_{w,t})_{NI}$ /$E_{w,t}$ is practically unity. At depths near the end of the proton range beyond the dose maximum, the N.I. induce in E(z) changes by a different amount in water and tissue, and the ratio $(E_{w,t})_{NI}$ /$E_{w,t}$ is 1.04. As far as the SOBP is concerned, the differences between mean energies in water and tissue are less than 1 %.

7. Conclusions

The results so far described shall be completed by further calculations, in order to gather a sufficient amount of data useful for the quality specification of a proton beam. The complete results will be reported in a forthcoming paper. A conclusion that may be drawn from the preliminary results so far obtained is that the effect of nuclear interactions should be never overlooked in determinining the proton beam parameters at energies above 100 MeV.

References

[1] Berger M. J. (1993) Proton Monte Carlo transport program PTRAN, *National Institute of Standards and Technology, Report NISTIR-5113*

[2] Fassò A., Ferrari A., Ranft J., and Sala P.R. (1995) *Specialists Meeting on Shielding Aspects of Accelerators, Targets and Irradiation Facilities, Arlington Texas (USA) April 28-29, OECD/NEA Publ. pg. 277*

[3] Medin J. and Andreo P. (1997) Monte Carlo calculated stopping-power ratios, water/air, for clinical proton dosimetry (50 - 250 MeV), *Phys. Med. Biol.* 42, 89-105

[4] Laitano R. F., Rosetti M. and Frisoni M. (1996), Effects of nuclear interactions on energy and stopping power in proton beam dosimetry, *Nucl. Instrum. and Meth. (A)* 376, 466-476

[5] ICRU Report 49 (1993) Stopping powers and ranges for protons and alpha particles, *International Commission on Radiation Units and Measurements, Washington D.C.*

[6] ICRU Report 44 (1989) Tissue substitutes in radiation dosimetry and measurements, *International Commission on Radiation Units and Measurements, Washington D.C.*

[7] Vynckier S., Bonnett D.E. and D.T.L. Jones D.T.L., Code of practice for clinical proton dosimetry, Radioter. Oncol. 20, (1991) 53.

DE98F5418

Carbon ion dosimetry at GSI using ionization chambers

G. Hartmann, P. Heeg*, O. Jäkel, Ch. Karger, A. Krießbach

German Cancer Research Center, Heidelberg
* Clinical Radiology of the University Heidelberg

Introduction

The Heavy Ion Therapy Project at GSI, Darmstadt, Germany, which is being carried out as a joint project of the Heavy Ion Research Laboratory (GSI), the German Cancer Research Center (DKFZ) and the University Heidelberg (Department of Clinical Radiotherapy) will presumably start with patient treatments at the end of 1997. Due to the advantageous properties of carbon ions compared to other light ions [1], this ion type has been selected for the irradiation. For clinical proton dosimetry, a recent recommendation [2] suggests standard thimble ionization chambers to be used as the reference dosimeter. For our carbon ion dosimetry the same approach was adopted. This paper presents the methods applied at GSI to determine absorbed dose to water, $D_w(P)$, at a point of interest P.

Dosimetry protocol

In contrast to already existing protocols for protons [3] and heavy ions [4], our dosimetry protocol is based on thimble ionization chambers which have been calibrated at Secondary Standard Dosimetry Laboratories (SSDL) in terms of absorbed dose to water, $D_{w,Co-60}$, using C0-60 gamma radiation.

$$D_{w,Co-60} = M \cdot N_{w,CO-60} \tag{1}$$

One advantage of this approach is that $N_{w,Co-60}$ is obtained with better accuracy than if it is derived through successive steps from the air kerma formalism [5,6]. Then the absorbed dose to water at the field of carbon ions is obtained by:

$$D_{w,C-12} = M \cdot N_{w,CO-60} \cdot k_{C-12} \tag{2}$$

where M is the electrometer reading at a carbon dose measurement in water (or water equivalent material) corrected for deviations from reference conditions such as temperature and air pressure and $N_{w,Co-60}$ is the absorbed dose to water calibration factor supplied by a SSDL. The quality factor, k_{C-12}, corrects the calibration factor, $N_{w,Co-60}$, for the difference in beam quality between C0-60 gamma radiation used at SSDL and that of the carbon ions.

k_{C-12} is essentially containing the differences of the physical properties between C0-60 gamma radiation and the radiation of carbon ions. With that the nuclear fragmentation of the primary carbon ion has to be additionally taken into account. It causes a significant alteration of the radiation field with increasing depth in water: while the number of primary particles is decreasing due to nuclear collisions along the path, a build-up of lower-Z-projectile fragments will occur.

The quality factor is obtained as:

$$k_{C-12} = \frac{\left(\dfrac{\overline{S}}{\rho}\right)_{air}^{water} \left(\dfrac{\overline{w}}{e}\right)_{air}^{C-12}}{\left(\dfrac{\overline{L}}{\rho}\right)_{air}^{water} \left(\dfrac{W}{e}\right)_{air}^{Co-60}} \cdot \frac{p_{C-12}}{p_{Co-60}} \tag{3}$$

where

$\left(\dfrac{S}{\rho}\right)_{air}^{water}$	=	ratio of mean mass stopping power water to air for the ions (primary particles + fragments)
$\left(\dfrac{L}{\rho}\right)_{air}^{water}$	=	ratio of mean mass stopping power water to air for Co-60 using Bragg-Gray formalism
$\left(\dfrac{W}{e}\right)_{air}^{Co-60}$	=	W-value for (normally) humid air in the C0-60 gamma radiation
$\left(\dfrac{w}{e}\right)_{air}^{C-12}$	=	mean w-value for (normally) humid air in field of carbon ion
p_{Co-60}, p_{C-12}	=	perturbation correction factors to be applied individually to each chamber type to account for the substitution of water by the chamber

Physical factors used in the quality factor k_{C-12}

The physical factors given below apply to the PTW Farmer chamber (type 30001) and to the 0.13 ccm thimble chamber IC 15 from Wellhöfer Dosimetrie. Values for C0-60 gamma radiation are given in Tab. 1.

Tab. 1: . Values of the physical factors used for C0-60 gamma radiation

parameter	value		1σ - uncertainty [%]
$\left(\dfrac{W}{e}\right)_{air}$	33.73 J/C		0.2
$\left(\dfrac{L}{\rho}\right)_{air}^{water}$	1.133		0.4
	Farmer	IC 15	
p	0.994	1.00	0.5

Mean w value for carbon ions

There is a far larger uncertainty in choosing the correct values in the nominator of the k_{C-12} equation (3). This especially applies to the mean w value. For light ions at middle and high energies experimental data are very rare and no international recommendation exists. A compilation of various experimentally obtained values for protons as well as for ions is given in Fig. 1. For protons a new international recommendation of 34.8 J/C with an uncertainty of 2% was recently given [2]. According to Verhey and Lyman [7], the difference between the w value between protons and light ions up to Z=10 should be smaller than 1% at energies above 5 MeV/u. It therefore appears reasonable to use the same value for carbon ions as well as for the lighter fragments, i.e. w/e = 34.8 J/C, as long as further experimental data do not require a modification of this assumption.

A second problem is energy dependence of the w value. Again, since the experimental proton data do not show any significant increase down to energies of 0.1 MeV (Fig. 1), use of a constant value of 34.8 eV down to 1 MeV/u seems to be a reasonable assumption also

for the mean w value of carbon ions.
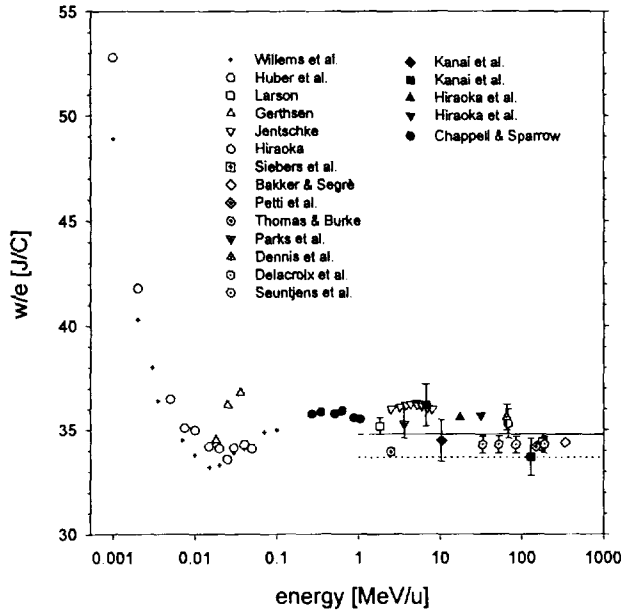
Fig. 1: Compilation of data on w/e values in air for protons and light ions. All open data points refer to protons and all filled data points refer to light ions. The solid line is the recommendation for protons from ICRU 59 (1997), the dotted line represents the recommendation of the AAPM report 16 (1986)

Based on calculated data of the particle fluence differential in energy as a function of depth [8], the relative contribution of particles below 1 MeV/u to total dose was estimated as shown in Fig. 2. It demonstrates that a possible increase of w below 1 MeV/u does not introduce a major uncertainty even at the Bragg peak region if generally using a constant mean w value.
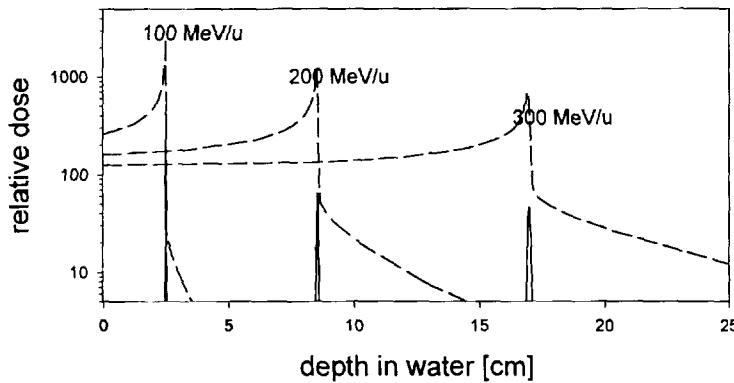
Fig. 2: Depth dose curves for 100, 200 and 300 MeV/u normalized to dose per fluence at depth zero. Solid lines show the dose contribution from all particles (primary ions + fragments) with energy below 1 MeV/u.

Mean mass stopping power ratio for ions

The correct expression for the mean mass stopping power ratio water to air is given by:

$$\left(\frac{\bar{S}}{\rho}\right)^{water}_{air} = \frac{\sum\limits_{Z=1}^{6} \int\limits_{0}^{E_{max}} \Phi_Z(E) \cdot \left(\frac{S_Z(E)}{\rho}\right)^{w}_{ion} \cdot dE}{\sum\limits_{Z=1}^{6} \int\limits_{0}^{E_{max}} \Phi_Z(E) \cdot \left(\frac{S_Z(E)}{\rho}\right)^{air}_{ion} \cdot dE}$$

(4)

This ratio also shows an energy or depth dependence. A calculation, again based on the differential particle fluence, yielded an increase of a few percent for several millimeters close to the Bragg peak as compared to zero depth. Therefore, if for practical reasons a constant value is used for all depths, the dose absorbed to water will be slightly underestimated close

to the Bragg peak. We are using a constant value of 1.13 which is the mean value of the mass stopping power ratio of protons as well as for alphas in the energy region between 10 MeV/u and 1000 MeV/u taken from [9].

Perturbation factor p for ions
There is some controversy whether for ions a perturbation factor, in particular a chamber wall correction factor is needed at all. We observed that the chamber signal is varying a few percent depending on (a) free air or in phantom measurements, (b) chamber wall thickness, that means there is a wall effect. On the other hand, Hiraoka et al. [10] did not found any effect. More studies are certainly required. Currently, we use a perturbation factor of 1.00.

Results and discussion

A dosimetry comparison experiment between the Japanese and the German heavy-ion therapy facilities was carried out with the 290 MeV/u carbon beam at HIMAC in December 1996. Using different dosimetry protocols, the values obtained by the ionization chambers are in excellent agreement within experimental errors for all measurement conditions [11]. The values obtained by fluence methods, however, are always lower than that by ionization chambers in the order of 5% to 10 %. A similar observation was reported by Kanai et al. [12]. In spite of the excellent agreement obtained between our dosimetry protocol and the Japanese dosimetry protocol for carbon ions, the discrepancy is considered as a serious problem for ionization chamber dosimetry for carbon ions. It may be concluded that one or several of the factors in the numerator of equation (3) are lower than given above.

References

[1] Kraft G: The radiobiological and physical basis for radiotherapy with protons and heavier ions. Strahlenther Onkol 166 (1990) 10-13

[2] ICRU 59: Clinical proton dosimetry; Part 1: Beam production, beam delivery and measurement of absorbed dose. (in press)

[3] Vynckier S, Bonnet DE, Jones DTL: Code of practice for clinical proton dosimetry. Radiother Oncol 20, (1991) 53-63

[4] AAPM Report 16: Protocol for heavy charged particle therapy beam dosimetry. A report of task group 20. Am Inst Phys, New York, 1986

[5] Andreo P:Absorbed dose beam quality factors for the dosimetry of high-energy photon beams. Phys Med Biol 37 (1992) 2189-2211

[6] Medin J, Andreo P, Grusell E, Mattson O, Montelius A, Roos M: Ionization chamber dosimetry of proton beams using cylindrical and plane-parallel chambers. Nw versus Nk ion chamber calibrations. Phys Med Biol 40 (1995) 1161 ,

[7] Verhey LJ, Lyman JT: *Some considerations regarding w values for heavy charged-particle radiotherapy.* Med Phys 19 (1992) 151-153

[8] Haberer T: Entwicklung eines magnetischen Strahlführungssystem zur tumorkonformen Strahlentherapie mit schweren geladenen Teilchen. GSI Report 94-09, 1994

[9] ICRU 49: Stopping powers for protons and alpha particles. ICRU, Bethesda, 1993

[10] Hiraoka T, Omata K, Fukumura A, Takeshita M: Dosimetry of particle beams with different wall ionization chambers. Med Phys 24 (1997) 1051

[11] Fukumura A, Hiraoka T, Omata K, Takeshita M, Kawachi K, Kanai T, Matsufuji N, Tomura H, Futami Y, Hartmann GH: Small-scale dosimetry comparison for therapeutic carbon beam at HIMAC. NIRS Annual Report 1997

[12] Kanai T, Kuhno T, Minohara S, Sudou M, Takada E, Soga F, Kawachi K, Fukumura A: Dosimetry and measured differential w value of air for heavy ions. Radiat Res 135 (1993) 293-301

DE98F5417

First results on
Magic Cube 3D dosimeter

R. Cirio[1], M. Donetti[2], F. Marchetto[1], C. Peroni[1]
[1] *University and INFN Torino, Via P. Giuria 1, I-10125 Torino, Italy*
[2] *ASP, V.le Settimio Severo 65, I-10133 Torino, Italy*

In a scanned hadron beam treatment the performances of the accelerator and the control system complex needs to be checked globally on a routine basis. Within the TERA program, it has been developed a dosimeter (nicknamed *Magic Cube*) to measure the relative 3D energy deposition. It is a sandwich of 12 parallel plate (25×25)cm² ionization chambers interleaved with tissue equivalent slabs of adjustable thickness. The anodes of the chambers are segmented into 64 strips 0.4cm wide, which are oriented along two orthogonal directions. Each strip is read out by an individual electronic channel. The chamber gap is 3mm and is filled with Nitrogen. The front-end electronics are based on a current to frequency converter and are implemented with VLSI technology, built at the AMS foundry, Austria. A single VLSI chip contains the circuitry for one chamber and it is placed few centimeters away from the chamber. With this solution the noise is minimized, and the sensitivity can be set as low as 0.2 pC/count.

The dosimeter has been tested on a Carbon beam at GSI.

The linearity is better than 1 % for a beam intensity spanning over three orders of magnitude. The response uniformity over the chamber area, prior to any corrections, is better than 3 %. The beam position and width are measured with a precision of about 1mm.

Dosimeter overview

The dosimeter is housed in a steel box. The lower section is occupied by a sandwich of twelve ionization chambers (active part) and absorber plates. In the upper section the printed circuit boards, the electronic front-end, the cabling, the inlet and outlet of the gas are housed. Two ionization chambers are placed at the beam entrance to monitor the beam position and intensity in the plateau region. Between the two chambers and the remaining ten chambers there is room to insert a plastic (Tissue Equivalent) absorber. The thickness of the absorber has to chosen to match the depth through the proximal edge of the Spread Out Bragg Peak (SOBP). The remaining ten chambers are stacked in a way to leave room for additional absorber plates to cover the entire SOBP.

Each chamber has a single plate cathode while the anode is splitted into strips. The chambers are built in a unique way, but the strips can alternatively be oriented along X or Y, being the beam along the Z-axis. The mechanical structure of the dosimeter can be well described by a box 80.5cm long, 69cm wide and 69.5cm high. It is mainly made of aluminium plates 10mm thick to ensure the necessary rigidity and precision. The mechanical tolerances which have been required are of 0.1mm. Flatness and tilt are within the specified tolerances. The replacement of the absorbers can be done from a lateral side, which has free access.

The active area of a single ionization chamber is a square of 25×25cm² which is defined by two plates of vetronite (electrodes) 0.1mm thick where the electrical conductivity is ensured by a 35μm Copper film. While the cathode is a continuous conductor, the anode is splitted into 4mm wide strips. The gap between two adjacent strips is 0.1mm. The electric field is provided by the negative high voltage applied to the cathode plates, while the strips are grounded through the front-end electronics. The average value of the leakage current is 400pA/chamber.

For typical therapeutical beam intensity, the current generated inside the chamber is in the nanoampere range. This indicates that one has to minimize the electric noise to obtain reliable measurements. Thus to avoid the *em* pickup caused by long cables, the front-end electronics has been placed very close to

the chamber. Namely the board hosting the circuitry is directly installed onto the chamber with a standard printed circuit connector, whilst the mechanical sturdiness is ensured by two side slids. The conductive roads form the strips to the inputs of the front-end are between 5cm and 10cm long and add only a negligible contribution to the input capacitance. The capacitance of a strip toward ground is $\simeq$ 24pF.

The basic concept of the front-end is the recycling capacitor or current to frequency converter. 64 identical channels are integrated in a single VLSI chip, custom made for our application (treated in detail in a poster in this conference *A VLSI circuit for the charge measurement of a strip ionization chamber*, G.C.Bonazzola et al.). Thus only one chip is enough to serve one chamber. The data acquisition has been based on a Personal Computer MacIntosh connected to a VME crate. The data at the counter output (20 bits) from the chip through the buffer interface and the addresses (10 bits) are sent to a 32-bit Dual Port Memory 32k deep. The number of words necessary for a complete read out (cycle) is 768. The memory fetch speed is kept to a 1.5μs/word, and a cycle is lasting 1.5μs $\times$ 768 $\simeq$1.2ms. To limit the amount of data we match the super cycle with the beam spill. A cycle is then performed every 50ms or 40 times per spill.

We remark that there is no dead time built into the system. In fact during all the above mentioned operations the counters of the chip keep on running. Furthermore the number of *pictures* was considered largely sufficient. The same would stand for the continuous beam of a cyclotron.

Test results

In this section we report the results from a data taking on a test beam of C^{+6} performed at GSI in March 1997. The beam intensity was ranging between 10^6 and 10^8 ions/spill, with a spill length of $\simeq$ 2s and the kinetic energy was between 100 and 270 MeV/nucleon. Both beam intensities and energies were in the range expected for therapeutical treatments. The transverse beam dimension was kept between 4mm and 10mm.

The test was aimed at studying:

- linearity of the ionization chamber and read out;

- uniformity over the chamber area;

- capability to reconstruct position and width of the beam.

Let us begin by showing the integrated number of counts as a function of time along the beam spill for a strip overlapped to the beam shape and for a strip out of the beam, shown in the 2 plots in next page. Note that the end range of the vertical scales of the two plots differ by a factor 10000. It is remarkable that for strips out of beam the integrated number of counts (pedestal) is negligible. The limited value of the pedestal of a strip relaxes the degree of complexity of the pedestal analysis and subtraction. To study linearity we summed up the integrated number of counts at the end of spill over all strips after pedestal subtraction. The beam intensity was measured indipendently with a telescope of scintillator counters installed in the beam line downstream the gas chambers. The expected counter rate is by far too large and it is then necessary to reduce the beam. We inserted a 20cm thick plastic absorber in front of the telescope, thus the counter rate was kept in the kHz range. The number of pulses summed over the strips crossed by the beam as a function of telescope counts for several beam intensities (ranging between 10^6ions/s/cm^2 and 2×10^8ions/s/cm^2) deviate from the straight line less than 2% for the whole range.

The response uniformity over the entire chamber surface is important; it avoids correction factors which are function of the position where the beam impinges on the chamber. Disuniformities can be caused by several contributions (deviation of the gas gap as a function of the position, different gains of

electronic channel, charge collection efficiency as a function of the beam position along the strip). The measurement of the disuniformity is rather complex being unknown the absolute value of the beam intensity at each beam position. The response of each chamber was then normalized to the entrance chamber read out as a function of the transverse beam position. The average response has been found within ±2% and the spread has a r.m.s. value again of 2%.

In next page it is shown the energy deposition along the detector as reconstructed on line. One can appreciate the shape of the deposited energy at several depths. This particular plot shows the energy deposited on the last 10 chambers of the *Magic Cube*, to focus on the Bragg peak zone. Note that the pulse heights of the central strip of the first chambers tend to decrease: this is due to the broadening of the beam due to multiple scattering and fragmentation and to the signal sharing between adiacent strips; in fact the integrals on the whole chamber follow the Bragg curve shape. Note also that, downstream of the Bragg peak, two chambers have very low signals, probably due to fragmentation of the incoming ions.

The capability to reconstruct position and width of the beam was the goal of a data taking session at GSI. In this experiment two chambers having 2mm and 4mm wide strips respectively have been put on a gaussian Carbon beam with FWHM varying from 4mm to 10mm. By illuminating the setup with ~100 ions, the center of gravity (c.o.g.) of the beam seen by the two chambers was computed and the difference plotted. The width of the output gaussian distribution was measured to be 1.5mm, which proves that a 4mm wide strip measures the c.o.g. of the deposited charge to better than 1.5mm. Moreover, the difference of widths of the two distributions had a RMS value of 1mm. The detailed description of this test can be found in a paper (*Strip ionization chambers as 3D detector for hadron therapy*, C.Brusasco et al, Nuclear Instruments and Methods in Physics Research A389 (1997) 499-512). These very positive results are not at all surprising because both the beam position and width are the result of several indipendent measurements from adjacent strips, thus the precision ought to be a fraction of the strip dimensions.

Conclusions

After three years of work the final prototype of *Magic Cube* performs even better than what was initially foreseen for all the parameters that have been discussed in this report. The omogeneity and uniformity of response are at present still under detailed study and will be available in few weeks. We do not foresee any problem arising from this matter as it can eventually be corrected for with beam calibration. It has to be noted that the dimensions of this prototype, indeed quite big, will be reduced in the next version to approximately $50 \times 50 \times 80 cm^3$.
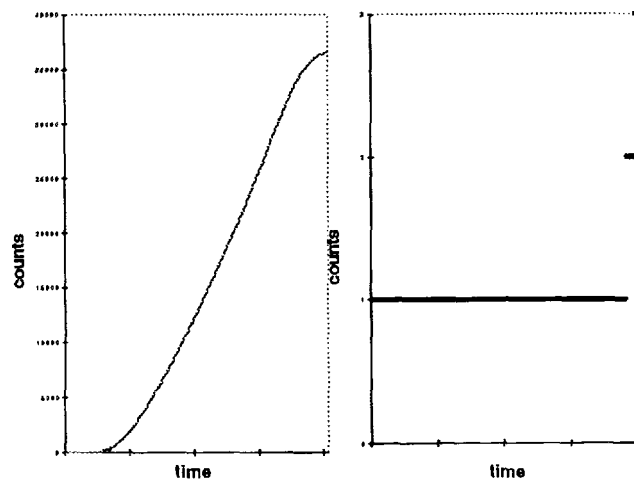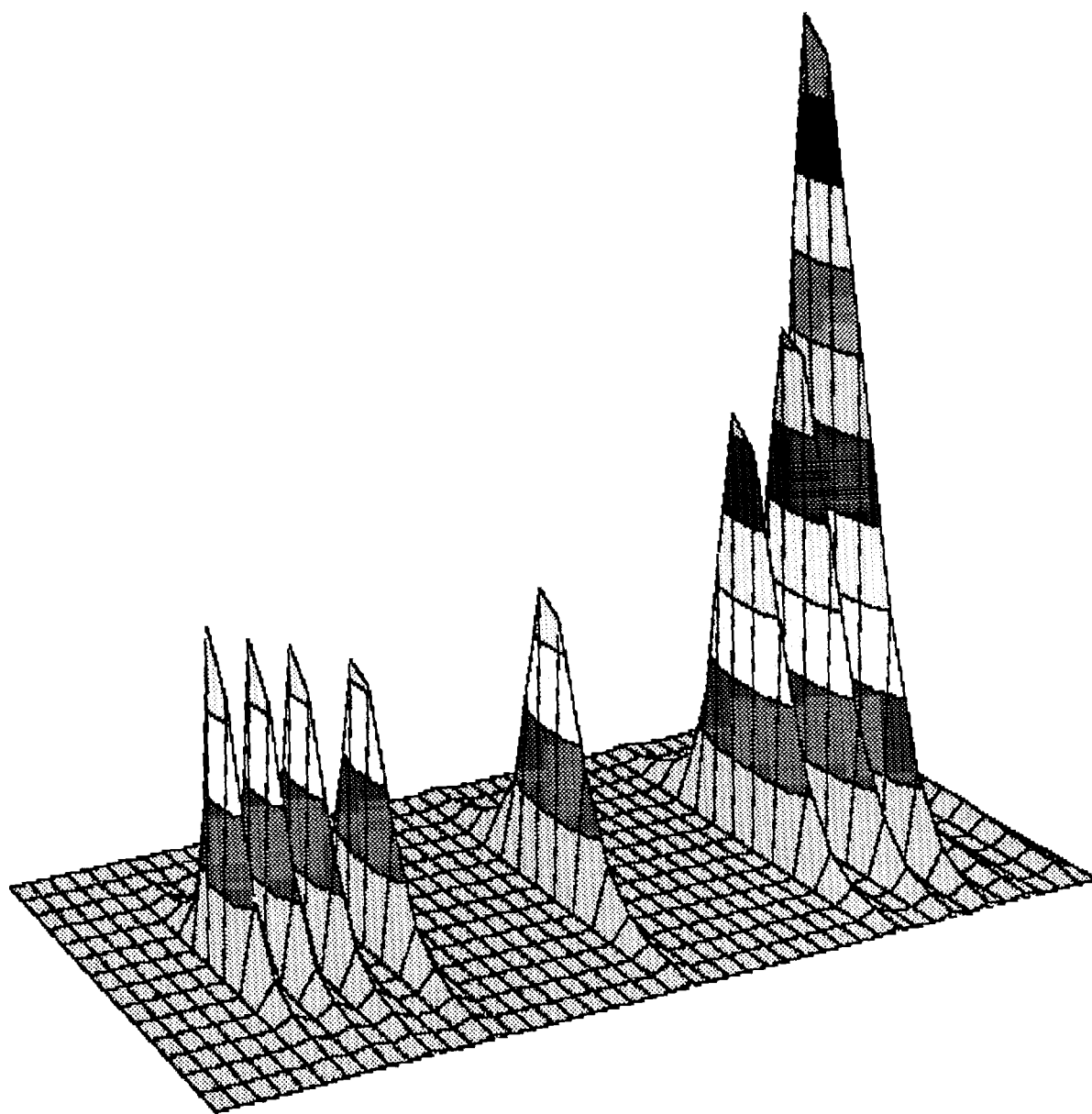
DE98F5416

TLD Dosimetry of Heavy Ion Beams

O. Geiß, M. Krämer, G. Kraft

GSI, Planckstrasse 1, D-64291 Darmstadt, Germany

Introduction

Thermoluminescence detectors (TLD) are widely used in conventional radiation detection and dose verification. Their main advantages are tissue equivalent composition and small dimensions. The forthcoming radiotherapy at GSI has triggered investigations if TLDs could possibly be used for dose verification in heavy ion irradiation.

Thermoluminescent materials as well as biological systems exhibit differences in dose response between low and high LET radiation due to the different spatial distribution of ionisation events. To account for the difference between low and high LET radiation quantitatively, one defines the efficiency $\eta = (TL/D)_{HI}/(TL/D)_{ref}$ as the ratio of TL light output per dose for heavy ions to TL light output per dose for some low LET reference radiation. Knowledge of the energy and projectile charge dependence of the efficiency η is essential for dose verification in a mixed heavy ion field. We therefore measured and calculated the TLD efficiency for different ions and energies.

Experimental setup

We used LiF chips (TLD-700) of Harshaw Chemical Co. ($3\times3\times0.38$ mm^3). Readout was done with Harshaw Series 8800 system. After irradiation TLDs were preheated at a temperature of 100 °C for 10 s, then heated to a temperature of 300 °C with a constant heating rate of 25 °C/s. Chips were held at this temperature for 20 s, followed by a 400 °C annealing for 20 s. ^{137}Cs-γ radiation (E_γ=662 keV) as well as 250 kV X-rays were used as a reference for all efficiency measurements.

To verify dose distributions in a mixed heavy ion field TLD-700 detectors were irradiated at different positions of a polystyrene stack (assumed to be waterequivalent).

Calculations

There are a number of models describing the TL response to γ and heavy ion irradiation [1, 2, 3]. In contrast to other models our calculations do not use any free parameters like characteristic dose or sensitive radius.

Our model is based on the assumption that knowledge of the radial dose distribution $D(r)$ around the ions path and the detector response to reference radiation $TL_{ref}(D)$ is sufficient to calculate the efficiency $\eta(E, Z)$. Results of Monte Carlo calculations [4] were parametrized leading to a radial dose distribution according to

$$D(r) = \begin{cases} k & : \quad r \leq r_0 = 1\text{Å} \\ k(r_0/r)^2 & : \quad r_0 < r < R_{el} \end{cases} \tag{1}$$

with the constant k taken from

$$2\pi \cdot \int_0^{R_{el}} D(r)\, r\, dr = \rho^{-1} \cdot (dE/dx). \tag{2}$$

The maximum range of secondary electrons R_{el} is calculated from the electron energy E_{el} using $R_{el} \propto E_{el}^{3/2}$. The energy loss $dE(E)/dx$ is calculated with the code ATIMA [5]. The calculation algorithms are similar to the ones used by Scholz and Kraft [6] in their cell survival model. A comparison between our calculations and experimental results are presented in fig.1. In order to check calculated efficiency tables $\eta(E, Z)$ as well as therapy planning algorithms, we verified three dimensional dose distributions in water equivalent material. Therefore the calculated TL response

$$TL(\vec{r}) = const \cdot \sum_Z \int_0^{E_{max}} \left(\frac{dN(E, Z, \vec{r})}{dE} \right) \cdot \left(\frac{dE(E, Z)}{dx} \right) \cdot \eta(E, Z)\, dE \tag{3}$$

was compared with the measured TL signal at different positions $\vec{r}$.

Results

The calculations of efficiency $\eta(E, Z)$ shown in fig.1 are in good agreement with experimental data. The TLD efficiency η decreases with decreasing energy E, and it can not
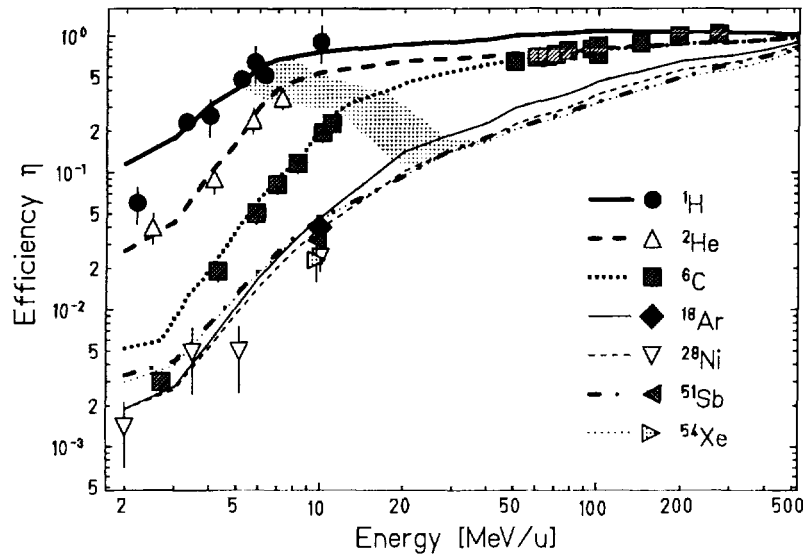
Figure 1: Efficiency of TLD-700 detectors as a function of energy – comparison between experimental (symbols) and calculated (lines) results. Experimental errors are mainly due to the CR39 fluence measurement, whereas statistical errors are smaller than 10%. The shaded area represents energies (including 20% uncertainty) for which the ion range equals the detector thickness ($d = 0.38$mm).

be assumed constant even for hydrogen ions. For a given energy the efficiency decreases with projectile charge Z, except for very low energies, where the efficiency increases with projectile charge (cp. ^{28}Ni and ^{51}Sb below 5 MeV/u). Differences between $\eta(E, Z)$ and $\eta(E, Z \pm 1)$ curves decrease with increasing charge.

The comparison between the measured and the calculated TL response (according to eqn.(3)) is another possibility to review the efficiency calculations. On the other hand it is thus possible to check some of the therapy planning algorithms. As shown in fig.2 there is a good agreement between the calculated and measured TL signal. This means that the actual depth dose profile should agree with the calculated one (dashed line in fig.2), which verifies the planning algorithms.

The results presented above show that it is possible to use thermoluminescent detectors for verification of three dimensional dose distributions even for a mixed heavy ion field.
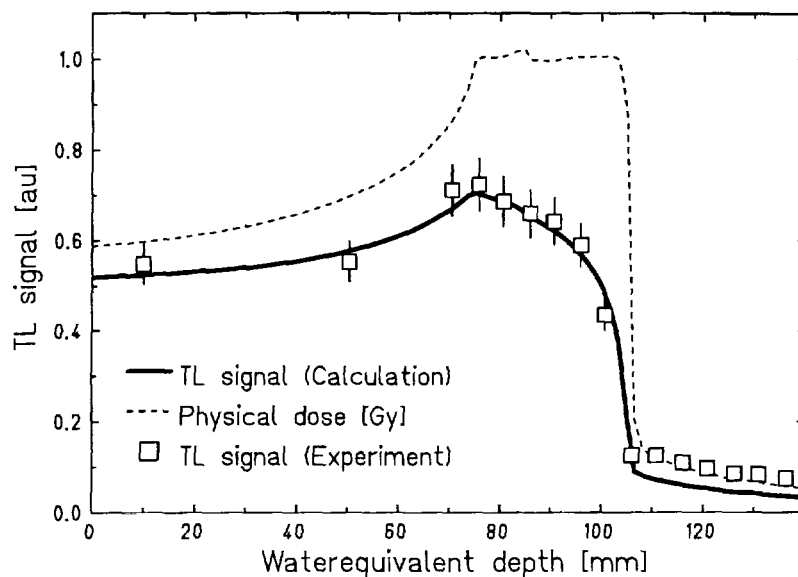
Figure 2: Verification of a three dimensional dose distribution using TLD-700 detectors. The calculated TL signal (solid line) is in good agreement with the experimental data (symbols). Therefore the actual irradiation dose should agree with the calculated dose (dashed line), which verifies the efficiency calculations as well as the planning algorithms.

References

[1]   V.G. Chernov, B.I. Rogalev: *Rad. Prot. Dos.* **33**, No. 1/4, pp. 51-54, 1990

[2]   Y. Horowitz: *Rad. Prot. Dos.* **33**, No. 1/4, pp. 75-81, 1990

[3]   R. Katz, S. Sharma, M. Homayoonfar: *Nucl. Instr. Meth.* **100**, pp. 13-32, 1972

[4]   M. Krämer: *Nucl. Instr. Meth. B* **105**, pp. 14-20, 1995

[5]   Th. Schwab: GSI Report 91-10 (1991)

[6]   M. Scholz, G. Kraft: *Adv. Space Res.* **18**, No. 1/2, pp. 5-14, 1996

EFFECTS OF THERMAL CONDUCTION AND CONVECTION ON TEMPERATURE PROFILE IN A WATER CALORIMETER FOR PROTON BEAMS

E. Gargioni°, R.F. Laitano*, A.S. Guerra* and C. Manfredotti°

*Istituto Nazionale di Metrologia delle Radiazioni Ionizzanti, ENEA, Roma
°Dipartimento di Fisica dell'Università di Torino (Italy)

Abstract. In water calorimetry, in addition to the temperature increase due to beam energy deposition in water, unwanted thermal effects occur during and after calorimeter irradiation. This should be accounted for by applying proper corrections to the experimental results. In order to determine such corrections heat flow calculations were performed using the "finite element" method. This method applies even to complex 3D geometries with not necessarily symmetric conditions. Some preliminary results of these calculations are presented together with a description of the analytical method for the evaluation of the correction factors that should be applied to the experimental results to account for the above thermal effects.

1. Introduction

In the framework of the TERA project a water calorimeter was recently built at the national standards institute for ionizing radiation (INMRI-ENEA), aiming at developing a primary standard for proton beam dosimetry. In ideal conditions the temperature profile occurring in the calorimeter water after irradiation, would remain stable for a sufficiently long time. Actually this does not happen to an extent depending on calorimeter design as well as on irradiation conditions. In addition to the temperature increase due to beam energy deposition in water, unwanted thermal effects occur during and after calorimeter irradiation. The present calorimeter is of the "sealed water type" [1] and some of these effects are minimised either by suitable measurement procedures or by a proper design of the glass ampoule containing hyperpure and gas saturated water. However in some operational conditions some of the above effects may give rise to not negligible variations of the temperature increase induced by irradiation of water. This should be accounted for by applying proper corrections to the experimental results. In order to determine such corrections heat flow calculations were performed with regard to different experimental conditions. To this end a very accurate method was utilised to obtain the numerical solutions of the Navier-Stokes equations describing heat convection and conduction effects in a fluid. The effects accounted for in this calculation were those deriving from the following physical events:

a) Temperature gradients occurring between the ampoule glass and the inner water as a consequence of the heat excess in the irradiated glass.

b) Temperature gradients induced between central and boundary regions of the ampoule, if the beam size is smaller (as in the case of proton beams) than the ampoule section.

2. Transport equations

To describe conduction and convection effects in water, the Boussinesq approximation for the Navier-Stokes equations [2] has been used. This approximation, which is realistic in our experimental conditions, is based substantially on assuming for water only laminar motion and constant viscosity, specific heat capacity and thermal conductivity with respect to temperature. Moreover variations of water density are assumed to cause only buoyant forces.

The three Navier-Stokes equations describe: the water flux conservation in the volume considered (1), the water motion (2) and the heat transport (3), respectively. With the above approximations the Navier-Stokes equations can be written as:

$$\nabla \cdot \vec{u} = 0 \quad\text{...1)}$$

$$\frac{D\vec{u}}{Dt} = -\frac{1}{\rho}\nabla p + \nu\nabla^2\vec{u} - \vec{g}\beta\Delta T \quad\text{................2)}$$

$$\frac{\partial T}{\partial t} + \vec{u}\cdot\nabla T = \alpha\nabla^2 T + \frac{Q}{\rho c} \quad\text{....................3)}$$
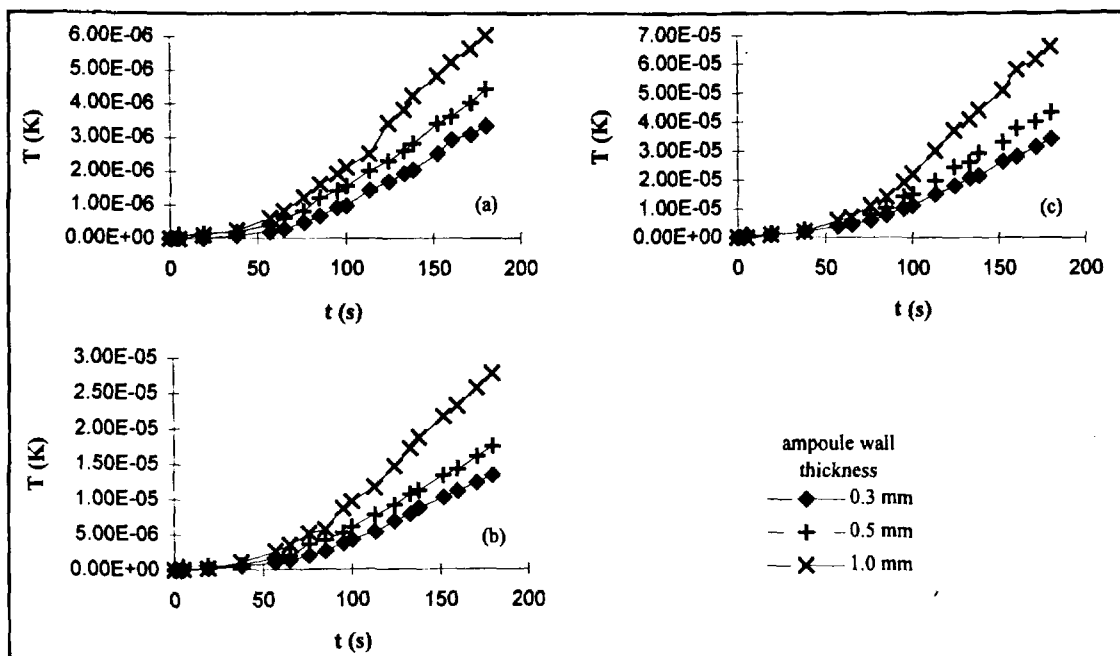
where:

Fig. 1. Temperature increase at the measurement point, in a water ampoule of 18 mm radius (as in the present calorimeter) with different wall thickness (0.3, 0.5 and 1 mm, respectively), as a function of the time elapsed after the end of irradiation. The temperature increase is due to the heat excess in the ampoule glass wall and hence to conduction and convection effects caused by the different temperature ΔT between glass and water in the ampoule. Convection effects are however negligible. The graphs (a), (b) and (c) refer to different ΔT values. The working temperature is 297 K. The ΔT values of 0.04 (graph a), 0.16 (graph b) and 0.4 mK (graph c) are due to different absorbed doses delivered in a fixed time of 60 s, at dose rates of 0.5, 2 and 5 Gy/min, respectively. In the present calculation the absorbed dose at the measurement point was assumed to be spatially uniform over a cubic volume of 10x10x10 cm^3. This is an approximation of a proton beam with 10 x10 cm^2 field size and a 10 cm spread-out peak.

D is the derivative of the fluid velocity vector, g the gravity acceleration, Q represents the heat rate per unit volume from any source (due to irradiation and others), the following parameters refer to the water fluid: u is the velocity, p the pressure, T the temperature, ρ the density, ν the kinematic viscosity, α the thermal diffusivity, β the volumetric expansion coefficient and c the specific heat. The solution of the non linear Navier-Stokes equations can be found by numerical methods. To this end the "finite element" method [3] was used in the present study. This method applies even to complex 3D geometries with not necessarily symmetric conditions. In the "finite element" method the volume of interest is subdivided into a number of regions referred to as finite elements. The equations for any individual element are then formulated to obtain numerical solutions that are interpolated within each element. These solutions are as much accurate as smaller the volume element is. The interpolated solutions referring to any individual element are suitably assembled to represent the whole region, by imposing continuity at the element boundaries.

To find the numerical solutions of the Navier-Stokes equations the code ANSYS, version 5.2, [4] is being used. This is a powerful FORTRAN code that gives the possibility of describing, even in not homogeneous materials, very complex geometries, dynamic and stationary states, interpolating functions, etc. so allowing high accuracy in the results. The heat source term, Q, in equation 3) was assumed to be constant during the irradiation time and spatially uniform over the different water regions (i.e. for small and large beams, respectively) considered in the present calculations. The change of Q in the region corresponding to the glass wall of the ampoule was duly accounted for. To calculate the temperature changes after the end of irradiation the heat source term, Q, was put equal to zero.

3. Preliminary results

A preliminary series of calculations was made to assess the effect of the heat excess in the ampoule glass on the temperature at the measurement point, P, in the centre of the ampoule.
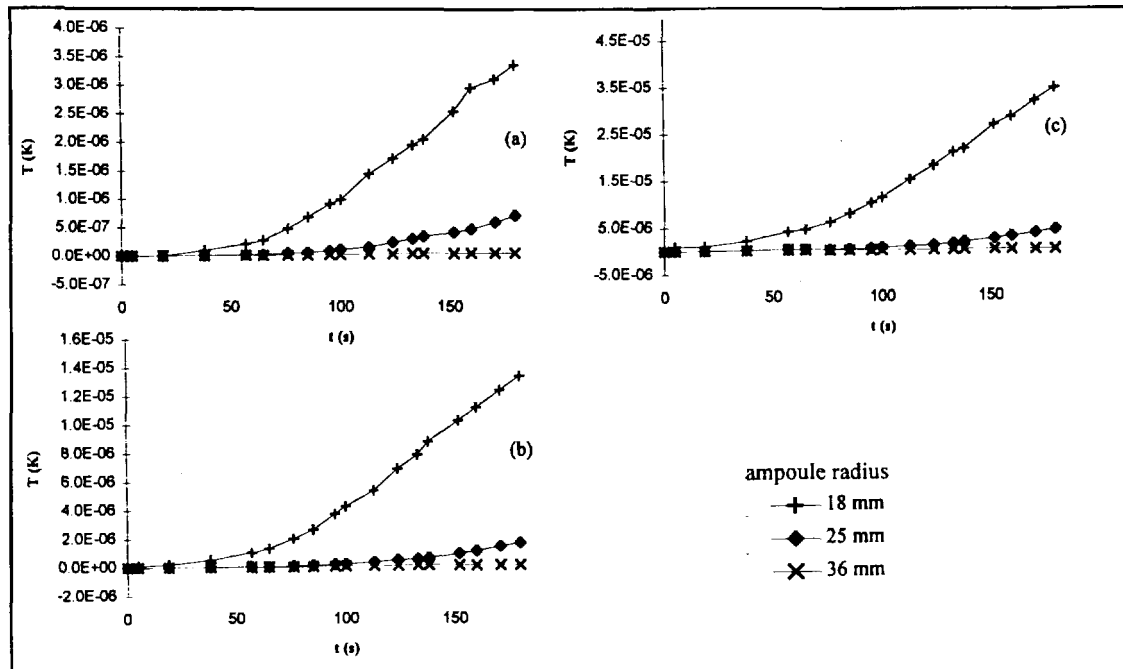
Fig. 2. Temperature increase at the measurement point, in water ampoules of different size (18, 25 and 36 mm radius, respectively) with 0.3 mm wall thickness (as in the present calorimeter) as a function of the time elapsed after the end of irradiation. The temperature increase is due to the heat excess in the ampoule glass wall and hence to conduction and convection effects caused by the different temperature ΔT between glass and water in the ampoule. Convection effects are however negligible. The graphs (a), (b) and (c) refer to different ΔT values. The working temperature is 297 K. The ΔT values of 0.04 (graph a), 0.16 (graph b) and 0.4 mK (graph c) are due to different absorbed doses delivered in a fixed time of 60 s, at dose rates of 0.5, 2 and 5 Gy/min, respectively. In the present calculation the absorbed dose at the measurement point was assumed to be spatially uniform over a cubic volume of 10x10x10 cm³. This is an approximation of a proton beam with 10 x10 cm² field size and a 10 cm spread-out peak.

This heat excess gives rise to a difference of temperature, ΔT, between the ampoule glass and the water within the ampoule. This is the case a) referred to in the Introduction. The results in Figs. 1 and 2 show that for ΔT values originating from typical absorbed doses of 0.5, 2 and 5 Gy, respectively, the temperature increase in P after irradiation are not negligible if the time, τ, elapsed between the end of irradiation and the temperature measurement is larger than two minutes about. The temperature increase in P due to the heat excess in the ampoule glass was found to be negligible in the time interval during the irradiation, if irradiation times and absorbed doses are not much different from those considered in the present calculation. The results in Fig. 1 apply to an ampoule size (18 mm radius) like that used in the present calorimeter. The above results show also that, if the measurement time, τ, is less than two minutes about, the ampoule wall thickess can change from 0.3 to about 1 mm without increasing appreciably the heat flow rate and hence the conduction effects due to the heat excess in ampoule wall. For ampoules of larger radius, these effects will be obviously lower, as is shown in Fig. 2. The role of convective effects was found to be negligible in the experimental conditions referred to in Figs. 1 and 2. On the other hand increasing the ampoule radius might increase the role of the convective effects mostly in irradiations with large local energy deposition. This is likely to be the case of small beams and small spread-out peaks with absorbed doses larger than those so far considered. Some preliminary results regarding these effects are summarised in Fig. 3. These results show that heat losses in P occur both during irradiation and after the end of irradiation if using beam sizes (5 mm and 10 mm radius, respectively) smaller than the ampoule section and with small spread out. As expected the heat loss in P is slower for the larger beam. Even in the conditions referred to in Fig. 3 convective effects are negligible If however the absorbed dose is larger than 10 Gy and if the ampoule radius is larger than 30 mm, the convective effects are likely to start. This is shown from preliminary calculations which will be reported elsewhere as soon as completed.
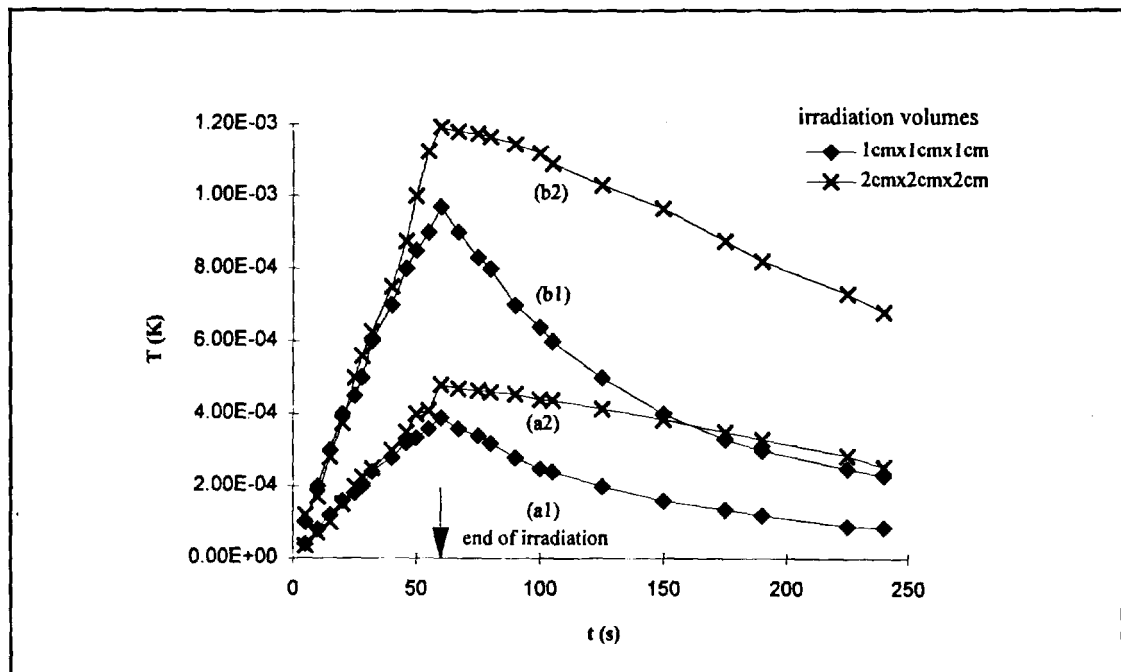
Fig. 3. Temperature variation at the measurement point, within the water ampoule, as a function of the time during and after irradiation in an ampoule of 18 mm radius, as in the present calorimeter. The temperature variation is due, in this example, to a gradient caused by small beam irradiation inducing a localized heating in the central region of the ampoule. The effects due to beams with 0.5 cm and 1 cm radius, respectively, are reported. In the present calculation the absorbed dose at the measurement point was assumed to be spatially uniform over a cubic volume of 1x1x1 cm³ and 2x2x2 cm³, respectively. This is an approximation of proton beams with 1x1 cm² (2x2 cm²) field size and 1 cm (2 cm) spread-out peak, respectively. The working temperature is 297 K. The graphs (a) and (b) refer to different absorbed doses delivered in a fixed time of 60 s, at dose rates of 2 and 5 Gy/min, respectively.

4. Conclusions

The optimization of the ampoule dimensions requires to account for many possible variables. For the present calorimeter it is envisaged to use possibly different ampoule sizes when dealing with extreme beam conditions. These conditions include very small beams with small spread-out peak and large doses, or beams with very low dose rates giving rise to possible heat losses even during the irradiation time. In addition to the effects originating from such experimental conditions, the heat variations in P due to other possible effects, with particular regard to the extra heat on the thermistor probes and in the calorimeter front window are being determined even with regard to the experimental conditions in proton beams. The final results will be reported elsewhere.

References

[1] S. Domen (1994) " A sealed water calorimeter for measuring absorbed dose", J. Res. of the NIST, 99, 121.
[2] R.B. Bird, W.E. Stewart and E.N. Lightfoot (1960) "Transport Phenomena", J. Wiley & Sons.
[3] J. O. Reddy, (1995) "An introduction to the finite element method", J. Wiley & Sons.
[4] ANSYS Inc.

WATER CALORIMETRY WITH THERMISTOR BRIDGE OPERATED IN DC AND AC MODE: COMPARATIVE RESULTS

A. S. Guerra, R. F. Laitano and A. Petrocchi

Istituto Nazionale di Metrologia delle Radiazioni Ionizzanti,
ENEA, C. R. Casaccia, c.p. 2400 Roma (Italy)

Abstract
An experimental study was carried out to find out the optimal conditions for measuring the output signal in a water calorimeter. To this end the thermistor bridge of the calorimeter was operated in AC and in DC mode, respectively. A comparative analysis of these two alternative methods was then made. In the AC mode measurement a lock-in amplifier based experimental assembly was used and compared to the more conventional system based on a high-sensitivity DC amplifier. The AC system resulted to be preferable as far as the short term and long term reproducibility is concerned.

1. Introduction

A calorimeter of the "sealed water" type [1] was recently built at the national standards institute for radiation measurement (INMRI-ENEA) to operate as a primary standard of absorbed dose to water for proton beams. To this end the calorimeter was designed to perform measurements with horizontal beams and with the measurement point (the thermistor probe) movable along variable depth in water. A shematic drawing of the calorimeter is shown in Fig.1.

When working with protons, at accelerators with energy up to 250 MeV, some practical problems are met which may influence the measurement result. These problems arise from the particular environment of an accelerator, where the possible presence of stray electro-magnetic fields (EMF) and other possible effects from non ideal electrical grounding may interfere with measurements of very weak voltage signals just as those generated by a water calorimeter. Such problems are likely to be enhanced by the large length of the instrument cables extending from the accelerator site to the console room. In some cases these cables have to cover distances by more than 30 m. In general the experimental situation in these accelerator buildings is rather different from that existing in standards laboratories. To this end a comparison between two measuring methods of the calorimeter output was made to establish the most accurate procedure in different operational conditions.

The calorimeter output is a very small voltage signal, down to some nanovolt, obtained by balancing a sensitive resistor bridge. To find the optimal conditions in the signal-to-noise ratio, output measurements were made by operating the calorimeter bridge with alternating and direct voltage, respectively. A comparative analysis of the results obtained by these two methods is described in the following.

2. Measurement procedures with the calorimeter bridge

The temperature increase of water caused by irradiation is determined by measuring the change of resistance of two thermistors placed in an glass ampoule filled with hyperpure water. The variations of the thermistor resistance are measured by a Wheatstone bridge two opposite arms of which are formed by the resistance of each of the two thermistors. The use of two thermistors (instead of one) increases by a factor two the bridge sensitivity. Accordingly, if the thermistors have the same sensitivity, the temperature variations of water

are determined as $$\Delta T = (1/2\ \alpha)\ (\Delta R/R) \qquad (1)$$

where ΔR is the variation of the bridge balancing resistor R and α is a sensitivity parameter of the thermistor. The thermistor resistance in the ENEA calorimeter is about 10 kΩ and the ΔR values are of the order of 0.1Ω for tipical irradiation conditions. These ΔR values give rise to a bridge output voltage of the order of microvolt. This in turn requires an accuracy of the output measuring system of the order of nanovolt. The measuring system is based on a
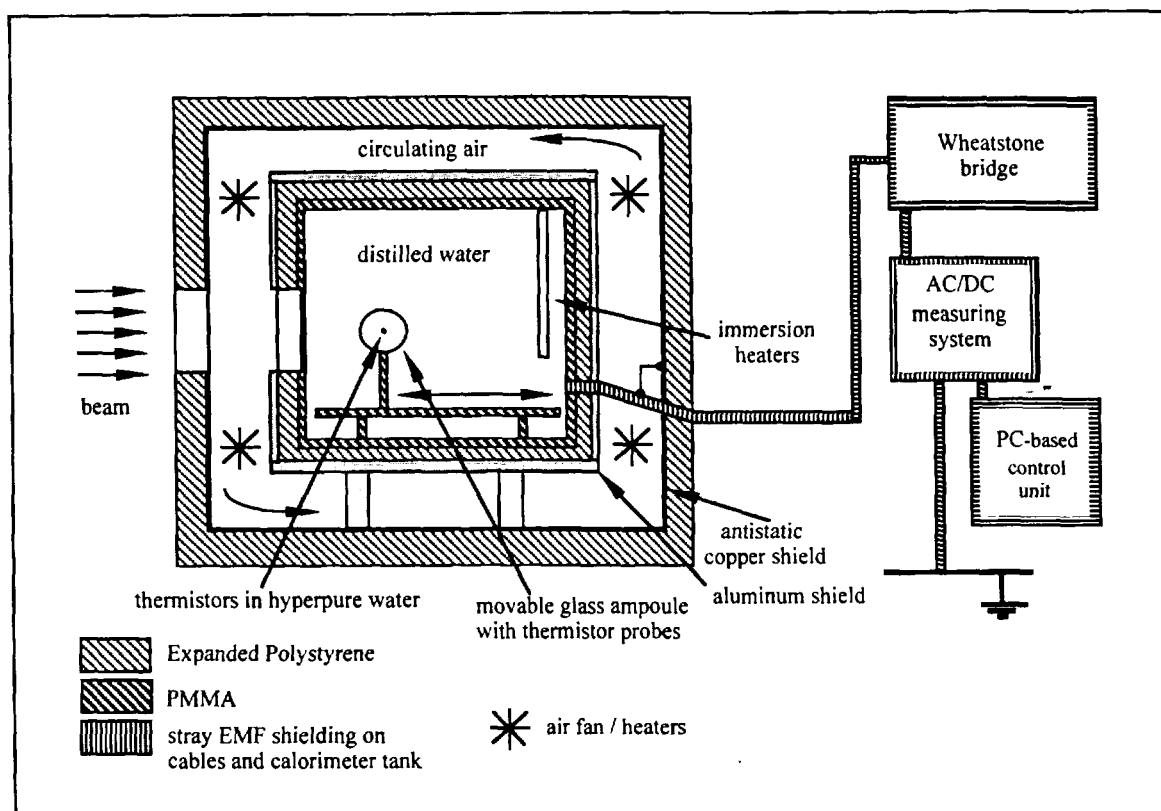
Fig. 1. Schematic diagram of the water calorimeter at INMRI-ENEA. The thermistor probe in the "sealed water" ampoule can be positioned at variable distances (2 - 25 cm) from the calorimeter window. The working temperature is at present 296.5 K. An alternative thermostatic system is available to keep the water temperature also at 277 K, corresponding to the maximum water density to furtherly minimise unwanted temperature gradients in water.

DC or AC amplifier, according to the type of voltage source (DC or AC) adopted for the bridge power supply. Measurements with both the systems were performed to choice eventually the method characterised by the best signal-to-noise ratio and hence by the best precision. The schematic diagram of the AC mode calorimeter circuitry is shown in Fig. 2. For measurements in DC mode the components generically denoted in Fig. 2 as "lock-in amplifier" were substituted by a high precision nanovoltmeter DC amplifier and the AC power supply was accordingly replaced by a DC power supply. The DC mode system calls for very accurate cable shielding and reduction of spurious emf sources, because of the very low output signals. Intrinsic circuit drift signal should be also minimised in DC mode measurements. These conditions were as far as possible accomplished in the present measurements. The above problems are on principle less important if working in AC mode. In this case however the measurement results may depend on the possible circuit reactance. The inductance and capacitance of bridge resistors and circuit cables are never exactly null, so causing a circuit reactance. In balancing the AC bridge the following equilibrium condition should be fulfilled:

$$Z_1 Z_2 = Z_3 Z_4 \qquad (2)$$

where Z_1 is the "complex" impedence of each arm of the bridge. The impedence of cables connecting the bridge to the measuring circuit should be also included in Z_1. In the complex representation of Z, Eq. 2 should be satisfied both in the real (resistive) and imaginary (reactive) part. If using a (two-phase) lock-in amplifier for AC output measurement, the above condition is equivalent to set to zero the two amplifier outputs V_x and V_y. V_x is related to the resistive and V_y to the inductive and/or capacitive components of Z. In the AC mode
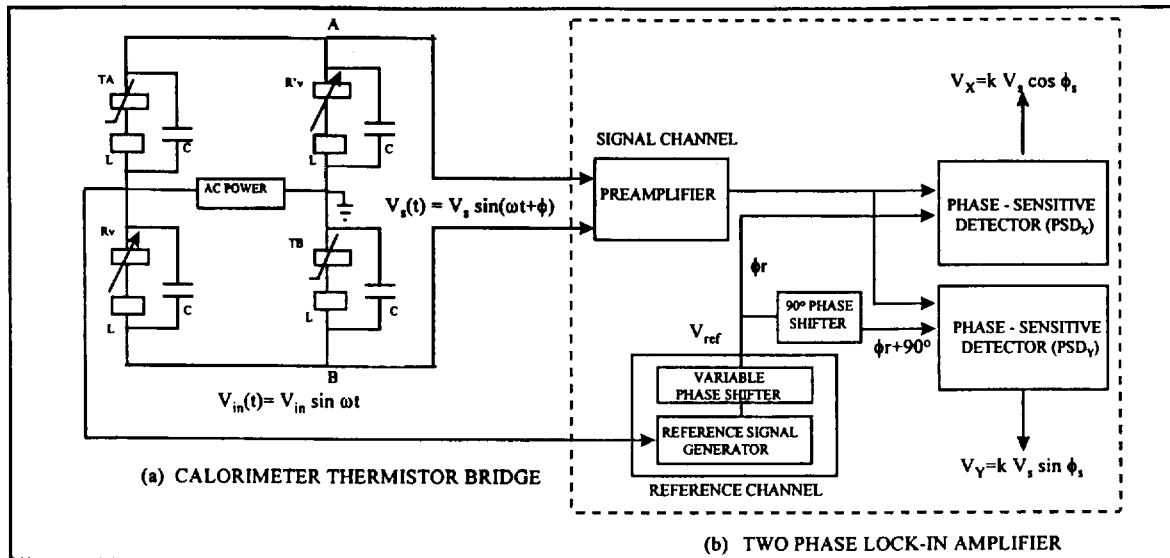
Fig. 2. *Calorimeter thermistor bridge (a) with the phase-sensitive amplifier (b) for AC mode operation. Stray inductances (L) and capacitances (C) are reported in the bridge diagram together with the thermistors (T_A, T_B) and the variable resistors (R_v, R'_v). V_x and V_y are the amplifier outputs related to the resistive and reactive components, of the circuit impedance Z, respectively.*

operation the frequency, ω, of the AC voltage source is also a critical parameter to be suitably choiced to be able to optimise the bridge output. In the present circuitry the possible reactance is due just to stray capacitance and inductance of cables and resistors as is schematically shown in Fig. 2. It not easy to introduce at the proper place in the circuit variable additional reactances, therefore the only practical way to minimise V_y is by choicing a proper value of ω. Since this value depends also on the circuit cable characteristics (i.e. cable type and length), the choice of the optimal frequency should be made for each specific experimental condition. The results of AC measurements are reported in the following, compared with the DC mode measurements.

3. Results with the DC and AC measuring methods

The optimal value of the frequency ω in the AC measurement mode was made with regard to two connecting cable lengths: 1 m (bridge test conditions) and 15 m (calorimeter measurement conditions). As expected different frequency values were obtained to minimise V_y. This is shown in Fig. 3. A comparison was then made with measurements performed in DC mode. The comparison concerned the long term and the short term reproducibility of the two methods. To be able to detect even small variations between the methods, this
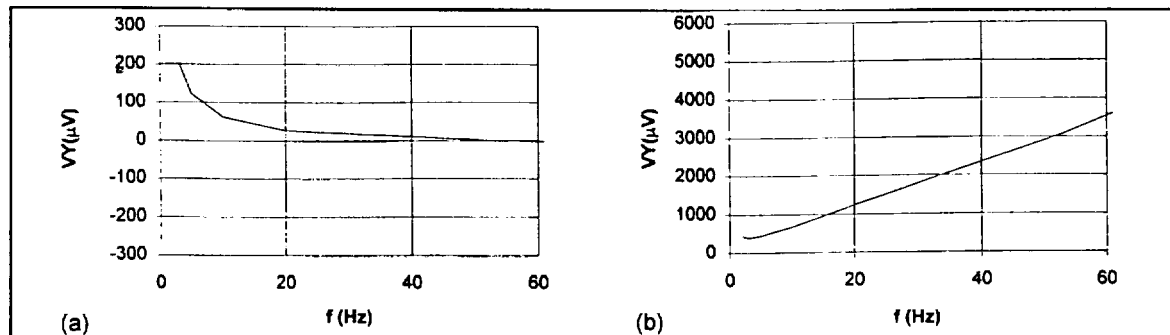
Fig. 3. *Dependence of the amplifier output, V_y, on the frequency of the lock-in amplifier. The frequency that minimises V_y (depending on the circuit reactance) changes from 53 to 3 Hz about if the length of the bridge signal cable is changed from 1m (a) to 15 m (b).*

comparison was made in very reproducible conditions not dependent on the thermal instability of the water in the calorimeter tank. To this end two precision resistors were put in place of the calorimeter thermistors and their resistance was accurately varied to simulate the thermistor resistance change. Table 1 shows the results referring to different input voltage values V_{in}. These values correspond to different electric power, P, which would be dissipated in the thermistors. The reproducibility of AC and DC systems is practically the same over 10 μW of dissipated power. The actual working values of P should be however lower than 5 μW to avoid unwanted thermal gradients in water around the thermistor probes. Below 10 μW the reproducibility of the AC system is certainly better than that of the DC system. The advantage of the AC system is evident also with regard to the long term stability as is shown in Fig. 4.

Table 1. Measurement reproducibility with the AC and DC systems in terms of standard deviations σ_{DC} and σ_{AC}, respectively, of 10 series of repeated measurements. Different bridge input voltages, V_{in}, were used in each series of measurements, corresponding to different electric power, P, dissipated in thermistors. V_{out} (theor) is the bridge output as expected from calculation, $V_{out(DC)}$ and $V_{out(AC)}$ are the output voltages measured in DC and AC mode, respectively.

V_{in} (V)	P (μW)	V_{out} (theor) (μV)	$V_{out(DC)}$ (exper) (μV)	σ_{DC} (%)	$V_{out(AC)}$ (exper) (μV)	σ_{AC} (%)
0.35	2.9	3.33	3.35	0.6	3.33	0.1
0.50	5.9	4.76	4.76	0.5	4.76	0.1
0.70	11.6	6.67	6.67	0.2	6.66	0.1
1.00	23.8	9.52	9.54	0.1	9.50	0.1
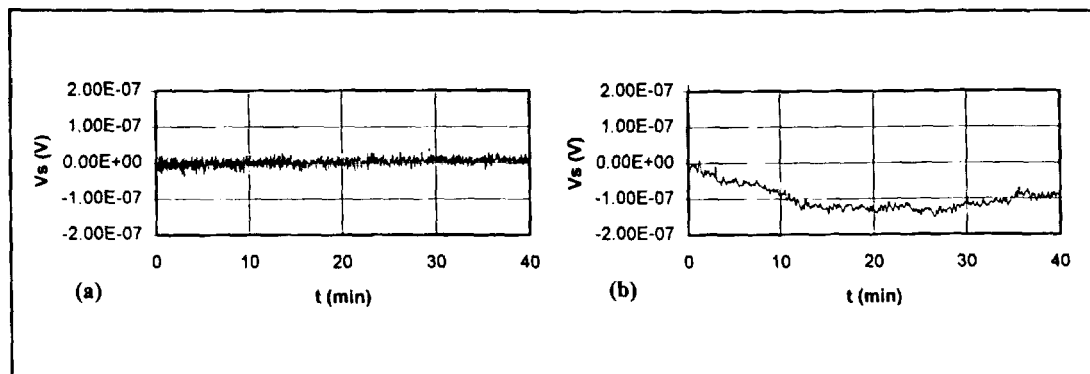
Fig. 4 . The curves (a) and (b) show the long term stability of the bridge measuring systems operated in AC mode and DC mode, respectively. The drift of the DC system depends only on the circuit characteristics and not on possible thermal instabilities of water in the calorimeter.

4. Conclusions

The results obtained in the present work show that in calorimetric measurements the bridge operation in AC mode gives more reproducible results if compared to measurements performed with a DC amplifier based nanovoltmeter. However in using AC measuring systems based on lock-in amplifier, the proper working frequency (i.e. the frequency that minimise the non-in-phase bridge output, V_y) should be determined each time cable type and length are changed. This aspect should not be overlooked in particular when moving to proton accelerators where the signal cables must be much more long than those used in current laboratory work.

References

[1] S. Domen (1994) " A sealed water calorimeter for measuring absorbed dose", J. Res. of the NIST, 99, 121.

Film Dosimetry with Heavy Charged Particles

B. Bathelt, M. Krämer, G. Kraft

Gesellschaft für Schwerionenforschung, Planckstr.1, 64291 Darmstadt

Introduction

A three-dimensional dose verification with photographic emulsions (films) is planned in the upcoming heavy ion therapy at GSI. In contrast to other radiation detectors, like e.g. thermoluminescence detectors [1] or ionizing chambers [2], photographic emulsions offer the advantage of a relatively easy handling. When arranged as a film stack, the calculated dose distribution can be verified with a high spatial resolution in transversal direction. In addition, the physical information on films is permanent and not destroyed by the readout procedure like TLD's. The analysis of the films follows promptly after irradiation and takes only several minutes. Moreover, films have the advantage that they can be kept for medical documentation for a long time.

An irradiated film is characterized by its blackening. The blackening can be measured with a densitometer, consisting mainly of a light source and a detector e.g a photo diode to measure the light transmission. Light with an incoming intensity I_{in} is attenuated by the blackened film, the intensity decreases to I_{out}. The blackening is defined as the logarithm of the ratio $S = log\frac{I_{in}}{I_{out}}$ of the incoming intensity I_{in} to the outgoing intensity I_{out}. To describe the characteristics of a film, the blackening can be presented as a function of dose, energy or other parameters. The resulting graphs are the so called blackening curves.

In general film dosimetry with heavy ions is difficult for three reasons. First, at high doses, photographic emulsions have no linear response, this leads to saturation effects. Second, photographic emulsions respond differently to various types of radiation, due to the different spatial distribution of ionisation events. Third, one has to consider the fragmentation of the primary beam in the absorbing material resulting in a mixed radiation field. Figure 1 shows a calculated fragment spectrum of a
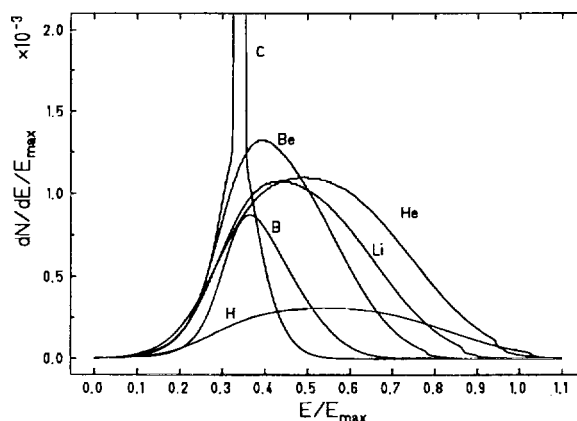
Figure 1: Calculated fragment spectrum of a 270 MeV/u carbon beam in water at a depth of 120 mm [3]

270 MeV/u carbon beam in water at a depth of 120 mm [3]. The graph of figure 1 shows that each fragment has its own continous energy spectrum $dN(E, Z, \vec{r})/dE$. Therefore the total physical dose $D(\vec{r})$ is produced by different particles (Z=1 to Z=proj) with different energies,

$$D(\vec{r}) = \sum_{Z=1}^{Z=proj} \int_0^{E_{max}} \frac{dN(E, Z, \vec{r})}{dE} \cdot \frac{dE(E, Z)}{dx} \cdot dE \tag{1}$$

and can be calculated by integrating over the energy interval $E = [0; E_{max}]$ of each fragment and finally summing up over all fragments.

Our aim is to use films not only to verify the correct three-dimensional field shape, but also to verify the applicated dose quantitatively. Thereby the physical parameter is the blackening efficiency,

$$\eta(E, Z) = \frac{S_{HI}(E, Z)}{S_{ref}} \tag{2}$$

which describes the difference between densely and sparsely ionizing radiation as the ratio of blackening for heavy ions to the blackening of a reference radiation, e.g. 200 kV x-rays or ^{60}Co at the same dose level. We want to develop a model, based on experimental data, to calculate the blackening efficiency of photographic emulsions as a function of particle energy E and atomic number Z_i $\eta(E, Z_i)$. This model should be similar to the model for calculation of cell survival [4] or the model for calculating the efficiency of thermoluminescence detectors [2]. These models are parameter free and take into account only the photon response and the heavy ion track structure. If we know the blackening efficiency, the energy loss and the fragment spectra of each projectile we can predict the expecting film blackening for an applicated dose at any location in the irradiation volume. The blackening can then be calculated as followed:

$$S_{HI}(\vec{r}) = \frac{1}{\rho} \cdot \sum_{Z=1}^{Z=proj} \int_0^{E_{max}} \frac{dN(E, Z, \vec{r})}{dE} \cdot \frac{dE(E, Z)}{dx} \eta(E, Z_i) \cdot dE \tag{3}$$

For the use within the heavy ion therapy project at GSI, it is necassary to collect experimental data on blackening curves for a carbon beam in the range of 80 to 450 MeV/u as well as its fragments.

Materials and Methods

For the following experiments we used the KODAK X-OMAT V film (24 x 30 cm^2). The films were irradiated using the GSI rasterscan system. After irradiation, the films were processed using the developing machine CURIX 60 of Agfa. The quality of the developing machine was controlled by a combined sensitometric and densitometric measurement. The deviations between these measurements were in the order of approximately 5 %. Finally the film blackening was determined quantitatively with a calibrated densitometer with a maximum deviation of 2 %.

Results

First experimental data were recorded at the SIS for 100 MeV/u und 300 MeV/u carbon ions and at the DKFZ in Heidelberg at a ^{60}Co source.

Blackening Curves for 100 and 300 MeV/u C-Ions and ^{60}Co
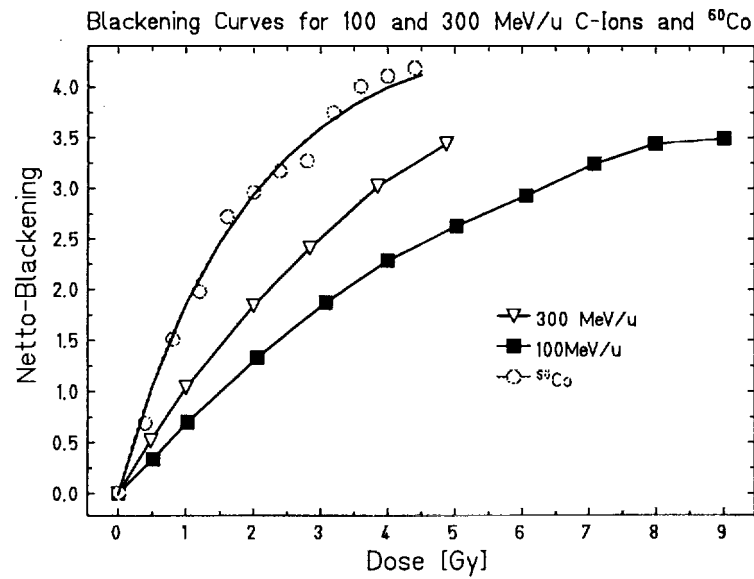
Figure 2: Blackening curves as a function of dose for carbon ions (100 MeV/u und 300 MeV/u) and ^{60}Co.
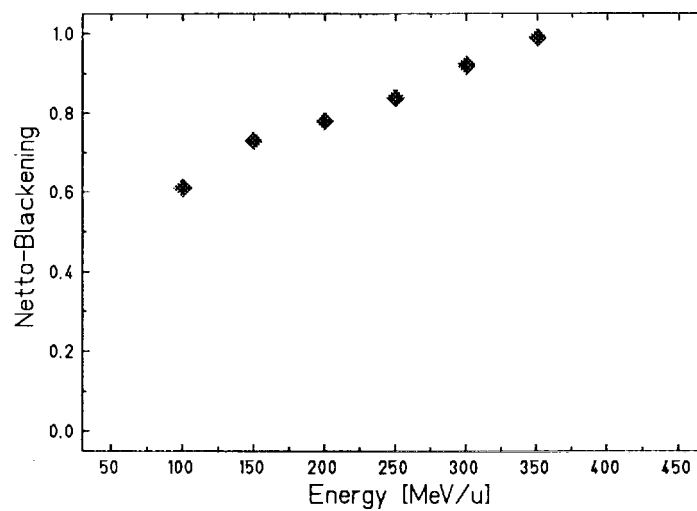
Figure 3: Blackening as a function of projectile energies for carbon ions, with the dose kept constant 1 Gy.
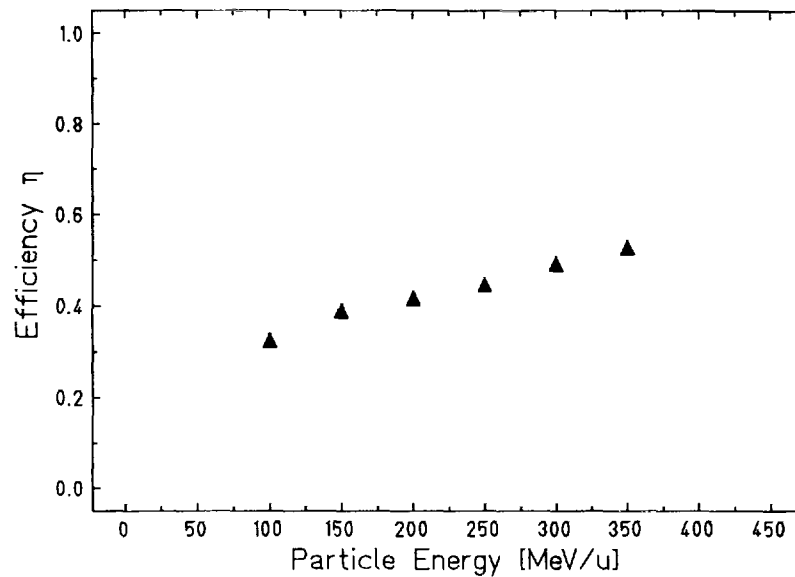
Figure 4: Blackening efficiency η as function of particle energy for carbon ions in the range of 100 to 350 MeV/u.

Figure 2 shows the netto-blackening (bias subtracted of film background) as a function of dose. In another experiment the energy of the carbon ion beam was varied between 100 MeV/u and 350 MeV/u in steps of 50 MeV/u. Figure 3 shows the netto-blackening as a function of projectile energy at 1 Gy. Inserting the experimental data from figure 2 and 3 into equation 2 yields the blackening efficiency graphed for a carbon ion beam in figure 4. This is the first step to establish an experimental blackening efficiency table for the therapy relevant carbon ion beam and its fragments. Further measurements and a semiempirical model will allow a complete dose verification with photographic emulsions.

References

[1] O. Geiss, PhD thesis
[2] C. Brusasco, GSI Report 97-01 (1996)
[3] Th. Haberer, GSI Report 94-09 (1994)
[4] M. Scholz, Radiation Protection Dosimetry, Vol.52, Nos 1-4,pp 29-33 (1994)

DE98F5412

DE010814110

A VLSI circuit for the charge measurement of a strip ionization chamber

G.C.Bonazzola[1], M. Donetti[2], G. Mazza[1]

[1] *University and INFN Torino, Via P. Giuria 1, I-10125 Torino, Italy*
[2] *ASP, V.le Settimio Severo 65, I-10133 Torino, Italy*

ABSTRACT

In this paper we report the design of a 64-channel VLSI chip to perform the current to frequency conversion for parallel plate strip ionization chambers. The chambers measure the intensity and the geometrical characteristics of a therapeutical beam.

Proofs should be sent to:
Roberto Cirio, Via Giuria 1, I-10125 Torino TO, Italy
tel: +39-11-6707332, fax: +39-11-6699579, email: cirio@to.infn.it

1 Introduction

We have developed a 64-channel VLSI chip to instrument a set of parallel plate ionization chambers to measure the beam intensity in hadrontherapy cancer treatments.

The use of hadron beams requires a measurement of the relative dose (or deposited energy) with a spatial accuracy better than the voxel dimensions, which are typically a few millimeters along each of the three coordinates. It is then necessary to map the dose in the plane transverse to the beam direction with a precision of ~1mm. The same is true for the longitudinal dose deposition.

Furthermore the charge deposition measurement has to be kept within a precision of a few percent over all the dynamic range.

To fulfill these requirements we developed a detector based on parallel plate gas ionization chambers with the anode plate segmented into strips. The strips are placed perpendicular to the beam direction and they collect the ionization charge which is proportional to the energy deposited in the gas and ultimately to the dose delivered along the three axes.

The necessity of a large integration scale has been dictated by several reasons, like reduction of the noise effect due to the strip capacitance (the chips are placed quite close to the strips avoiding long conductive paths), number of channels (which are of the order of hundred for each chamber), modularity and compactness. Indeed it might be necessary to add several chambers along the longitudinal coordinate without modifying the mechanical structure of the detector.

The circuit is based on the idea of counting the number of times a capacitor is charged by the input current and discharged by a reset circuitry.

2 Design of the VLSI chip

In Fig.1 we show the block diagram of a single channel. The input of the circuit is a current with an intensity proportional to the fraction of beam flux crossing the strip area. The input stage of the converter is basically a charge integrator. This is obtained with an Operational Transconductance Amplifier (OTA) with a 600fF capacitor, $C1$, in feedback connection. Whenever the voltage across $C1$ due to the charge build up exceedes a given threshold V_T, the comparator, $COMP$, fires a logic circuit PG that generates a 100ns pulse. The pulse is sent both to: a) the asyncronous counter CN and b) the circuitry that resets the feedback capacitor. This is the most delicate part of the circuit. The number of pulses counted by CN is proportional to the deposited energy and is read out by the data acquisition system at any given time interval.

We now examine the systems used to reset the feedback capacitor, $C1$. To avoid any dead time we implemented a circuitry, shown in Fig.2, which for
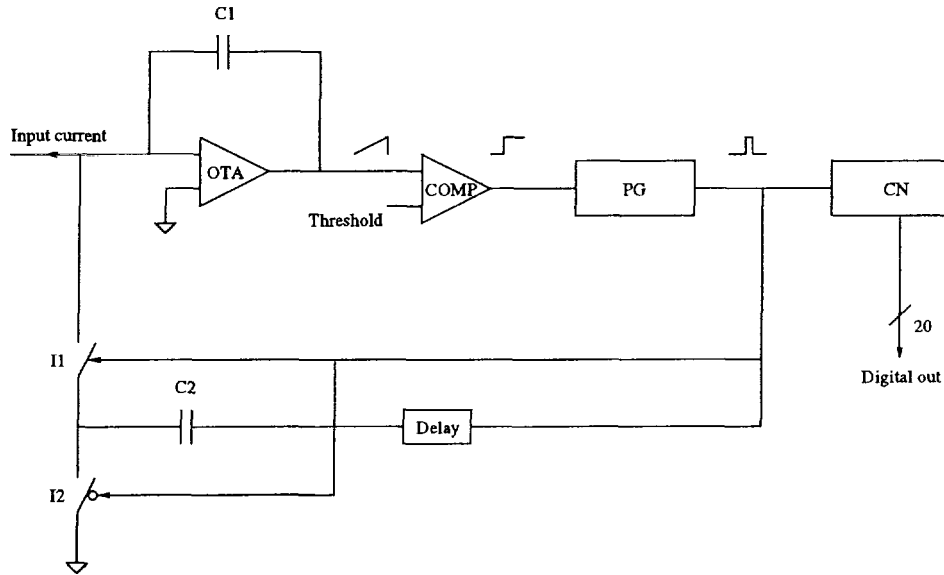
Figure 1: Block diagram of a single channel of the circuit.

each pulse subtracts a constant amount of charge, Q_T, feeding a pulse through a 200fF capacitor, $C2$. At the leading and at the trailing edge two equal charges of opposite sign are injected. The leading edge, which would inject a current with the same sign of the input current, is shorted to ground through the switch $I2$. On the other hand at the trailing edge arrival the switch $I1$ is closed and $I2$ opened and the charge is properly subtracted. The delay line has been adjusted to provide the correct synchronization. Charging and discharging of the feedback capacitor are analog operations which are dealt in parallel with no dead time. There is a maximum input current, $i_M = Q_T/T_{Min}$, where T_{Min} is the minimum interval between two pulses, above which the rate of charge subtraction becomes too slow and it could be necessary to discharge completely the feedback capacitor. Thus the main drawback of this scheme is the maximum current the circuit can deal with: decreasing Q_T increases the sensitivity of the system but decreases the current value for which the saturation occurs.

CN is a 20-bit digital counter which serves each channel output. The channel address can be externally selected and the number of counts can be read out at any time. The counter output is latched; in this way is possible to freeze the value of all the counters value at any intermediate time without stopping the counting.

The circuit was realized in AMS 0.8 μm CMOS technology. The chip size is 6×7mm^2.

2
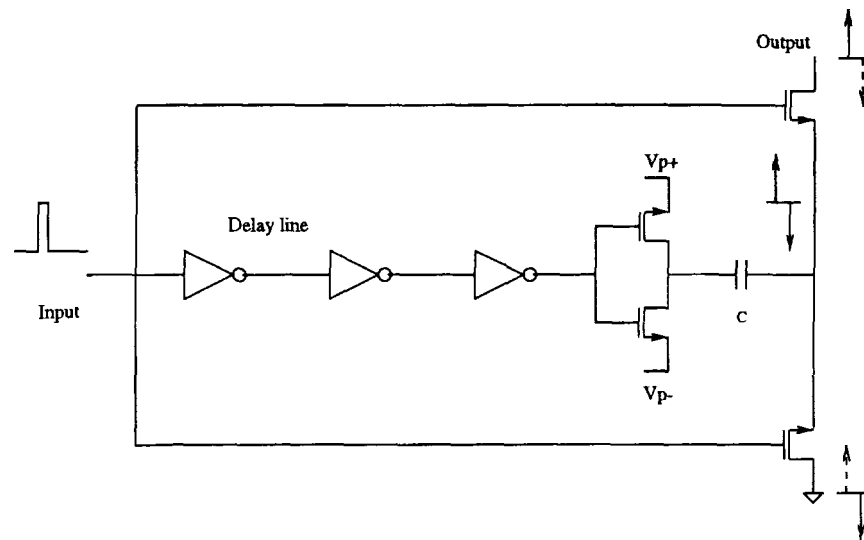
Figure 2: Circuit diagram of the reset circuit.

3   Measurements

The chip is presently under test. We have already fully tested a 14-channel prototype designed in AMS 1.2 μm CMOS technology that has shown a deviation from linearity of less than 1% in the range between 1 nA and 600 nA. The gain spread for channels of a given chip is less than 0.5%. Furthermore, the gain uniformity from chip to chip is remarkable, being the overall r.m.s. equal to 0.8%.

A further important parameter is the stability in time of gain. We repetedly measured the gain as a function of time over several days for several channels. the gain drift r.m.s. was measured to be less than 1%.

A detection system for the verification of 3D dose distributions in light-ion radiotherapy

Caterina Brusasco (GSI, Darmstadt and INFN, Torino), Bernd Voss,

Dieter Schardt, Uli Weber (GSI, Darmstadt)

For routine dose verification at GSI we have developed a detection system which can verify in a short time the treatment plans released. Such a device can be optimized according to the characteristics of the active beam-delivery system at the GSI therapy unit. This system produces the 3-dimensional dose distributions by a combination of fast beam scanning with an active variation of the beam energy, corresponding to different depths of the Bragg peak. For each slice of the target volume, corresponding to a different beam entry energy, a pencil-like ion beam is scanned over the target area according to the calculated treatment plan.

According to this tecnique of a sequential build up of the final 3D dose distribution, the 3D dose measurement can be also separated in two independent measurements: the location of the beam in a plane perpendicular to the beam using a multi wire proportional counter (MWPC) and the dose distribution along the beam axis using a stack of ionization chambers (IC), sandwiched between tissue-equivalent absorbers.

A sketch of the GSI detection system is shown in fig. 1. Along the beam path 36 ionization chambers, sandwiched between 5 mm thick removable plastic plates, will provide the depth dose profile measurement. The collecting gas gap is 1 cm with N_2 as filling gas and the active area is (25x25) cm². Due to the variable beam energies and intensities (10^6 to 10^8 ions per spill 2 sec long), the read-out current will range approximatly from 1 nA up to 1 μA. For the electronic read-out of the ICs we use an integrator following the principle of the recycling capacitor. The current detected by the chamber is transformed in a frequency with a gain adjustable from 5 to 50 pC/count and the digitized output-signals are summed for each beam energy by a CAMAC scaler.

Because the region of interest in the target volume can be situated at different penetration depths a range shifter will be used to position the extended Bragg-peak in the region of the ionisation chambers. The range shifter can also be used to improve the granularity of the measurement along the beam path, that would be otherwise determined a priori by the thickness of the plastic foils interleaved to the ICs. In front of the range-shifter a MWPC with a fast single-wire read-out electronics, originally developed for the beam-monitor system[1], will follow the movement of the beam over the transverse treatment area. To monitor the time dependence of the beam intensity during the scanning of the beam, a first ionization chamber is placed in front of the range-shifter and read with the same time resolution of the MWPC.

For each beam energy the total charge is integrated in each chamber of the stack in order to obtain the total dose delivered with this energy. Then the fractions of this total dose are distributed to each pixel-position as measured by the MWPC according with the time

Position and beam intensity measurement

Depth dose profile measurement

MWPC + IC   Range shifter   Stack of ion. chambers with
                              5 mm PMMA slabs interleaved
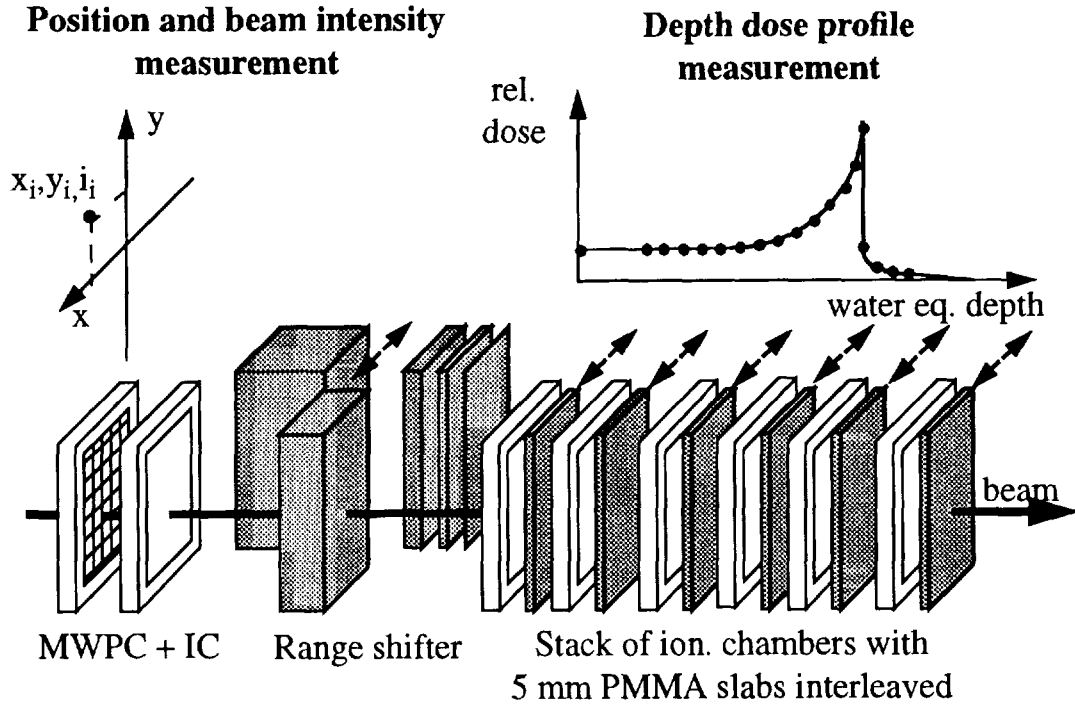
Fig. 1: sketch of the 3D dose verification system. It consists of a stack of ionization chambers sandwiched between 5 mm thick removable plastic plates and a range-shifter to center the enlarged Bragg maximum on the chambers. The depth dose profile is normalized to a first chamber placed in front of the range shifter. The MWPC provides the bidimensional position information over the transverse treatment area for the three-dimensional reconstruction of the dose deposition

differential readings of the ionisation chamber in front of the range shifter.

We initially did some tests with a prototype version consisting of a stack of 10 small ionisation chambers [2] [3]. First we compared the recombination in different gases as a function of the electrode voltage finding that Ar and N_2 reach at very low voltage the saturation plateau while for example air still shows for high voltages a significant increase in the chamber output.

In addiction we measured the energy dependence of the gas-to-water stopping power ratio, that correlates the dose received by the detector to the one that would be released in water (patient reference-medium). In fact according to the Bethe-Bloch formula, the gas-to-water mass stopping-power ratio for the $^{12}C^{+6}$ in the energy range from 300 MeV/u to 1 MeV/u shows for Ar a variation of 10% compared to less than 1% for N_2.

As a result of these measurements N_2 seems to be a good choice for the filling gas of the chambers used for the depth dose measurement.

We then proceeded in the costruction of ten ionisation chambers with the final active area of (25x25) cm^2 and 6 μm aluminized kapton foil as windows. The test of the detectors with a $^{12}C^{+6}$ beam of 270 MeV/u showed a not smooth depth dose profile with relative fluctuations

Effects of the inhomogeneity between wall and gas in ionometric proton dosimetry

E. Casnati, C. Baraldi, C. Bonifazzi, A. Tartari

Università di Ferrara and INFN, Sezione di Ferrara, I-44100 Ferrara (Italy)

P. Boccaccio

INFN, Laboratori Nazionali di Legnaro, I-35020 Legnaro (Italy)

B. Singh

Punjabi University, Patiala (India)

Gray's cavity theory permits the evaluation of the dose absorbed in a small mass of a homogeneous medium uniformly irradiated by ionizing photons from the knowledge of the mass ionic charge collected in the gas enclosed in a cavity centred on that mass. This theory is the basis of the ionometric dosimetry. In order to give a precise meaning to measurements, the medium enclosing the cavity must be thick enough to assure the flow in gas of the slowing down spectrum of secondary electrons; this is the task accomplished by the ionization chamber wall. In Gray's theory, the interaction probability of photons in gas is considered negligible; only the wall secondary electrons cause ionization. The relation between the dose D_d absorbed in the wall medium and the mass ionic charge J_g collected in gas is

$$D_d = \overline{\left(\frac{S_d}{S_g}\right)} \frac{J_g W}{e}$$

W is the mean energy expended in the gas per ion pair formed and e is the elementary charge $(1.602 \cdot 10^{-19}$ C). S_d is the mass stopping power of the secondary electrons in wall medium d; S_g is the stopping power of the same electron spectrum in gas g. Great attention was devoted in the past to the analysis of W dependence on photon energy and gas atomic number and to the finding of the procedure most appropriate to give correct values of $\overline{S_d/S_g}$ average ratio. The results were tabulations of both W values for various gases and average stopping power ratios of some wall media mainly coupled with dry air. W values appeared to be independent from the energy of the secondaries produced by the photons commonly used in radiotherapy [1]. The stopping power ratios were calculated for the slowing down spectrum numerically corrected for the presence of delta rays [2]. The energy below which an electron belongs to delta rays is the one permitting to the electron just to cross the gas cavity. The probability of photon interactions in cavity gas is still negligible. The effect of photon interactions with the cavity medium on the stopping power average ratio was described by Burlin [3], mainly in connection to condensed state detectors (luminescent solid materials, chemical liquids and gels, etc.).

From the point of view of ionometric dosimetry, protons differ from photons because they belong to the directly ionizing radiations and interact with both wall medium and cavity gas. Moreover, proton beams of radiotherapeutic energies give rise to secondary radiation, mainly protons in nuclear reactions and electrons in atomic collisions. The contribution of secondary protons to the absorbed dose in proton radiotherapy as it is measured by ionization chambers need a specific treatment. But most of the absorbed dose arises from collisions with atomic electrons, which can gain an appreciable kinetic energy. For primary pro-

tons of 100 MeV these electrons have ranges that can be of the order of 10^{-2} g/cm^2, i.e. about 10 cm in dry air at STP conditions.

The effect produced by secondary electrons in ionometric measurement of absorbed dose can be examined in the particular simple case of an infinitely large gas slab enclosed in a homogeneous solid medium. The slab is irradiated by a parallel proton beam the axis of which is perpendicular to the slab surface. This arrangement suitably simulates the situation presented by the dosimetry of proton beams carried out by a plane-parallel ionization chamber. The problem cannot be solved by means of Monte Carlo codes commonly used in proton transport analyses because the lower threshold energy of secondary electrons is too high for the phenomenology under examination. A simple and manageable procedure to obtain preliminary practical data on the effect of secondary electrons produced by protons in the solid wall and the gas cavity is given by Kobetich and Katz empirical treatment [4] also used by Laulainen and Bichsel [5] and by Bichsel [6] in the solution of problems partially similar to the present one. The Kobetich and Katz model defines a characteristic thickness, associated to the electron energy, and a transmission probability of that electron to a distance of its origin along the depth of such thickness. The empirical relation between characteristic thickness and electron energy, with the medium atomic number as a parameter, the inverse relation and the probability expression are given by the same authors. The direction of the characteristic thickness normal is linked by the square cosine law to the maximum energy fraction transferred from the primary proton to the secondary electron. An elaboration of this model permits the evaluations of the relative contributions given to the dose absorbed in the gas by secondary electrons arising from collisions in both gas and wall medium. The dose D_g absorbed in the cavity gas is the sum of the internal and external contributions, D_i and D_e. D_i is the mass energy released to gas by protons, which collide with its atoms, reduced of the part taken out of the cavity by secondary electrons. D_e is the mass energy released in gas by secondary electrons generated in the wall and entering the cavity. One has

$$D_g = D_i + D_e$$

The relative values of these contributions $D_{ri} = D_i/D_g$ and $D_{re} = D_e/D_g$, calculated by the empirical model neglecting all the second order effects, are given in Table 1. Two gases of common use in dosimetry, dry air and tissue equivalent gas (methane based) (TE), were considered. Four typical wall materials, graphite, polystyrene, tissue equivalent plastic A-150, air equivalent plastic C-552, have been coupled with dry air. Graphite and A-150 plastic were the wall materials for TE gas. The calculations were carried out for gas slab thicknesses of 1 and 2 mm. The required properties of those materials were taken from ICRU Report 49 [7].

As a consequence, the dose absorbed in the cavity gas is not simply proportional to the gas stopping power S_g, but to the product of S_g and a weighting factor f_{gd} taking into account internal and external fractional contributions. f_{gd} is the inhomogeneity factor because it equals one for a combination of gas and wall homogeneous in respect of their interactions with protons, whereas differs as more from one as larger the inhomogeneity is. Values of f_{gd} factor are given in Table 2 for the previous gas-wall couplings. It may be seen that for some of them, f_{gd} factor is appreciably far from unity, certainly above the limit of its uncertainty. Therefore, in order to correctly evaluate the wall absorbed dose D_d, the basic expression written by neglecting the secondary electron effect [e.g. 8] must be completed as follows

$$D_d = \frac{J_g \bar{w}}{e} \frac{\int_0^\infty \Phi(E)\,[S(E)/\rho]_d\,dE}{\int_0^\infty \Phi(E)\,f_{gd}\,[S(E)/\rho]_g\,dE}$$

w is the differential value of the mean energy necessary to produce an ion pair, which depends on proton energy, and $\bar{w}$ is its average on the proton spectrum.

These preliminary results suggest that the effects of secondary electrons in proton ionization dosimetry should deserve more attention and detailed treatments.

[1]   ICRU, Int. Comm. Radiat. Units Meas., Washington, DC, Report 31 (1993).
[2]   L.V. Spencer and F.H. Attix, Radiation Res. 3 (1955) 239.
[3]   T.E. Burlin, in 'Radiation Dosimetry' Vol.1, F.H. Attix and W.C. Roesch Eds., Academic Press, New York, NY (1968).
[4]   E.J. Kobetich and R. Katz, Phys. Rev. 170 (1968) 391.
[5]   N. Laulainen and H. Bichsel, Nucl. Instr. and Meth. 104 (1972) 531.
[6]   H. Bichsel, private communication.
[7]   ICRU, Int. Comm. Radiat. Units Meas., Washington, DC, Report 49 (1993).
[8]   AAPM, American Institute of Physics, New York, NY, Report 16 (1986).

Table 1: Relative contributions of inside and outside proton interactions to the dose absorbed in gas slab							
		Proton Energy	1 MeV		10 MeV		100 MeV	
Gas gap	Gas	Wall	D_{ri}	D_{re}	D_{ri}	D_{re}	D_{ri}	D_{re}
1 mm	Dry air	graphite	.987	.013	.901	.099	.835	.165
		polystyrene	.986	.014	.893	.107	.824	.176
		A-150	.985	.015	.892	.108	.822	.178
		C-552	.987	.013	.902	.098	.838	.162
	TE	graphite	.988	.012	.910	.090	.854	.146
		A-150	.986	.014	.902	.098	.842	.158
2 mm	Dry air	graphite	.993	.007	.932	.068	.851	.149
		polystyrene	.993	.007	.926	.074	.841	.159
		A-150	.993	.007	.925	.075	.839	.161
		C-552	.994	.006	.933	.067	.854	.146
	TE	graphite	.994	.006	.937	.063	.869	.131
		A-150	.993	.007	.931	.069	.857	.143

Table 2: Inhomogeneity factors for different material couplings at three proton energies and two gas thicknesses					
			f_{gd}		
Gas gap	Gas	Wall	1 MeV	10 MeV	100 MeV
1 mm	Dry air	graphite	1.000	1.002	1.004
		polystyrene	1.002	1.010	1.018
		A-150	1.002	1.012	1.020
		C-552	1.000	1.000	1.000
	TE	graphite	0.998	0.991	0.986
		A-150	1.000	1.000	1.001
2 mm	Dry air	graphite	1.000	1.001	1.004
		polystyrene	1.001	1.007	1.016
		A-150	1.001	1.008	1.018
		C-552	1.000	1.000	1.000
	TE	graphite	0.999	0.994	0.988
		A-150	1.000	1.000	1.001

Development and Application of an Initial Quality Assurance Program for Dosimetry at GSI

P. Heeg, Universitätsklinik Heidelberg,
G. Hartmann, O. Jäkel, C. Karger, A. Krießbach, DKFZ Heidelberg,
D. Schardt, GSI Darmstadt

At the heavy ion therapy facility at GSI the dose distribution in a given target volume is generated in the two lateral dimensions by scanning a Carbon ion beam and in the third dimension by varying the beam energy[1]. This tumor conform irradiation technique, together with heavy ion specific characteristics, has several particular consequences on quality assurance procedures. In some cases they differ strongly from those applied in the more conventional therapy using electron linacs. This contribution gives an overview of the dosimetry part of the quality management program developed for the GSI therapy facility.

Introduction

Mainly two characteristics of the heavy ion beam used at the GSI therapy facility are responsible for important differences in the dosimetric techniques when compared to those applied at photon and electron beams in radiotherapy.

First, the energy lost by an ion beam in tissue is deposited nearly locally. Therefore dose measurements are, in first order, independent of the material surrounding the detector or the film. This can be an advantage, for example when measuring geometric field parameters, as no additional buildup material is required. Absorbers other than air are in principle only used to put the detector at the desired depth of the depth dose distribution.

Secondly, the beam scanning technique implies that the dose rate in a given target volume is position and time dependent, requiring a set of simultaneously measuring detectors located at different positions inside the volume to get the dose distribution. The limits of the field in three dimensions are also generated dynamically by the beam scanner, a fact which gives additional importance to the verification of the field geometry. These are substantial differences to, for example, a photon field where the dose distribution is usually measured by scanning a single probe within the field and recording the dose rate as a function of the position, and where constancy checks of the field size can be performed easily by comparing film exposure and light field.

The measurement techniques of numerous other parameters, however, are similar to those in conventional radiotherapy and the initial quality assurance program has been developed in close analogy to the existing standards for electron linacs.

Monitor Calibration

The dose monitors consist of large - area parallel - plate ionization chambers[2], [3] which have to cover a scanning range of approximately 20cm x 20cm. One task of the constancy checks is the verification of the calibration factor and the investigation of the dependence of this factor on parameters like the beam position within the monitor, the particle fluence and the flux.

The setup for the measurements using monoenergetic fields consists of a "Farmer" thimble type ionization chamber (PTW) with an active volume of 0.6 cm^3 in a tissue

equivalent plate positioned at the isocenter. The field size is 5cm x 5cm and thus much larger than the Farmer chamber while completely inside the large monitor chamber. The particle fluence is deduced from the dose measured by the Farmer chamber and compared to the number of monitor units from the monitor chamber.

The calibration factor K is given by

$$K = \frac{N_{ion}}{m.u./V} \quad , \qquad N_{ion} = 6.241 \ 10^7 \frac{\Delta x \Delta y}{S/\rho} D$$

where m.u./V is the number of monitor units per scanner position divided by the electronic amplification factor, N_{ion} the number of beam particles per scanner position, Δx, Δy the step size of the beam scanner in mm, S/ρ the stopping power at the position of the ionization chamber in MeV/(g/cm^2) and D the measured dose in Gray.

From this formula it is clear that reproducible and correct results require a well defined geometry of the field and a sufficient homogeneity of the dose. As the monitor calibration is energy dependent, its constancy as a function of time is checked for 6 selected energies (100 to 350 MeV/u in steps of 50). This most fundamental test is performed every day during beam time. Every year or whenever a monitor chamber has been replaced, the dependence from the particle fluence and flux is checked for three different energies at doses of 0.2, 0.5 and 1.0 Gy and at beam intensities of 6·10^6, 3·10^7 and 2·10^8 particles per spill, respectively (one spill lasts about 2 seconds).

For daily checks of the constancy of dose the Farmer chamber is exposed to a three dimensional cube - like irradiation field within a PMMA phantom. The field has the dimension (5cm)^3 and is positioned at a water equivalent depth of 11.3cm. This test differs significantly from the measurements described above as many beam energies are involved. The same setup is used to check the independence of the monitor calibration from the beam position: dose cubes of the same shape and dose are placed at different lateral positions.

For all the checks concerning the monitor calibration the intervention threshold was set to $\pm$3%.

Lateral dose distribution

The homogeneity of the lateral dose distribution is one of the most critical functional performance characteristics of the irradiation facility, as it is influenced by a very large number of beam parameters and settings. Examples are the settings of focus width and step size of the beam scanner at the isocenter, see figure 1, beam intensity fluctuations on a microsecond time scale and the walk of the beam spot when entering the scanner, quantities which themselves depend on innumerable settings of the heavy ion synchrotron and of the beam line elements. Thus by measuring the lateral dose distribution a lot of parameters are controlled simultaneously.

For the initial acceptance test, the lateral dose distribution for different monoenergetic fields (squares up to 18cm x 18cm at 100 to 350 MeV/u in steps of 50 MeV/u) has been measured simultaneously by a set of 10 small thimble type ionization chambers (Wellhöfer IC15, active volume 0.14 cm^3) free in air and by photographic emulsions. The ionization chambers permit relative dose measurements with an accuracy of better than 1%.

As the slope of film blackening curves depends strongly on the ion energy, an absolute dose measurement within threedimensional fields by means of photographic emulsions is
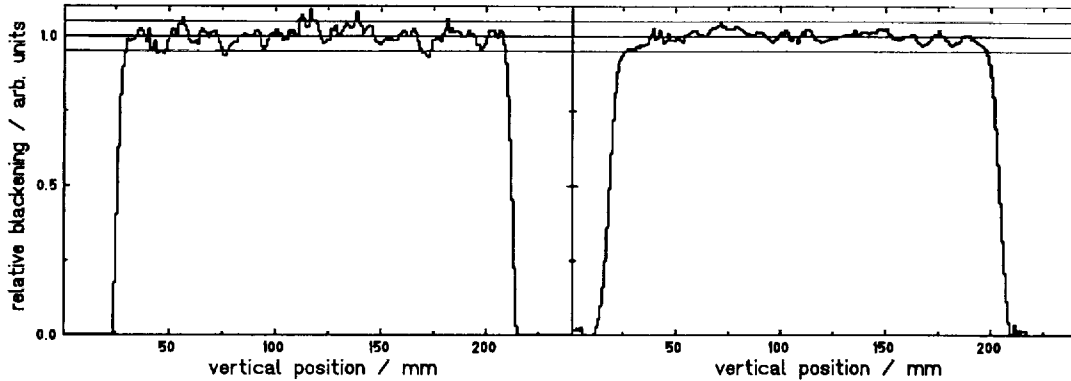
Figure 1: Densitometric scans of films irradiated by 18cm x 18cm wide fields of 300 MeV/u carbon ions. The dose is about 1 Gy. Non correct combinations of beam width and raster step size are easily detected as is shown in the example on the left side. With appropriate values the homogeneity is within the ±5% - limits (right), which are indicated as straight lines together with the mean values.

not possible. For monoenergetic fields however a constant optical density means a constant dose, at least in the linear range of the characteristic curve around one Gy[4]. Moreover relative variations of the optical density correspond to the same relative dose variations and therefore films are very well suited for constancy tests of the homogeneity of the lateral dose distribution.

Depth dose distribution

For checking the homogeneity of the longitudinal dose distribution, target volumes in the form of rectangular parallelepipeds with different lateral extensions ($(2.5 \text{ cm})^2$ up to $(18\text{cm})^2$ and several cm thick) and in different depths (up to 20 cm water equivalent) have been planned with constant dose. As the dose at any depth in such a target volume is an individual superposition of the contributions of a varying number of beam energy steps, any error in the energy dependent monitor calibration or in any other energy specific parameter would influence the homogeneity of the longitudinal dose distribution.

The dose measurement has been performed in a water phantom, using again the 10 small ionization chambers which were positioned in a way not to cover each other when seen in beams eye view. As outlined at the beginning, depth dose measurements using a single detector which is moved along the beam axis during irradiation are not possible.

For the checks concerning the dose homogeneity the intervention threshold was set to ±5%.

Field geometry

The field geometry is verified by means of a film and a specially formed PMMA phantom which allows to determine simultaneously the lateral and distal limits of an irradiation volume in the form of a rectangular parallelepiped. For the measurement of the distal extension of the target volume, the phantom contains a wedge which transforms a heavy ions range into a position on the film, see figure 2.
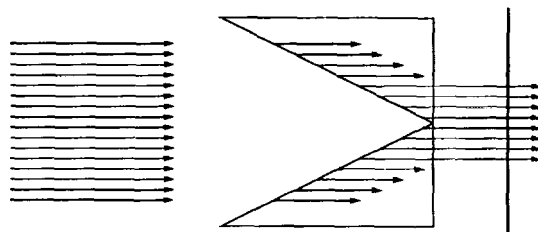
Figure 2: Determination of the distal field limits of a cube - like irradiation field. The ions (left) penetrate into a PMMA - wedge (center), the range of the most energetic ions is indicated by arrows. Where the range exceeds the PMMA width, a film (right) is blackened. The wedge angle is chosen in a way that the extension of the exposed film area equals the maximum range of the ions in water. It can be read directly from the film after irradiation.

Constancy checks

During the acceptance test a very comprehensive program of measurements as described above has been performed and a large set of baseline values established. The planned frequencies of the constancy checks are listed in the following table which resumes also the measurement devices and the intervention thresholds.

measurement	device	frequency	threshold
monitor calibration	Farmer chamber	daily	3%
constancy of dose	Farmer chamber	daily	3%
lateral dose distribution	verification film	once per beam time	5%
depth dose distribution	10 IC15 chambers	once per beam time	5%
field geometry	verification film	once per beam time	2 mm
influence of fluence	Farmer chamber	yearly	3%
influence of flux	Farmer chamber	yearly	3%

Summary

A set of test procedures has been developed for dosimetric quality inspections at the heavy ion therapy facility at GSI. In some cases new test principles had to be established to meet the requirements at the heavy ion beam. As a first application the acceptance test has been carried out during the technical commissioning of the facility.

References

[1] Th. Haberer, W. Becher, D. Schardt and G. Kraft: Magnetic scanning system for heavy ion therapy, Nucl. Instr. Meth. A330 (1993) 296

[2] D. Schardt, H. Stelzer, H. Junk, U. Arndt: Bragg Curve Measurements with Ionization Chambers, GSI 93-1, 336

[3] B. Voss, private communication

[4] B. Bathelt et al.: Film dosimetry with heavy charged particles, these proceedings

[5] G. Hartmann et al.: Carbon dosimetry at GSI using ionization chambers, these proceedings

Absorbed Dose Distribution Measurements in Radiotherapy

M. Radojcic[1], B. Secerov[1], B. H. Milosavljevic[1], J. Petkovic[2], G. Bacic[2]

[1]VINCA Institute of Nuclear Sciences, P.O.Box 522, 11001 Belgrade, and [2]Faculty of Physical Chemistry, University of Belgrade, P.O.Box 137, 11001Belgrade, Yugoslavia

Introduction

The knowledge of three-dimensional (3D) dose distribution is important in all aspects of radiation research, but radiotherapy presents specific problems for dosimetric quality control. Radiographic films are not adopted to the wide therapeutic dose range and 3D dose distribution is difficult to measure and quantify. Therefore, in routine medical practice 3D dosimetry is performed using mobile ionization chamber which moves inside the water tank. The accuracy then depends on the size of the ionizing chamber and precision of its positioning. Such devices are not suitable for dose distribution measurements in small irradiated volumes (e.g. ~ 1 cm^3) and problems are even greater in determining dose distribution for high LET particles.

Our aim was to develop a set of dosimeters which can be used for mapping the 3D dose distribution in the wide range of radiation sources. Ideally, these should be able to cover wide range of doses and different modes of irradiation (continuous, pulse, scanning beam), with sufficient spatial resolution to be applicable for both low LET (e$^-$, γ) and high LET (heavy ions) particles. Therefore, we investigated the applicability of magnetic resonance techniques for determination 3D dose distribution. It has been shown that EPR dosimetry is reliable in industrial radiation processing, but only few applications of EPR dosimetry in radiotherapy have been reported (1). MRI assessment of 3D dose distribution is based on the ability of this technique to map the spatial distribution of radiation induced species (2). However, this technique is still in its infancy and numerous technical problems need to be solved. In addition, we try to use radiochromatic dye films, in conjunction with laser microdensitometry, for high resolution dose distribution measurements.

Materials and Methods

The principle of MRI dosimetry is the radiation induced oxidation of ferrous into ferric ions which affects proton relaxation times. The Fricke infused gel was composed of 1 mM $FeSO_4$, 50 mM H_2SO_4, 1 mM NaCl, and 5% (w/w) agarose. The gel is used to reduce the diffusion of Fe^{3+} ions thus enabling localized measurements of dose distribution. Plastic bottles (~ 250 ml) were filled with gels and irradiated with 10 MeV X-rays using a Mevatron 74 (Siemens) linear accelerator (4x4 cm, FF = 90 cm). The dose was 20 Gy. MRI images of irradiated phantoms were obtained with a 0.5 T Privilege (Elscint) MR imager using standard T1W spin-echo and inversion-recovery imaging sequences.

EPR dosimetry is based on measurements of radiation-induced free radicals in alanine crystals. Alanine dosimeters in the form of a thin film were prepared by mixing polycrystalline DL-α-alanine and low-density polyethylene (60/40 %, w/w). homogeneous mixture was press-molded into 0.5 mm thick plates, from which 5x10 mm dosimeters were cut. The stack of alanine dosimeters interspersed with plastic spacers of variable thickness (total length around 6 cm) was irradiated under the same conditions as for MRI phantoms. EPR spectra were obtained using a Varian X-band EPR spectrometer.

Poly(vinyl butural) was a host matrix for hexahydroxyetilpararosanilincynide (HHEPRC) and a film of uniform thickness of 40 μm was cast out of it. HHEPRC is a radiochromic dye that undergoes a heterolitic cleavage upon irradiation producing the stable, blue colored cation radical (λ_{max} = 605 nm). To determine the right dye concentration for the particular dose range, the G-value for the creation of blue colored radical was measured as a function of HHEPRC concentration in the film. The calibration was performed against standard Fricke dosimeter using γ-source. For dose distribution measurements, a stack of films interspersed with spacers of variable density and thickness was used (Fig. 2). The samples were irradiated with electrons from a Febetron 707 accelerator. Following irradiation, each film was scanned using a Pharmacia LKB Ultrascan XL microdensitometer.

Results

Magnetic resonance dosimetry

Figure 1 shows the sketch of the EPR dosimeter and dose distribution along the beam. Accuracy of dose determination was around 20% mainly due to a relatively high signal of the radicals present prior to irradiation (induced during the manufacture of dosimeters).

X-rays
20 Gy

Alanine
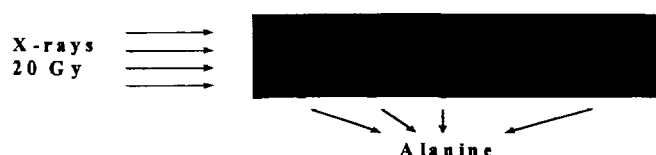
Figure 1a Scheme of EPR dosimeter
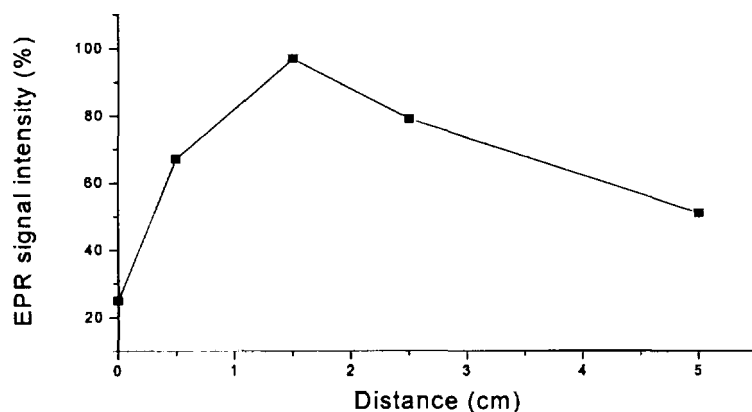
Figure 1b. Dose distribution (100% intensity corresponds to 20 Gy)

MR images of irradiated gels (data not shown) were in qualitative agreement with the dose distribution determined using both EPR and routine dosimetry, i.e., we observed the dose build-up at around 2 cm from the surface (longitudinal images) and sharp decrease of the MRI signal at the edge of radiation field (transversal images). They also showed that measurements of signal intensity alone were insufficient for accurate determination of dose distribution and that maps of relaxation times must be used instead.

Radiochromatic dye films

Figure 2 shows the experiment in which the dose distribution in a specimen irradiated with electrons from a Febetron 707 pulsed accelerator (78 modules, 26 kV per module) was measured. The odd numbers denote radiochromatic films (40 micrometer thickness), while the even numbers denote spacers (200 microns Al sheets). Figure 3 shows dose distribution along the beam direction.
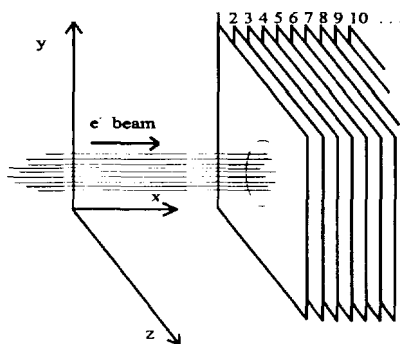
Figure 2. Films irradiation layout
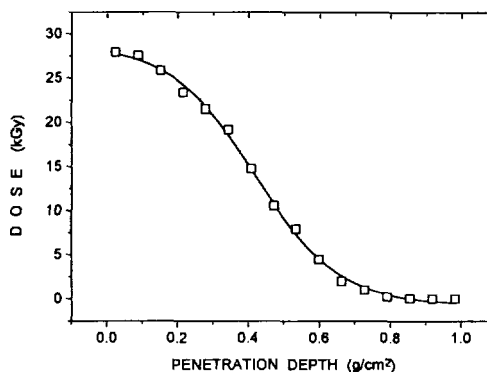
Figure 3. Absorbed dose as a function of penetration depth.

The penetration depth resolution is 0.06 g cm^{-2}, which is sufficient enough not only to obtain spatial dose distribution, but also to determine energy distribution of e$^-$ in the incident beam. Namely, actual dose distribution was compared with the dose distribution expected for monoenergetic electrons. The observed variations enabled calculations of energy distribution, which is an important factor in beam quality assessment. This method can also be used for high LET radiation, since a 10 μm thin radiochromatic films, used without spacers, can provide spatial resolution of 8 x 10^{-5} g cm^{-2}.

Horizontal distance from center [mm]
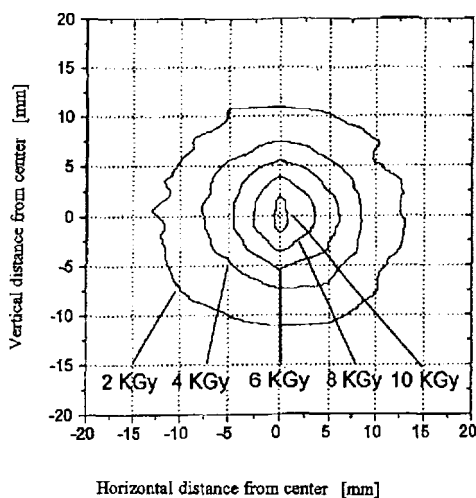
Figure 4. Dose distribution orthogonal to the e$^-$ beam from a Febetron 707 accelerator at a depth of 0.48 g cm^{-2} from the surface.

Figure 4 clearly indicates dose gradient orthogonal to the beam, i.e. that electron fluence is not homogeneous. This method enables assessment of beam homogeneity with the spatial resolution of 40 μm.

Discussion

Our result demonstrated that all methods used in this work can give dose distribution during a single act of irradiation. Each method has its advantages and limitations:

MRI is probably the most convenient method for measurements of 3D dose distribution since dosimeter (phantom) consists of homogeneous, tissue equivalent medium and MR images can be acquired to give 3D data set from which dose distribution in any selected plane can be obtained. Spatial distribution depends on the type of MR imager used as well as on the sample size, but the lower limit appears to be around 200 μm for the most of commercially available machines. Measurable dose ranges are within doses used in radiotherapy, but accurate calibration is difficult to achieve solely on the MRI data. In addition, MR imaging of the phantoms has to be performed within few hours after irradiation, otherwise the diffusion of Fe^{3+} from the site of its creation will smear the image.

EPR dosimetry provides long lasting record of absorbed dose. Spatial resolution along the beam is dictated by the thickness of the dosimeter and sensitivity of EPR spectrometers. In routine use, resolution of 100 - 200 μm should be easily achievable. Detailed dose distribution in the plane perpendicular to the beam can not be achieved with such resolution. Accuracy at low doses (< 2 Gy) is rather poor due to the background EPR signal, but that can be improved by careful preparation of dosimeters.

Radiochomatic dye film dosimeters provide superb spatial resolution in all directions. System investigated here is not well suited for therapeutic dose range, but new developments of radichromatic films undergoing the radiation induced chain reaction will enable their use for low-dose range.

In conclusion, neither of described dosimeters is ideal, but the proper combination of these methods should be able to cover all situations encountered in radiation dosimetry. All measurements were performed using low LET radiation (e⁻, γ), however, exceptional spatial resolution of these dosimetry systems (bellow 200 μm) makes them good candidates for 3D dose distribution measurements for high LET radiation as well.

References:

1. M.F.Desrosiers. Research and development activities in electron paramagnetic resonance dosimetry. Rad. Phys. Chem. 46(1995)1181-4.
2. D.R.Olsen and J.Hellesnes. Absorbed dose distribution measurements in brachytherapy using ferrous sulphate gel and magnetic resonance imaging. Br. J. Radiol. 67(1994)1121-6.

Heavy Ion Dosimetry with Magnetic Resonance Imaging of Polymer Gels

U. Ramm, C. Thilmann, M. Damrau, H.D. Böttcher
Universitätsklinikum, Klinik für Strahlentherapie, Frankfurt/Main, Germany
O. Geiß, M. Krämer, G. Kraft
GSI, Darmstadt, Germany

Introduction

Magnetic Resonance Imaging (MRI) can be used to measure the dose distribution produced by ionizing radiation absorbed in tissue-equivalent gels [1]. Recently a new polymer-gel (BANG) was developed [2], taking advantage of radiation induced free-radical chain polymerization of acrylic monomers, dispersed in an aqueous gel matrix. The local changes in the polymer molecular structure and dynamics affect the water proton MR longitudinal and transverse relaxation times, T_1 and T_2. The changes are large enough to be mapped with high spatial resolution, thus allowing the verification of three-dimensional dose distributions produced by ionizing radiation. Our first results on dose response of polymer-gels due to low LET photon radiation will be reported. In addition, we will outline our proposed investigations of MR imaging for 3D dose verification in heavy ion radiotherapy.

Material and Method

The BANG polymer–gel is composed of electrophoresis–grade 3% acrylamide monomer, 3% N, N'-methylene–bisacrylamide (bis) crosslinker, 5% gelatin of type A (acid derived), and 89% water obtained from an ion–exchange purifier [2]. Since oxygen inhibits free-radical polymerization [3] ultra-high-purity nitrogen gas is bubbled through the gel during preparation. To prevent reoxygenation and light induced polymerization the samples are stored in glass-vessels and wrapped in a lightproof cover. For calibration the samples were irradiated with 6 and 25 MV photons of an electron linear accelerator (SL25, Philips, Crawley, UK). Doses of up to 20 Gy were applicated at a field size of 5 cm * 5 cm to determine the dose-response curve. The MR images were measured with a 0.5 T whole body scanner (Privilege, Elscint, Tel Aviv, Il) using a quadrature head coil. Series of spin echo sequences $90^0 - \tau - 180^0-$ acquire, for different τ were performed. Repetition time TR = 6 sec and time to echo TE = 11, 100, 200, 400 and 600 msec were chosen. As the temperature at the time of imaging has a significant effect, the temperature was kept constant at 25^0 C.

Results and Discussion

The transverse MR relaxation rate $R_2 = 1/T_2$ of the water protons was taken as a measure of the radiation dose absorbed in the gel. Since the absolute value of relaxation time is not essential for dosimetry, two images with different echo times TE were required.

The relative signal in a spin-echo MR image produced by a dose D is given by:

$$S(TE_1)/S(TE_2) = e^{-R_2(D)(TE_1 - TE_2)} \tag{1}$$

where S_i are the signals at echo time TE_i. For low LET photon radiation the yield of polymerization increases with the energy transfered to the gel. The linearity up to 10 Gy allows to generate a R_2 map at given acquiring parameters for converting the MR signals to absolute dose. At higher doses the curve shows a saturation effect. The mapping technique of MR imaging of radiation induced polymerization in a tissue-equivalent aqueous gel allows to verify complex dose distributions in conventional low LET radiotherapy.

Proposed high LET investigations

In the track of heavy ions the ionization density increases. Saturation effects due to high doses in the center of the track are expected. As it is known from solid state and biological systems the dose response depends on the atomic number and the energy of the heavy ions. For heavy ion irradiation the cross sections are increasing with the energy transfer, exhibit a maximum around LET = 200 keV/μm, but decreasing for higher LET values. In analogy to i.e. the radiobiological efficiency (RBE) of high LET radiation the dose response of polymer-gels is defined by the efficiency ϵ:

$$[S(TE_1)/S(TE_2)]_{high} = \epsilon * [S(TE_1)/S(TE_2)]_{low} \tag{2}$$

where the relative MR signal of low LET photon radiation is taken as reference. The implementation of the MR imaging system for high LET heavy ion irradiation is still in progress. First experiments are proposed to be performed with the raster scan facility at GSI [4]. Monoenergetic ^{12}C ions with a fluence of around 10^7/cm^2 will be scanned over a wide area in order to ensure a homogeneous distribution over the polymer gels. The experimental data will be compared with computed efficiencies according to an adaption of a model developed at the GSI [5]. These calculations are based only on track structure and the experimentally determined photon response. This method was already successfully applied to describe thermoluminescence detector (TLD) responses and cell survival probabilities after heavy ion irradiation. Once the dependence of the gel efficiency on energy and charge of heavy ions is determined the MR imaging of tissue-equivalent aqueous polymer-gel will be a convenient method to verify three-dimensional dose distributions in high LET heavy ion radiotherapy.

References

[1] J.C. Gore, Y.S. Kang, and R.J. Schulz. *Phys. Med. Biol.*, **29**:1189–1197, 1984.

[2] M.J. Maryansky et al. *Magn. Res. Imag.*, **11**:253–258, 1993.

[3] M.J. Maryansky et al. *Phys. Med. Biol.*, **39**:1437–1455, 1994.

[4] T. Haberer et al. *Nucl. Instr. and Meth.*, **A330**:296–305, 1993.

[5] M. Scholz and G. Kraft. *Radiat. Prot. Dosim.*, **52**:29–33, 1994.

H

Clinical Results of Particle Therapy and New Techniques

G. Munkel (Chair)

Oral Presentations

1. Gudrun Munkel
(PSI Villingen, Switzerland)

Introduction

2. Ira Spiro
(Harvard Uni. Boston, USA)

Clinical Experience with Protons at the Harvard Cyclotron Laboratory and Future Plans at the North-East Proton Therapy

3. J.Slater
(Loma Linda, USA)

Loma Linda Results

4. Hirohiko Tsujii
(Nat. Inst. of Rad. Snc. Chiba, Japan)

Clinical Trials of Carbon-Ion Therapy at NIRS

5. Jörg Pawelke
(FZ Rossendorf, Dresden, Germany)

Positron Emission Tomography for Quality Assurance of Heavy Ion Therapy

6. Terence Boehringer
(PSI Villingen, Switzerland)

Quality Assurance Procedures for the Proton-Therapy Project

7. Christian Schilling
(PSI Villingen, Switzerland)

Real Time Tumor Tracking

8. Bernd Voss
(GSI Darmstadt, Germany)

Fast Position Sensitive Beam Monitor System

Poster

9. Rainer Hinz
(FZ Rossendorf, Dresden, Germany)

Pre-Clinical Studies on PET Monitoring of Heavy Ion Therapy at GSI Darmstadt

10 Martin Moosburger
(LMU Munich, Germany)

A Detectorsystem for Proton Radioagraphy at PSI

New Techniques and Clinical Results of Particle Therapy - Introduction

Gudrun Munkel
Proton Therapy Project - Division of Radiation Medicine
Paul Scherrer Institute, CH - 5232 Villigen PSI, Switzerland

New developments in radiation medicine have been made since the beginning of the x-ray era, the result was and is a continuous increase in technical sophistication and possibilities for medical use. Conventional radiotherapy is worldwide established, and the trend of this cancer treatment modality is improving precision and conformation of the delivered dose. Since 1954, particle radiotherapy is establishing it's great value, pioneered by the Lawrence Berkeley Laboratory and performed at many treatment installations. Protons and heavier ions have proven to be beneficial in treating selected benign and malignant lesions. More than 22000 patients have been treated worldwide with charged particles, some centers reached patient numbers of over 2000, the HCL-MGH group being the absolute leader with over 7000 patients. It was (and is) due to the inherent physical properties of the charged particles that selected anatomical sites and lesions could be treated with superior success compared to conventional radiotherapy, though the technology of the various therapy installations was simple. PSI, the former SIN, developed the first dynamic, conformal beam application technology for pion therapy, and it took more than 30 years - since the first patient treatment with protons in Berkeley - to take the world's first hospital based proton facility and a gantry into operation (at the Loma Linda University Medical Center). Meanwhile PSI has again made a novel development with the world's first compact proton gantry using spot scanning, raster scannning with heavier ions will be implemented at GSI. Accelerators are available today for medical purpose, which means for operation also under conditions with limited space like in hospitals. The next major step towards integration of proton therapy in hospitals will be the Northeast Proton Therapy Center in Boston on the campus of the Massachusetts General Hospital. Heavier ions have found a new major home at NIRS in Chiba, Japan, GSI in Darmstadt will soon treat the first European patient with scanned heavy ions, and we see a worldwide activity for building more particle therapy centers.

A driving force behind this international effort is the particular fascination of physics and technology. But in the end it is the translation into medical success which matters. We have to prove that we can keep the balance between cost and benefit in both the economical and medical sense. Every outcome of a medical activity is a clinical result. Particle therapy in general is facing strong and challenging competition from conventional radiation therapy and other oncological methods. The outstanding success of proton radiation for selected tumors has not only to be maintained but also to be established in a changing environment. Selecting carefully indications and treatment technology will help to give particles a serious role in cancer therapy. Looking back on the worldwide experience will hopefully prevent us from believing superficially in the idea that a machine is already the medical success. We are challenged to proof - by absolutely serious and disciplined work - that our tools (particles, accelerators, gantries, scattering, scanning, advanced treatment planning etc.) are essential for modern and future cancer treatment.

CLINICAL TRIALS OF CARBON-ION THERAPY AT NIRS

Hirohiko Tsujii
Research Center of Charged Particle Therapy
National Institute of Radiological Sciences
Inage-ku, Anagawa 4-9-1, Chiba, Japan

INTRODUCTION

Construction of the HIMAC (Heavy Ion Medical Accelerator in Chiba), the world's only heavy ion accelerator complex dedicated to cancer therapy in a hospital environment, was completed at the National Institute of Radiological Sciences(NIRS) in 1993(1). Following pre-clinical studies including determination of RBE values of heavy ion beams chosen for therapy, Phase I/II clinical trials were started in June 1994 to evaluate toxicity and clinical efficacy of heavy-ions in cancer therapy(2). Potential indications of heavy ions have been suggested by treatment results of neon-ion therapy at LBNL as well as from those of fast neutrons. The reported data has indicated that, compared to conventional photon techniques, the high-LET radiation therapy can bring advantage in relatively slow growing tumors such as salivary gland tumors, paranasal sinus tumors(non-squamous cell tumors), head and neck tumors, soft tissue sarcomas, prostate carcinomas, and melanomas (3,4,5). Deep-seated tumors, however, were not found to give satisfactory results in both therapy. This could be due to the fact that, in neon-ion therapy, the doses delivered were too conservative for radical irradiation and limited flexibility of patient positioning because of only fixed horizontal beam lines available. In neutron therapy, the possible advantage of it was frequently difficult to deliver adequate dose to deep-seated tumors because of its poor dose distribution. The major mission of the HIMAC project is to find out in what type of human cancers the differential effects could exist between the therapeutically resistant neoplasms and normal tissues that favor the latter. For this purpose, Phase I/II toxicity study has been performed in various type of tumors.

METHODS AND MATERIALS

Selection of ion species for therapy

Biological effects(RBE) of high-LET radiation are larger than those of low-LET radiation, and the RBE values vary according to ion species and the position measured along the beam path(5,6,7). In selecting ion species to be used for cancer therapy, we have compared characteristics of several ion species from physical and biological aspects. It has been indicated that the ratio of the biologically effective dose in the peak to that in the entrance/plateau region is higher in carbon-ions than in other heavy ions, suggesting that carbon-ions could be optimal in terms of delivering both physically and biologically effective dose to the tumor while delivering lower doses to the surrounding normal tissues. In heavy-ion irradiation, however, unfavorable exit dose is added to some extend in the region beyond the distal edge, which generally becomes larger with larger atomic number. By taking into account for these factors, we decided to employ carbon-ions in the initial clinical trials. Based on preclinical studies on five human cell lines and mouse skins as well as previous cninical experiences of fast neutron , the RBE values of carbon-ions relative to ^{60}Co gamma rays were estimated to be 3.0 at the distal part of the SOBP.

Organization of clinical network

For successful performance of this study, organization of effective networks with major institutions was an urgent requirement. Therefore, interdisciplinary working groups were organized, which have encouraged activity of the study, designed protocols and reviewed treatment results.

Materials and methods

The protocols were designed for various tumor sites including the head and neck, brain, lung, liver, uterine cervix, and prostate. The initial pilot study was directed to head and neck tumors, thereafter the range of application has been expanded to many other tumors. During June 1994 and February 1997, a total of 230 patients(233 tumors) were treated with carbon-ions(Table 1). Of them,

150 patients who were followed-up until death or at least 6 months were evaluated for radiation response. For scoring radiation toxicities, the RTOG criteria was used from the commencement of therapy through 3 months, thereafter the RTOG/EORTC criteria was used for late effects. The initial doses employed were assumed to be 10-20% lower than those possibly tolerable for musculo-connective tissues. The doses have been escalated by 10% increments for every 3 to 5 patients based on careful observation of the normal tissue morbidity as well as tumor response.

RESULTS

As with radiation-related toxicities, three patients developed Grade 3 acute reactions. Of them one patient with maxillary cancer developed moist skin reactions which healed completely by conservative treatment; and two patients with lung cancer developed cough and dyspnea accompanied by patchy to dense appearance on CT images which also subsided after steroid therapy. Eventually, none of the patients experienced any type of major morbidity at later phase(Table 2). The overall response rate determined by tumor size(CR+PR) are 57%(Table 3). The local control rates in all patients are 73.0% at one year and 67.% at 1.5 years, and in patients with head and neck tumors the local control rate is 91.3%(21/23) at 2 years.

DISCUSSION

Recently, there have been significant improvement in radiation techniques for concentration of the dose within a target volume using 3-D conformal irradiation technique and stereotactic irradiation technique. However, for a certain type of malignancies such as locally advanced tumors, non-squamous histologies, or slow growing tumors are usually resistant to low-LET radiation, it may be desirable to use heavy ions with curative intent. Although the follow-up periods are still short and radiation doses initially employed might be too conservative for primary cure, preliminary results do appear to demonstrate promising effects on non-squamous tumors such as adenocarcinoma, adenoid cystic carcinoma, malignant melanoma, and soft tissue sarcoma. In malignant gliomas, however, adequate dose fractionations might have not been met yet. As our clinical trials have only begun to be studied, there remain numerous developments waiting to be achieved for a successful performance of heavy ion therapy, and worldwide collaborations should be extensively established.

ACKNOWLEDGMENT

REFERENCES

1. Kawachi,K., *et al., J.Jpn.Soc.Ther.Radiol.Oncol.* 1,19-29(1989).
2. Tsujii,H., In *Proc of NIRS International Seminar on the Application of Heavy Ion Accelerator to Radiation Therapy of Cancer in connection with XXI PTCOG Meeting, NIRS-M-103, HIMAC-008,* 1994, pp212-218.
3. Castro,J.R., In *Proc of the 5th International Meeting on Progress in Radio-Oncology,* 1985, pp.643-648.
4. Linstadt,D.E., *et al., Int.J.Radiat.Oncol.Biol.Phys.* 20,761-769 (1991).
5. Schmitt,G.,et al, *Radiother.Oncol.* 17,47-56(1990).

6. Leith,J.T., *Adv.Radiol.Biol.* 10,191-236(1983).
7. Petti,P.L.,et al, *Ann.Rev.Nucl.Part.Sci.* 44,155-197(1994).

Table 1 . Patient characteristics in carbon-ion therapy at NIRS (June 1994 ~ February 1997)

Sites	1994	1995	1996	Total
1. Head & neck I	7	10	(closed)	17
2. Head & neck II	-	-	19	19
3. Brain	6	8	10	24
4. Lung	6	11	27(28)	44(45)
5. Liver	-	12	13(14)	25(26)
6. Prostate	-	9	18	27
` Uterine cervix	-	9	13	22
8. Bone/soft tissue	-	~	9	9
9. Esophagus	-	-	1	1
10. Miscellaneous	2	24	16(17)	42(43)
Total	21	83	126(129)	230(233)

( ) : Number of tumors irradiated

Table 2 . Normal tissue morbidity in carbon-ion therapy in 150 patients treated
between June 1994-August 1996

Site	Early(<3mo)					Late(6mo)				
	No	0	1	2	3	No	0	1	2	3
Skin										
Scalp	15	3	7	5	0	15	15	0	0	0
Head & neck	27	0	11	13	3	26	16	9	1	0
Chest	29	0	23	6	0	28	0	28	0	0
Abdomen	49	13	28	8	0	49	25	24	0	0
Others	31	2	20	9	0	31	7	24	0	0
Total	151	18	89	41	3	149	63	85	1	0
(%)	(100)	(12)	(59)	(27)	(2)	(100)	(42)	(57)	(1)	(0)
Mucosa	31	9	13	9	0	30	27	3	0	0
Lung	29	25	1	1	2	28	25	3	0	0
Intestine	29	24	5	0	0	29	24	1	4	0
Bladder	29	18	8	3	0	29	20	7	2	0

Grade [a]

a) according to RTOG(early) and RTOG/EORTC(late)

Table 3. Local tumor response in 146 patients treated with carbon-ions from
June 1994 to August 1996 at NIRS.

Site	GyE /fr	Total No	CR	PR	NC	PD
Head & neck	48.6 /18	3	0	3	0	0
	54.0 /18	3	0	1	1	1
	59.4 /18	4	3	1	0	0
	64.8 /18	3	0	1	2	0
	70.2 /18	2	0	2	0	0
Head & neck II	52.8 /16	5	1	4	0	0
	57.6 /16	3	0	2	1	0
rain:						
Astrocytoma	50.4 /24	7	0	1	5	1
Malig.glioma	66.8 /33*	7	0	1	4	2
	68.4 /33*	1	0	0	0	1
Lung: St. I	59.4 /18	5	0	4	1	0
	64.8 /18	4	0	1	3	0
	72.0 /18	17	1	6	10	0
St. IIIA	59.4 /18	3	0	2	0	1
Liver	49.5 /15	2	1	0	1	0
	54.0 /15	3	0	2	0	1
	60.0 /15	5	2	3	0	0
	66.0 /15	8	0	7	1	0
Prostate 54.0 /20	3	0	2	1	0	
	60.0 /20	3	0	1	2	0
	66.0 /20	7	0	2	5	0
	72.0 /20	4	0	1	3	0
terine cervix	52.8 /24	5	4	1	0	0
	57.6 /24	5	3	2	0	0
	62.4 /24	1	0	1	0	0
Miscellaneous	48.0~57.6 /12~20	31	3	13	14	1
Total		146 (CR+PR: 57%)	18	65	55	8

a): X-ray(50Gy/25fr) + Carbon (8fr)

Positron Emission Tomography for Quality Assurance of Heavy Ion Therapy

J. PAWELKE[1], W. ENGHARDT, B.G. HASCH, R. HINZ, K. LAUCKNER AND M. SOBIELLA

Forschungszentrum Rossendorf e.V., PF 510119, D-01314 Dresden, Germany

The specific physical and radiobiological properties of highly accelerated heavy ions in the mass range between carbon and neon are expected to increase the chances of curing compact tumours of low radiosensitivity growing in close vicinity to organs at risk [1]. For a safe application of such a precision therapy in-situ treatment plan verification and dose localization are highly desirable. The technique of positron emission tomography (PET) provides an indirect method of verifying the precision of dose deposition and its correspondence to the treatment plan through the measurement of the range of the projectile ions in the target medium. Basically two approaches are feasible:

- The treatment plan verification and even the therapy is performed by means of beams of β^+-radioactive ions (e.g. ^{11}C, ^{19}Ne). However, beams of stable nuclei are preferred for radiotherapy, because there are no advantages in dose distribution or biological efficiency using a radioactive beam but great expense to produce and shield such a beam.

- The position of the irradiated region within the body of the patient is deduced from the spatial distribution of β^+-emitters, which results as a byproduct of each therapeutic irradiation from nuclear fragmentation reactions between a minor part of the stable beam particles and the atomic nuclei of the tissue (autoactivation).

A pronounced β^+-activity maximum exactly at the position corresponding to the range of the projectiles having almost no background activity is obtained by injecting a beam of positron emitting nuclei [2-4], (cf. Fig. 1, left). The activities at the Lawrence Berkeley Laboratory (LBL), California, where heavy ion radiotherapy was pioneered and performed until 1992, because of shutting down the accelerator, involved initial attempts to utilize PET for in-situ treatment plan verification. This resulted in a method, where low-intensity beams of β^+-active isotopes were used to measure the range of ions in the target volume prior to the therapy with a beam of stable ions [2].

In contrast to this, a beam of stable ions generate a β^+-activity distribution which is peaked near the range of the primary projectiles [5-7], (cf. Fig.1, right). In addition to this rather broad peak, a constant activity along the path of the beam is generated. Furthermore, the concentration of positron emitters is more than one order of magnitude lower compared to that obtained by using a radioactive beam. As an example the β^+-activity distribution obtained by irradiating polymethylmethacrylate (PMMA) with a monoenergetic beam of radioactive ^{19}Ne ions [3] and of stable ^{20}Ne projectiles [6], respectively, are shown in Fig. 1.

There are only two facilities in the world at which a heavy-ion radiotherapy is presently carried out or at which preparation is almost finished: at the Heavy Ion Medical Accelerator in Chiba (HIMAC), Japan and at the Gesellschaft für Schwerionenforschung (GSI) in Darmstadt, Germany. Both investigate the application of PET-monitoring of autoactivity to therapy control. There are two ways of imaging the activity distribution. Either the patient is transferred to a conventional PET-scanner immediately after the irradiation or a dedicated PET-scanner is integrated into the medical beam line. The first concept has been followed at HIMAC [8], whereas as a contribution of the Forschungszentrum Rossendorf (FZR) a double-head positron camera has been installed at the treatment site at GSI in 1996 [3].

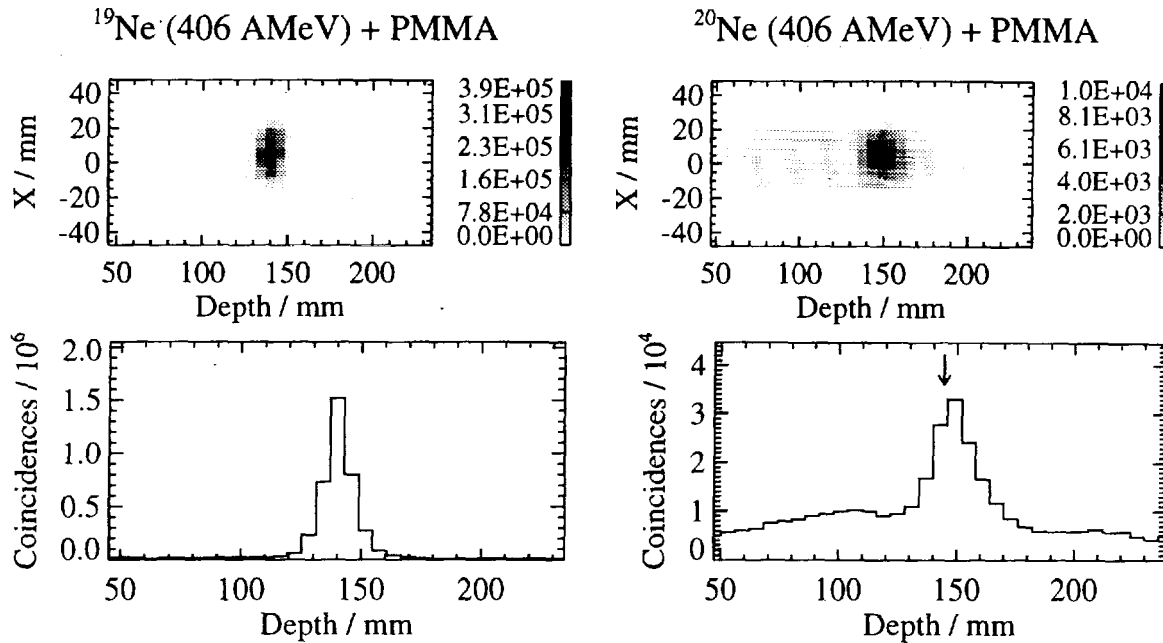
[1]email: pawelke@fz-rossendorf.de

Fig. 1 *Distribution of β^+-acitivity obtained by irradiating a lucite phantom with approx. 10^{11} particles of a monoenergetic beam of ^{19}Ne (left) and ^{20}Ne ions (right), respectively. On the top: a tomogram representing a 2 cm thick slice through the plastic phantom containing the beam axis. The lateral beam position is denoted by X. Below: the depth distribution obtained by projecting the tomogram onto the beam axis. The calculated range of ^{20}Ne is indicated by an arrow.*

In a series of in-beam experiments and calculations we studied the relation between the spatial distributions of dose and positron emitters [9]. In Fig. 2b a measured depth profile of β^+-activity is shown. This distribution obtained by irradiating PMMA with a monoenergetic ^{12}C beam shows a pronounced maximum of β^+-emitting projectile fragments. In the region where the primary projectiles are stopped (II in Fig. 2b), this maximum is superimposed onto an activity plateau (cf. Fig. 2b, regions I and III) that is caused by target fragments. Table 1 illustrates this by giving the observed relative abundances of positron emitters in these regions. The fraction of ^{15}O that can only be produced by target fragmentation is considerably lowered in region II, since ^{11}C and ^{10}C as fragments of the ^{12}C projectiles come to rest there. To deduce the Bragg peak position in the target from the depth distribution of β^+-emitters a procedure has been developed: A realistic model calculation will provide a prediction of both the distribution of the dose and the β^+-emitters. From these the correlation of the Bragg peak depth with the depth of the projectile fragment peak position is deduced. After that it is possible to determine the experimental Bragg peak position from the projectile fragment peak position extracted from the measured PET data (Fig. 2).

The results of applying this procedure to therapeutically relevant dose distributions suggest two modes of PET application to quality assurance in heavy ion therapy:

- Retrospective dose localization following each therapy fraction and thus, if it appears necessary, a treatment plan optimization before applying the next fraction.

- In cases of treatment with very high precision requirements, a pre-therapeutic treatment plan verification at some prominent or critical sites of the target volume using very low doses (approx. 10 % of a typical dose per fraction, i.e. 1-2 Gy).

Results of further investigations, aimed to integrate these PET-techniques in the quality assurance system of the therapy are reported in [10]. A comparison of all PET-monitoring systems applied to heavy ion therapy control is given in Table 2.
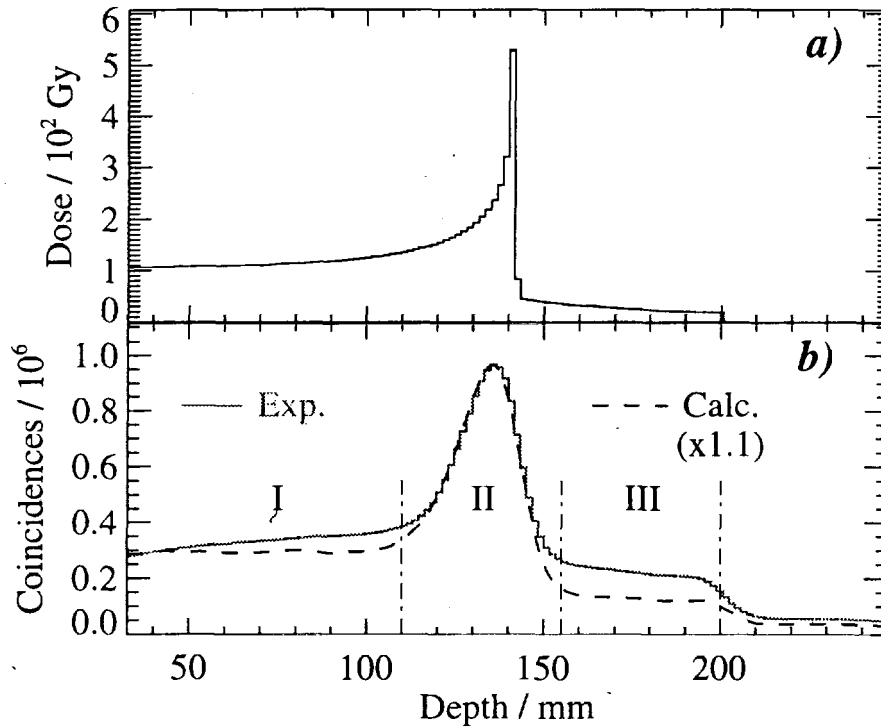
Fig. 2 *The relation between the calculated depth dose distribution (a) of a monoenergetic ^{12}C beam (E=292.5A MeV) and the β^+-activity distribution (b) generated by this dose distribution. The measured activity data (b, solid line) are compared with those obtained by the calculation (b, dashed line).*

Table 1 *Relative abundances of positron emitters in different regions of the activity depth distribution according to Fig. 2b.*

β^+-emitter	^{10}C	^{11}C	^{13}N	^{15}O
Depth profile region				
I	88±6	1000±6	30±12	390±6
II	83±3	1000±3	–	195±4
III	83±9	1000±4	–	404±4

Acknowledgement

Table 2 *Comparison of PET-monitoring systems for quality assurance of heavy ion therapy.*

	LBL (1981-1992)	FZR/GSI (1996-)	HIMAC (1996-)
Scanner position	at therapy beam	at therapy beam	nearby the therapy site
Patient transfer	not needed	not neeeded	required
Source of activity	β^+-active diagnostic beam	fragmentation of stable therapy beam	fragmentation of stable therapy beam
PET scan	before therapy irradiation	before, during, after therapy irradiation	after therapy irradiation
Scanner design	double-head camera	double-head camera	ring tomograph
Acceptance angle	0.69 sr	1.13 sr	2.50 sr
Patient port width	34 cm	82 cm	82 cm
Scanner operation mode	3D, no septa shield	3D, no septa shield	2D, septa shield
Projection data set	incomplete	incomplete	complete
Image reconstruction	matrix inversion, iterative	iterative	filtered backprojection
Pre-therapeutic treatment plan verification	yes	yes	no
Simultaneous PET-imaging	impossible	possible	impossible
Retrospective dose localisation	no	yes	yes
Measurement of short-lived isotopes	yes	yes	no

References

[1]   G. Kraft, Strahlenther. Onkol. **166** (1990) 10-13

[2]   J. Llacer, Nucl. Sci. Appl. **3** (1988) 111-131

[3]   J. Pawelke et al., Phys. Med. Biol. **41** (1996) 279-296

[4]   T. Tomitani et al., In: K. Ando and T. Kanai (eds.), Proc. Third Workshop on Physical and Biological Research with Heavy Ions, Sep. 2-3, Chiba, Japan (1993) 22-23

[5]   C.A. Tobias, Radiology **108** (1973) 145-158

[6]   W. Enghardt et al., Phys. Med. Biol. **37** (1992) 2127

[7]   T. Tomitani et al., In: T. Kanai and E. Takada (eds.), Proc. XXI PTCOG Meeting at Chiba, Japan **NIRS-M-103/HIMAC-008** (1994) 125-130

[8]   T. Tomitani et al., Sub. Second Int. Symp. on Hadrontherapy Sep. 9-11, Villigen, Switzerland (1996)

[9]   J. Pawelke et al., Conf. Rec. of the 1996 IEEE Nucl. Sci. Symp. Nov. 2-9, Anaheim, California **vol. 2** (1996) 1099-1103

[10] R. Hinz et al., this issue

Quality Assurance Procedures for the PSI Proton Therapy Project

T. Boehringer, A. Coray, S. Lin, A. Lomax, G. Munkel, E. Pedroni, B. Rohrer, H. Staeuble
Division of Radiation Medicine, Paul Scherrer Institute, CH-5232 Villigen PSI, Switzerland

Quality assurance procedures, with the aim of insuring the readiness of the PSI proton therapy unit and the safety of the daily patient treatments, are described in the following report. The beamline as well as the gantry devices have to be setup, checked and made ready for the daily activities. Moreover, the dose application has to be verified for both spatial and dose accuracy. The safety of the dose application is also verified by producing artificially four safety relevant interlocks, and checking that the apparatus response is as expected. One can distinguish daily, weekly, monthly and yearly checking procedures. We are in the process of determining when a particular procedure should be done.

Real Time Tumor Tracking

S. Kirsch, C. Schilling, and P.G. Seiler

Paul Scherrer Institut, 5232 Villigen PSI, Switzerland

Abstract

This paper introduces a position measurement system to track a miniaturized coil in three-dimensional space. The coil can be placed near a tumor inside or outside the body to follow its movement. The system provides the position of the coil with an accuracy of 1 − 2 mm, and the coil orientation within 1°. Measurement frequency is at a rate of 50 times per second. Applications in minimal invasive surgery or tele-medicine are possible. Swiss and international patents are pending.

Introduction

For tumor irradiation the patient is usually firmly positioned in the reference frame of the irradiation facility. But certain tumors move due to respiration, circulation and peristalsis. Therefore, to precisely irradiate the tumor, its position should be measured directly. A real-time position measurement system to track moving tumors was proposed at the 'Second Symposium on Hadrontherapy September 9-13, 1996 at PSI and CERN'.

The device can be considered to have two main parts, one stationary and one mobile. The stationary part is a tetrahedron shaped gradiometer array, which serves as a reference frame (see figure 1). Each of the six gradiometers is formed by two coils with opposite polarity. The mobile part is a miniaturized marker coil, which is connected to a moving object (see figure 2). The position and direction of the marker coil can be determined with respect to the tetrahedron by generating a slowly modulated magnetic field in either all gradiometers or the marker coil, and measuring the magnetic coupling between them. The magnetic field penetrates the human body undisturbed. A computer algorithm calculates the position and orientation of the marker coil from these couplings. For more details concerning the algorithm see [1] and references therein. The miniaturized marker coil is implanted, inserted, or attached such that it is connected to the tumor and moves with it. Therefore, determination of the marker coil position is also a determination of the tumor position.

In the first prototype system the magnetic field was generated with the marker coil and the gradiometers were used to measure the magnetic field derivatives. [1]. For the system described in this paper the function of the field generating marker coil and field sensing gradiometers were exchanged. Each gradiometer now generates a differential magnetic field. The fields
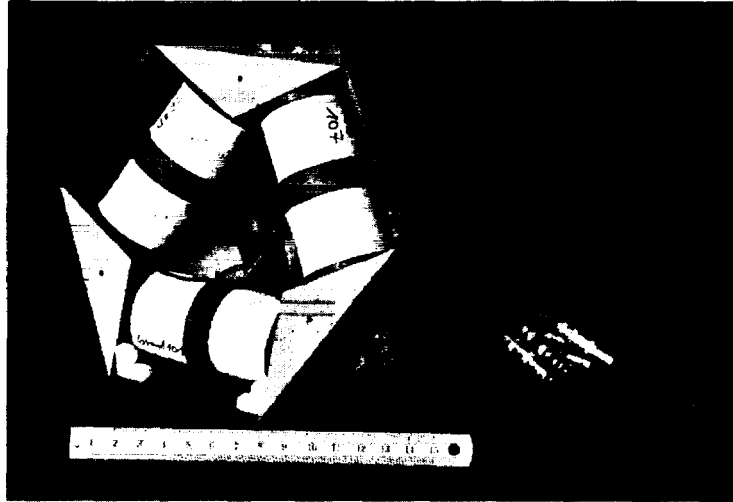
Figure 1: Tetrahedron shaped gradiometer array

of the different gradiometers are time or frequency multiplexed. Using the marker coil as a sensor has several advantages:

- There is no power fed into the miniaturized coil, and thus no heating of the tissue.

- It is possible to measure multiple sensors at the same time.

- Reference coils with a known constant position can be measured to decrease the influence of stray fields and to improve system reliability.

- Stronger fields can be produced to increase signal to noise ratio.

For the method described above Swiss and international patents are pending [3].

Data Acquisition

A digital signal processor (DSP), a specialized microprocessor for real time data analysis, generates numerical signals used to drive the gradiometers, collects measured data, and calculates position and direction of the miniaturized coil (see figure 3). A digital to analog converter (DAC) creates voltage signals from the numerical signals produced by the DSP. A power converter is needed to produce sufficient field strengths with the gradiometers. The marker coil picks up a voltage signal that is conditioned by a low noise amplifier and a filter. An analog to digital converter (ADC) converts these signals into time-discrete numerical values for the DSP. The processor calculates amplitude and phase of the signals, which are then used in a χ^2 fit (see [1]) to determine position (X_m, Y_m, Z_m) and orientation (φ_m, ϑ_m) of
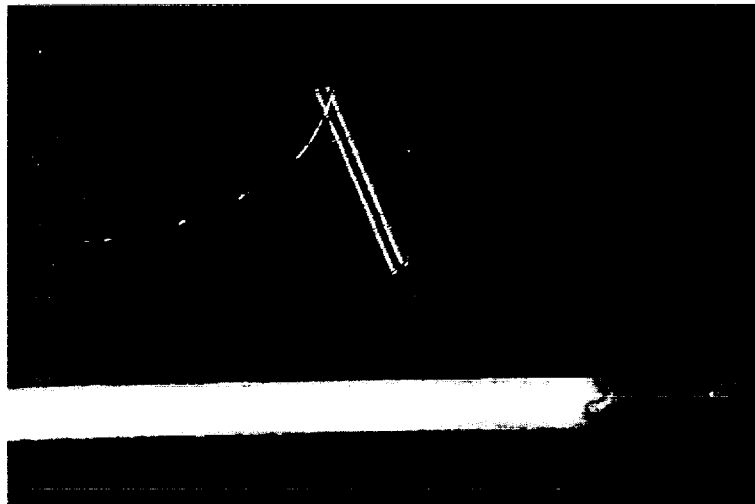
Figure 2: Miniaturized marker coil

the marker coil. The last step is to transfer the results to a client computer using a standard interface.

Results

The prototype tetrahedron has a height of 170 mm (see figure 1), the length of the marker coil is 10 mm with a diameter of $\approx$ 1 mm and 70 windings (see figure 2). In our laboratory the distance between tetrahedron and marker coil is typically 500 mm. The position can be determined with a standard deviation of $\approx$ 1-2 mm in all three coordinates. For the marker coil orientation the standard deviation is $\approx$ 15 mrad (1°). The position measurement is repeated 50 times per second to ensure continuous tracking of tumors in the body.

Discussion and Outlook

Precise irradiation techniques using charged particles or photons should benefit from a tumor position measurement with an accuracy of 1 - 2 mm, especially when the tumor is in the vicinity of critical structures [2]. In these selected cases the inconvenience of inserting or implanting an ensemble of marker coil and cable may be compensated by a more precise irradiation.

If still higher precision is needed, the best approach is to decrease the distance between the tetrahedron and marker coil, since the magnetic field strength decreases with the third power of this distance. Another possibility to improve precision is to increase the magnetic field strength by increasing the gradiometer current, cross-sectional area, or number of coil windings.
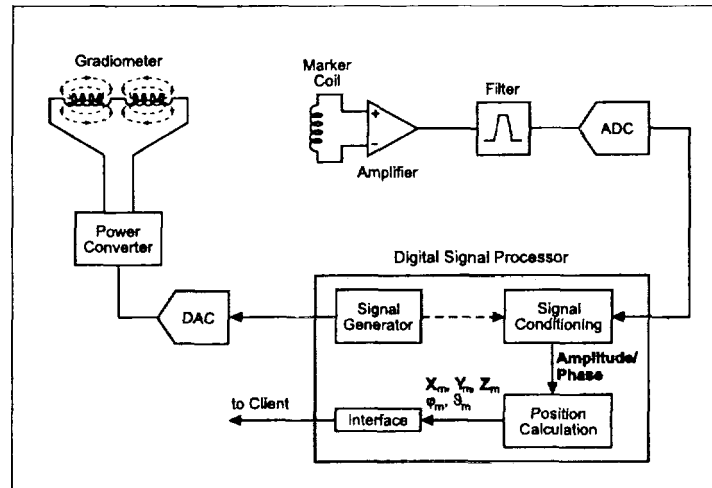
Figure 3: Data acquisition schematic

But both have only a linear effect on the signal to noise ratio.

The position measurement system will be used at PSI in a first step for tracking the tumor position in an animal patient during irradiation. Another interesting application for this technique is the tracking of medical instruments, like catheters and endoscopes inside or outside the body for minimal invasive surgery or tele-medicine. Applications in virtual reality are also possible.

Acknowledgment

The authors thank H. Blattmann from the department of radiation medicine at PSI, H.U. Boksberger and U. Greuter from engineering and technical support department at PSI for fruitful discussions and support.

References

[1] S. Kirsch *et al.*, *Real Time Tracking of Tumor Positions of Precise Irradiation*, to be published in "Proceedings of the Second Symposium on Hadrontherapy September 9-1, 1996", Elsevier Science, Excerpta Medica, International Congress Series 1132.

[2] I. Daftari *et al.*, *The effect of motion on dose uncertainty in charged particle irradiation for lesions encircling the brain stem or spinal cord*, Med. Phys. 18, 1991, 1105-1115.

[3] Swiss patent application 797/96
International patent application PCT/CH97/00132

DE010814219

DE98F5402

Requirements, design and performance of a monitoring system for heavy-ion radiotherapy

B. Voss, T. Haberer, D. Schardt, H. Stelzer, U. Weber
(GSI Darmstadt)

For the sucess of tumor conformal radiotheraphy with heavy ions using **active beam scanning** systems – as realized at the facility at GSI – the precision of the **beam delivery** system and the control methods for the patient positioning are essential. Furthermore, safety requirements and quality insurance are quite different from conventional therapy:
The radiation field is generated sequentially using a pencil beam and irradiating the different parts of the target volume in 3 dim. slice by slice and point by point. In consequence the safety system has to guarantee, that the absolute position of the beam inside the patient, its width, its migration from pixel to pixel and the amount of particles per irradiated point is correct and follows the precalculated values of the treatment plan. In case of intolerable discrepancies the beam has to be aborted as fast as possible.

At GSI, the treatment volume will be dissected into max. 64 slices of same beam penetration depth. The 253 energy steps equally distributed in range from 80 to 430 MeV/u available from a predefined library pulse to pulse from the accelerator cover the complete range of realistic tumor geometries with a sufficiently dense pattern.
The irradiation is performed consecutively slice by slice starting with the highest energy at the distal part of the tumor. Every slice is subdivided into pixels, each about 3x3 mm^2 in size and 1 to 5 mm apart from each other. The irradiation of such a layer requires 1 to 2 spills in practice. The beam intensity – available from the accelerator in 15 discrete steps – has to be adapted to meet the dynamic properties of the scan system. The extraction time is held constant with a flat top of 2 s (3 s totally), the beam intensity will be varied through the SIS filling instead in a range from 10^6 to 10^8 ions/spill. The finite dynamics of the raster scan system gives an upper limit for the scanning velocity of the therapy beam. Therefore the integral number of particles in one spill should be kept within + 30% -50% of the requested value.

Due to the high scanning velocity and the short reaction times necessary the whole treatement is executed automatically without any manual interference exept an emergency interrupt. A **control system** consisting of the electronics for the data aquisition and data control as well as DSP-based computer cards each developed at GSI takes care of this task.
Furthermore, a **supervisory system** based on industrial control software is providing the graphical user interface for the operators to all components including peripheral parts (e.g. dosimetry). Additionally it performs the necessary continuous monitoring and/or interlocking of all equipement such as power supplies, gas delivery, high voltage supplies for the detectors.

In order to meet all above mentioned requirements, a **detector setup** and its appropriate electronic was developed and installed at the medical cave. For safety reasons the beamline is designed such that the beam undefleted beam passes over the patient when the rasterscan magnets are

switched off. To check the correct beam alignment a small wire chamber (CG) with current readout combined with an ionization chamber measure the position, the focus and the intensity of the undeflected beam at the exit of the beampipe. Additionally the beam is visualized on a scintillation target with a camera system.

When the rasterscan magnets are operating, the beam is deflected to the target region around the reference point. In this case a set of transmission counters measures the lateral position and width of the scanned beam with a refresh rate of 5 to 6 kHz and its intensity with 80 kHz. For reasons of redundancy and failsafeness it consists of two identical **Multi Wire Proportional Chambers** (MWPC) and **Parallel Plate Ionisation Chambers** (IC), respectively, located just behind the vacuum window roughly 90 cm upstream the reference point. A third IC with a different electronic readout concept serves as an independent intensity monitor for safety reasons.

The whole detector setup is mounted on a common support which can be aligned to be orthogonal to the central beam axis within 1 mm in each direction by the help of a laser system.

Optionally, a scintillating-target/digital-camera system or a CG together with and IC, respectively, may serve to judge the beam quality directly at the reference point.

The **intensity measurement** is done for each IC separately. For two of them the charge produced in the 10 mm active IC gap is integrated and digitized every 12.5 μs. This is – in accordance to the „Abtasttheorem" – 10 times faster than the maximum frequency inherent in the time structure of the beam extraction. The ICs are operated with a reduced field of about 3200 V/cm and read out by a current amplifier. The decay time of the signals is 70 μs which defines the minimum time for generating a beam interrupt signal. After comparison of the digitized particle numbers with the ones of the treatment plan a synchonisation pulse tells the system to go one with the irradiation of the next point. Any deviation from the planned numbers outside a predefined tolerance band or a mismatch of the particle numbers evaluated by the two independent ICs are considered as failure case causing the generation of an interrupt signal and termination of the irradiation. The maximum overload at one point is variable but constant for a specific treatment plan. In order to assure a reliable measurement of the particle numbers, the effective ranges of the electronics has to be chosen properly. Consequently, the variation of the particle numbers with time has to be kept constant within a factor of 5 in a 300 μs time interval for a secure function even if the spread is a factor of 10 above the mean value. The third IC serves for a redundant measurement of the intensity, using an independent charge-to-frequency converter based on the recyling-capacitor principle. Preset values for the maximum intensity per point, per slice and for the whole treatement are supervised this way. A transgression of any of these threshold values leads to an interrupt.

The **position determination** by the MWPCs – operated in current readout mode – is done within a measuring interval of 150 μs. This is three times faster than the maximum velocity of the scanning system. During this time background subtraction and evaluation of the centroid with an accuracy of 0.5 mm and the width of the beam from the raw charge distribution of all 112 wires per plane is done by the assigned DSP boards separately for each detector. A negative comparison of one of the calculated positions with the ones requested by the treatment planning leads to an immediate termination of the running irradiation. The tolerances bands are $\pm 1mm$

for any requested position and 20% for its requested width, available from 4 to 10 mm in 7 fixed steps.

The anode voltage of +1600 V has been optimized to assure optimal operation for all beam intensities.

As the beam is moved by the scanning magnets with a maximum velocity of 2 cm/ms (horizontally) the recognition of a misplacement and the abortion time of the beam extraction has to be much faster than 1 ms in order to avoid that a significant dose will be deposited outside the target volume. The delaytimes introduced in the measurement by the charge collection, amplifiers, ADCs, μ-processors and the magnetic scanning system itself sum up to approx. 210 μs. The time which is necessary to switch from one point to the next one amounts to 75 μs (max. 400 μs), minimum irradiation time at one point is 500 μs. Thus the irradiation of each point takes at least 785 μs during which only 3 sucessive position measurements can be performed. Consequently, one can accept only 2 consecutive mismeasurements by the detector system in order to cope with the demand to be able to detect any misplacement of the beam. With the actual time structure of the spill, which exibits intensity variations in the same pulse of factors 2 to 5, this is a very hard restriction to deal with.

All detectors are operated with a constant flow of Ar:CO$_2$ (80:20 Vol.-%) at atmospheric pressure. The gasflow of 2 l/h per unit, its temperature and pressure inside the chamber (in case of the ICs) as well as the high voltage supplied are monitored and protocolled continuously once a minute by VME processor cards and ADCs. Any malfunction gives rise to an alarm message by the supervising system.

After adjustment and optimization of the **detector design** and its **operational parameters** the whole monitoring system was recently completed and put into operation.

Some specific **problems** which had to be taken into account, investigated **properties** of the detectors and first results obtained on the **performance** of the detection system will be presented.

Pre-clinical studies on PET monitoring of heavy ion therapy at GSI Darmstadt

R. Hinz, W. Enghardt, B.G. Hasch, O. Jäkel[t], K. Lauckner, J. Pawelke, M. Sobiella
Forschungszentrum Rossendorf e.V., Postfach 510119, D-01314 Dresden, Germany
[t]DKFZ Heidelberg, Im Neuenheimer Feld 280, D-69120 Heidelberg, Germany

Introduction

Since January 1996 the positron emission tomograph for in-situ control of the tumour irradiations at the experimental heavy ion therapy unit of the Gesellschaft für Schwerionenforschung (GSI) Darmstadt has been running continuously. So we could investigate the capabilities and limitations of the PET system by carrying several phantom irradiations through. In addition to previous findings [1] and [2], results and conclusions from new experimental studies will be introduced in the following.

The determination of particle ranges from β^+-activity profiles

An essential aim of the PET therapy monitoring is the determination of the range of the primary particles from measured β^+-activity profiles.

In order to establish a relation between the shape of the β^+-emitter depth profile and the primary particle range we analyzed the results from Monte Carlo simulations at first [3]. These computer simulations take into account the stopping of the primary projectiles and their fragments in matter, the cross sections and kinematics of the fragmentation reactions, the decay of β^+-emitters, the transport and the annihilation of the positrons and the propagation and detection of the photons by the camera. The outputs of these computations were the three-dimensional distributions of dose and β^+-emitters in the target area.

The β^+-activity depth profiles were obtained by projecting the back projected distribution onto the beam axis. These depth profiles were parameterized by an analytical model. The fit function consisted of two terms: a polynomial of degree m ($2 < m < \approx 10$) and a skewed Gaussian with four parameters. These $m+5$ free parameters were determined by minimizing χ^2 using the least squares method.

It was observed that the estimated primary particle range can be expressed in terms of the parameters characterizing the skewed Gaussian. This range formula found heuristically was applied to experimental data obtained by irradiating homogeneous PMMA blocks with monoenergetic ^{12}C beams of energy values between 91.5 and 306 AMeV corresponding to ranges between 2 and 16 cm in this material. As an example, Figure 1 shows the measured and computed profiles in comparison for a particle range of 96 mm.

In all monoenergetic cases the particle range could be determined with an accuracy better than one millimetre. For more sophisticated irradiations using a set of different energy values the profiles have to be decomposed into their monoenergetic components by simulating each cut of the raster scan prior to the determination of the particle range from these profiles.
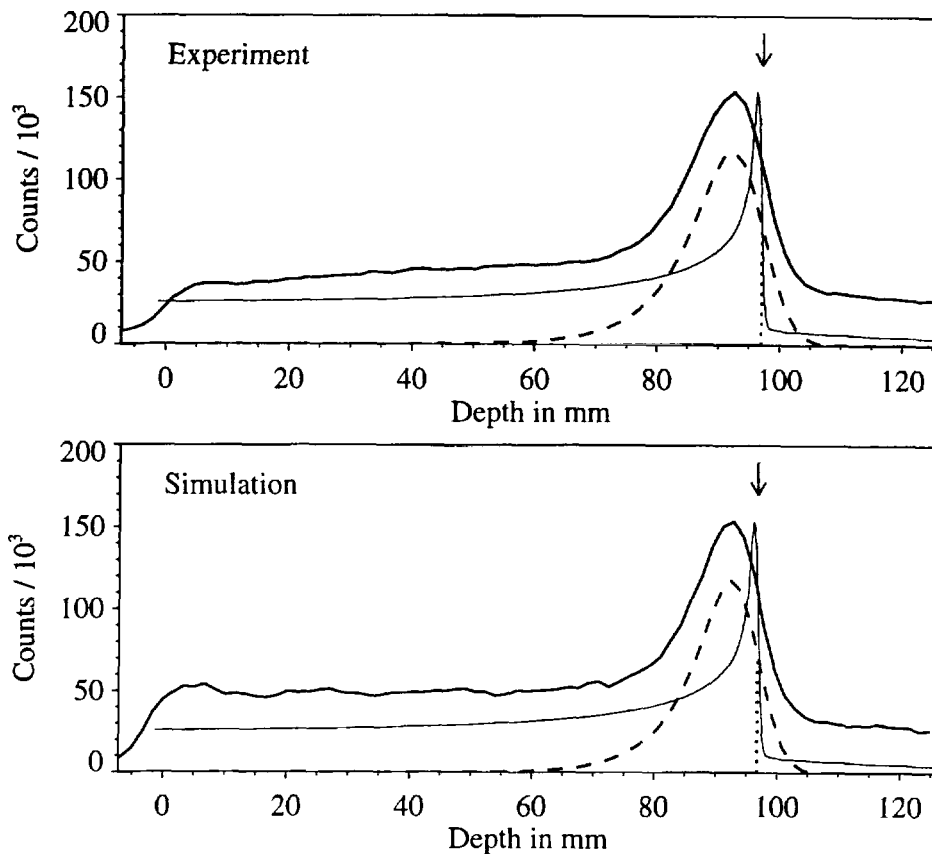
Figure 1 Profiles (thick solid lines) of β^+-activity obtained from the irradiation of a PMMA block with 234 AMeV ^{12}C (above) and from the simulation of this experiment (below). The thin solid lines depict the computed dose depth profile. The dashed lines are the fitted skewed Gaussians, and the arrows indicate the estimated ranges (dotted lines).

Range resolution studies

The discrete energy values of the ^{12}C beam provided by the heavy ion synchrotron (SIS) for the medical treatment have been defined in such a way that the particle range difference between two adjacent energy steps is one millimetre in water. If a treatment error were made the dose distribution would be mispositioned. The PET imaging of the treatment has to reveal discrepancies between planned and applied dose of a therapy fraction in order to modify the plan of the irradiation before next fraction.

PMMA phantoms were irradiated with monoenergetic ^{12}C beams of four consecutive energy steps. The β^+-activity distribution was back projected into the 3D image space and thereafter projected onto the beam axis (Figure 2). Although the shift between two adjacent profiles is only about 0.8 mm, the profiles can be clearly distinguished.
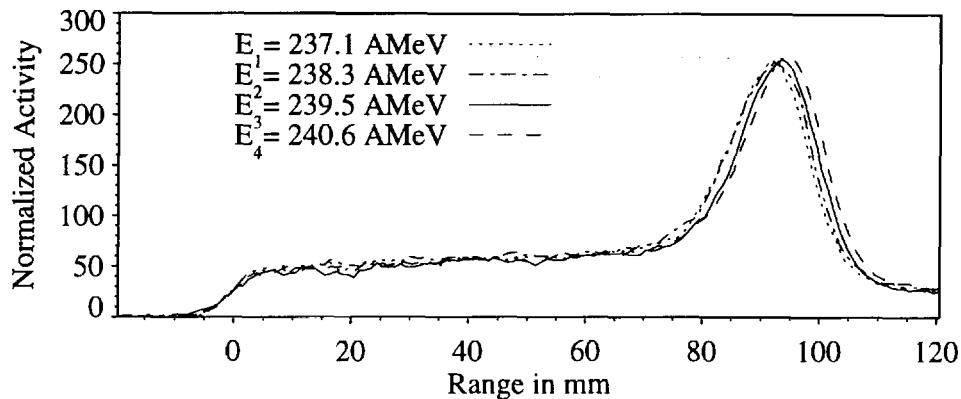
Figure 2 β^+-activity profiles of four monoenergetic irradiations of PMMA block targets with ^{12}C beams.

The irradiation of an Alderson head phantom
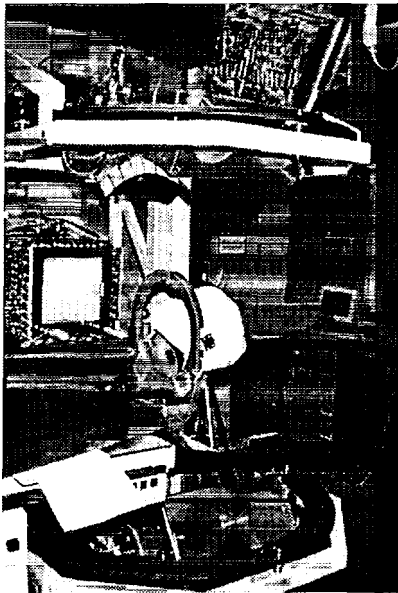
Figure 3 Photo of the experimental treatment site. In the foreground the Alderson head phantom is mounted on the patient couch. The beam comes from the left, the detector heads of the PET scanner are above and below the phantom.

To demonstrate the compatibility and combination of all components required for the heavy ion therapy, a realistic experiment with a head phantom made of tissue equivalent material (Alderson phantom) was carried out. It followed the multi-step procedure of planning, performing and verifying the treatment as it will be performed for patients:

- Based on a set of X-ray computed tomograms (CT) of the phantom the 3D treatment plan was computed by the planning system VOXELPLAN under supervision of the physician as usual in radiotherapy [4]. The desired dose distribution was defined, and the raster scan control data were derived from this individual treatment plan.

- The phantom was positioned on the patient table using the stereotactic positioning and fixation sytem (Figure 3). The position was immediately verified by means of two X-ray images.

- The irradiation was performed, simultaneously the PET scanner acquired the coincidence data. The PET measurement proceeded about 20 minutes after the irradiation while the phantom remained on its position.

- The simulation mentioned above computed the expected β^+-activity distribution. It took into consideration the CT data of the target region, the raster scan program and the record of the actually delivered beams.

- The measured as well as the simulated PET data were reconstructed iteratively. Therefore the maximum likelihood algorithm has been adapted to the limited angle geometry of the in-beam PET scanner and low activity concentrations produced by ^{12}C irradiations with doses being typical of the therapy.

- Both PET images were superimposed onto the CT slice intersecting the isocentre (Figure 4). Considering the position of the β^+-activity relative to anatomical details (e.g. bones or cavities) the recent therapeutical fraction can be validated [4].
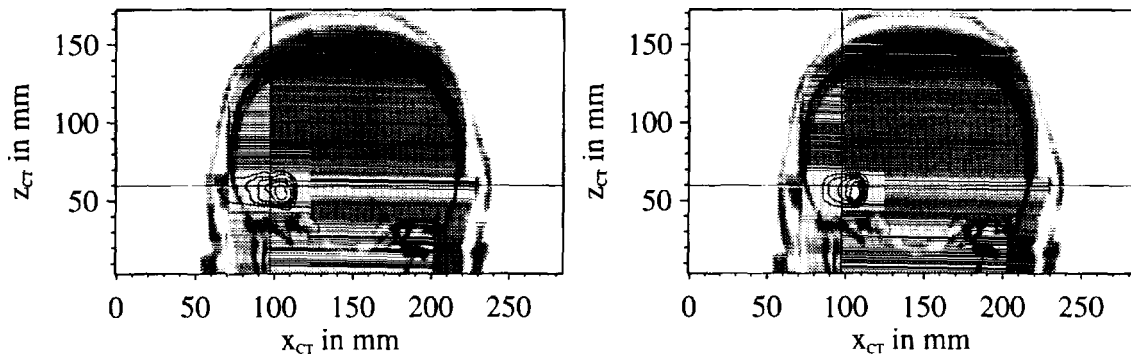
Figure 4 Superimposing of CT slice (grey values) and reconstructed PET image (contour plot). On the left: experimental data, on the rigth: simulated data. The ^{12}C therapy beam entered the head phantom by the right ear. The cross marks the isocentre of the treatment.

Conclusion and outlook

All components of the heavy ion therapy monitoring by PET have been proved. The PET scanner works reliably, the simulated data agree with the measured to a large extend, powerful image processing and reconstruction software has been developed. The pre-clinical studies demonstrated the capabilities of in-situ PET at the treatment site from which the heavy ion therapy can benefit.

Further studies will focus on the influence of physiological processes like blood flow, breathing and metabolism on the dose localisation by PET. A series of fractionated irradiations of six minipigs has already been prepared.

Acknowledgement

References

[1] J. Pawelke et al., In-beam PET imaging for the control of heavy-ion tumour therapy, IEEE Nucl. Sci. Symp. Conf. Rec. vol. 2 Nov. 2-9, 1996, Anaheim, California, p. 1099-1103.

[2] R. Hinz et al., A method for in-vivo treatment plan verification of heavy-ion tumour therapy by positron emission tomography, Physica Medica 12 (1996) 3, p. 157.

[3] J. Pawelke et al., Positron emission tomography for quality assurance of heavy ion therapy, this report.

[4] O. Jäkel et al., Clinical implementation and quality assurance of treatment planning at the German heavy ion facility, this report.

DE98F5400

A Detector System for Protonradiography at the Paul–Scherrer–Institute *

M. Moosburger, J. Besserer, J. de Boer, M. Dellert, C. Gahn
Sektion Physik, Ludwig–Maximilians–Universität München,
85748 Garching, Germany

P. Pemler, U. Schneider
Stadtspital Triemli, 8063 Zürich, Switzerland

E. Pedroni, H. Stäuble
Paul–Scherrer–Institute, 5232 Villigen, Switzerland

For the proton gantry of the Paul–Scherrer–Institute a detector system for fast in–vivo protonradiography was developped and installed [1]. The main goal of this system is the quality assurance for tumor therapy with protons. Protonradiographs are taken under exactly the same conditions as proton–therapy itself is carried out. The range and the range uncertainty of the protons are measured and compared to the predictions of the treatment planning. In this way, inhomogeneities parallel to the beam direction, which are difficult to handle by the treatment planning software, can be detected. With a fast data–acquisition system, computer–assisted evaluation and image processing it is possible to verify the actual position of the patient on the gantry. The good density resolution of proton radiographs also allows to obtain images of low–contrast lesions for diagnostic purposes. For comparable image quality the dose to the patient is lower than in routine X–ray examinations by an order of magnitude [2,3]
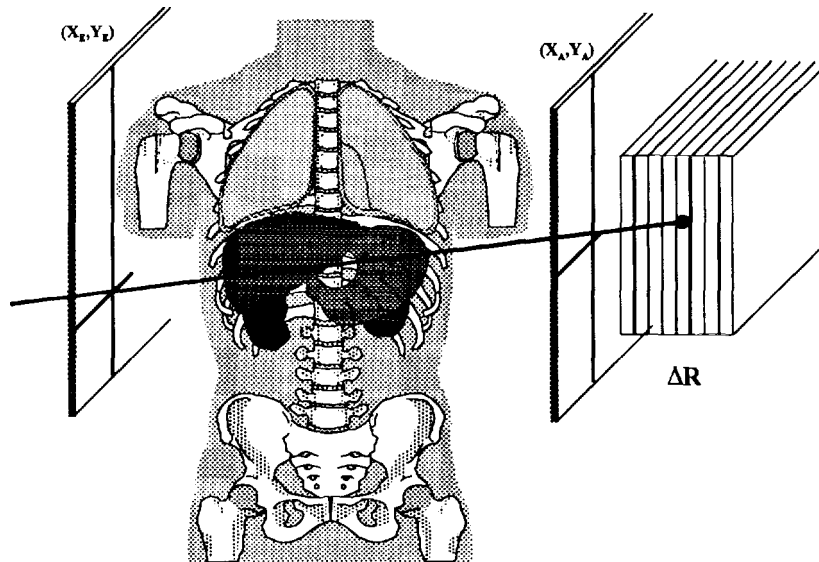
Figure 1: Principle of radiography with protons

In Fig. 1 the principle of a fast radiography system with protons is presented [4]. For each proton the entrance coordinates (X_E, Y_E) and the exit coordinates (X_A, Y_A) are measured in coincidence. Additionally for each proton the residual range (ΔR) after passing the human body is determined. Hodoscopes are used as position–sensitive detectors, combining the techniques of scintillating fibers and multi–channel photomultipliers. Using two shifted layers of 2 mm square fibers, a spatial resolution of 1 mm can be achieved. The residual energy of the protons is measured by a telescope of scintillator plates. The scintillators are coupled to the photomultipliers by wave–length shifting fibers placed in grooves milled into the plates.

A fast front–end electronic and data–acquisition system enables us to register protons at a rate of up to one million events per second. Thus it takes only a few seconds to register an entire protonradiograph with a size of 20 cm × 20 cm.

The complete detectorsystem was successfully tested at the gantry of the
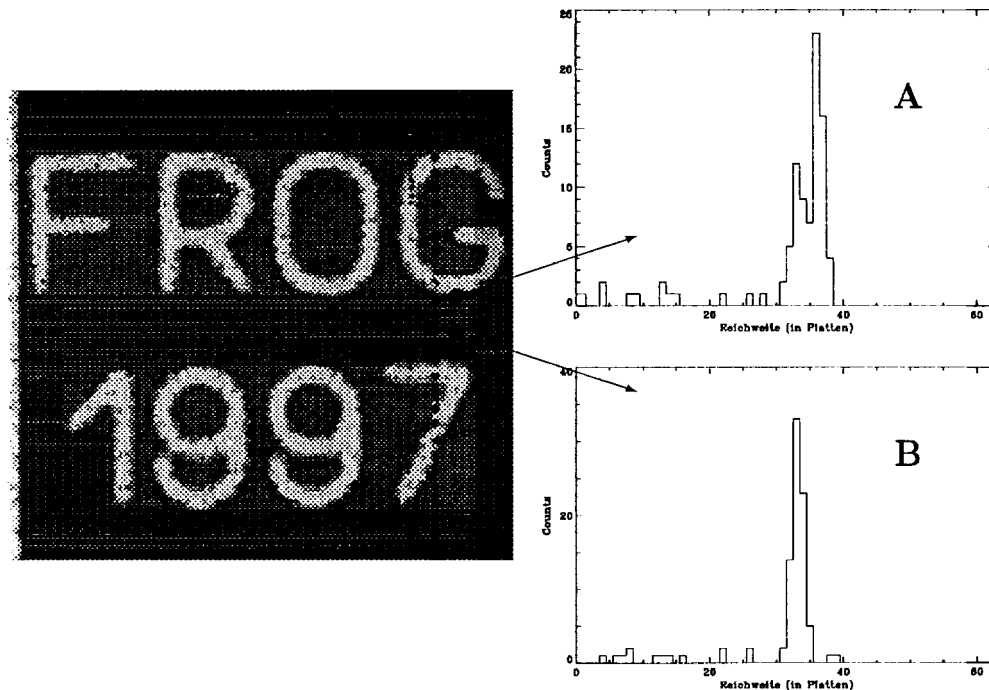
Figure 2: Protonradiograph of a lucite phantom with engraved letters. The grey scale corresponds to the calculated range of the protons (left side).
FROG = **F**ast **P**roton **R**adiography **O**n The PSI **G**antry
Right side: Range spectra for a phantom with constant thickness (B) and and with an inhomogeneity in beam direction (A).

Paul–Scherrer–Institute. The results show that the detector can be operated as expected and as predicted by Monte–Carlo simulations. First radiographs were taken of lucite phantoms. Letters were engraved 8 mm into a plate of lucite with a thickness of 15 mm. The thickness of the lines was 5 mm. For each pixel the mean range and the range uncertainty of all protons hitting these coordinates are determined. This is done in an iterative way with a gaussian weight distribution around the previously calculated mean value. The result can be seen in Fig. 2 (left side).

In the thin phantom plate multiple Coulomb scattering of the protons in the phantom is negligible. Therefore the spatial resolution is limited by the pixel

size of the position sensitive hodoscopes (1 mm × 1 mm) alone.
Images obtained from various phantoms demonstrate that the residual range
of the protons can be determined with an accuracy of better than 0.5 mm.
This means that a density resolution of 0.1 % was achived , as expected.

The two range spectra on the right side of Fig. 2 were created at the edge of
a letter and at a position with a homogeneous thickness of the phantom as
marked in the image of the phantom. A comparison shows that the width
of the range distribution can be used to identify additional straggling caused
by inhomogeneities in the tissue.

Summarizing, a fast and highly integrated system of detectors for in–vivo
protonradiography has begun operation at the gantry of the Paul–Scherrer–
Institute. First measurements with phantoms show that protonradiography
can be used as a standard tool for quality control of the high precision proton
therapy at the PSI gantry.

References

[1] E. Pedroni, et al., Med. Phys. 22(1), 37 (1995).

[2] U. Schneider, E. Pedroni, Med. Phys. 22(4), 353 (1995).

[3] U. Schneider, in *Ion Beams in Tumor Therapy*, Ed. U. Linz, (Chapmann, Weinheim, 1995), p. 300.

[4] P. Pemler, Dissertation, München, 1997.

I

Status Reports and Future Developments

Oral Presentations

1. U. Amaldi (Chair)
   (CERN, Geneva, Switzerland)

Overview of the World Landscape of Hadrontherapy and the Projects of the TERA Foundation

2. G. Kraft
   (GSI Darmstadt, Germany)

Heavy-Ion Therapy at GSI - A Status Report

3. T. Auberger
   (Uni. Vienna, Austria)

Status AUSTRON

4. P.J. Bryant
   (CERN Geneva, Switzerland)

Progress of the Proton-Ion Medical Machine Study (PIMMS)

5. M. Pavlovic
   (GSI Darmstadt, Germany)

Gantries for light-ion cancer therapy

6. S. Frullani
   (Ist. Sup. San. Rome, Italy)

A Linear Accelerator for Oncological Protontherapy: TOP-LINAC

OVERVIEW OF THE WORLD LANDSCAPE OF HADRONTHERAPY AND THE PROJECTS OF THE TERA FOUNDATION

Ugo Amaldi

CERN, Geneva and TERA Foundation, Novara

1. THE INTERNATIONAL SCENERY

For brevity this review concentrates on generic accelerators issues related to deep hadrontherapy with beams of charged hadrons, protons in particular.

In Europe the main protontherapy centres are, till now, Uppsala and Orsay. This year the new PSI (Villigen, Switzerland) and GSI (Darmstadt, Germany) beamlines, approved in the years 1993 - 1994, have been commissioned and will soon demonstrate the advantages of active scanning with protons (at PSI) and with carbon ions (at GSI). In this workshop these facilities are presented in dedicated reports ; hence they will not be dealt with here.

Since 1993 - 1994 another important development took place: the moving of hadrontherapy from physics laboratories to fully dedicated centres which feature more than one room for treating patients. These centres are for brevity called "hospital based", even if they collect patients from more than one hospital. The effect of this major change in the clinical application of a technique, first suggested fifty years ago, is not yet seen. In fact, about 90% of the 19 000 protontherapy treatments performed in the world till now have used beams produced by accelerators constructed for fundamental research in nuclear and particle physics. Only about 10% of the treatments of deep seated tumours have been done at the American *Loma Linda University Medical Center,* the only existing fully dedicated facility. Over the next years this percentage is expected to rapidly increase. As far as *ions* are concerned, since 1994 HIMAC treats patients with carbon ions.

As no hospital based centre exists in Europe, the recent increase of interest in hadrontherapy throughout our continent is quite natural, as in the year 2000 there will be *two* hospital-based centres for deep hadrontherapy in the United States and *six* in Japan. In fact, when considering only hospital centres fully devoted to the treatment of deep-seated tumours and having more than one treatment room, the world situation is as follows.

Running at present:

• *Loma Linda = Loma Linda University Medical Center.* This is the first hospital-based protontherapy centre in the world for which a total investment of 80 million $US was granted by public and private funds. It features three isocentric gantries and a room with fixed beams.

• *HIMAC = Heavy Ion Medical Accelerator Centre* in Chiba, near Tokyo. Built with a total investment of 350 million $US, since 1994 HIMAC treats patients in three rooms with *carbon ions.* About 200 patients had been irradiated by the end of 1996.

Fully financed and under construction:

NPTC = Northeast Proton Therapy Center (Boston, USA). This *protontherapy* centre, built for 55 million $US by the Massachusetts General Hospital (MGH) in Boston, will be ready in 1998 and aims at treating 1'000 patients/year. It is based on a cyclotron built by IBA.

Kashiwa Proton Treatment Facility - (Japan). This *protontherapy* centre is almost identical to NPTC. The cyclotron is being built by IBA in collaboration with the Japanese company Sumitomo. The centre will be ready in 1998 with three rooms for protontherapy.

Hyogo Charged Particle Facility - (Japan). Direct follower of HIMAC, this centre is in construction to the North of Kobe by Mitsubishi Electric. It will start irradiation in 2001 with *proton and carbon ions.* The investment, including a 50-bed hospital, is 275 million $US.

Shizuoka . Located about 150 km West to Tokio. The centre will have *only proton* beams. The project is fully financed and soon the construction will start.

Wasaka Gulf Project (Japan). Situated North-East Kyoto, this *protontherapy* centre is supported by the *Science Agency* and the Hitachi will be responsible for the construction of the facility.

PMRC = *Proton Medical Research Centre* (Japan). Located near Tsukuba, inside the University Campus, this *protontherapy* centre is fully financed with 70 million $US. The project foresee two gantries rooms and one experimental room.

It has to be remarked that the TOP centre of Istituto Superiore di Sanità in Rome, to be discussed in Section 5, has been financed for the part which accelerates protons to about 65 MeV, but later it will reach the 200 MeV needed for the therapy of deep tumours.

2. THE ITALIAN PROGRAMME

More than two hundred physicians, physicists, engineers and informatics experts form the *Hadrontherapy Collaboration,* which aims at bringing Italy to the forefront of tumour radiotherapy by the beginning of next century and to foster hadrontherapy in Europe. The *Hadrontherapy Programme* was initiated in spring 1991 and the *TERA Foundation* was created in fall 1992 to collect funds and employ a staff fully devoted to the Hadrontherapy Programme. In 1997 more than twenty people are working fulltime on the TERA projects.

Three Committees coordinate the research and development activities done in the framework of the Hadrontherapy Programme: the *Pathologies and Treatments Committee,* the *Radiobiology Committee* and the *Dosimetry and Microdosimetry Committee*

Three studies of the potential Italian patients have been completed by physicians of AIRO, the Italian Association of Oncological Radiotherapy. They have been published in the Blue Book (1994, Ref. 1), the Green Book (1996, Ref. 2) and the Red Book (1997, Ref. 3).

The last study (R. Orecchia et al in Ref. 3) shows that about 12'000 persons are diagnosed annually as having a tumour or lesions which could benefit from the treatment with *proton beams* having a maximum energy of 200-250 MeV; for 825 of these patients the treatment with protons is the elective cure; these are classified as Category A patients. The relevant tumour sites and the figures are given in Table 1.

Table 1 *Elective indications for protontherapy already clearly supported by clinical data. These patologies are classified in Category A of the three Italian studies. (The column b gives the percentages of treatable tumours and column a the numbers.)*

Category A	Patients/y	Treatable with protons	
		a	b
Uveal melanoma	370	370	100 %
Chordoma of the base of skull	30	30	100 %
Chondrosarcoma of the base of the skull	40	40	100 %
Meningioma of the base of the skull	250	125	50 %
Paraspinal tumours	140	140	100 %
Schwannona of the acoustic nerve	300	45	15 %
Hypophysis adenomas	750	75	10 %
TOTAL	**1'880**	**825**	**44 %**

Since about 120 000 italians are treated with X rays every year, the total number of Categories A and B corresponds to about 10% of X rays patients. Studies conducted some time ago at the European level are, probably, less conservative and give as conclusion percentages for protontherapy which are in the range 30-40%.

Carbon ion beams of 4'500 MeV are particularly indicated for the treatment of deep-seated tumours, which are radio-resistant both to X-rays and to protons. These are about 10 % of all the tumours treated with X-rays, and therefore in Italy about 10'000 patients a year.

3. THE PROJECTS OF THE TERA FOUNDATION

The design work of the part of the Hadrontherapy Programme promoted by the TERA Foundation is organized in three projects:

(1) The creation of an informatics and organisational network, called *RITA (Italian Network for Hadrontherapy Treatment)*, which will connect the Associated Centres – distributed throughout Italy and abroad, and situated in the public oncological institutions and in private clinics – with the Centres where proton and ion beams will be made available.

(2) The design and construction of small and relatively cheap *novel* hadrons accelerators, which could be built by Italian industries. A facility based on one of these accelerators should treat at least 300 patients a year with a single beam line and double that number with an added treatment room. This is the *"compact" accelerators project* called PACO. (The term "compact" is a shortland for an accurate definition not reported here).

(1) The planning and the construction in Milano of a National Centre for Oncological Hadrontherapy (CNAO for "Centro Nazionale di Adroterapia Oncologica"), a healthcare and research structure of excellence which will be the focal point of all the hadrontherapy activities and – being equipped with *proton and ion beams* to be used in parallel in many treatment rooms – will treat with protons and carbon ions more than 1'000 patients per year. This is the *"CNAO Project"*

The work done by the members of the Hadrontherapy Collaboration in these three areas, (and in hadron radiobiology and dosimetry), have been published in the already quoted Blue Book [1], Green Book [2] and Red Book [3].

4. THE RITA NETWORK

We now discuss the three projects of the TERA Foundation. The first one is the network RITA, wich has the purpose of connecting, through multimedia connections, the specialised medical and physics staff of all the Italian oncological institutes who want to profit from the Hadrontherapy Programme (they are called *Associated Centres*) with the experts of CNAO and those of the other protontherapy centres. By using the most modern informatics techniques, they will exchange diagnostics images and discuss each case, so that the patient will travel to one of the centres where hadron beams will be availabel only if the tumour can be treated with a clear advantage. Some of the physicians at these Associated Centres (sometimes after using conventional radiotherapies) will even be able to plan a successive hadron treatment for their patients, who will successively be irradiated in one of the hadrontherapy centres. The implementation of the RITA network is well advanced: connection tests between two oncological centres were fully successful and a clinical folder has been produced and accepted by the Italian radiotherapy Association AIRO.

5. THE "COMPACT" ACCELERATORS PROJECT - PACO

Concerning PACO, the Green Book [2] responds to the needs of Istituto Superiore di Sanità. In fall 1993 the Physics Laboratory of ISS, in its continuous and long action in the fields of proton radiobiology and dosimetry, decided to request special funds for the construction of a prototype of a "compact" accelerator (and its rotating gantry) and to finance R&D programmes in the fields of radiobiology, dosimetry, networking, pathology and treatment planning. This programme is now known as the *TOP Project* of ISS, where TOP stands for "Terapia Oncologica con Protoni".

In the framework of the Hadrontherapy Programme, in the years 1993-1995 four working groups have designed four novel medical proton accelerators: two synchrotrons, a

superconducting cyclotron and a high-frequency (3 Ghz) proton linac. They are described in the Green Book. In September 1995 advanced copies of this book were distributed to the members of the Scientific Committee of the TOP project. The decision was to construct the first part of the high-frequency proton linac , whose injector will also be capable of producing PET isotopes. In 1997 an agreement has been signed between ISS and ENEA for the construction of the accelerator. An agreement with TERA is under discussion.

The initial ISS funds (6 million kLit, i.e. 6 million DM) were allocated in 1994 and appropriated in March 1996 with the understanding that about 80% of this sum has to be spent for the linac. A further contribution of 2.3 million kLit was granted at the end of 1995. Requests for about 10 million kLit are pending; they will allow the completion of the linac and of three treatment areas, one of them with a rotating gantry.

6. THE CNAO PROJECT

From the beginning of 1992, the Foundation is engaged in the design and realization of the hadrontherapy centre CNAO based on a synchrotron which can accelerate protons to at least 250 MeV and carbon ions to at least 4500 MeV (i.e. 4500/12 = 375 MeV/u). This will be a centre of excellence devoted to tumour hadrontherapy of more than one thousand patients/year, to clinical research in cancer therapy and to R&D in the fields of radiobiology and dosimetry. The first study was completed in spring 1994 and published in the Blue Book [1]. The National Oncological Commission gave its positive opinion on the CNAO project in December 1995. Since the beginning of 1996 Dr. Giorgio Brianti, past CERN Tecnical Director, is the Chairman of the Project Advisory Committee (PAC).

CERN partecipated in the European study called EULIMA: the design of the synchrotron (proposed in parallel with the superconducting cyclotron and eventually chosen by the Committee) was due to Dr. P. Lefevre from CERN and his collaborators. After the demise of EULIMA and the start up of the CNAO design study, Lefevre and other CERN experts have been helping the TERA project group. In 1995 CERN created a small research activity (the TERA Group) formed of part-time physicists and engineers who, since then, contribute to the design of the medical synchrotron for protons and ions, which is at the hearth of the CNAO project. At the end of 1995 the TERA Foundation has drawn the interest of CERN in the design of an *optimized* synchrotron for light ion therapy to be then built nationally by those European countries who will decide to invest the needed funds.

At the beginning of 1996, the CERN management agreed, and a new optimized study of such a synchroton was started at CERN (PIMMS = *Protons and Ions Medical Machine Study*) under the leadership of Dr. Philip Bryant. Five TERA staff members and two doctoral students from the AUSTRON Project (Vienna) partecipate in the study, which aims at finding new optimized solutions for the synchrotron and the isocentric proton gantries. GSI, which since long is working in the field of hadrontherapy with ion beams, partecipates with the responsability for the design of the ion injector and of a gantry for carbon ions. This common activity of CERN, TERA, AUSTRON and GSI aims at a first document to be ready by the end of 1997. The rest of this Section is devoted to CNAO. Austron and GSI are preparing proposal for constructing facilities based on PIMMS design; they will be presented to the Austrian and German authorities in 1998.

In 1996, while initiating the European collaboration on PIMMS, TERA offered six Hospital, oncological Institutes of Milano and Pavia and three lombard Universities to form a consortium and realize the National Centre for Oncological Hadrontherapy in Milan. The instrument of understanding was signed in June 1996 by *Salvatore Maugeri Foundation* , (Pavia), *TERA Foundation* (Novara), *European Institute of Oncology* (Milan), *National Institute for Tumour Research and Cure* (Milan), *National Neurological Institute Besta*, (Milan), *Ospedale Maggiore Polyclinic* (Milan), *San Matteo Polyclinic* (Pavia), *Polytechnical School* (Milano), *University of Milano* and *University of Pavia*.

The Polyclinic of Milano put at the disposal of CNAO a wonderful site located close to the Mirasole Abbey, South of Milan, on the road going to Pavia. In March 1997, the bylaws of the *Fondazione Medico Scientifica Mirasole*, a non-for-profit Foundation which will be responsible for the construction and the management of CNAO, were approved. The founding Members are engaged in finding public and private funding sources for the construction and the initial management; in the long run the Foundation income will be sufficient to finance its operation, including the payment of salaries for the personnel (about 70 people). At the beginning of June 1997 Ospedale Maggiore asked 33 million kLit to the Lombardy Region for the buildings and conventional plants of CNAO. This sum is requested on the basis of an existing law for hospital construction which reserves, over the next six years, about 1600 million kLit to the Lombardy Region. TERA has requested the Charity Compagnia di San Paolo (Turin) 16 million kLit for the synchrotron and the controls. Answers are expected by fall 1997.

References

[1] *The TERA Project and the Centre for Oncological Hadrontherapy*, Vol.I and Vol.II, U.Amaldi and M Silari Eds, INFN, Frascati, 1995. The collection is called the *"Blu Book"*.

[2] *The RITA Network and the Design of Compact Accelerators*, U.Amaldi, M.Grandolfo and L. Picardi Eds, INFN, Frascati, 1996. The *"Green Book"*.

[3] *The National Centre for Oncological Hadrontherapy at Mirasole*, U. Amaldi Ed., INFN, Frascati, 1997. The *"Red Book"*.

DE98F5398

Heavy-Ion Therapy at GSI - A Status Report

G. Kraft for the HITAG Collaboration, Darmstadt-Heidelberg-Dresden

In 1993 GSI, Darmstadt, the Radiological Clinic of Heidelberg University and the German Cancer Research Center in Heidelberg proposed to the German government to build a heavy-ion therapy unit at the heavy-ion synchroton SIS at GSI. These institutes then already had a long tradition in heavy-ion radiobiology and beam delivery as well as in the introduction of new modalities to cancer treatment, as for example the tumorconform irradiation with conventional beams. As a consequence a particle therapy was proposed, making use of the highly specialized knowledge of the collaboration. The FRZ, Dresden, disposing of many experts in positron emission tomography (PET) then joint the group.

As a result of this brains trust, HITAG is now based on a 3-D target-conform treatment using active energy variation for the depth modulation and lateral magnetic scanning, that is intensity modulated, in order to cover each range slice with the appropriate inhomogeneous particle fluence distribution.

The 3-D treatment planning system VOXELPLAN of the DKFZ was adapted to the different physical properties of heavy particles. The variation of the biological efficiency of these particles was also taken into account. All this resulted in the first truely 3-D tumorconform and biology-based treatment system for radiotherapy.

In the past four years the therapy unit has been constructed and put into operation: In 1996 the construction of the medical-treatment area and the additional medical annex was completed. Also the first carbon beam was tuned to the medical beamline at that time.

In order to fulfill the requirements for the patients' safety a new system for the beam control by the rasterscan and a novel safety system have been developed and installed. An asymetric beam deflection with an offset of 20cm to the zero position is used for the rasterscan. This system guarantees that in case of a complete power failure the beam will not remain in the patient's body but pass above it. For the active beam monitoring a position-sensitive multiwire chamber determines the center of gravity of the beam every $100\mu sec.$ and compares the measured result to the required position. If two out of four measurements diverge the beam will be aborted in the synchroton within less than a millisecond. Other safety systems can interrupt the beam delivery within the same time span.

Another critical safety problem was the development of an appropriate dosimetry coupled with a quality assurance that guarantees the long-term constant quality of the measurement (cf. to G. Hartmann et al., B. Bathelt et al. and P. Heeg et al. this section). In recent experiments all the simulations necessary for the governmental approval have been documented and submitted to the government. The final approval and the start of patient treatment is expected for the end of this year.

In the presentation an overview of the treatment facility will be given together with the results of some key experiment.

DE98F5397

PROGRESSOFTHEPROTON-IONMEDICALMACHINESTUDY(PIMMS)

PIMMS Group

reported by P.J. Bryant, CERN

DE010814264

The Proton-Ion Medical Machine Study (PIMMS) was set up following an agreement between Professor U. Amaldi of the TERA Foundation (Italy) and Professor M. Regler of the Med-AUSTRON (Austria) to join their efforts in the design of a medical synchrotron that could later be adapted to national needs.CERN agreed to host this study inside its PS Division and to contribute one full-time member to the study team.The study group has worked in collaboration with GSI (Germany) and was more recently joined by Onkologie 2000 (Czech Republic).Work started in January 1996.

The agreed aim of the study was to investigate and design a generic facility that would allow the direct clinical comparison of protons and ions for cancer treatment.Generic in this context meant a common design that could be modified with the minimum of effort to meet the particular requirements of each partner in the study.The machine was to be designed primarily for high-precision active beam scanning for both protons and carbon ions, but was also to be capable of delivering proton beams by passive scattering.

A synchrotron with slow extraction offers the flexibility needed for dual-species operation and the variable energy needed for active scanning. The principal design requirement is that of a smooth spill.This leads to an extraction technique that maintains all transverse optical parameters constant while using a betatron core to accelerate the beam into the resonance.In addition, the machine will be made less sensitive to power converter ripple by using an empty rf bucket to channel the particles more rapidly into the resonance.The choice of a synchrotron has the consequence that the extracted beam has unequal transverse emittances and that a more advanced technique is required for matching to the rotating gantry.This technique uses a device known as a rotator.The slow-extracted beam is not only asymmetric in terms of emittance, it is also asymmetric in terms of the shape of its 'footprint' in phase space.In the vertical plane, the beam occupies the usual elliptical area, whereas, in the horizontal plane, it is a narrow 'bar'.The positive aspect of this behaviour is that it provides an independent 'handle' on the control of the beam size in the horizontal plane.This is just one aspect of the flexibility needed for the treatment planning.In the vertical plane a different technique is used to control beam size.The extracted beam intensity can be varied either by controlling the

initial intensity in the synchrotron or by varying the acceleration rate of the betatron core.The scanning speed of the beam spot can be varied over a wide range and a chopper is included to cleanly switch the spill on and off.One extra peculiarity of the slow-extracted beam is that the asymmetric phase-space footprints affect the way in which the beam scanning should be performed.Finally, the high magnetic rigidity of the carbon ions led to an investigation of an alternative gantry design.Thus, the extraction and beam delivery systems for a synchrotron with slow extraction differ significantly from the more conventional designs used with cyclotrons.

The performance parameters are defined by the clinical needsThus, the maximum energy of the machine is set to 400 MeV/nucleon for carbon ions and 250 MeV for protons.The beam intensities and repetition rates have been adjusted so as to deliver a single treatment, or fraction, in about two minutes.It is understood that in the rare instance that a dose level, or volume, causes the capacity of the machine to be exceeded, the treatment time can be extended.For active scanning, it is assumed that a 'nominal' fraction would be 2 Gray in 2 liters (or equivalent combination) delivered by 60 spills in 2 min.For passive scanning, it is assumed that a 'nominal' fraction would be 2 Gray in 7.5 liters (or equivalent combination) delivered by 120 spills in 2.5 min.

GANTRIES FOR LIGHT-ION CANCER THERAPY

*Márius Pavlovic**

GSI Darmstadt, Planckstrasse 1, D-64291 Darmstadt, Germany

DE010814273

1 INTRODUCTION

It is an aim of any radiotherapy to deliver the highest possible dose to the tumour while keeping the dose delivered to surrounding healthy tissue under a tolerable level. This aim can be best achieved if the dose is delivered in a tumour-shape conformed way (3D-conformal radiotherapy). Beams of light ions offer high physical selectivity (Bragg peak) combined with enhanced biological effectiveness (ions heavier than helium), which makes them an ideal tool for 3D-conformal tumour targeting. The highest degree of conformity could be achieved by combination of a rotating gantry with an advanced beam delivery technique (for example raster- or spot-scanning [1, 2]). This trend can be recognised in recently built or currently proposed light-ion cancer therapy facilities, especially in dedicated hospital-based facilities where a high level of flexibility of the beam delivery system is required to treat a large spectrum of tumour sizes and sites. The basic parameters of the existing gantries are collected in Tab. 1 (after [2 - 9]).

Tab. 1. Proton therapy gantries worldwide

Facility / Year	Beam	Type	Parameters
Loma Linda University Medical Centre (U.S.A.) 3 gantries 1st - 1991, 2nd and 3rd - 1994 Science Applications International Corporation	250 MeV protons weak focusing synchrotron	corkscrew	Overall diameter: 13 m, Weight: 96 t Drift to the isocentre: 3 m Rotation: 360 degree on ball bearings Anti-seismic blocking system Double-scattering system, max. field 40x40 cm Achromatic optics Acceptance: 24π mm.mrad, $\Delta p/p = \pm 0.5\%$ Magnet alignment: < 0.2 mm Beam position accuracy: < 1.6 mm
Paul Scherrer Institute Villigen (Switzerland) November 1996 Spot-scanning: - mag. sweeping horiz. - - patient table shift vert. - - range shifter longitud. - Schär Engineering AG	225 MeV protons degraded from 590 MeV beam cyclotron	single-plane eccentric compact	Overall diameter: 4 m, Weight: 120 t Drift to the patient: 1.1 m Rotation: 360 degree Achromatic optics Acceptance: 40π mm.mrad, $\Delta p/p = \pm 0.8\%$ Alignment precision: < ± 0.2 mm Isocentre mechanical precision: < ± 1 mm Power consumption: total - 185 kW last 90° dipole - $\approx$60 kW Quadrupoles: L_{eff} = 30 cm, ap. = 10 (8) cm max. field = 0.7 T Sweeper magnet: length = 40 cm, gap = 5 cm Dipoles: max. field = 2 T, gap = 7 cm Beam-path in the gantry: $\approx$13 m

* On leave from the Slovak Institute of Metrology, phone: ++49 6159 71 2330, fax: ++49 6159 71 2985, E-mail: pavlovic@clri6a.gsi.de

Tab. 1. Proton therapy gantries worldwide (continued)

Facility / Year	Beam	Type	Parameters
Northeast Proton Therapy Centre, MGH Boston (U.S.A) 2 gantries 1998 (planned) Ion Beam Applications & General Atomics	235 MeV protons fixed energy isochronous cyclotron	single-plane large-throw	Overall diameter: ≈9 m, Length: ≈9 m Drift to the patient: 3 m Beam transport: 4 quads, 45° bend-up, 5 quads, 135° bend down Acceptance: 32 mm.mrad, Δp/p = ±0.5% Achromatic optics tunable for scattering/wobbling (10 mm radius waist) or scanning (pencil beam) Beam delivery: telescopic nozzle containing scatterers, scanning magnets, range modulators and beam monitoring elements Energy selection system upstream the gantry => the gantry transports the beams with different energies
Proton Treatment Facility at NCC Hospital East, Kashiwa (Japan) 2 gantries half of 1998 (planned) Sumitomo Heavy Industries Ltd	235 MeV protons fixed energy isochronous cyclotron	single-plane large-throw	The overall concept of the facility including the gantries is identical with the NPTC Accuracy of the isocenter: ± 1mm Accuracy of stop angle: ± 0.5 degree Rotational speed: 1 rpm One of two gantries is equipped with a multi-leaf collimator consisting of 30 pairs of nickel blocks 1 cm thick Status: gantries tested at the works and re-assembled in the hospital, tests of the extracted beam scheduled in autumn 1997
Hyogo Ion Beam Medical Centre (Japan) 2 gantries (protons only) 2001 Mitsubishi Electric	proton beam 70 - 230 MeV carbon beam 70 - 320 MeV/n p/C synchrotron	single-plane large-throw (protons)	Overall diameter: 10.4 m, Weight: 120 t Drift to the isocentre: 3.2 m Rotation: 360 degree on ball bearings Anti-seismic blocking system Precision: 1 mm Beam-optics and mechanical concepts similar to the NPTC Boston and the NCC Kashiwa gantries Field size diameter: 5 - 15 cm

2 GANTRIES FOR LIGHT IONS HEAVIER THAN PROTONS

For light ions heavier than protons, the construction of a gantry is more difficult due to the higher beam rigidity. Figure 1 shows the ranges of protons and carbon ions in water as a function of the beam rigidity. For treatment of deep-seated tumours a range of about 25 - 30 cm is necessary, which translates to the beam rigidity ≈2.2 Tm for proton and ≈6.3 Tm for carbon beam. A large-throw gantry for carbon beam would exceed a total radius of 6.5 m consisting of the bending radius (6.3 Tm / 1.8 T = 3.5 m) and drift to the patient (3 m), and can hardly be considered as an optimum solution for a hospital-based facility. The gantry radius can be reduced by placing the scanning system upstream the last bend-down dipole. Feasibility of such a solution has been proved in refs. [10 - 13]. However, even in this case the total gantry radius would still be of about 5 m (3.5 m bending radius + 1.2 m drift to the patient) and the last dipole would have to have a large

aperture allowing for beam scanning (consequently it would be correspondingly heavier). Another possibility is using a superconducting dipole(s) in order to reduce the bending radius [11 - 13]. However, a gain brought by the reduction of the bending radius is partly lost by an extra space required for cryogenics and shielding of stray-fields. In addition to this, using superconducting elements in a rotating structure certainly complicates operating of the gantry and requires a careful and quite conservative design of the superconducting elements to prevent quenching and to guarantee a desirable level of patient safety [14]. That is why, our opinion is that the superconducting gantry would be justified only if it could be considerably **smaller and lighter** than a normalconducting one.
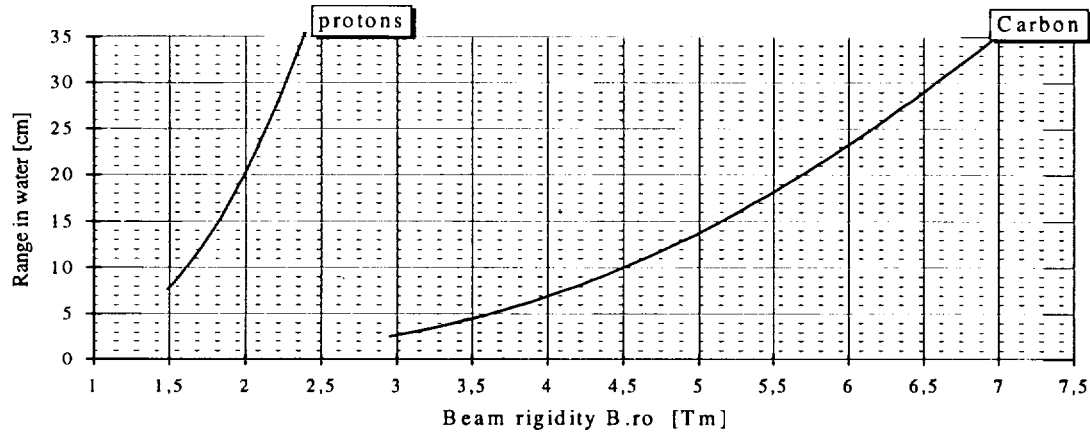

Fig. 1. Ranges of ions in water as a function of the beam rigidity. Three times higher rigidity is necessary for carbon ions compared to protons to reach the same range.

In order to answer the above formulated criterion, both normalconducting and superconducting gantry alternatives are being studied at GSI. Each gantry alternative is represented by one reference design, a plenty of other possible gantry mutations are expected to be close enough to these reference designs. The normalconducting gantry has a two-direction scanning option and can be assumed as the largest possible case. It has conical shape, the total radius of 4.7 m, length 17 m and the volume generated by gantry rotation is 1200 m^3. On the other hand, superconducting gantry (only last dipole is superconducting) does not have any active scanning option and can be considered as the smallest possible case. It has also conical shape, the total radius of 3.35 m, length 10.5 m and the volume generated by gantry rotation is 370 m^3. The size of both gantries (especially the length) will still be refined after optimising the beam transport systems of the gantries. All other compromise solutions, for example a combination of an active scanning in one direction with movement of the patient table in the other direction are expected to be inbetween these two boundary cases. We believe that working out those two reference designs shall help to make a decision, whether a gantry for carbon beam should be constructed using superconducting magnet(s) or not.

2. 1 Other gantry alternatives

So far, we have assumed only the isocentric 90 °gantries (it means that isocentre sits on the axis of gantry rotation, and that the angle measured between the beam directions at the entrance and the exit of the gantry is 90°). In contrast to this, eccentric gantries have isocentre located off-axis opposite to the last dipole, which brings a saving by a factor of 2 in the gantry radius and 4 in the volume generated by gantry rotation. A disatvantage is that the patient table moves during the gantry rotation. Because this feature was strongly

disliked by radiotherapists and radiation oncologists, we have rejected eccentric gantries from our present considerations. The main argument against was an unreliable check of the target position if the patient moves with respect to the fixed room coordinate system [15].

A significant space-saving could also be achieved by bending the beam in the last dipole less than 90° while preserving the isocentricity. A similar configuration, but in a static form, is proposed at the Hyogo Ion Beam Medical Centre (45° beam line). By using a proper combination of the gantry and patient table rotations, the gantry could be fully equivalent to a 90° gantry, of course in the restricted angular sector only, as the angles higher than the angle of the last bend can never be achieved. A design of a 60° version of this gantry type has presently been introduced at GSI [16].

3 DISCUSSION AND CONCLUSIONS

Recent development of hospital-based proton therapy facilities clearly indicates that gantry becomes an inevitable component of medical accelerator complexes. For beams of ions heavier than helium, both superconducting and normalconducting gantries are under consideration, but the final decision has not been done yet. A criterion for such a decision has been formulated in this paper. Eccentric gantries are not to be preferred because moving of the patient table makes the routine check of the target position difficult. Another possibility could be a gantry with oblique output beam, which can be rather compact but covers only a restricted angular sector.

REFERENCES

[1] Th. Haberer, W. Becher, D. Schardt, G. Kraft, Nucl. Instr. and Meth. A330 (1993) 296.

[2] E. Pedroni, H. Enge, Med. & Biol. Eng. & Comput. 33 (1995) 271.

[3] J. B. Flanz, Large Medical Gantries, Proc. 16th Int. Particle Accelerator Conference PAC, Dallas, TX, USA, May 1-5, 1995, 2004.

[4] Y. Hishikawa, private communication, Hyogo Prefectural Government, June 1997.

[5] Ch. Steinbach, Visit to Therapy Synchrotrons around the Pacific, Presentation at the Med-AUSTRON Workshop, Wiener Neustadt, Austria, January 18, 1997.

[6] Y. Jongen, The Proton Therapy System for MGH's NPTC: Equipment Description and Progress Report, NIRS-M-103, HIMAC-008, Proc. Int. Seminar on the Application of Heavy Ion Accelerator to Radiation Therapy of Cancer in connection with XXI PTCOG Meeting, Chiba-shi, Japan, November 14-16, 1994, 59.

[7] E. Pedroni, Beam Delivery, Proc. 1st Int. Symposium on Hadrontherapy, Como, Italy, October 18-21, 1993, 434.

[8] J. M. Slater, J. O. Archambeau, J. F. Dicello, J. D. Slate, Proton Beam Irradiation: Toward Routine Clinical Utilisation, Proc. 1st Int. Symposium on Hadrontherapy, Como, Italy, October 18-21, 1993, 130.

[9] T. Ogino et al., Proton Treatment Facility at NCC, Kashiwa, Japan: A Progress Report, in: J. Sisterson (ed.), Particles #20, July 1997, or J. Sisterson (ed.), Abstracts of the XXVI PTCOG Meeting, Boston, MA, USA, April 30 - May 2, 1997, 22.

[10] J. Janik, M. Müller, Nucl. Instr. and Meth. B84 (1994) 117.

[11] L. G. Vorobiev, H. Wollnik, M. Winkler, GSI-Report-97-06 (1997).

[12] M. Pavlovic, GSI-Preprint-95-83 (1995).

[13] M. Pavlovic, Recent Development of Gantry Design Activities at GSI Darmstadt, Proc. 5th Int. European Particle Accelerator Conference EPAC96, Sitges (Barcelona), Spain, June 10-14, 1996, 2665.

[14] A. Broadbent, private communication, Oxford Instruments, August 1997.

[15] F. Wenz, private communication, University Clinic of Heidelberg, June 1997.

[16] M. Pavlovic, An Alternative Solution for a Light-Ion Cancer-Therapy Gantry, GSI-Preprint, to be published.

A linear accelerator for oncological protontherapy: TOP-LINAC

S. Frullani[1], L. Picardi[2], C. Ronsivalle[2], A. Vignati[2]

[1]Physics Laboratory, Istituto Superiore di Sanità, Rome, Italy; [2]Innovation Department, ENEA, Frascati, Italy

The TOP LINAC [1] is the linear accelerator of the TOP (Terapia Oncologica con Protoni, Oncological Protontherapy) project launched by the Italian National Institute of Health (Istituto Superiore di Sanità, ISS) to explore in collaboration with the biggest Oncological Hospital in Rome (Istituto Regina Elena, IRE) the potentialities of the therapy with accelerated protons and establish guide lines for the application of this new type of radiotherapy in comparison with the more traditional electron and xrays radiotherapy. In addition, the project aims to verify the feasibility of a practical design of a compact accelerator, that could be replicated and installed in some already existing Italian hospitals to diffuse the protontherapy on the National territory.

The concept of a compact accelerator for protontherapy applications bore within the Italian Hadrontherapy Collaboration (TERA Collaboration) [2], having realised that to fully exploit the potentiality of the new treatment at a National level, apart a design for an integrally new hospital facility hosting a relatively large accelerator having also light ions capability, a design should also have been developed for a small proton accelerator that could be housed in already existing hospitals, requiring then a limited space and limited shielding.

The TOP project aims to build a proton accelerator that can give the possibility to develop some other research activity related to biomedical studies that could be carried out with proton beams. Moreover this facility could provide a beam for production of PET radioisotopes in order to allow the use of this powerful diagnostic and clinical tool in the area.
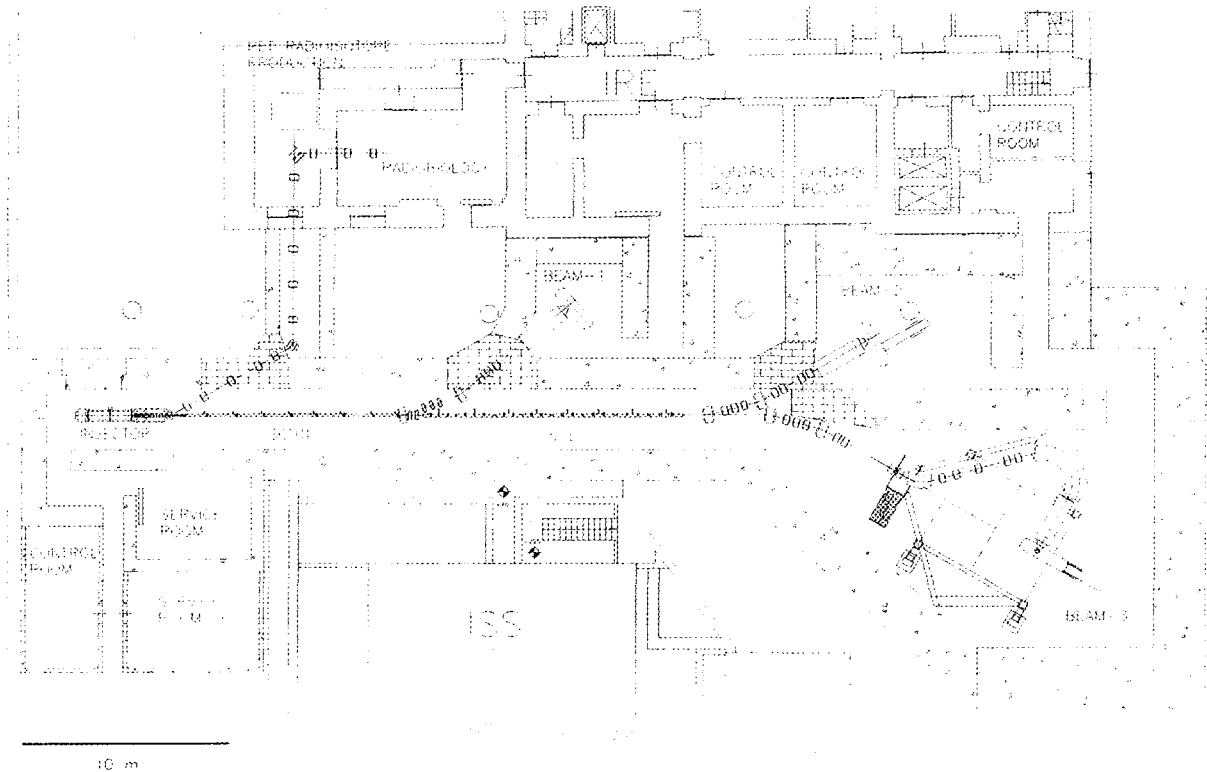

Fig. 1 The TOP linac layout

The TOP project benefits of many Italian scientific institutions already active in the field of accelerators and biomedical research, like ENEA, INFN, TERA, IRE, Universities, and other

oncological hospitals. In particular the accelerator is developed in strong collaboration with ENEA whose design was adopted by the Scientific Committee of the TOP Project.

The figure 1 shows the TOP Linac layout in the ISS area in Rome.

It is a sequence of linear accelerators. It is composed by a 7 MeV injector working at low frequency, 428 MHz, a subharmonic of 3 GHz, followed by a 3 GHz accelerating section, 10 m long, named SCDTL (Side Coupled Drift Tube Linac, from the type of the accelerating structure) that accelerates the beam up to 65 MeV. The section is divided into 8 modules powered by a single klystron whose power is divided by power dividers. The 65 MeV beam will be used for the eye melanoma treatment or injected to be accelerated by the subsequent section.

The last accelerating section, boosting the energy to 200 MeV, and providing a variable energy beam is composed by other 8 modules of Side Coupled Linacs whose cavities, of course have a length equal to $\beta\lambda/2$ that for the proton velocity in the interval 65 - 200 MeV are shorter than 5 cm at 2.998 GHz. The linac ends with the gantry which will rotate the beam around the patient and by means of a deflecting magnetic system.

As to the 7 MeV injector, the triple use (protontherapy linac injector, PET production and radiobiology experiments) needed by the ISS program, requires a versatile machine. PET radionuclide production requires much higher currents (20-100 μA) than the other two. The main injector characteristics are reported in table 1.

Table 1. Main Injector Parameters

	Protontherapy	PET	Radiobiology
Energy, MeV	7	7	7
Max. Ave. Current, μA	0.05	100	0.005
Rep Frequency, Hz	400	100	10 - 400
Pulse Duration, μs	5	100	5
RF Frequency, MHz	428.3 or 750		

The rest of the machine works with 3 GHz accelerating structures. Applying the 3 GHz technology to the proton acceleration is surely very innovative, because only low frequency linac were used to this purpose up to now.

The development of the SCDTL [3] structure that provides acceleration in the medium energy range is key issue in the TOP Linac design. This structure is composed of several little drift tube linacs coupled together in a standing wave side coupled arrangement by coupling cavities, in correspondence of which, on the axis is placed a permanent magnet quadrupole for the beam focusing.
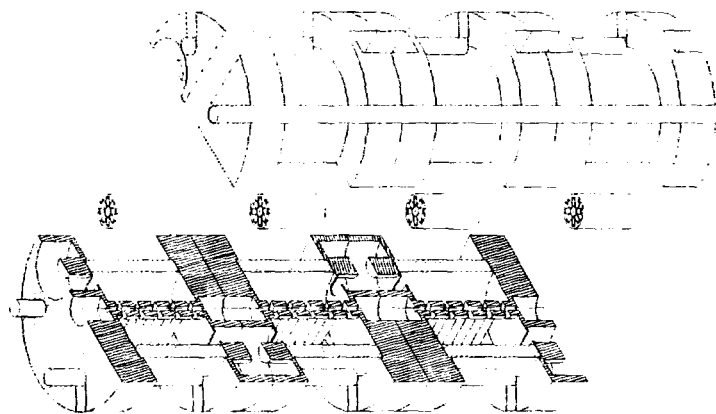

Figure 2. Longitudinal section of three tanks of the SCDTL

Some cold models have been constructed and measured on the microwave bench. They have shown shunt impedance and axial electric field distribution (see figure 3) behaving in agreement with SUPERFISH design values.
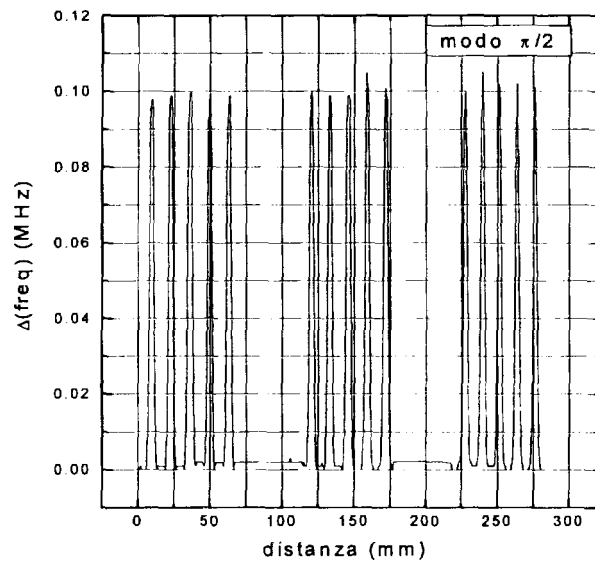
Figure 3 - Axial electric field measured by the bead pull method. On the vertical axis is the frequency variation of the resonance (proportional to the axial electric field squared) vs axial position

Cooling of the drift tubes and stems is one of the major problems in the structure development, and large effort is being carried out to find a practical satisfactory solution. Eight permanent magnet quadrupoles have been acquired and checked for tolerances, that are within design prescription.

SCL design is in principle simpler than SCDTL because it uses a standard structure, but at these frequencies it has been applied up to now only to electrons, and a development is therefore necessary. However a TERA program exists called LIBO, that is developing a 3 GHz linear accelerator to boost the energy of the existing cyclotrons, and it is foreseeable that we can take advantage of these studies.

The status of the project will be extensively reported in the oral presentation and in the related paper.

References

1) *"The TOP-LINAC for the Protontherapy Project of the Italian National Institute of Health (ISS)"* S. Frullani, M. Grandolfo, L. Mancini, L. Picardi, C. Ronsivalle, A. Vignati, Proc of the 2nd International Symposium on Hadrontherapy, Geneva, Sept. 1996, to be published.
2) *"The RITA Network and the Design of Compact Proton Accelerators"*, U. Amaldi, M. Grandolfo, L. Picardi editors, Aug. 1996, Publ. by INFN-LNF
3) *"Measurement of cavities of the side coupled drift tube linac (SCDTL)"*, L. Picardi, C. Ronsivalle, A. Vignati, Proc. EPAC96, Sitges, July 1996.

CONTRIBUTERS

Amaldi, Ugo (Chair) (CERN, Geneva, Switzerland)	I1
Ando, Koichi (Nat. Inst. Rad. Science, Chiba, Japan)	D1
Auberger, T. (Klin. für Strahlentherapie, Munich, Germany)	I3
Bathelt, Belinda (GSI Darmstadt, Germany)	G10
Belli, Mauro (INFN, Rome, Italy)	A4
Boehringer, Terence (PSI Villingen, Switzerland)	H6
Brusasco, Caterina (GSI Darmstadt, Germany)	G12
Bonazzola, G.C. (INFN, Torino, Italy)	G11
Campa, Alessandro (Inst Sup. San. and INFN, Roma, Italy)	E3
Casnati, E. (Uni. Ferrara and INFN, Italy)	G13
Choudhary, D. (Jawaharlal Nehru Univers., New Dehli, India)	D7
Coray, Adolf (PSI, Villingen, Switzerland)	G2
Debus, Jürgen (Univers. Heidelberg, Germany)	D2
Distel, L. (Univers. Erlangen-Nürnberg, Germany)	D5
Donetti, Marco (INFN, Torino, Italy)	G6
Durante, Marco (Univers. Federico „Neapel II", Italy)	C2
Dusemund, Bernd (Univers. d. Saarlandes, Germany)	A6
Laitano, R.F. (ENEA, Rome, Italy)	G8
Fournier, Claudia (GSI, Darmstadt, Germany)	D3
Fritsch, Mirjam (Uni Erlangen, Germany)	D13
Frullani, S. (Ist. Sup. San. Rome, Italy)	I6
Füssel, Karin (GSI, Darmstadt, Germany)	C3
Gargioni, E.	G14
Geiss, Oliver (GSI, Darmstadt, Germany)	G7
Grossi, Gianfranco (Inst Sup. San. and INFN, Roma, Italy)	D11
Guerra, Antonio (ENEA, Rome, Italy)	G9
Hartmann, Günter (DKFZ Heidelberg, Germany)	G5
Heeg, Peter (Uni. Klin. Heidelberg, Germany)	G15

Rosetti, Maurizio
(ENEA, Rome, Italy) G4
Rothkamm, Kai
(Univers, Gießen, Germany) A5
Rydberg, Björn
(LBNL Berkeley, USA) A2
Schäfer, Manfred
(DLR Cologne, Germany) B3
Schardt, Dieter
(GSI, Darmstadt, Germany) F6
Schilling, Christian
(PSI Villingen, Switzerland) H7
Schimmerling, Walter
(NASA, Washiington, USA) B1
Schmidt, Paul
(Strahlenzentrum,Univers. Gießen, Germany) C9
Scholz, Michael
(GSI, Darmstadt, Germany) E2
Schonert, Wolfgang
(GSI, Darmstadt, Germany) A10
Slater, J.
(Loma Linda, USA) H3
Spiro, Ira
(Harvard Uni. Boston, USA) H2
Srivastava, Mayank
(Jawaharlal Nehru Univers., New Dehli, India) D9
Streibel, Thomas
(Univers. Siegen, Germany) B2
Takada, Yoshihisa
(Uni. Tsukuba, Japan) F3
Tano, Shigemitsu
(Jap. Atom. Energ. Res. Inst, Takasaki, Japan) C7
Taucher-Scholz, Gisela
(GSI, Darmstadt, Germany) A3
Tilly, Nina
(Uni. Stockholm, Sweden) E6
Touati, A.
(Univers. Paris 7 and 6, France) D10
Tsujii, Hirohiko
(Nat. Inst. of Rad. Snc. Chiba, Japan) H4
Voss, Bernd
(GSI Darmstadt, Germany) H8
Watanabe, Hiroshi
(Jap. Atom. Res. Energ. Inst., Takasaki, D4
Japan)
Weber, Uli
(GSI, Darmstadt, Germany) F4
Wei, Zengquan
(Chin. Aca. of Sc. Lanzhou, China) A7
Weiland, Barbara
(Uni. des Saarlandes, Homburg, Germany) A11
Yatagai, Fumio
(Inst. Phys. Chem.Res.,Saitama, Japan) C5
Zukowski, Daniel
(Uni Mainz, Germany) D12

Rainer Hinz
(FZ Rossendorf, Dresden, Germany)   H9
Hoffmann, Anne-Kathrin
(Uni. des Saarlandes, Homburg, Germany)   A12
Höglund, Erik
(Uppsala Univers., Sweden)   A8
Bryant, P.J.
(CERN Geneva, Switzerland)   I4
Jäkel, Oliver
(DKFZ, Heidelberg, Germany)   F1
Kanai, Tatsuaki
(Chiba, Japan)   G1
Katz, Robert
(Univers. of Nebraska, USA)   E5/C8
Keller, Daniela
(GSI, Darmstadt, Germany)   A9
Kellerer, A.
(LMU, Munich, Germany)   E1
Kiefer, Jürgen
(Strahlenzentrum,Univers. Gießen, Germany)   C4
Kraft, Gerhardt
(GSI Darmstadt, Germany)   I2
Krämer, Michael
(GSI, Darmstadt, Germany)   F2
Lokajicek, Milos
(Acad. of Sc. Prague, Czech Republic)   D6
Menapace, Enzo
(ENEA, Bologna, Italy)   F5
Mitaroff, Angela
(GSI, Darmstadt, Germany)   F8
Moosburger, Martin
(Ludwig-Max.-Univers. München, germany)   D8
Moosburger, Martin
(LMU Munich, Germany)   H10
Munkel, Gudrun
(PSI Villingen, Switzerland)   H1
Onori, S.
(Ist. di San., Rome, Italy)   G3
Ottolenghi, Andrea
(Uni. Milano, INFN, Italy)   E4
Pavlovic. M.
(GSI Darmstadt, Germany)   I5
Pawelke, Jörg
(FZ Rossendorf, Dresden, Germany)   H5
Petrovic, Ivan
(Vinca, INS, Belgrade, Yugoslavia)   F7
Prise, Kevin
(Mount Vernon Hospital, Northwood, UK)   A1
Radojcic, Marija
(VINCA Belgrade, Yugoslavia)   G16
Ramm, Ulla
(Uni. Klin. Frankfurt, Germany)   G17
Rink, Hermann
(Univers. Bonn, Germany)   C6
Ritter, Sylvia
(GSI, Darmstadt, Germany)   C1